UNIVERSITÉ DU QUÉBEC

THÉSE PRÉSENTÉE À
L'UNIVERSITÉ DU QUÉBEC À CHICOUTIMI
COMME EXIGENCE PARTIELLE
AU DOCTORAT EN INGÉNIERIE

PAR
ZSOLT PÉTER

MODELLING AND SIMULATION OF THE ICE MELTING PROCESS ON A CURRENT-CARRYING CONDUCTOR

MODÉLISATION ET SIMULATION DE PROCESSUS DE DÉLESTAGE DE GLACE PAR FONTE SUR UN CONDUCTEUR EN PRÉSENCE DE COURANT

AVRIL 2006

Bibliothèque Paul-Émile-Boulet

UQAC Université du Québec à Chicoutimi

Mise en garde/Advice

Afin de rendre accessible au plus grand nombre le résultat des travaux de recherche menés par ses étudiants gradués et dans l'esprit des règles qui régissent le dépôt et la diffusion des mémoires et thèses produits dans cette Institution, **l'Université du Québec à Chicoutimi (UQAC)** est fière de rendre accessible une version complète et gratuite de cette œuvre.

Motivated by a desire to make the results of its graduate students' research accessible to all, and in accordance with the rules governing the acceptation and diffusion of dissertations and theses in this Institution, the **Université du Québec à Chicoutimi (UQAC)** is proud to make a complete version of this work available at no cost to the reader.

L'auteur conserve néanmoins la propriété du droit d'auteur qui protège ce mémoire ou cette thèse. Ni le mémoire ou la thèse ni des extraits substantiels de ceux-ci ne peuvent être imprimés ou autrement reproduits sans son autorisation.

The author retains ownership of the copyright of this dissertation or thesis. Neither the dissertation or thesis, nor substantial extracts from it, may be printed or otherwise reproduced without the author's permission.

ABSTRACT

The general objective of this PhD study is to develop mathematical models that determine the current and energy requirements of thermal de-icing and ice prevention methods based on the Joule effect under various meteorological and current transmission conditions. The analytical model predictions were compared to experimental results for the purpose of assessing the predictive power of the models.

First, an ice prevention model was established to calculate the minimum current intensity required to inhibit ice formation on a single power line conductor. Correction factors, taking into account water runback on the conductor surface as well as deviation of the water layer from the thermal equilibrium state, are introduced for three specific ACSR conductors. The model results accord well with the measurements taken in an icing research wind tunnel. In order to complete the model, it was necessary to assess the overall heat transfer coefficient (HTC) for stranded conductors. The overall HTC for bare overhead conductors with different surface geometries was obtained from measurements and from numerical simulations.

Secondly, a computational model using finite differences was developed which calculates the current and energy requirements for de-icing partially ice covered conductors. Two heating techniques were analyzed, namely Joule heating by ac current and by impulse current, for a large number of atmospheric parameters. Both techniques can be used with different strategies depending on the time of interaction in the ice accretion process. In order to complete the model, the assessment of radial equivalent thermal conductivity of the ACSR conductor is required. This thermal conductivity was estimated from both experiments and various theoretical models.

Thirdly, experimentally validated analytical approaches have been proposed to determine the shedding time and corresponding energy required to de-ice a completely ice covered conductor by heating with increased nominal ac current. This procedure is able to give a fast estimation of the required Joule heat to totally remove the ice around the conductor as a function of the different influencing factors.

This thesis presents experimentally validated mathematical models, which can efficiently be used to calculate the current and energy requirements of de-icing conductors or of preventing ice accretion on a single power line conductor.

RÉSUMÉ

L'objectif général de cette thèse de doctorat est de développer des modèles mathématiques permettant d'évaluer l'énergie requise pour le dégivrage thermique par effet Joule des conducteurs aériens de transport de courant et ainsi prévenir la formation de glace dans des conditions météorologiques et de transmission électrique variées. Les prédictions de ces modèles analytiques ont été validées expérimentalement dans le but d'évaluer la puissance prédictive de ces modèles.

Premièrement, un modèle a été établi pour calculer l'intensité de courant minimum nécessaire pour empêcher la formation de glace sur un conducteur de ligne à haute tension. Des coefficients de correction, tenant compte de d'eau de ruissellement sur la surface du conducteur, de même que la dérivation du film d'eau à partir de l'état d'équilibre thermique, ont été introduits pour trois conducteurs spécifiques. Les résultats des modèles s'accordent bien avec les observations effectuées dans des conditions correspondantes simulées dans une soufflerie réfrigérée. Afin de compléter le modèle, il était nécessaire d'évaluer le coefficient moyen de transfert de chaleur pour les conducteurs toronnés. Ce coefficient a été obtenu pour des conducteurs nus de lignes aériennes avec différentes géométries de surface, en utilisant des mesures et des simulations numériques.

Deuxièmement, un modèle basé sur le principe des différences finies a été développé pour calculer le courant et l'énergie requis pour le dégivrage des conducteurs partiellement couverts de glace. Deux types de chauffage thermique par effet Joule ont été analysés, le courant alternatif et le courant d'impulsion, et ce, pour un grand nombre de paramètres atmosphériques. On a trouvé que ceux deux techniques de chauffage peuvent être utilisées selon des stratégies différentes dépendamment du temps d'interaction nécessaire au cours du processus d'accumulation de glace. Afin de compléter le modèle, il a fallu évaluer la conductivité thermique radiale équivalente des conducteurs toronnés par le moyen de modèles théoriques avec validation expérimentale.

Troisièmement, des approches analytiques validées expérimentalement ont été proposées afin de déterminer le temps et l'énergie nécessaires pour le dégivrage d'un conducteur complètement recouvert de glace en utilisant la chaleur dérivée d'un courant alternatif nominal augmenté. Cette procédure peut donner une estimation rapide de la chaleur par effet Joule exigée pour enlever totalement la glace autour d'un conducteur en fonction des différents paramètres l'influençant.

En conclusion, cette thèse propose des modèles mathématiques validés expérimentalement, qui peuvent être utilisés efficacement pour calculer le courant et l'énergie requis pour le dégivrage des conducteurs à haute tension ou pour prévenir l'accumulation de glace sur ceux-ci.

ACKNOWLEDGEMENTS

I would like to express my thanks to the director of my Ph.D. program, Professor Masoud Farzaneh, who is the Chairholder of the NSERC/Hydro-Quebec Industrial Chair on Atmospheric Icing of Power Network Equipment (CIGELE) and the Canada Research Chair on Atmospheric Icing Engineering of Power Network (INGIVRE) at the Université du Québec à Chicoutimi. He has contributed his talent and energy not only to reviewing this thesis carefully, but directing my work for many years.

I express particular appreciation to Professor László I. Kiss, the co-director of the project. His philosophy and humble attitude towards research I have adopted as my own. His ideas and the discussions we have had have helped immensely with this study.

I am grateful to the researchers, professionals and technicians at CIGELE, who supported me in this study with personal support, technical support and suggestions. These great people include Dr. László E. Kollár, Dr. Anatolij R. Karev, Dr. Christophe Volat, Dr. Konstantin Savadjiev, Dr. Issouf Fofana, Xavier Bouchard, Pierre Camirand, Denis Masson and Jean Talbot. I am thankful for the time they have taken with me. Thanks also to Elise Mitchell for her work in editing this thesis.

I am extremely pleased to have participated in the Ph.D. program offered by the Université du Québec à Chicoutimi, where I have developed my skills and met excellent friends.

Last, but not least, I am also most grateful to my fiancée, Erika Deák, and to my family for the patience they have shown during my absence due to my work and for their unconditional support and encouragement.

CONTENTS

LIST OF FIGURES

LIST OF TABLES

LIST OF SYMBOLS

Latin letters

a	Contact radius, *m*
A	Cross-section, m^2
	Surface, m^2
Bi	Biot number, *1*
B	Deformation factor, *1*
c	Specific heat, *J/kgK*
C	Constant of integration, *1*
d	Diameter, *m*
D	Diameter, *m*
E	Collection efficiency, *1*
	Energy, *J*
	Modulus of elasticity, *Pa*
E.f.	Expansion factor of inflation layers, *1*
f	Frequency, *Hz*
Fo	Fourier number, *1*
H	Height, *m*
i	Current density, A/m^2
I	Electric current, *A*
h	Heat transfer coefficient, W/m^2K
k_e	Equivalent thermal conductivity, *W/mK*
k_{ce}	Effective contact thermal conductivity, *W/mK*
k	Thermal conductivity, $W/m \cdot K$
k_s	Skin effect coefficient, *1*
k_t	Transformer effect coefficient, *1*
K	Constant of integration, *1*

l	Latent heat, *J/kg*
L	Length, *m*
m	Mass, *kg*
M	Differential modulus, *1*
n	Number of strands in the conductor, *1*
N	Normal force on strands, *N*
	Number of prismatic layers, *1*
	Number of nodes, *1*
Nu	Nusselt number, *1*
p	Pressure, *Pa*
P	Porosity, *1*
Pr	Prandtl number, *1*
q	Heat flux, W/m^2
q_w	Volumetric heat source, W/m^3
Q	Heat transfer rate, *W*
r	Radius, *m*
	Recovery factor, *1*
r_i	Radius of the outer surface of the ice, *m*
R_L	Electrical resistance of 1 m long conductor, Ω/m
R	Radius, *m*
	Thermal resistance, $m^2 \cdot K/W$
Re	Reynolds number, *1*
S	Shape factor of the cylinder, *1*
T_∞	Air temperature, *K*
T_w^*	Critical temperature of the ice layer's outer surface, *K*
T_{melt}	Melting temperature of ice, *K*
T	Temperature, *K*
T_m	Peak time, *s*
Tu	Turbulence intensity
v	Velocity, *m/s*

V	Velocity of free stream, *m/s*
	Volume, m^3
W	Liquid water content (LWC), kg/m^3
y^+	Dimensionless distance of first node, *1*
Δt	Time step, *s*
ΔT_0	Reference temperature difference through the ice sleeve, *K*
ΔU	Potential difference between the surfaces of the hollow cylinder, *V*
Δy	Thickness of prismatic elements, *m*
x, y	Cartesian coordinates

Greek letters

α	Angle from stagnation point, *degree*
	Thermal diffusivity, m/s^2
α_{20}	Temperature coefficient at 20 °C, *1/K*
β	Constant of SST model
β^*	Constant of SST model
δ	Penetration depth, *m*
ξ	Dimensionless coordinate, *1*
θ	Dimensionless temperature, *1*
κ	Correction factor, *1*
μ	Magnetic permeability, *H/m*
	Dynamic viscosity, Ns/m^2
ν	Kinematic viscosity, m^2/s
	Poisson's ratio, *1*
ρ	Electric resistivity, Ωm
	Mass density, kg/m^3
σ	Electric conductivity, $1/\Omega m$
τ	Time, *s*

Subscripts

a	Air
al	Aluminium
c	Conductor
eq	Equivalent
f	Fluid
g	Gas
i	Ice
	Location along radius
imp	Impulse
k	Time step
KLL	Krischer Low Limit model
m	Maximum
melt	Melting point
s	Auxiliary node
	Solid
	Surface
w	Outer surface, wall
	Wetted
0	Reference, origin
∞	Air, free stream

Superscripts

*	Critical
	Reference case

CHAPTER 1

INTRODUCTION

1.1 The problem

In many cold regions atmospheric icing is responsible for damage to a large number of infrastructures including overhead power lines and communication networks. It is common knowledge that in these regions significant ice layers may accumulate on the line cables and conductors, and can produce two types of problem. One of the problems is related to the wind-induced instability known as galloping, associated with aerodynamically unstable ice profiles [52]. The other problem involves the extreme ice and wind-on-ice loads on overhead power lines. Both phenomena cause fatigue of the line conductors, various types of structural damage and, in the worst-case scenario, it triggers the breakdown of the conductors. The consequences of the ice storm that hit Québec and the Eastern part of Ontario in January 1998 are well known. Such ice storms hit also Asian and European countries and even some southern US states such as Arkansas and Texas (December 2000). These ice storms cause damage to power networks, produce electrical outages, and increase the risk to human life. Damage to the power distribution system alone cost several hundreds of millions of dollars after the Quebec ice storm.

In order to bring electrical lines back into service, limit damages, and assure continuous electrical service to sustain human activities in hospitals, schools and other public areas, an adequate design for de-icing or anti-icing needs to be developed. Before the ice storm in

1998 around 15 techniques had been developed; new technologies to remove the ice or to assuring anti-icing protection were also in different stages of development. These methods can be classified in four categories [31]:

- Thermal techniques
- Mechanical techniques
- Passive techniques
- Other methods (based on different physical mechanisms)

Since the present study is in the category of thermal techniques, only the main heating techniques are overviewed in the following section. The following three methods have been specifically developed for removing ice from overhead power lines:

- Over-intensity of current
- Short circuit
- Ferromagnetic wires

All three techniques have already been successfully applied.

By raising current intensity or short-circuiting overhead lines, a higher current will flow in the conductor than the nominal current. These two techniques are based on heating the conductors by Joule effect. Ferromagnetic wires have also been developed in which eddy current is induced. These techniques are operational, but require a high energy level (0.1÷1.1 kW/m) [31].

However, artificially produced ice shedding must be performed carefully, because it can cause failures in the electrical lines. A large unbalanced force is produced when the ice falls off non-simultaneously [15]. This unbalanced tensile force can produce structural damage to the electrical conductors. It was also observed that when large pieces of ice fall off suddenly, the electrical conductor can clash to the ground wire, thereby short-circuiting the electrical line [15].

The aforementioned reasons are why more economical, practical, and efficient techniques are being researched. To develop such methods, the physics of ice shedding and accumulation and the effect of different factors that influence ice shedding are both important areas of research.

The electrical heating of aluminium steel-reinforced conductors (ACSR) by Joule effect offers a potential method for ice accretion mitigation. This study investigates two techniques of Joule heating: raised nominal current and impulse current. Also, two mitigation methods based on electrical heating of conductor are analysed: the ice prevention method and the de-icing method. The ice prevention method prevents ice formation on the conductor surface by keeping the conductor surface temperature above the freezing point. This prevention method should be activated for a certain time both before and during freezing precipitation. The de-icing method allows an ice layer to form on the conductor. The ice layer may be removed after or during the icing event. Both methods and strategies are analysed as a function of various influencing parameters (current and atmospheric conditions) from an energy conservation standpoint.

1.2 Objectives

The general objective of this study is the development of mathematical models that determine the current and energy requirements for thermal de-icing as well as ice prevention methods under various meteorological and current transmission conditions. In the following text the detailed objectives of this PhD study are introduced.

A. Determination of the critical current intensity necessary to prevent ice accretion on overhead conductors

This objective concerns the determination of the electric current requirements for an anti-icing technique based on the Joule effect. The minimum current intensity needed for preventing ice formation depends on certain conductor parameters, including external nominal diameter, electrical resistance, and surface geometry (number and diameter of external strands). It also depends on meteorological conditions, such as air temperature, wind velocity, and liquid water content. This study comprises the elaboration of a mathematical model and the laboratory experiments necessary for validation for the purpose of investigating the influence of these parameters.

B. Determination of the current intensity needed for the de-icing of a partially ice-covered conductor

Two main cases can be distinguished: a) the conductor is partially covered with ice along its perimeter, b) the conductor is completely covered with ice. This part of the study focuses on case a), when the ice accumulates on a non-rotating conductor or the ice

accumulation is in the starting period, when the ice is only accreted on the windward side of the conductor.

Two electrical heating techniques are studied, namely Joule heating by raising the nominal ac current and Joule heating by impulse current. Mathematical models are developed for both heating techniques. The energy requirements are analysed under a large number of influencing parameters including impulse peak value/electric current magnitude, equivalent frequency, wind velocity, equivalent thermal conductivity, ice thickness and air temperature.

C. Determination of the current intensity needed for the de-icing of a completely ice-covered conductor

This objective is related to the energy required to shed a symmetrical ice sleeve from an electrical conductor (case b) by Joule heating with increased nominal ac current. The current required to trigger and maintain melting until the ice deposit is completely gone depends on a large number of parameters; those investigated include air temperature, ice thickness, electrical resistance of the conductor and magnitude of increased current. This procedure allows, as a function of the different influencing factors, a quick estimation of the Joule heat required to completely remove the ice around the conductor.

D. Analysis of the convective heat transfer around a bare overhead conductor

An assessment of the overall heat transfer coefficient for stranded conductors is required in order to complete the ice prevention model. Therefore, the objective of this part of the study is to determine the convective heat transfer around stranded and twisted

cylindrical conductors with different surface geometries. The local convective heat transfer coefficient distribution along the perimeter of stranded conductors and the corresponding mean convective heat transfer are computed from numerical simulation results. These numerical results are validated by wind tunnel experiments.

E. Determining the equivalent radial thermal conductivity of an ACSR conductor

It is known that the heat conduction in stranded conductors is quite complex, mainly due to its heterogeneous structure. In order to complete the mathematical de-icing models, it is necessary to assess the radial-thermal conductivity of an ACSR conductor. Consequently, theoretical models of various complexities are established for the purpose of estimating an equivalent radial thermal conductivity. The theoretical models take into account various influencing parameters including strand diameter, contact radius between adjacent strands, and contact pressure.

1.3 Methodology

A. Determination of the critical current intensity preventing ice accretion on conductors

First, an analytical model was established to calculate the minimum energy required to prevent ice accumulation on overhead power line conductors, based on the Joule heating effect and taking into account different conductors and atmospheric parameters. The general heat balance of an icing conductor was adapted from relevant literature, in which certain improvements were proposed in order to permit ice inhibition calculations.

Correction factors were introduced in the heat loss term, accounting for the influence of impinging water droplets. The analytical model was validated under a wide range of current and atmospheric conditions for various types of ACSR conductors. A total of 80 tests were carried out in the closed CIGELE icing research wind tunnel for the purposes of this study.

B. Determination of the current intensity needed for the removal of a partially ice-covered conductor

The model, which calculates the required current intensity for the removal of partially accreted ice by impulse heating, was constructed from various modules. In the first step, a so-called steady-state calculator calculates the initial temperature distribution in a conductor-ice composite under nominal ac current and given atmospheric conditions. The results are the input parameters in the core module, which solves the finite difference equations of the corresponding transient heat conduction problem. Naturally, the core module as well as the steady-state calculator requires the current intensity distribution for impulse current and for 60 Hz, ac current, respectively. The non-uniform current intensity distribution is calculated using a commercial finite element code, namely Maxwell SV. The outputs of the core model are the shedding time, the number of required impulses to shed the ice sleeve and the temperature distribution of the conductor-ice composite along the radius. In the case of Joule heating by raised nominal current, the calculation procedure is simpler, as current distribution due to impulses and the steady state are not calculated.

C. Determination of the current intensity needed for the de-icing of completely ice-covered conductors

Generally, two main periods can be distinguished during de-icing of completely ice-covered conductors. The first, or transient, period is from the start of the Joule heating until the melting conditions are reached at the conductor-ice interface. The second, or melting, period consists of the complete melting of the ice sleeve. The total shedding duration and the corresponding required energy can be calculated as simply the sum of the two periods. The transient period can be calculated using the finite difference method as presented in previous sections. The melting period is obtained analytically; two different approaches for calculating the melting period are developed. The experimental study was performed to validate the analytical approaches as well as to better understand the melting process on Joule-heated conductors.

D. Analysis of the convective heat transfer around a bare overhead conductor

The overall heat transfer coefficient around various ACSR conductors is estimated from wind tunnel measurements. This estimation method is based on the heat balance of an electrically heated conductor under steady state and dry airflow conditions. Furthermore, the numerical prediction of convective heat transfer around smooth, stranded and twisted cylindrical conductors is obtained by using a computational fluid dynamic (CFD) code, namely Ansys CFX-10. The estimated overall heat transfer coefficient is obtained from numerically calculated local heat transfer coefficient distribution.

E. Determining the equivalent radial thermal conductivity of ACSR conductors

The equivalent radial thermal conductivity is established from an experimental study performed in the CIGELE wind tunnel. It is also estimated by adapting different theoretical models found in relevant literature as well as conductivity models developed by the candidate. Furthermore, a qualitative analysis based on an analogy with electric conductivity was performed.

CHAPTER 2

LITERATURE OVERVIEW AND FIRST ESTIMATIONS

2.1 Brief literature overview

While ice accumulation is a relatively well-researched area, much less work has been done on the ice melting process on a current-carrying conductor. CIGELE, however, is active in this field, the first work has been the subject of a Ph.D. thesis [5].

Basically, three main methods of investigations into the ice shedding process exist:

1. Developing a mathematical computation model
2. Experimental analysis of ice shedding using a closed or open wind tunnel
3. Field measurements of shedding rate, performed simultaneously with the collection of the meteorological variable

The first method involves a theoretical model that describes the shedding/melting process in order to better understand the physical mechanisms. These numerical models require as input the meteorological variable associated with shedding/melting events. Frequently the meteorological conditions change during a short period, and it becomes difficult to determine the appropriate input data.

The wind tunnel experiments, the second method, have the advantage in that the flow and thermal conditions can be controlled and measured. Therefore, the influence of flow

and thermal parameters can be determined. However, it is difficult to achieve a one-to-one correspondence between real and experimental conditions [52].

The third method involves a large database on ice shedding. These databases can be used to determine the input parameters for the mathematical model or to validate the numerical model. Unfortunately the installation of such a measurement site is costly.

References [15] and [16] analyzed the conditions of the conductor ice shedding experimentally. Data on ice shedding of non-energized conductor have been collected for the three consecutive winter season at the outdoor experimental line. As a result of that three different mechanisms of the ice shedding (melting, sublimation, mechanical breaking) were characterized by specific atmospheric conditions.

Poots in [52] organized the developed theoretical models of accretion kinetics in a systematic way. The models are based on principles of heat and mass transfer using mathematical and numerical techniques. He also gives an excellent overview of the knowledge of ice and snow accretions to 1996.

A mathematical model based on the boundary element method was developed and applied successfully by Bouamoul [5] for the analysis of ice melting on overhead power lines. That study deals with natural ice shedding; therefore, the effect of external convective heat transfer on the phase change problem in two-dimensional cylindrical coordinate system is determined, but without an electric current in the conductor. The model was applied for symmetrical ice deposits around the conductor.

Later in the candidate's Master's thesis [48], ice melting was also analyzed and three periods of the melting process were defined as follows:

- First period: from the changing of the ambient conditions to the start of melting at one point on the ice deposit.
- Second period: from the end of the first period to the instant at which every point of the ice deposit reaches zero degrees (in [5], this is called the pre-melting period). This period exists only if the heating of the outer ice surface can trigger melting.
- Third period: from the end of the second period to the end of the melting process.

Table 2-1 Melting period durations obtained for 20 mm ice layer on Bersfort conductor under 1000 A electric current and air temperature of 10 °C. The initial thermal condition for the ice-conductor composite was - 10 °C.

Melting periods	Analytical results	Numerical results	
	no heat source	no heat source	with heat source
First period	h=40W/m^{2}K→67min h=60W/m^{2}K→38min	h=40W/m^{2}K→9.3 min h=60W/m^{2}K→5.6 min	h=40W/m^{2}K→7.0min h=60W/m^{2}K→4.7min
Second period	9.6 min	10.8 min	5.56 min
Third period	h=40 W/m^{2}K→8.5 h h=60 W/m^{2}K→5.6 h	-	-

The durations of these periods were estimated both analytically and numerically [48], and Bouamoul also made some numerical and experimental tests in her Ph.D. thesis [5]. Although these results do not consider all influencing factors, they showed that the first and the second periods are negligible in comparison with the third period. It can also be seen

from the numerical results [48] that the inner Joule heat and the augmentation of the external heat transfer shortens these periods (see Table 2-1).

2.2 The effect of the critical radius of the ice sleeve

The thermal resistances due to conduction and convective heat transfer are serially connected. Resistance due to convective heat transfer decreases, as long as the resistance due to conduction increases with increasing external radius as seen in Eq. 2.2-1.

$$R_h = \frac{1}{2 \cdot k_i \cdot \pi} \cdot \ln(r_i / r_c) + \frac{1}{2 \cdot r_i \cdot \pi \cdot h} \qquad \text{Eq. 2.2-1}$$

where k_i is the thermal conductivity of the ice deposit (W/m·K), r_c is the radius of conductor (m), r_i is the radius of the outer surface of the ice deposit (m), h is the heat transfer coefficient (W/m^2K). The first term on the left-hand side is the resistance due to conduction and the other term is thermal resistance due to convection. Hence the addition of these terms has an extreme value, where the thermal resistance has a minimum value. Taking the derivative of heat resistance to external radius and making it 0, the value of the critical radius is obtained (see Eq. 2.2-2 and Eq. 2.2-3).

$$\frac{dR_h}{dr_i} = \frac{1}{2 \cdot \pi \cdot k \cdot r_i} - \frac{1}{2 \cdot r_i^2 \cdot \pi \cdot h} = 0 \qquad \text{Eq. 2.2-2}$$

The solution of Eq. 2.2-2 is as follows:

$$r_{crit} = \frac{k}{h} \qquad \text{Eq. 2.2-3}$$

As shown, the value of the critical radius depends on just two parameters: the thermal conductivity of ice, k_i , and on the convection coefficient, h.

The sum of the serially connected resistances increases with increasing ice thickness only to the point when the external radius of the ice layer reaches the value of the critical radius and decreases after that (see Figure 2.1). As a result of that the required electrical current to trigger melting at the inner ice surface increases with increasing ice thickness (see Figure 2.2), when the convective heat transfer term is small. The opposite occurs when the convective heat is significant (see Figure 2.3).

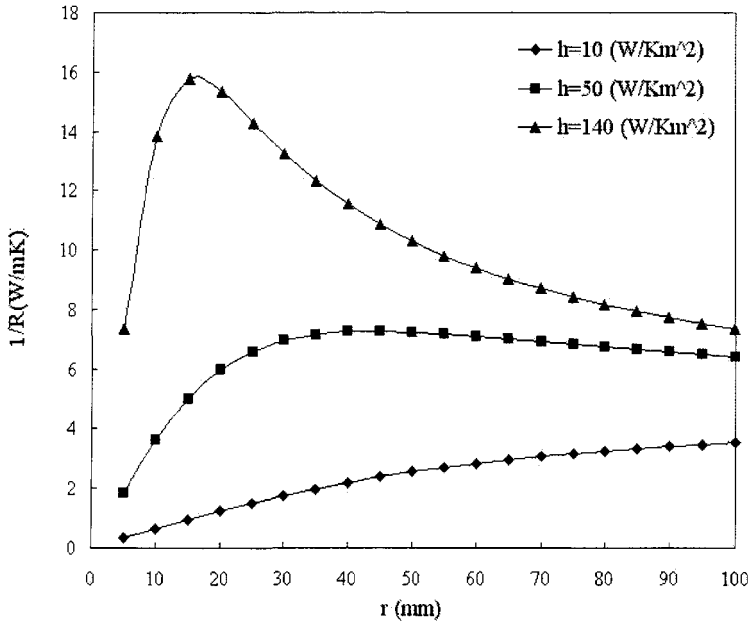

Figure 2.1 Reciprocal thermal resistance of ice deposit as a function of ice layer radius

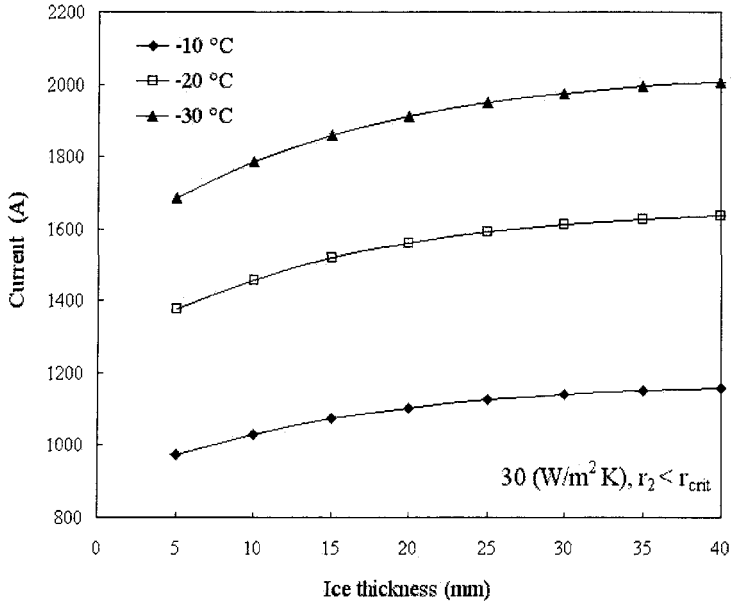

Figure 2.2 Minimum current required to trigger ice melting versus ice thickness on Bersfort conductor at 30 W/m^2K

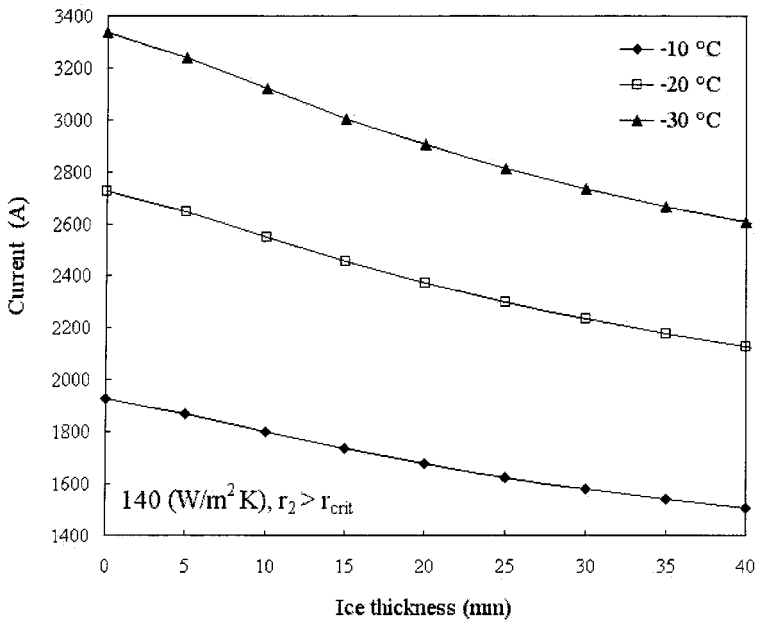

Figure 2.3 Minimum current required to trigger ice melting versus ice thickness on Bersfort conductor at 140 W/m^2K

2.3 Intensity of natural ice melting

The following section investigates the melting intensity of an outer ice surface exposed to convective and solar heating. The problem is assumed to be one-dimensional along a radius. The energy balance during melting is described by Eq. 2.3-1.

$$-\rho \cdot l \cdot dV = h \cdot A \cdot (T_{\infty} - T_{melt}) \cdot d\tau \qquad \text{Eq. 2.3-1}$$

where ρ is the ice density (kg/m^3), l is the latent heat of ice (J/kg), dV is the melted volume (m^3) of ice under dτ time (s), h is the "average" heat transfer coefficient (W/m^{2}K), A is outer surface of ice sleeve (m^2), T_{∞} is the air temperature (K) and T_{melt} is the melting temperature of ice (K). The left side of Eq. 2.3-1 contains the required heat to melt dV (volume of the ice), while the right side shows the thermal heat required to reach the melting at the ice layer surface. The propagation velocity of the melting surface is described in Eq. 2.3-2, obtained by reorganizing Eq. 2.3-1.

$$\frac{dr}{d\tau} = -\frac{h \cdot (T_{\infty} - T_{melt})}{\rho \cdot l} \qquad \text{Eq. 2.3-2}$$

Equation 2.3-2 shows that the outer radius of the ice deposit decreases linearly in time. Thus, Eq. 2.3-2 determines the rate of the melting layer propagation that depends intrinsically on two atmospheric parameters, namely the "average" heat transfer coefficient and the external air temperature. The ice melting rate is also developed in dimensionless form in the candidate's Master's thesis [48].

The de-icing time under natural conditions is estimated using Eq. 2.3-2. A 20 mm thick layer of ice accumulated on 35 mm diameter conductor is assumed. The ice sleeve is perfectly symmetrical and the air temperature is 5 °C. The results are shown in Figure 2.4.

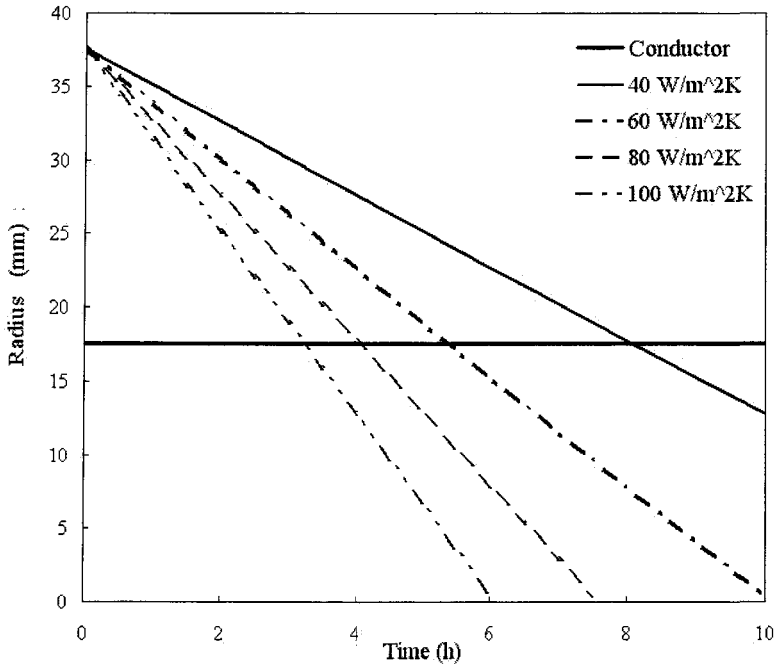

Figure 2.4 Ice melting propagation from outer surface under -5 °C air temperature

CHAPTER 3

ANALYZING THE MELTING CONDITIONS OF ICE ACCUMULATED ON CONDUCTORS

3.1 Introduction

This chapter focuses on reaching ice melting conditions under various heating and atmospheric parameters. Reaching ice melting conditions depends on many parameters, including conductor diameter, mean heat transfer coefficient, electric current, ice thickness, thermo-physical parameters of the ice and the conductor as well as ambient air temperature. In order to reduce the large number of parameters, the melting conditions were examined in dimensionless form. The melting may start at either side or both sides of the ice layer. The ice melting at the outer surface may be triggered by heat convection and/or solar radiation, while the ice could melt on the inner surface due to Joule heating of the electrical conductor. This study assumes perfectly cylindrical and symmetrical ice deposits around the electrical conductor.

A mathematical model based on the finite difference method was developed that describes the heat transfer in the ice-conductor composite. With this model, the transient periods as well as the temperature in every nodal point may be calculated after the desired time steps. The applied explicit schema is more favourable as the implicit schema because its simplicity. Note that in the case of explicit schema the number of nodal points and the chosen time step are not independent from each other. The methodology was applied to

identify those conditions that provoke the melting either on the inner or the outer surface of the ice deposit.

Certain dimensionless numbers are defined in order to regroup a large number of influencing parameters. These are briefly introduced in the following sections.

3.2 Dimensionless numbers of the model

The dimensionless temperature is defined in such a way as to incorporate both the inner Joule heating and the outer heat exchange. In this particular case, when the temperature of the ice-conductor interface reaches the melting point, the heat flow balance is as written in Eq. 3.2-1.

$$\dot{Q} = I^2 \cdot R_L = \left(T_{melt} - T_w^*\right) \cdot S \cdot k_i \qquad \text{Eq. 3.2-1}$$

where I is electric current in conductor (A), R_L is the electrical resistance of 1 m long conductor (Ω/m), T_{melt} is the ice melting temperature (K), T_w^* is the critical temperature of the ice layer's outer surface (K) and k_i is the thermal conductivity of ice (W/mK). The shape factor of the cylinder, S, is defined by Eq. 3.2-2.

$$S = \frac{2\pi}{\ln(r_i / r_c)}, \qquad \text{Eq. 3.2-2}$$

where r_i and r_c are the ice sleeve and conductor radius (m), respectively.

The melting on the inner surface of the ice layer never occurs if the outer ice surface temperature is lower than T_w^* under I electrical current in the conductor (see Figure 3.1).

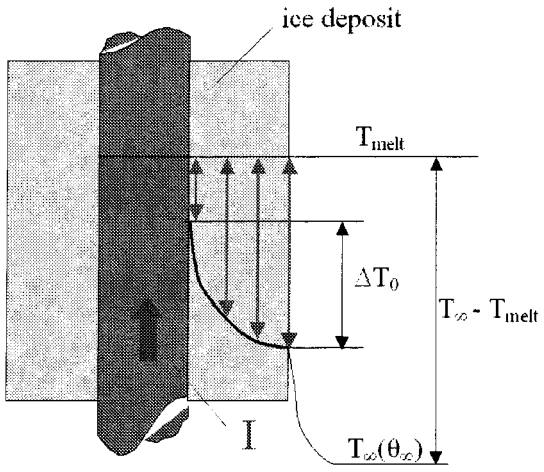

Figure 3.1 Temperature distribution in ice sleeve accumulated on electric conductor

The left hand side of Eq. 3.2-1 contains the Joule heat produced by electric current, I. The right side of the Eq. 3.2-1 shows the generated temperature drop through the ice sleeve, when the temperature at the ice-conductor interface reaches the melting point. This temperature difference serves as a reference value in the following equations. The ΔT_0 is a temperature difference through the ice sleeve that triggers melting at the inner surface of the ice deposit under an electrical current flow, I, in the conductor (see Figure 3.2).

$$\Delta T_0 = \frac{I^2 \cdot R_L}{S \cdot k_i} \qquad \text{Eq. 3.2-3}$$

The temperature difference in the ice deposit depends uniqely on the thermal resistance due to conduction. The temperature difference between the ice surface and air depends on the thermal resistance due to convection. In other words, the heat convection determines the ice surface temperature, while the inner heating determines the temperature drop through the ice deposit.

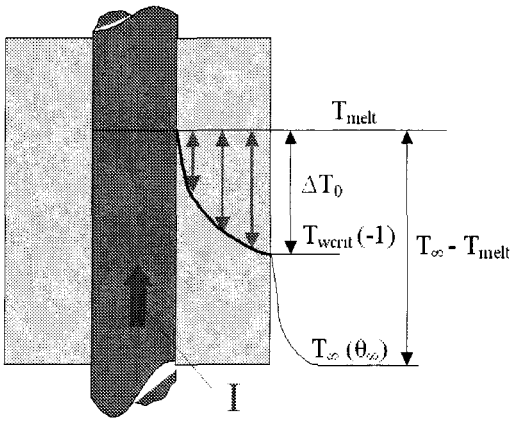

Figure 3.2 Reaching the melting point at inner surface of ice sleeve

Two characteristic numbers are defined: the dimensionless ice temperature by Eq. 3.2-4 and the dimensionless air temperature by Eq. 3.2-5.

$$\theta = \frac{\Delta T}{\Delta T_0} = \frac{T - T_{melt}}{\Delta T_0} \qquad \text{Eq. 3.2-4}$$

$$\theta_\infty = \frac{T_\infty - T_{melt}}{\Delta T_0} \qquad \text{Eq. 3.2-5}$$

The dimensionless ice temperature can be interpreted as the ratio of the difference between the ice temperature and the melting point (see Figure 3.2) and the temperature difference produced by Joule heating (see Figure 3.1).

The dimensionless ice temperature is equal –1 at the outer surface of the ice sleeve when the melting point is reached at the conductor-ice interface (see Figure 3.2). In this particular case, the ice surface temperature is called the critical temperature, because at lower temperatures melting does not occur even after an infinite time.

In order to obtain dimensionless coordinates the conductor radius ($d_c/2$) is chosen as reference. The defined dimensionless variable is as follows:

$$\xi = \frac{r}{(d_c/2)} \qquad \text{Eq. 3.2-6}$$

Thus, $\xi=1$ at the conductor–ice interface, $\xi=0$ at the origin of conductor, $\xi=d_i/d_c$ at the outer surface of the ice deposit.

The Fourier number is used as a dimensionless time as defined by Eq.3.2-7.

$$Fo = \frac{4 \cdot \alpha_i \cdot \tau}{d_c^{\,2}} \qquad \text{Eq. 3.2-7}$$

where τ is the time (s), and α_i is the thermal diffusivity of ice (m/s^2).

The Biot number is used to characterize the dimensionless boundary condition of the third kind, as follows:

$$Bi = \frac{h \cdot d_i}{2 \cdot k_i} \qquad \text{Eq. 3.2-8}$$

where d_i is the diameter of ice layer (m), h is the mean heat transfer coefficient (W/m^2K) and k_i is the thermal conductivity of ice (W/mK).

3.3 The mathematical model

First, the spatial and time derivatives are expressed with dimensionless numbers, as follows:

$$\frac{\partial T}{\partial \tau} = \frac{\partial T}{\partial \theta} \cdot \frac{\partial \theta}{\partial Fo} \cdot \frac{\partial Fo}{\partial \tau} = \frac{4 \cdot \Delta T_0 \cdot \alpha_i}{d_c^2} \cdot \frac{\partial \theta}{\partial Fo} \qquad \text{Eq. 3.3-1}$$

$$\frac{\partial T}{\partial r} = \frac{\partial T}{\partial \theta} \cdot \frac{\partial \theta}{\partial \xi} \cdot \frac{\partial \xi}{\partial r} = \frac{2 \cdot \Delta T_0}{d_c} \cdot \frac{\partial \theta}{\partial \xi} \qquad \text{Eq. 3.3-2}$$

$$\frac{\partial^2 T}{\partial r^2} = \frac{4 \cdot \Delta T_0}{d_c^{\,2}} \cdot \frac{\partial^2 \theta}{\partial \xi^2} \qquad \text{Eq. 3.3-3}$$

3.3.1 Dimensionless form of model equations

3.3.1.1 Dimensionless form of a boundary condition of the second kind

The heat flow balance at the conductor-ice interface is as follows:

$$m_c \cdot c_c \frac{\partial T_c}{\partial \tau} = A_i \cdot k_i \left. \frac{\partial T_i}{\partial r} \right|_{r=(d_c/2)+0} + I^2 \cdot R \cdot L \qquad \text{Eq. 3.3-4}$$

where A_i is the inner surface of the ice deposit (m^2), m_c is mass (kg) and c_c is thermal capacitance (J/kgK) of conductor, r is the location along the radius (m), τ is the time (s). The corresponding dimensionless form of Eq. 3.3-4, after substituting the appropriate dimensionless numbers and derivations is as follows:

$$\frac{(\rho c)_c}{(\rho c)_i} \frac{\partial \theta}{\partial Fo} = 2 \frac{\partial \theta}{\partial \xi} + 2 \frac{1}{\ln(r_i / r_c)}, \qquad \text{Eq. 3.3-5}$$

where subscripts i and c refer to the ice sleeve and conductor, respectively, ρ is the density (kg/m^3).

3.3.1.2 Dimensionless heat equation in cylindrical coordinates

The heat equation without a heat source in the cylindrical coordinate system is as follows:

$$\frac{\partial T}{\partial \tau} = \alpha_i \left(\frac{\partial^2 T}{\partial r^2} + \frac{1}{r} \frac{\partial T}{\partial r} \right) \qquad \text{Eq. 3.3-6}$$

Subsequently, substituting the derivatives expressed by Eq. 3.3-1÷Eq. 3.3-3 into Eq. 3.3-6, the following dimensionless form is obtained:

$$\frac{\partial \theta}{\partial Fo} = \frac{\partial^2 \theta}{\partial \xi^2} + \frac{1}{\xi} \cdot \frac{\partial \theta}{\partial \xi} \qquad \text{Eq. 3.3-7}$$

3.3.1.3 Boundary condition of the third kind in dimensionless form

The convective heat transfer and the radiative heat exchange at the outer surface of the ice deposit mean boundary conditions of the third kind. Both previously mentioned heat transfer modes are taken into account by one mean heat transfer coefficient, h (W/m^2K). Eq. 3.3-8 describes the heat transfer at the ice-air interface.

$$k_i \frac{\partial T}{\partial r} = h(T_\infty - T_w) \qquad \text{Eq. 3.3-8}$$

where T_∞ is the air temperature of the free stream (K), T_w is outer ice layer temperature (K). The corresponding dimensionless form of Eq. 3.3-8 is written in Eq. 3.3-9.

$$\frac{\partial \theta}{\partial \xi} = Bi \frac{d_c}{d_i} (\theta_\infty - \theta) \qquad \text{Eq. 3.3-9}$$

The above equations demonstrate that the dimensionless ice temperature, θ, depends on certain parameters as follows:

$$\theta = \theta\left(\xi, Fo, Bi, \frac{d_i}{d_c}, \frac{(\rho c)_c}{(\rho c)_i}, \theta_\infty\right) \qquad \text{Eq. 3.3-10}$$

3.3.2 Finite difference equations in dimensionless form

The dimensionless equations should be written in finite difference form in order to solve them numerically. For discussion of dimensionless time (Fo), the forward schema has been used, while for dimensionless space discretization the central schema has been applied as follows:

$$\frac{\partial \theta_{i,k}}{\partial Fo} \approx \frac{\theta_{i+1,k} - \theta_{i,k}}{\Delta Fo} \qquad \text{Eq. 3.3-11}$$

$$\frac{\partial \theta_{i,k}}{\partial \xi} \approx \frac{\theta_{i+1,k} - \theta_{i-1,k}}{2 \cdot \Delta \xi} \qquad \text{Eq. 3.3-12}$$

$$\frac{\partial^2 \theta_{i,k}}{\partial \xi^2} \approx \frac{\theta_{i+1,k} - 2\theta_{i,k} + \theta_{i-1,k}}{(\Delta \xi)^2} \qquad \text{Eq. 3.3-13}$$

In above equations, subscript i designates the dimensionless location and subscript k denotes the dimensionless time step.

3.3.2.1 A boundary condition of the second kind in finite difference form

The dimensionless conductor temperature, after substituting Eq. 3.3-11 and Eq. 3.3-12 into Eq. 3.3-5 and after appropriate simplification, is as follows:

$$\theta_{c,k+1} = \frac{1}{M_1}\left(\theta_{2,k} + \frac{\Delta\xi}{\ln(r_i / r_c)}\right) + \theta_{c,k}\left(1 - \frac{1}{M_1}\right), \qquad \text{Eq. 3.3-14}$$

$$M_1 = \frac{\Delta\xi}{2\Delta Fo} \cdot \frac{(\rho c)_c}{(\rho c)_i} \qquad \text{Eq. 3.3-15}$$

The schema is numerically stable, if the $M_1>1$ condition is met (the constant of $\theta_{c,k}$ must be positive when explicit schema is used). Note that the thermal contact resistance is neglected, hence the dimensionless temperature at the conductor-ice interface is equal to the conductor temperature as $\theta_{1,k}=\theta_{c,k}$.

3.3.2.2 The heat conduction equation in finite difference form

The heat conduction in cylindrical coordinate system, Eq. 3.3-7 may be written with finite differences as shown in Eq. 3.3-16.

$$\frac{\theta_{i,k+1} - \theta_{i,k}}{\Delta Fo} = \frac{\theta_{i+1,k} - 2\theta_{i,k} + \theta_{i-1,k}}{(\Delta\xi)^2} + \frac{1}{\xi} \cdot \frac{\theta_{i+1,k} - \theta_{i-1,k}}{2(\Delta\xi)} \qquad \text{Eq. 3.3-16}$$

A differential modulus, M_2, is defined as follows:

$$M_2 = \frac{\Delta\xi^2}{\Delta Fo} \qquad \text{Eq. 3.3-17}$$

Thus, the appropriate form of Eq. 3.3-16 is as follows:

$$\theta_{i,k+1} = \frac{1}{M_2}\left[\theta_{i-1,k}\left(1 - \frac{\Delta\xi}{2\xi_i}\right) + \theta_{i+1,k}\left(1 + \frac{\Delta\xi}{2\xi_i}\right)\right] + \theta_{i,k}\left(1 - \frac{2}{M_2}\right) \qquad \text{Eq. 3.3-18}$$

where $\xi = 1 + (i-1)\cdot\Delta\xi$, and the schema is stable, if $M_2>2$ condition is met.

3.3.2.3 A boundary condition of the third kind in finite difference form

The dimensionless temperature at the outer ice sleeve is expressed in finite difference form with a so-called "auxiliary" node. Therefore:

$$\frac{\theta_{w,k+1}-\theta_{w,k}}{\Delta Fo}=\frac{\theta_{s,k}-2\theta_{w,k}+\theta_{w-1,k}}{(\Delta\xi)^2}+\frac{1}{\xi_w}\cdot\frac{\theta_{s,k}-\theta_{w-1,k}}{2(\Delta\xi)} \qquad \text{Eq. 3.3-19}$$

$$\frac{\theta_{s,k}-\theta_{w-1,k}}{2\cdot\Delta\xi}=Bi\frac{d_c}{d_i}(\theta_\infty-\theta_w) \qquad \text{Eq. 3.3-20}$$

where subscript w refers to the outer surface of the ice layer, w-1 designates the point in the conductor $\Delta\xi$ far from the ice-air interface, while subscript s denotes the so-called "auxiliary" node. With the help of Eq. 3.3-20 the auxiliary node temperature may be eliminated, and the finite difference form can be written as

$$\theta_{w,k+1}=\frac{2}{M_2}\theta_{w-1,k}+\theta_\infty\frac{C_1\cdot Bi}{M_2}+\theta_{w,k}\left(1-\frac{2+C_1\cdot Bi}{M_2}\right), \qquad \text{Eq. 3.3-21}$$

where the C_1 geometrical parameter is as follows:

$$C_1=2\cdot\Delta\xi\cdot\frac{d_c}{d_i}\left(1+\frac{\Delta\xi}{2\xi_w}\right) \qquad \text{Eq. 3.3-22}$$

Eq. 3.3-21 is numerically stable, if the $M_2 > 2 + C_1 \cdot Bi$ condition is met.

3.3.3 Calculation procedure

The computations were made using the following parameters:

- dimensionless grid space: $\Delta\xi = 0.1$

- differential modulus in the ice deposit: $M_2 = 3$
- dimensionless time step: $\Delta Fo = 3.3333 \cdot 10^{-3}$
- differential modulus at the conductor-ice interface: $M_1 = 20.53$
- initial thermal conditions in the ice deposit: $\theta_\infty = -2$
- geometrical parameter: $d_i/d_{al} = 3$

The atmospheric parameters are in a range of $-3 \leq \theta_\infty \leq 3$ and $0 \leq Bi \leq 8$. Note that Bi=0 means a perfectly isolated outer surface. The Fo numbers are computed at a fixed d_i/d_c value and varying θ_∞ values. The Fo number at which the melting process starts can be established from the calculated temperature distributions.

3.4 Calculation results

3.4.1 Reaching the melting point at θ_∞<-1

In this particular case melting can occur just at the inner surface of the ice sleeve. If the convective heat transfer increases (increasing Bi numbers) then the ice surface temperature may become lower than the critical temperature of the ice surface. In this case ice melting does not occur. It is shown in Figure 3.3 that there are related Bi numbers and dimensionless air temperatures when melting does not occur. For example, at $\theta_\infty = -2$, melting does not occur under convective heat transfer related to a Bi number greater than 1.

Consequently, atmospheric conditions characterized by two dimensionless numbers (Bi and θ_∞) can be determined, in which cases melting does not occur and/or starts at inner surface (see Figure 3.3). In the following section, the equation of the curve that separates these two cases is determined.

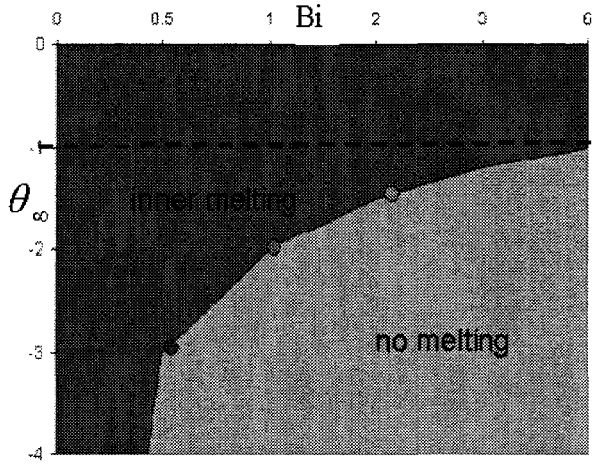

Figure 3.3 Melting cases

3.4.2 Steady state as an asymptotic solution of the problem

In order to determine the equation of the separating curve the steady state problem has been solved. The thermal heat balance of the conductor-ice composite, when the melting point is reached at the inner surface of ice sleeve, is expressed by Eq. 3.4-1.

$$I^2 R_L = \frac{T_{melt} - T_\infty}{\frac{\ln(r_i - r_c)}{2k_i\pi} + \frac{1}{d_i\pi h}} \qquad \text{Eq. 3.4-1}$$

The dimensionless form of the critical air temperature, under which the ice does not melt, is obtained after the necessary manipulations of Eq. 3.4-1. It is expressed with Eq. 3.4-2.

$$\theta_{\infty}^{*} = -\left(1 + \frac{1}{Bi \cdot \ln(r_i / r_c)}\right) \qquad \text{Eq. 3.4-2}$$

If the $\theta_{\infty} < \theta_{\infty}^{*}$ condition is met then the ice deposit does not melt even after infinite time. Consequently in these cases, it has no meaning to calculate the time necessary to reach the melting condition.

3.4.3 Reaching the melting point at $-1 < \theta_{\infty} < 0$

For the case where the dimensionless air temperature is between –1 and the melting point, the inner heating is greater than the outer heating. Therefore, melting starts at the inner surface as well. Contrary to the previous case, the increasing heat convection helps the ice to reach its melting point. The time required to reach the melting point depends only on the Bi number. The Fo number tends towards a constant value with an increasing Bi number (see Figure 3.5). This value can be calculated analytically by prescribing a boundary condition of the first kind on the outer ice surface.

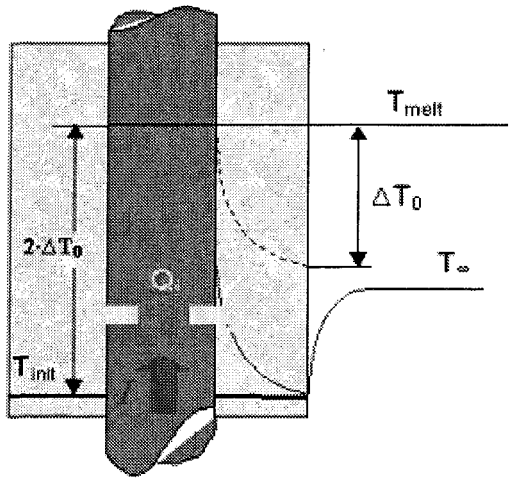

Figure 3.4 Reaching the melting conditions

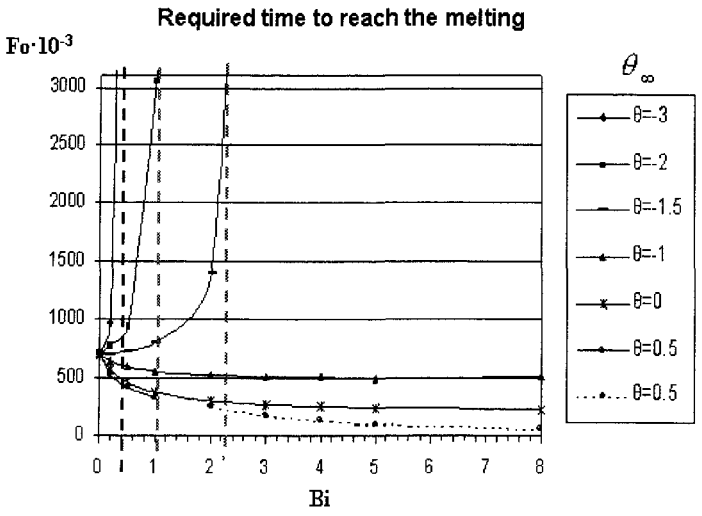

Figure 3.5 Time (Fo) required to reach the melting point versus Bi number

3.4.4 Reaching the melting point at $\theta_\infty > 0$

In the present case, at positive air temperatures melting may start at both surfaces of the ice sleeve, at the inner and/or at the outer (see Figure 3.6). As Figure 3.7 shows, melting starts along the inner ice surface at small Bi numbers, while under intensiver heat convection the melting is triggered at the outer surface.

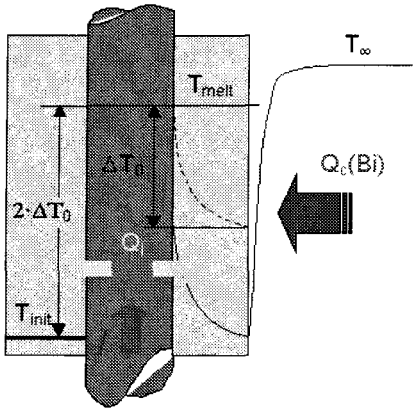

Figure 3.6 Reaching the melting conditions

It requires less time to reach the melting conditions with increasing Bi numbers. In Figure 3.7 the lines have a split, at which point the inner and external heating effects are equivalent.

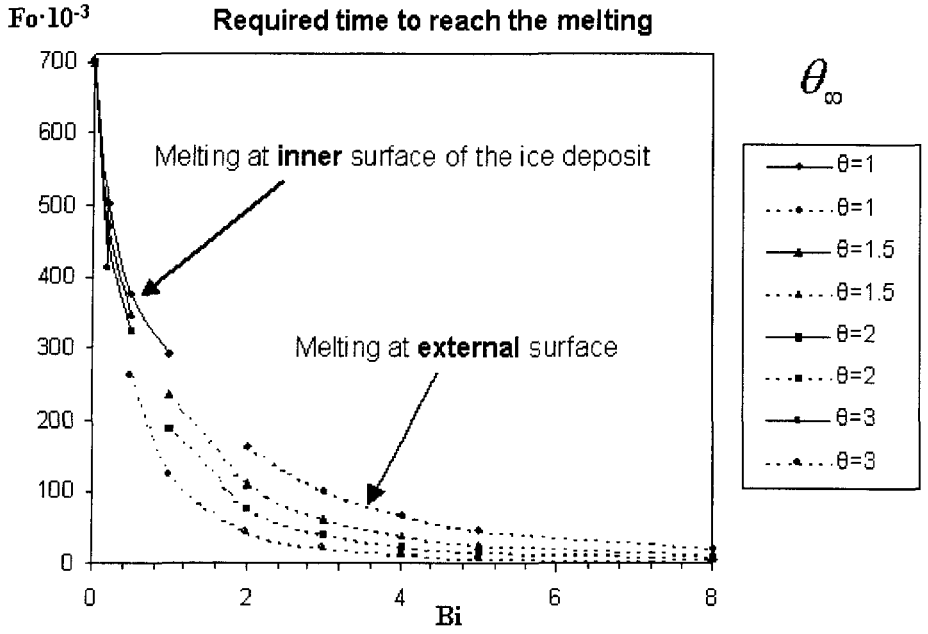

Figure 3.7 Time (Fo) required to reach the melting point versus Bi number

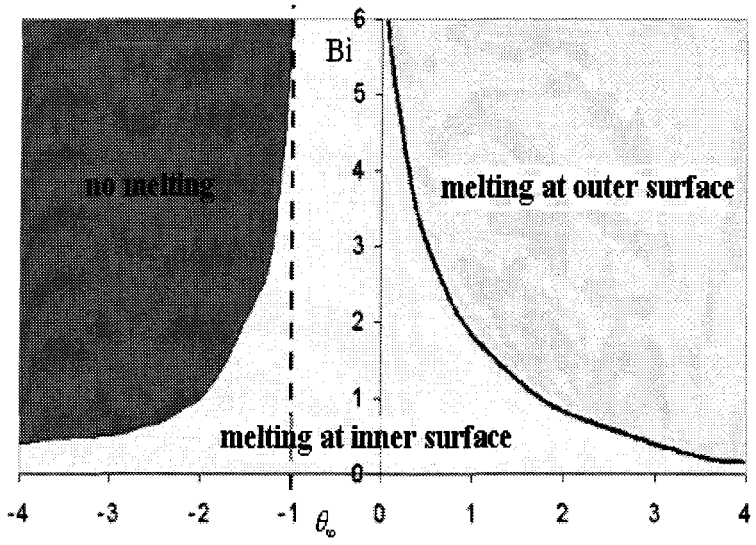

Figure 3.8 Overview of ice melting scenarios

In this part of the study, different cases are defined depending on the ratio of inner and outer heating. For each defined case the melting conditions are determined. A general overview is shown in Figure 3.8. Note that the melting conditions are described with two dimensionless numbers and to convert them to concrete cases their definition must be used.

The following is a brief overview of the previously presented investigations.

To reach melting conditions at the conductor-ice interface:

- Air temperature should be higher than the critical value, $\theta_\infty \geq \theta_\infty^*$.
- If $\theta_\infty < -1$, then time to reach melting increases with increasing Bi numbers.
- If $-1 < \theta_\infty < 0$, then the melting condition is reached under all Bi numbers, but the Fo number tends towards constant value with increasing heat convection.
- In case of $\theta_\infty > -1$ the time required to reach the melting point decreases with increasing Bi numbers.
- In the case of Bi=0, the required Fo number to reach the melting point is independent from the dimensionless air temperature.

For reaching ice melting at the outer ice sleeve surface:

- The air temperature should satisfy: $\theta_\infty \geq 0$ condition.
- At appropriate Bi numbers, the inner and outer heating effects are equivalent.

CHAPTER 4

ICE PREVENTION METHODS BASED ON JOULE HEATING TECHNIQUE

4.1 Introduction

The main objective of the present study is to analyze the energy requirements of icing prevention methods based on the Joule heating technique, a so-called anti-icing method. This protection technique should be applied a certain time before as well as during the freezing precipitation. In the present technique, namely ice prevention by the Joule effect, the nominal current in the overhead cable is increased to ensure a positive conductor temperature. In the following section the candidate mainly relies upon [50].

The first formula for calculating the current required to prevent ice formation on the power line conductors was suggested by J. E. Clem in 1930 [10], [18]. Only the forced heat convection is taken into account, since solar radiation was found to be negligible during ice storms. This is an empirical approach which assumes that a rise in temperature of 9 °C above the temperature of the air surrounding the conductor may be adequate to prevent ice accretion [10], [18]. For this reason, this approach is limited to "moderate" atmospheric parameters (generally air temperature no lower than -5 °C and wind speed not in excess of 5 m/s). Some results of the first rude tests (published earlier by other researchers) concerned with the conductor temperatures required to prevent sleet adherence on a special type of wires and cables were also reported in [10].

Later in 1978, McComber et al. combined the heat losses due to convection and impinging water droplets in their study [38]. They investigated the heat flux necessary to inhibit freezing on two types of smooth and relatively short (28 cm) stranded conductors, with cylindrical and trapezoidal strands. To the best of our knowledge, that work is the most comprehensive experimental study on energy requirement until now. It is shown that stranded conductors have power requirements for ice inhibition about 33% greater than with smooth cylinders at wind speeds above 10 m/s, because of the increased surface exposed to the airflow [38]. Furthermore, it was found that outer cylindrical strands have no influence on the required power at wind speeds not exceeding 10 m/s. However, the empirical equation derived for a special type of conductor is suggested for any stranded conductor without any consideration for the surface geometry [38]. Note that in [51] essentially the same work and empirical formulations are presented for both stranded and smooth cylinders, as in [38]. The energy balance of the heated wire adopted from ice accretion models (developed by Makkonen [35]) is compared with measurements performed by Personne and Gayet ([46], [47]) on Aster 148 and Aster 570 conductors with small cloud droplets ranging from 7 to 16 μm. The reliability of open wind tunnel tests is reduced by the fluctuations in wind velocity, liquid water content (LWC) and wire temperature (from 0.5 °C to 2 °C) in spite of the anti-correlation attempt. The weakness of the mathematical model presented in [46] and [47] is due to the local heat transfer coefficient (HTC) at stagnation point representing the convective heat loss of the whole conductor. Unfortunately, a single median volume diameter (MVD=12 μm) for water droplets in all validation tests were assumed.

Makkonen's general heat balance [35] is also adopted in the analytical model presented in [49] and in this paper. Two improvements based on well-controlled wind tunnel experiments are proposed in order to extend the analytical model to permit ice inhibition calculations. First, the overall HTC is estimated for certain ACSR conductors with different surface geometries. These approximations allow a more precise calculation of the convective heat loss for stranded conductors, as shown in [46] and [47]. Second, correction factors are introduced in the heat loss term, accounting for the influence of impinging water droplets. Measurements presented in [49] about the required current intensity for Carillon type conductors at different wind velocities are extended to three other conductor types. In this work, additional measurements were made to analyze the effects of LWC at different air temperatures. The required Joule heat measured in [38], [46] and [47] was simulated by a heating element built in the conductor. In this work, however, it was generated by raising the current intensity of the conductor. The atmospheric conditions that were simulated in the wind tunnel were in-cloud icing and freezing drizzle in small droplets. A total of 80 tests were carried out in the closed CIGELE icing research wind tunnel for the purpose of this study.

4.2 Mathematical model

The general heat balance equation of a power line conductor exposed to a two-phase air/water spray flow is as follows:

$$Q_j + Q_f + Q_k = Q_c + Q_e + Q_w + Q_r \qquad \text{Eq. 4.2-1}$$

where Q_j (W) is the rate of heat generation by Joule effect, Q_f (W) is the combined heat flow rate due to stagnation and friction effects in the boundary layer, Q_k (W) is the kinetic energy rate of the impinging water droplets, Q_c (W), Q_e (W) and Q_w (W) are the heat loss rates due to convection, evaporation and due to impinging water droplets respectively, and Q_r (W) is the rate of radiative heat exchange. The terms in Eq. 4.2-1 can be expressed as presented in the following from Eq. 4.2-2 to Eq. 4.2-9.

$$Q_j = I^2 R_{ac,c} L \qquad \text{Eq. 4.2-2}$$

where I (A) is the nominal current in the power line conductor, $R_{ac,c}$ (Ω/m) is the ac electrical resistance of the conductor per unit length at working temperature and L (m) is the length of the conductor. Generally, the electrical conductor handbooks supply the dc electrical resistance at 20 °C, $R_{dc,20}$, which allows the calculation of the appropriate ac resistance at conductor temperature. First, the dc resistance should be adjusted for the working temperature. It is well known that over a moderate temperature range (0 °C to 120 °C [1]), the electrical resistance changes linearly with temperature. Since the conductor temperature has to be maintained slightly above 0 °C during the ice prevention process, the dc resistance at conductor temperature, $R_{dc,c}$ (Ω/m) is formulated as follows [1].

$$R_{dc,c} = R_{dc,20}[1 + \alpha_{20}(T_c - 20)] \qquad \text{Eq. 4.2-3}$$

where T_c (°C) is the conductor working temperature and α_{20} is the temperature coefficient at 20 °C. The ac resistance is an apparent resistance, which makes allowance for the non-uniform current intensity distribution across the conductor cross-section. It can be formulated as follows:

$$R_{ac,c} = k_s k_t R_{ac,d} \qquad \text{Eq. 4.2-4}$$

where the skin and transformer effects are taken into account by coefficients k_s and k_t, respectively. It is well known that the skin effect results in an increase in current intensity toward the conductor surface. This change in the current intensity distribution may be realized by increasing the resistance of the conductor. The distribution of the current density in the ACSR conductors is also affected by the magnetic flux of the ferromagnetic core and the opposite spiralling of the nonferrous layers [1]. This phenomenon is known as the transformer effect. It is of importance only in the case of ACSR conductors with an odd number of aluminium layers [1]. The coefficients k_s and k_t are associated with different geometries of ACSR conductors, and can be drawn from charts found in the relevant literature or can be calculated from current intensity distributions, for individual cases. Naturally, the transformer effect coefficient k_t depends on the electric current, since the core flux varies with the load current. The other effects, such as hysteresis and eddy current effects were neglected in this work.

Terms in Eq. 4.2-5, Eq. 4.2-8 and Eq. 4.2-9 are borrowed from the ice accretion model introduced in [34], [35] and [37]. The correction factors, κ_1 and κ_2, in Eq. 4.2-9, were introduced in [50].

$$Q_f = h \cdot r \cdot v^2 \cdot A'/(2c_p) \qquad \text{Eq. 4.2-5}$$

where h ($W/m^2 \cdot K$) is the average HTC, c_p ($J/kg \cdot K$) is the specific heat of air, r is an empirical recovery factor (r=0.79 is assumed for a cylinder [35]), and where A' (m^2) is the fraction of the conductor surface in contact with the air superheated by stagnation and friction effects. In the present case, A' is the total exposed surface of the stranded

conductor. It should be calculated using the equivalent conductor diameter instead of the circumscribing diameter. The equivalent diameter, D_e (m), is defined in Eq. 4.2-6 and introduced in detail in [42].

$$D_e = d_s(1+(m/2)) \qquad \text{Eq. 4.2-6}$$

where d_s (m) is the aluminium strand diameter and m (1) is the number of strands in the outer layer. The contribution of the kinetic energy of the impinging water droplets, Q_k, to the general heat balance equation is not significant for stationary objects, under natural atmospheric conditions [34]. Consequently, this term can be neglected. The convective term is expressed by:

$$Q_c = hA(T_s - T_a) \qquad \text{Eq. 4.2-7}$$

where T_s (°C) is the conductor surface temperature, T_a (°C) is the air temperature, and where A (m^2) is the exposed conductor surface. The heat loss rate due to water layer evaporation from the conductor surface is expressed in Eq. 4.2-8.

$$Q_e = 0.622 \cdot h \cdot l_e \cdot A_w \cdot (p_{sat,s} - p_{sat,a})/(c_p \cdot p_a) \qquad \text{Eq. 4.2-8}$$

where l_e (J/kg) is the latent heat of evaporation, A_w (m^2) is the wetted surface of the conductor, $p_{sat,s}$ (Pa) and $p_{sat,a}$ (Pa) are the saturation vapour pressures at surface and air temperature over water, respectively, and where p_a (Pa) is the atmospheric pressure. The wetted surface is estimated as equal to half of the total surface area in the calculations. The saturation vapour pressures are taken from thermodynamic charts and tables, available in [9] and [54]. The rate of heat taken away by the impinging water droplets is formulated as

$$Q_w = \kappa_1 \cdot \kappa_2 \cdot W \cdot v \cdot E \cdot D_c \cdot L \cdot c_w \cdot (T_s - T_a) \qquad \text{Eq. 4.2-9}$$

where W (kg/m^3) is the liquid water content (LWC) of air, v (m/s) is the air velocity of the free stream, E (1) is the collection efficiency, D_c (m) is the conductor external diameter, and where c_w (J/kg·K) is the specific heat of liquid water. In Eq. 4.2-9, the water droplet temperature is assumed to be the same as air, because of their small impact velocity [37]. However, some larger water droplets should be supercooled. Furthermore, it is assumed in Eq. 4.2-9 that the air water droplet collection area is equal to longitudinal projection (D_c·L) of the conductor. The collection efficiency, E, is the ratio of the water content in the free stream to the water content collected after impinging on the conductor surface. E is smaller than unity because the small water droplets following air streamlines may bypass the conductor [37]. The leeward side of the conductor, though less exposed to droplets strikes, nevertheless gets wetted by runback water from the front side, as shown in Figure 4.1. The influence of the runback water flow toward the leeward surface of the conductor, as well the effect of supercooled water droplets are taken into consideration with the coefficient κ_1. As it means additional heat loss, this coefficient should be set to $\kappa_1 \geq 1$.

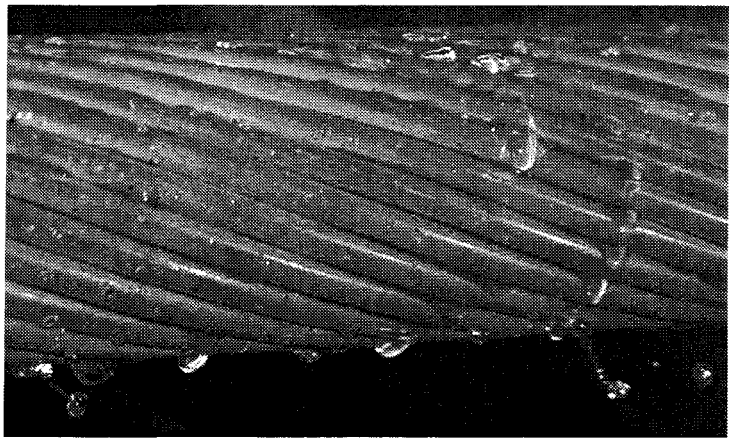

Figure 4.1 Wetted surface on leeward side of stranded conductor.

The non-uniform water film formed on the stranded surface (see Figure 4.1) by the impinging droplets cannot reach a perfect thermal equilibrium with the conductor. Let T_s be the water film temperature near to the conductor surface, and T_a a good approximation of the temperature at the water-air interface (see Figure 4.2). In theory, the average water film temperature, T_{av}, should be used in Eq. 4.2-9 instead of T_s. However, since the calculation of T_{av} is not feasible due to strong variations in water layer thickness, it is assumed to be the same as the surface temperature of the conductor. This effect is taken into account in the correction factor κ_2, which should be set less than unity ($\kappa_2 \leq 1$). Note that [38] also introduces a correction factor in the impinging water droplets term. In the setting of this term, the following factors are also taken into consideration: a slightly higher conductor temperature than 0 °C, the displacement of the water layer separation point, as well as the fact that the leeward side of the conductor is sometimes exposed to impinging water droplets in the turbulent wake.

Substituting the parameterized terms in the general heat balance equation Eq. 4.2-1, the electrical current in the conductor can be expressed as in Eq. 4.2-10. Radiative heat exchange will not be dealt within this study, as it has been extensively discussed in the literature on radiative heat transfer and on thermal ratings of overhead conductors. Several calculation methods of radiative heat exchange are offered depending on the involved variables, such as in [21], [22], [34], [42] and [52].

$$I = \left[\frac{D_e \pi}{R_{ac,c}} \left(h(T_s - T_a) - \frac{hrv^2}{2c_p} + \frac{0.622 h l_e (p_{sat,s} - p_{sat,a})}{2 c_p p_a} \right) + \frac{D_c}{D_e} \frac{\kappa_1 \kappa_2 EW v c_w (T_s - T_a)}{2\pi} \right]^{0.5} \quad \text{Eq. 4.2-10}$$

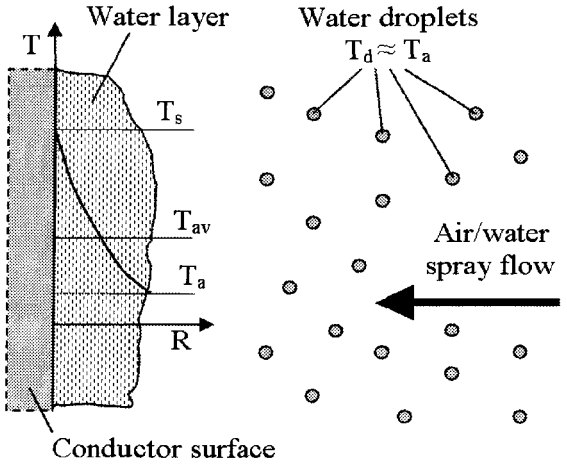

Figure 4.2 Schema of temperature distribution in water layer formed on conductor surface

At a conductor surface temperature (T_s) of 0 °C, where there is no ice accretion, the required minimum electrical current (I_c) can be calculated for the given atmospheric conditions using Eq. 4.2-10. The temperature gradient inside the ACSR do not play any role in the thermal balance, since the conductor surface temperature is assumed to be kept constant at 0 °C in the present mathematical model. The challenge in using Eq. 4.2-10 is to find the appropriate values of the collection efficiency, E, the overall HTC, h, as well as the κ_1 and κ_2 correction factors for stranded conductors. The relevant literature offers several methods to calculate the collection efficiency. In this part of the work the latest empirical formulations presented in [19] and [37] for cylindrical objects are used. This is presented briefly in the following section. Langmuir and Blodgett also offer tabulated results for E in [33]. As for the overall HTC, as well as the κ_1 and κ_2 correction factors, they were estimated from the experimental results obtained.

4.2.1 Collection efficiency

The collection efficiency, E, may be calculated by applying the empirical fit given in Eq. 4.2-11 to the numerically calculated data developed by Finstad, Lozowski and Gates ([19] and [37]). The numerical fit can be used accurately for Langmuir's parameter, Φ, in the range of $10^2 \div 10^4$ (which covers most near ground atmospheric icing) and for Stokes number in the range of 0.17÷1000 [19]. The collection efficiency, E, is given by

$$E = A - 0.028 - C(B - 0.0454) \qquad \text{Eq. 4.2-11}$$

where the A, B and C coefficient are defined as:

$$A = 1.066K^{-0.00616}\exp\left(-1.103K^{-0.688}\right) \qquad \text{Eq. 4.2-12}$$

$$B = 3.641K^{-0.498}\exp\left(-1.497K^{-0.694}\right) \qquad \text{Eq. 4.2-13}$$

$$C = 0.00637(\Phi - 100)^{0.381} \qquad \text{Eq. 4.2-14}$$

In Eq. 4.2-12 ÷ Eq. 4.2-14, K and Φ are dimensionless numbers defined as follows:

$$K = \rho_d d^2 v/(9\mu D_c) \qquad \text{Eq. 4.2-15}$$

$$\Phi = \mathrm{Re}^2/K \qquad \text{Eq. 4.2-16}$$

where Re is the droplet Reynolds number that is based on the free stream velocity, v, density of droplet, ρ_d, as well as on the water droplet diameter, d, and given by

$$\mathrm{Re} = \rho_d dv/\mu \qquad \text{Eq. 4.2-17}$$

In Eq. 4.2-15 and Eq. 4.2-17, the water droplet diameter can be closely approximated by the median volume diameter (MVD) of the dispersed water phase flow [37]. It is a good approximation for E, considering that E=0.01 for values of K lower than 0.17, and that E=0.99 for values of K higher than 1000 [19]. As seen from the above correlations, collection efficiency strongly depends on droplet size. Reference [37] emphasizes that for

sufficiently large MVD (e.g. in freezing rain) in most practical applications, E is estimated to be equal to 1. A good overview of the available approximations of collision and collection efficiencies for different types of freezing precipitation can be found in [37].

4.3 Measurements

The same experimental rig has been used for the minimum current measurements as well as for determining of the overall HTC. This will be discussed in detail in section 7.5. The appropriate wind speed was adjusted by controlling the fan speed. In the present study, the wind speed was measured using a hand held anemometer. The wind speed was adjusted with significantly greater error for the air/water spray flow, because water droplets reaching the fan eventually cause ice to accumulate on the blades, resulting in a drop in velocity. Hence, the air velocity was readjusted every 5÷10 minutes in order to keep the wind speed constant. It was found that such small wind speed variations as presented in Table 4-1 had no significant influence on the minimum current measurements. The LWC data were obtained from [25] and [26] for the corresponding water and air pressure settings in the nozzles. Table 4-1 shows the estimated accuracy of all measured parameters during the experiments.

The challenge with these measurements is to determine the minimum current required for preventing ice accretion on the conductor section. The minimum effective current is defined by the current intensity value when the outer layer strand thermocouple reads 0 °C at steady state, which means that both the conductor and air temperatures must be

continuously recorded. A typical temperature history of measurements is shown in Figure 4.3.

Table 4-1 Estimated accuracy of measured parameters

Measured parameter	Accuracy
Velocity of air/water spray flow	±0.2 m/s ÷ ±0.5 m/s
Liquid water content (LWC)	±5%
Load current below 2200 A	±2 A
Load current above 2200 A	±20 A
Temperature	±0.2 °C ÷ ±0.3 °C
Median volume diameter (MVD)	±4.5 μm

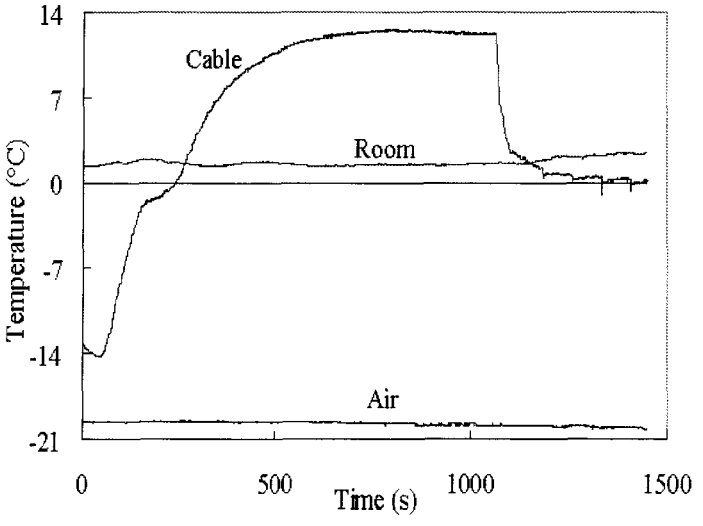

Figure 4.3 Temperature history of the cable at 10 m/s wind speed, in a range of air temperature $-19.6°C < T_a < -20.3°C$. LWC=5.512 g/m^3.

First, the conductor was heated from 7 to 20 °C under different wind speeds, in such a manner that, after being impinged with water droplets, its temperature did not fall below 0 °C. When water droplets hit the conductor, its surface temperature decreases markedly until

it reaches a new steady state. Then the electric current can be decreased slightly as it is shown in Figure 4.4.

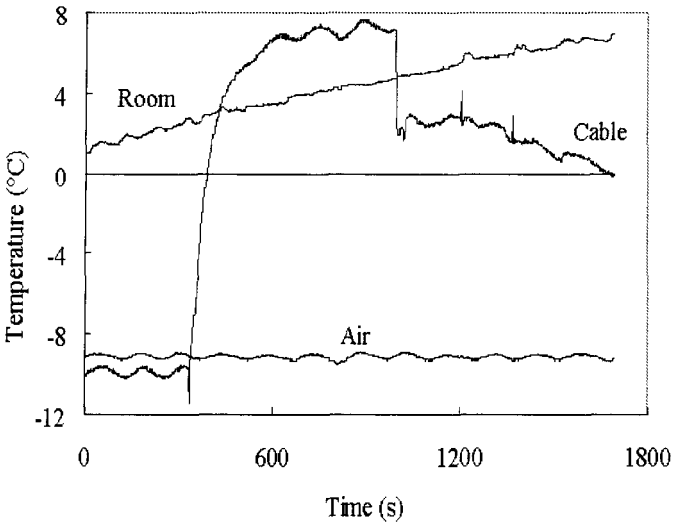

Figure 4.4 Temperature history of the cable under 30 m/s wind speed condition, in a range of air temperature $-8.9°C < T_a < -9.5°C$. LWC=5.69 g/m^3.

The median volume diameter (MVD) was measured using the collargol slide impact method presented in [20]. For nozzle water and air pressures of 40.5 and 40 psi, respectively, at 20 m/s wind speed, the MVD measured value is 51.38 μm. The resulting discrete droplet distribution is shown in Figure 4.5 for the same pressure combination set as the one used for the tests concerned with Figure 4.6 ÷ Figure 4.9. For other pressure combination sets, the MVD results from [24] and [29] were used.

The calculated maximal errors for the ice prevention experiments are based on the estimated accuracy of the LWC, wind velocity, air temperature and MVD measurements. These maximal errors are shown in Table 4-2 for each investigated conductor type.

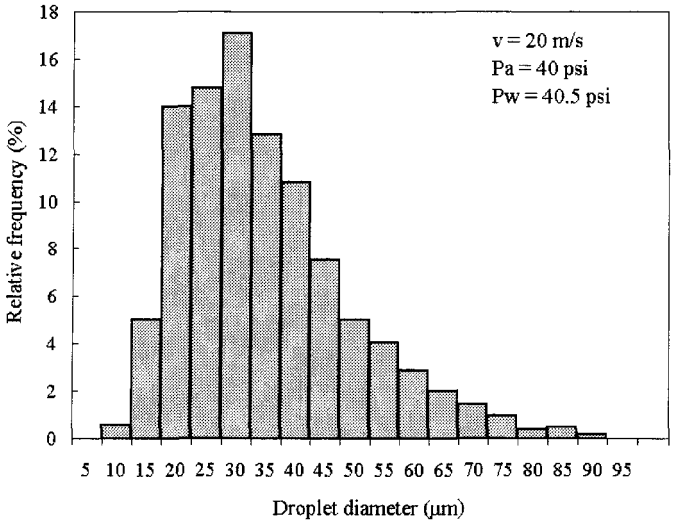

Figure 4.5 Relative frequencies of droplet appearance in discrete spectrum at a specific air-water pressure (Pa-Pw) combination in the nozzles based on measurement of more than 1000 traces.

Table 4-2 Calculated maximal errors of the established minimum current

Conductor type	Maximal error
Carillon	±17%
Condor	±9%
Drake	±9%
Geant 5P	±14%

4.4 Comparison of the results

4.4.1 Effects of surface geometry

This section deals with the effects of surface geometry. To this purpose, the measured minimum current required to prevent ice accumulation was compared with the one

calculated from the model (see Figure 4.6 ÷ Figure 4.9). These calculations were made by applying Eq. 8.2-10 to the tested conductors, with coefficients κ_1 and κ_2 set to unity.

As previously mentioned, the dependence of electrical resistance on temperature, as well the skin and transformer effects were taken into account. The electrical resistance was adjusted to the corresponding value at 0 °C instead of the working average temperature, in order to avoid a long iteration procedure. Naturally, with higher current intensities, the differences between the assumed and working temperatures are greater. The correction factor, which could improve our assumption with high current intensities, was in the range of k_t. The maximum estimated error due to the 0 °C assumption for working temperature is approximately 1%. The skin effect coefficient, k_s, for each conductor type was taken from the charts found in [1]: 1.037 for Carillon, 1.017 for Condor, 1.013 for Drake and 1.105 for Geant 5P, assuming a 0 °C conductor surface temperature. The coefficient related to the transformer effect, k_t, for Drake type conductors is unity, due to the even number of aluminium layers. The k_t values for the other conductors (three-layer ACSRs) were found in [1] to be a function of electric current and geometrical parameters, for an aluminium conductivity value of 62%. Since the minimum current also depends on k_t and vice versa, it was found by iteration. Within the range of the calculated minimum current for the Condor conductor, k_t was assumed to have a constant value of 1.037. The k_t value varied with the nominal current, and ranged from 1.028 to 1.035 for the Geant 5P type conductor and from 1.007 to 1.01 for Carillon.

The calculated current was always found to be within the maximal error range of the measurement, except for one measurement with Carillon. The closest fit between the

measured and calculated currents was observed for Drake type conductors, where the difference was 4.8% in the worst case. The difference was somewhat greater at 6.7% for Condor, 8.8% for Geant 5P and 10.7% for Carillon. The results at moderate air temperature correspond especially well with each other, while the evaporative and driving water terms are less important. At lower temperatures, of course, heat losses due to impinging water droplets and evaporation are more significant than at "moderate" temperatures.

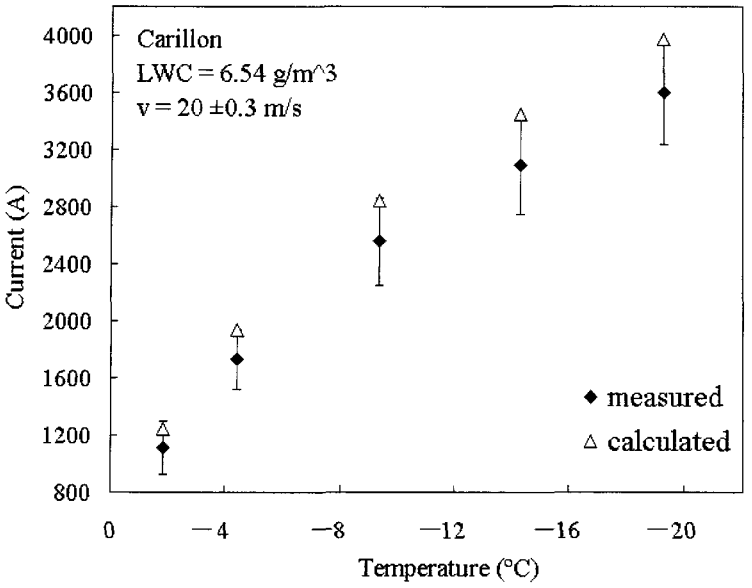

Figure 4.6 Measured and calculated minimum current required to prevent ice accretion on the surface of Carillon type conductors.

The calculated results take into account the effect of the strength loss of strands resulting in an overestimated HTC. This is discussed in section 7.5. Hence, the product $\kappa_1 \cdot \kappa_2$ can be roughly estimated from the difference between the measured and calculated minimum current for three conductor types, except for the Carillon type (due to experimental discrepancies). In fact, it is the only tested conductor, where one of the

calculated results is out of the range of the measurement error (see Figure 4.12), which is attributed to a weak contact between the strands of the outer layer.

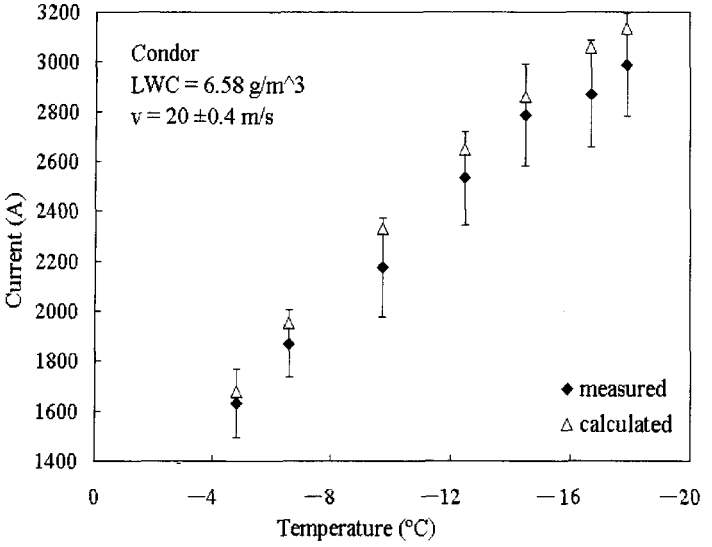

Figure 4.7 Measured and calculated minimum current required to prevent ice accretion on the surface of Condor type conductors.

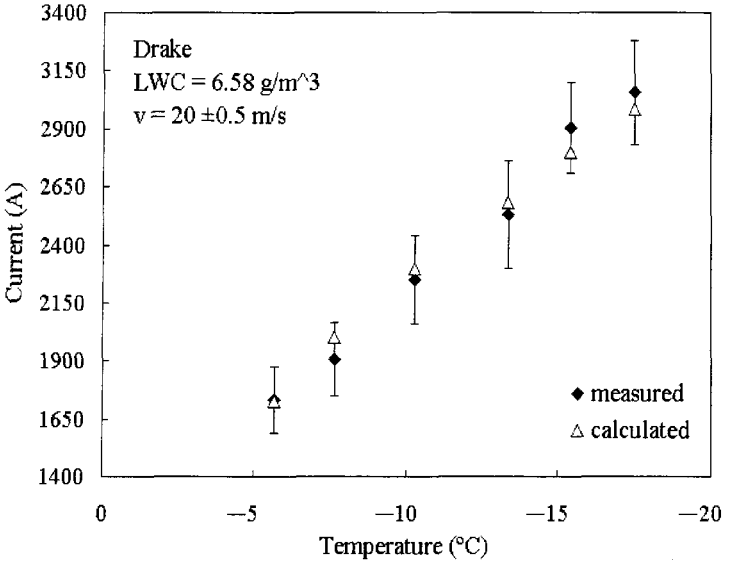

Figure 4.8 Measured and calculated minimum current required to prevent ice accretion on the surface of Drake type conductors.

For the Geant 5P and Condor type conductors, the product of the correction factors, $\kappa_1 \cdot \kappa_2$, was estimated at an average value of 0.7. Consequently, the effects associated with thermal non-equilibrium, affecting κ_2, are more significant than those related to additional heat losses, influencing κ_1, since $\kappa_2 \leq 1$ and κ_1 is always greater than unity. The measured and calculated currents for the Drake conductor were in good agreement. The product of the correction factors, $\kappa_1 \cdot \kappa_2$, was estimated at an average value of 1.03 for this conductor. In that case, it can be concluded that the phenomena related to κ_1 and κ_2 compensate each other.

It can be concluded from the measurement results presented in Figure 4.6÷Figure 4.9 that the analytical model can reliably be used to predict the minimum current required for preventing ice accretion on different types of power line conductors.

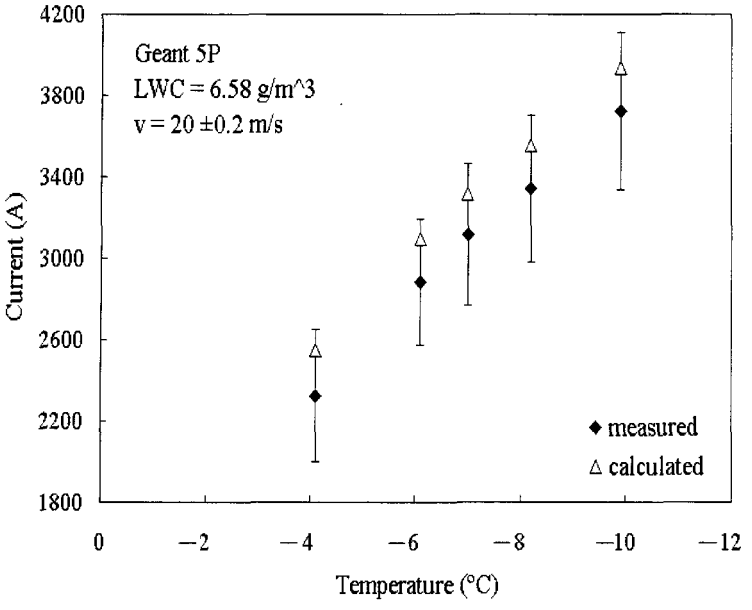

Figure 4.9 Measured and calculated minimum current required to prevent ice accretion on the surface of Geant 5P type conductors.

4.4.2 Effects of atmospheric parameters

In this section, analytical model predictions are compared to experimental measurements for different atmospheric conditions for the purpose of assessing the predictive power of the model. More precisely, the influence of three atmospheric parameters namely, air temperature, wind velocity and LWC, on the minimum current required to prevent icing was considered, but were limited to the Carillon type conductor. Figure 4.10 shows the minimum current intensity required to prevent ice accretion on the conductor as a function of LWC of air for different wind velocities at an air temperature of -10 °C. Obviously, the required current increases with wind speed and LWC. It can also be seen that wind speed has a stronger influence than LWC. In Figure 4.11, the required current is also presented as a function of LWC, but for different air temperatures.

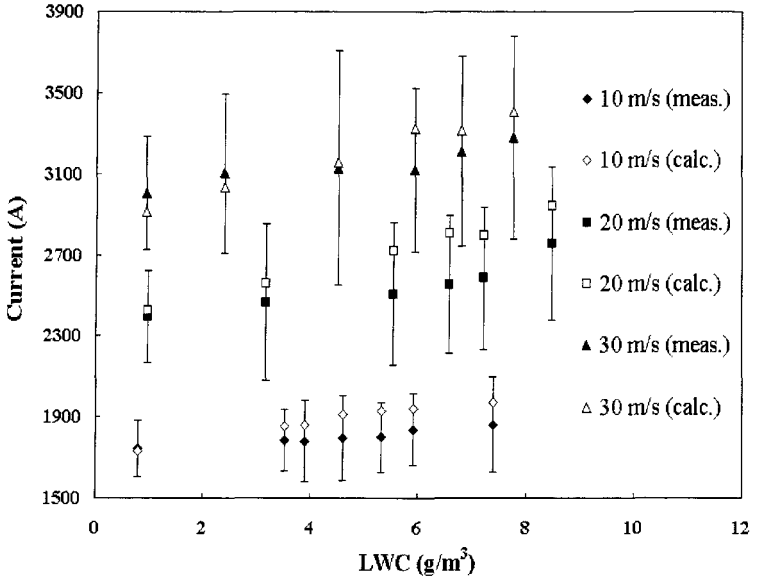

Figure 4.10 Minimum electric current required to prevent ice accretion on Carillon conductor versus LWC of air, in the range of air temperature -9.4<T_a<-9.7°C and median volume diameter 35<MVD<53 μm. The 30 m/s series comprises wind velocities in range 28.6<v<29.4 m/s.

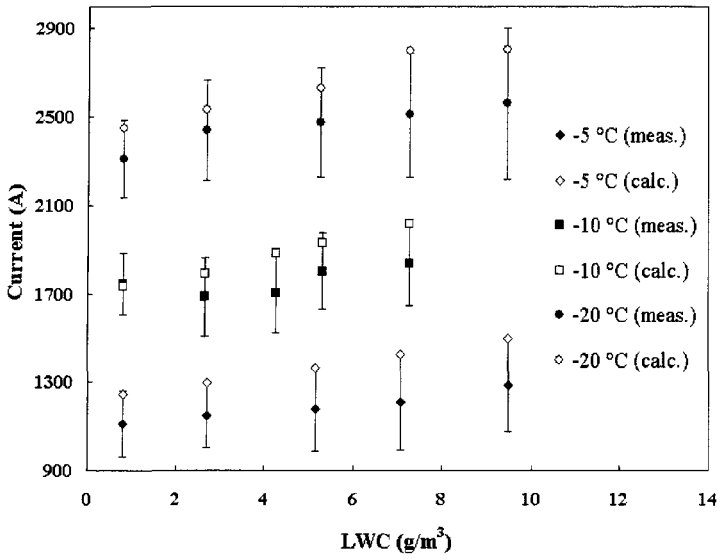

Figure 4.11 Minimum electric current required to prevent ice accretion on Carillon conductor as a function of LWC for different air temperatures. Wind speed 10 ±0.4 m/s, 35<MVD<53 μm.

Figure 4.12 shows the required current as a function of air temperature for different wind speeds. The series of measurements at 20 m/s wind speed were closest to the theoretical calculations making use of Eq. 4.2-10. The 10 m/s series showed a higher rate of increase, while the 30 m/s series had a lower rate with increasing air temperature compared to the theoretical calculations. Once again, all calculated results were within the range of the maximal error of the measurements, except for one case. This case occurred at very low temperature under intensive wind speed conditions, when the measurement uncertainties were high due to ice accumulation on the wind tunnel fan.

In brief, Figure 4.10 ÷ Figure 4.12 shows that the analytical model can provide a good prediction of the minimum current required to inhibit ice accretion on the surface of power line conductors under the atmospheric conditions considered.

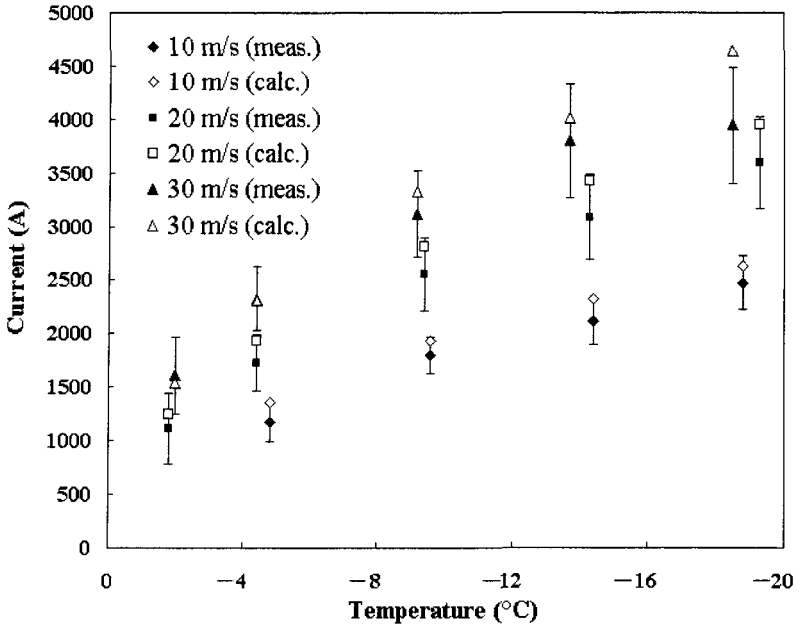

Figure 4.12 Minimum electric current required to prevent ice accretion on Carillon conductor versus air temperature. The 30 m/s series comprises air velocities in the range 29.1<v<29.4 m/s. The LWC is 5.26 g/m^3 at 10 m/s, 6.54 g/m^3 at 20 m/s and 5.72 g/m^3 at 30 m/s wind velocity. Median volume diameter in range 45<MVD<51 μm.

4.4.3 Required current at moderate storm conditions

Generally, freezing precipitations are associated with moderate climatic conditions. During ice accretion events, the wind speed is observed to be between 5 m/s and 15 m/s (with an average value of 7.5 m/s), at temperatures usually ranging from -1 °C to 0 °C with the coldest values recorded between -4 °C to -5 °C [57]. Reference [52] reports a typical LWC value of 0.3 g/m^3 and droplets size of 5÷20 μm for in-cloud icing cases. In contrast, [32] associates in-cloud riming with droplet size of 1÷45 μm and LWC below 1 g/m^3.

Let us consider, for example, atmospheric conditions characterized by a wind speed of 7.5 m/s, air temperature of -4 °C, LWC of 0.5 g/m^3 and MVD of 40 μm. In this case, the minimum current needed to prevent ice accretion on a Condor type conductor is 816 A,

based on the model calculations. However, for the same atmospheric conditions except for a more moderate air temperature of -1 °C, the required current drops to 412 A.

4.4.4 Wetted surface of stranded conductor in air/water spray flow

It was seen previously that the A_w wetted surface of the stranded conductor is one of the influencing parameters of the required electric current. It was estimated during previous calculations as being equal of half of the total surface area, since the exact wetting process of stranded surface has still not been defined. For this purpose observatory experiments have been made to improve the knowledge about the phenomena of runback droplets, water layer detachments and droplet flow in the inter-strand channels. From these observations different cases/classification can be distinguished depending on the present physical processes under the appropriate conditions (wind speed and LWC). In the following section just a short description is given. Table 4-3 presents a brief overview of the various tests performed. A more detailed description is given in APPENDIX 1. These classifications may be considered in future ice accretion and prevention modeling. One of the possibilities is to introduce a correction factor for the wetted surface, which is a function of wind speed and LWC.

On the windward surface of the conductor, water droplets are rarely observed, since they quickly disappear after they hit the conductor. The water droplets are conducted in inter-strand channels toward leeward surface and/or just simply they are detached at bottom and top of conductor depending on the wind speed. Additionally, certain droplets are driven away from windward side by the main airflow.

The leeward surface seems to be more wetted than the windward side. Water droplets arrive mainly from the windward side through the top of the conductor. At higher wind speeds a large amount of the water layer is detached at top of conductor, and in this case less water wet the leeward surface. Additionally, the leeward surface is wetted by smaller, "stationary" water droplets caused by the detached bubbles of air/water dispersed flow. Water layer detachment occurs also at the bottom of conductor due to gravity force. Here the water is conducted from both the windward and leeward side. At strong wind velocities this water layer also wets the leeward side somewhat (see APPENDIX 1).

Table 4-3 Wetted surface phenomena under different atmospheric conditions

Phenomena	**Atmospheric condition**			
	10 m/s; 5.6g/m^3	20 m/s; 6.6 g/m^3	20 m/s; 8.5 g/m^3	30 m/s; 5.3 g/m^3
"Top" layer	at 80°÷85°, not continuous	at 90°, almost continuous	at 90°, continuous	at 90°, not continuous
"Top" layer detachment	no	yes (droplets)	yes (droplets)	yes (layer)
"Bottom" layer	near -90°	leeward side (appr. -90°÷-95°)	leeward side (appr. -90÷-95°)	leeward side (appr. -90÷-95°)
Stationary sprays	not observed	leeward side	leeward side	leeward side, frequent
"Fast" runback water	yes, but not frequent	yes	yes	yes, but not frequent
"Slow" runback water	yes	yes	yes	yes

CHAPTER 5

DE-ICING OF PARTIALLY ICE-COVERED CONDUCTORS BY JOULE HEATING

Ice layer may accumulate on the overhead conductors under severe atmospheric conditions such as during ice storms. The ice accumulates mainly on the windward side of the conductor during the beginning period of ice formation. When significant ice accumulates, the conductor turns due to moment of gravity force acting on the ice layer. Finally, ice accumulates all around the conductor almost symmetrically.

The objective of the present techniques is to shed the ice layer, before the conductor rotates and a concentric ice sleeve is developed. The technique may also be used after a critical mass accumulates on the windward side, if the conductor rotation is blocked. Two possibilities are analyzed to shed the ice from non-rotating conductors depending on the Joule heating. In one technique the Joule heating is realized by impulse current superposed on the nominal ac current. Another heating technique is based on the simple increasing of the ac nominal current. Both techniques can be used with different strategies depending on the time of interaction in the ice accretion process (during or after icing event). For both heating techniques a thermal model is presented, which calculates the required current and energy to shed the ice from overhead conductors. The current and energy requirements are analyzed under various current and atmospheric parameters. These analyses are made using thermal models based on explicit finite difference method (EFD). The finite difference method is introduced in [45].

5.1 De-icing of partially ice-covered conductors by impulse current heating

5.1.1 Introduction

During certain unfavourable winter conditions, the Joule heat produced by nominal ac current in the conductors is not enough to keep the conductor surface temperature above freezing. The idea is to apply one or more impulse currents superposed on a nominal ac current in order to increase the current intensity near the surface of the conductor. A high enough current intensity concentrated into the thin skin depth region should remove the ice sleeve from the overhead conductor.

The main scope of this part of study is to analyze the effect of atmospheric and impulse current parameters on the shedding time and on the required number of current impulses. Furthermore, the influence of the equivalent thermal conductivity and the model parameters as well as the set of shedding conditions is investigated. The temperature distributions are plotted for certain simulation cases in order to better understand the heat generation and conduction in the conductor-ice composite with impulse current applied in the conductor.

5.1.2 The model

5.1.2.1 Model hypothesis

The heat conduction in the conductor-ice composite is considered one-dimensional, since the angular heat flow is assumed to be negligible compared to the radial heat flow.

The heat conduction is calculated along the conductor radius associated with the stagnation point. The conductor investigated is an aluminium conductor without a steel core. The heat conduction through strands is characterized with the equivalent radial thermal conductivity. The diameter of the conductor is 35 mm. The ice sleeve is assumed to shed from the conductor when the ice temperature is above the melting point in the thin ice layer close to the conductor surface. This means that the ice sleeve is detached due to the force of gravity after the adhesive force is eliminated at the conductor-ice interface.

5.1.2.2 Calculation procedure

First, the steady state temperature distribution of the conductor-ice composite should be calculated with 60 Hz, ac nominal current in the conductor under the given atmospheric conditions. It is obtained by using the steady-state calculator sub-module (see Figure 5.1), which supplies the initial temperature distribution (initial condition) into the core model of the impulse de-icing module. The steady-state calculator requires the set of material properties, the atmospheric conditions as well as the current intensity distribution. The heat source distribution is non-uniform along the radius due to a skin effect in the conductor. The non-uniform current intensity distribution is calculated using a commercial code, namely Maxwell SV. The steady state calculations are based on 1000 A nominal current. The same 60 Hz, ac current is present in the conductor during impulse heating. The impulse current also results in the non-uniform current intensity distribution along the radius according to the equivalent frequency of the impulses. The finite element Maxwell code is used again for current intensity distribution calculations at high frequencies, which is also an input parameter into the core module.

Figure 5.1 shows the schematic algorithm of the impulse de-icing model. The core module of the impulse de-icing model solves the established EFD equations of the corresponding transient heat conduction problem. Basically, it contains the same type of finite difference equations as the steady-state calculator. The differences are in the applied EFD modulus and in the input parameters including intensity distribution and initial temperature. The core module requires also a finer mesh as the steady-state calculator due to the current intensity is concentrated in the thin skin layer, as well as the applied time step is much smaller. Hence, the mesh size is chosen as 0.1 mm in the conductor and 0.125 mm in the ice layer. In order to keep the time step small enough, the differential modulus is chosen as 1/8 in the conductor, and 1/29 in the ice sleeve in the most of the cases. In some particular cases the set of mathematical parameters of the EFD equations was different.

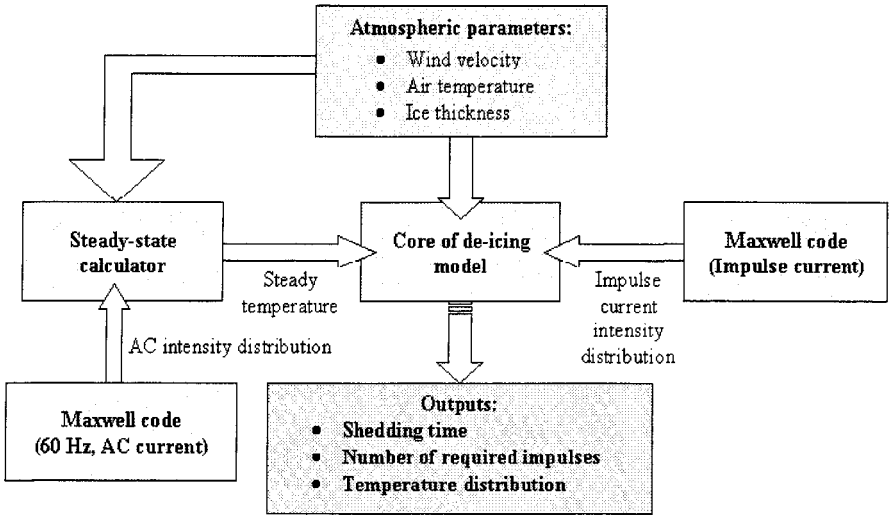

Figure 5.1 Schema of de-icing model using impulse current heating

The outputs of the core model are the shedding time, the number of the required impulses to shed the ice sleeve and the temperature distribution of the conductor-ice

composite along radius. The ice is considered to shed from the overhead conductor, when the ice sleeve temperature reaches 0 °C at 0.25 mm distance from the conductor surface.

5.1.3 Mathematical model

The general heat diffusion equation with source term in the cylindrical system is as shown in Eq. 5.1-1.

$$\frac{1}{\alpha}\frac{\partial T(r,t)}{\partial t} = \frac{\partial^2 T}{\partial r^2} + \frac{1}{r}\frac{\partial T}{\partial r} + \frac{q_v(r)}{k}, \qquad \text{and } r \neq 0 \qquad \text{Eq. 5.1-1}$$

where T is the temperature (°C), r is radius (m), k is thermal conductivity (W/mK) and q_v is the volumetric heat generation (W/m^3). The thermal diffusivity, α (m^2/s), is defined as follows:

$$\alpha = \frac{k}{\rho \cdot c}, \qquad \text{Eq. 5.1-2}$$

where ρ is the density of material (kg/m^3), and c is the specific heat (J/kgK).

5.1.3.1 Interior temperature of nodes in conductor and in ice sleeve

The volumetric heat generation, q_v is parameterized as:

$$q_v = 0 \text{ in the ice sleeve and} \qquad \text{Eq. 5.1-3}$$

$$q_v(r) = \rho_e (i_{ac} + i_{imp})^2 \text{ in the conductor,} \qquad \text{Eq. 5.1-4}$$

where i_{ac} is current density (A/m^2) due to 60 Hz, alternating current and i_{imp} is current density (A/m^2) due to impulse current. Naturally, the i_{imp} is set to zero in the steady state calculator, since there is no impulse current. The general heat diffusion equation is discretized with finite differences. For time discretization the forward schema and for space

(along radius) discretization the central schema is applied. After discretization, the temperature of each node in the conductor (i) and in the ice (j) is expressed with Eq. 5.1-5 and Eq. 5.1-6, respectively.

In conductor, for nodes $1 \leq i \leq N_c$-2,

$$T_i^{n+1} = T_{i-1}^n M_c\left(1-\frac{1}{2i}\right)+T_i^n(1-2M_c)+T_{i+1}^n M_c\left(1+\frac{1}{2i}\right)+\frac{M_c \cdot \Delta r_c^{\,2}}{k_c} q_v(r) \qquad \text{Eq. 5.1-5}$$

In ice sleeve, for nodes $1 \leq j \leq N_s$-1,

$$T_j^{n+1} = T_{j-1}^n M_s\left(1-\frac{1}{2\left(\frac{R_c}{\Delta r_s}+j\right)}\right)+T_j^n(1-2M_s)+T_{j+1}^n M_s\left(1+\frac{1}{2\left(\frac{R_c}{\Delta r_s}+j\right)}\right) \qquad \text{Eq. 5.1-6}$$

In the above equations, Δr_c and Δr_s are the sizes of mesh (m), N_c and N_s are the total number of nodes in the conductor and in ice sleeve, respectively. Subscripts i and j denotes arbitrary nodes in the conductor and ice sleeve respectively. Superscript n nominates the time step, while subscripts c and s designate conductor and ice sleeve material. The differential modulus, M, of the EFD equations is defined as follows:

$$M = \frac{\alpha \cdot \Delta t}{\Delta r^2}, \qquad \text{Eq. 5.1-7}$$

where Δt is the actual time step (s).

5.1.3.2 Temperature of the origin node in conductor

The general heat diffusion equation has singularity in the origin of the conductor (at r=0). Thus, the l'Hospital rule is used in order to exclude the singularity problem. In this case the diffusion equation becomes as follows:

$$2\frac{\partial^2 T}{\partial r^2}\bigg|_{r=0} + \frac{q_v(r)}{k} = \frac{1}{\alpha}\frac{\partial T}{\partial t} \qquad \text{Eq. 5.1-8}$$

After discretizing Eq. 5.1-8, introducing a fictitious node and applying the symmetry condition of origin, the temperature of the origin can be expressed as shown by Eq. 5.1-9.

$$T_0^{n+1} = T_0^n(1-4M_c) + 4M_c T_1^n + M_c \frac{q_v(r)\cdot \Delta r^2}{k_c} \quad \text{, at r=0, i=0} \qquad \text{Eq. 5.1-9}$$

5.1.3.3 Third kind of boundary condition at the surface of ice sleeve

The boundary condition of the third kind is prescribed at outer surface of the ice sleeve. It is parameterized as shown in Eq. 5.1-10.

$$k_s \frac{\partial T}{\partial r} = h(T_a - T_s) \quad , \qquad \text{Eq. 5.1-10}$$

where T_a and T_s are the air and ice surface temperatures (°C), respectively. The discretized form of Eq. 5.1-10 is substituted into discretized Eq. 5.1-1 of the surface node (N_s). Finally, the S surface temperature is expressed as shown in Eq. 5.1-11.

$$T_s^{n+1} = 2M_s T_{s-1}^n + T_s^n\left[1-2M_s\left(1+\frac{\Delta r\cdot h}{k_s}\left\{1+\frac{1}{2\left(\frac{R_c}{\Delta r}+N_s\right)}\right\}\right)\right] + T_a 2M_s \frac{\Delta r\cdot h}{k_s}\left(1+\frac{1}{2\left(\frac{R_c}{\Delta r}+N_s\right)}\right) \quad \text{, Eq. 5.1-11}$$

where h is the local heat transfer coefficient (W/m^2K) at S surface node. This particular node is in the stagnation point of the airflow, where the local heat transfer coefficient, h, can be parameterized in general form as in Eq. 5.1-12 [36].

$$Nu = \sqrt{\mathrm{Re}} \quad , \qquad \text{Eq. 5.1-12}$$

where Nu and Re are the Nusselt and the Reynolds numbers, respectively. After parameterization of the dimensionless numbers, the local heat transfer coefficient in the stagnation point is defined as:

$$h = \frac{k_a}{D}\sqrt{\frac{V \cdot D}{\upsilon_a}}, \qquad \text{Eq. 5.1-13}$$

where D is the diameter of the ice sleeve (m), V is the free stream velocity of air (m/s), k_a and ν_a are the thermal conductivity (W/mK) and the kinematic viscosity (m^2/s) of air, respectively.

5.1.3.4 Node temperatures at conductor-ice interface

The finite control volume approach is used for the calculation of temperatures near the interface of conductor and ice. Note that the interface node is denoted by C, the nearest node to the interface in the conductor with C-1 and the nearest point in the ice with C+1. No heat capacitance is assumed in node C as shown in Figure 5.2.

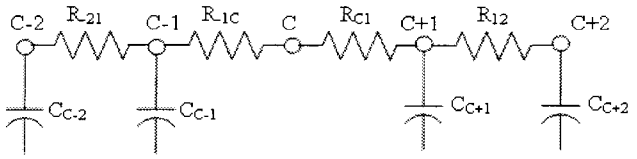

Figure 5.2 Equivalent heat flow network at the conductor-ice interface

The heat flow balance at node C is as expressed in Eq. 5.1-14, from which T_c can be easily obtained.

$$k_c \frac{T_c - T_{c-1}}{r_c - r_{c-1}} = k_s \frac{T_{c+1} - T_c}{r_{c+1} - r_c} \qquad \text{Eq. 5.1-14}$$

The heat equation in nodes C—1 and C+1 are also discretized as presented in Eq. 5.1-15 and Eq. 5.1-16, respectively.

$$C_c \frac{T_{c-1}^{n+1} - T_{c-1}^{n}}{\Delta t} = \frac{T_{c+1}^{n} - T_{c-1}^{n}}{R_{11}} - \frac{T_{c-1}^{n} - T_{c-2}^{n}}{R_{-21}} + q_v \cdot \Delta V \quad , \qquad \text{Eq. 5.1-15}$$

$$C_s \frac{T_{c+1}^{n+1} - T_{c+1}^{n}}{\Delta t} = \frac{T_{c+2}^{n} - T_{c+1}^{n}}{R_{12}} - \frac{T_{c+1}^{n} - T_{c-1}^{n}}{R_{11}} \quad , \qquad \text{Eq. 5.1-16}$$

where ΔV is control volume (m^3) of nodes, C_c and C_s are the thermal capacitances (J/m^2K) of conductor and ice sleeve respectively. The thermal capacitance in 1D is defined as next:

$$C = \rho \cdot c \cdot \Delta r \qquad \text{Eq. 5.1-17}$$

The resistances in above equations are defined as:

$R_{11} = R_{-1c} + R_{c1}$; $R_{-21} = \Delta r_c / k_c$,; $R_{-1c} = (r_c - r_{c-1}) / k_c$; $R_{c1} = (r_{c+1} - r_c) / k_s$; $R_{12} = \Delta r_s / k_s$.

Finally, the temperatures of nodes C-1 and C+1 can be written in the following forms:

$$T_{c-1}^{n+1} = T_{c-2}^{n} M_c + T_{c-1}^{n}\left[1 - \frac{\Delta t}{C_c}\left(\frac{1}{R_{11}} + \frac{1}{R_{-21}}\right)\right] + T_{c+1}^{n}\frac{\Delta t}{C_c R_{11}} + \frac{M_c \cdot \Delta r_c^{\,2}}{k_c} q_v(r) \qquad \text{Eq. 5.1-18}$$

$$T_{c+1}^{n+1} = T_{c-1}^{n}\frac{\Delta t}{C_s R_{11}} + T_{c+1}^{n}\left[1 - \frac{\Delta t}{C_s}\left(\frac{1}{R_{11}} + \frac{1}{R_{12}}\right)\right] + T_{c+2}^{n} M_s \qquad \text{Eq. 5.1-19}$$

5.1.3.5 Determining the steady state condition

The steady state is defined using Eq. 5.1-20 of the steady state calculator.

$$\Theta = \frac{T_1^n - T_a}{T_1^s - T_a} = 0.99 \qquad \text{Eq. 5.1-20}$$

where T_1^n is the temperature of the nearest node to conductor surface in the ice, after n time steps. T_1^s is the same node temperature in steady state. The steady state temperature difference across the ice layer can be formulated by Eq. 5.1-21.

$$T_1^s - T_a = I^2 \cdot R \cdot k_{skin}\left(\frac{1}{D\pi h} + \frac{\ln(D/d_c)}{2k_c\pi}\right), \qquad \text{Eq. 5.1-21}$$

where k_{skin} is the skin effect coefficient, D is the diameter of the ice sleeve (m), d_c is the diameter of conductor (m), R is the ac resistance (Ω/m) of 1 m long conductor and I is the electric current (A) present in the conductor.

5.1.4 Impulse current

In this part of the study triangular form current impulses with different peak values and time durations are investigated. The current intensity distribution along the radius due to impulse current is equivalent to the intensity distribution due to ac current at corresponding equivalent frequency.

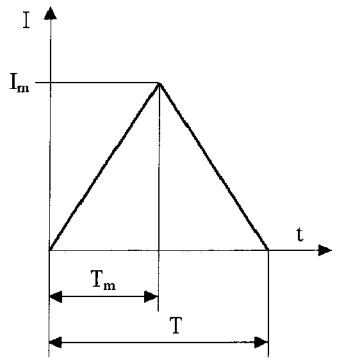

Figure 5.3 Triangular impulse form

The equivalent frequency, f_{eq} (Hz) of the impulse current can be calculated with Eq. 5.1-22.

$$f_{eq} = \frac{1}{\pi \cdot T_m} \qquad \text{Eq. 5.1-22}$$

where T_m is the peak time (s). The skin depth of the corresponding equivalent frequency is defined by Eq. 5.1-23.

$$\delta = \sqrt{\frac{\rho_e}{\pi \cdot \mu \cdot f_{eq}}} \qquad \text{Eq. 5.1-23}$$

where ρ_e is the bulk electric resistivity (Ωm) and μ is the absolute magnetic permeability (H/m) of the conductor. The current intensity that flows at the conductor surface decreases by 36.79 % (1/e) of its value at a distance of the skin depth from the surface. Table 5-1 shows the investigated impulse durations with the corresponding equivalent frequencies and skin depths, δ.

Table 5-1 Impulse current parameters of investigation

T (μs)	**f_{eq} (Hz)**	**δ (mm)**
2000	318.3	4.7373
1000	636.6	3.3497
500	1273.2	2.3686
212.2	3000	1.5431

5.1.5 Equivalent current intensity distribution due to impulse current

It has already been mentioned that the current intensity distribution along the conductor radius was simulated by using Maxwell SV, a commercial finite element code. The simulation was performed for different equivalent frequencies with 1 A nominal current in

the conductor. During the current intensity distribution simulations, a compact aluminium cylinder of A1 type with resistivity of 0.028264 μΩ·m is considered. It is known that the current intensity increases toward the conductor surface, and the rate of increase is greater at higher frequencies due to the skin effect. This is clearly shown in Figure 5.4.

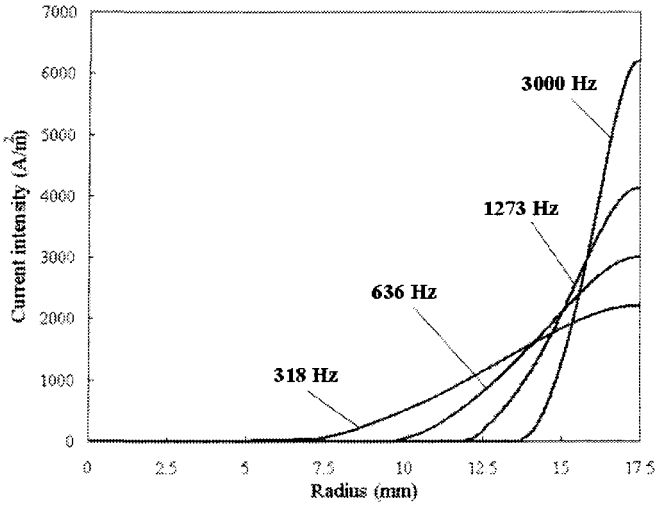

Figure 5.4 Current distribution along radius with 1 A nominal current in the conductor at various equivalent frequencies

5.1.6 Effect of impulse peak value and shedding condition

In this section, the effect of impulse amplitude and the influence of the defined shedding condition in the required time and number of impulses are examined. First, the ice shedding condition was prescribed at 0.125 mm from the conductor surface in the ice. Namely, the ice was considered to shed down when the ice sleeve temperature reaches 0 °C at this particular node. Secondly, ice layer detachment was assumed when ice temperature reaches the melting point at 0.25 mm from the conductor surface. The deviations in the

results obtained by two different shedding conditions are presented as follows. The study was performed for the following simulation cases:

- Ice thickness of 5 mm
- Air temperature of –5 °C
- Wind speed of 10 m/s
- Equivalent radial thermal conductivity of conductor: 7 W/mK
- Equivalent frequency of 1273.2 Hz
- Conductor diameter of 35 mm
- Differential modulus of EFD model of 1/8 in conductor, and of 1/29 in ice sleeve
- Mesh sizes of 0.1 mm in conductor, 0.125 mm in ice layer

As aforementioned, the computations assume 1000 A nominal current in the conductor during both initial condition calculation and de-icing by impulse heating. The results of the required shedding time and the corresponding number of impulses are shown in Figure 5.5 and Figure 5.6. Obviously both the shedding time and the number of required impulses are decreasing drastically with increasing amplitude of impulses. This is due to the high current density concentrated near the conductor surface. The deviations between the results obtained with two different sets of shedding condition can also be seen. Naturally, the required time obtained with the shedding condition established at 0.25 mm is longer than with that defined at 0.125 mm from the conductor surface. The differences between shedding times as well impulse numbers obtained with a different set of shedding

conditions are more significant for smaller impulse current amplitudes. The shedding condition established at 0.125 mm leads to more convenient results from the standpoint of energy conservation. However, in the following study, the shedding condition is defined at 0.25 mm. Consequently the level of security that the ice sleeve sheds is higher.

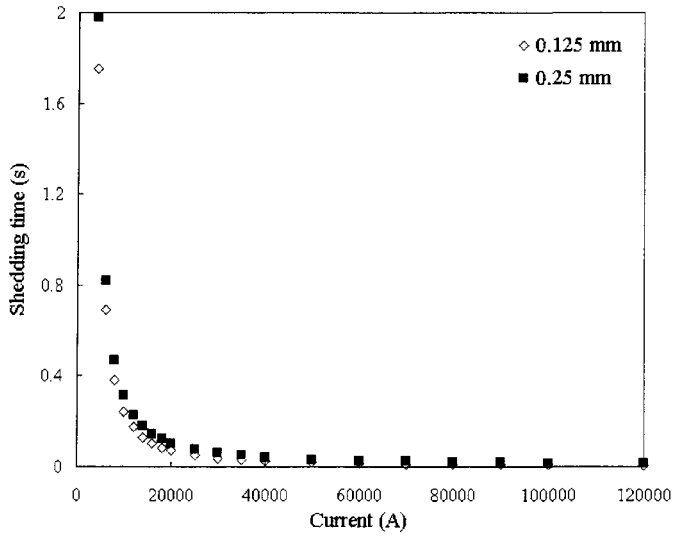

Figure 5.5 Shedding time obtained with different shedding conditions

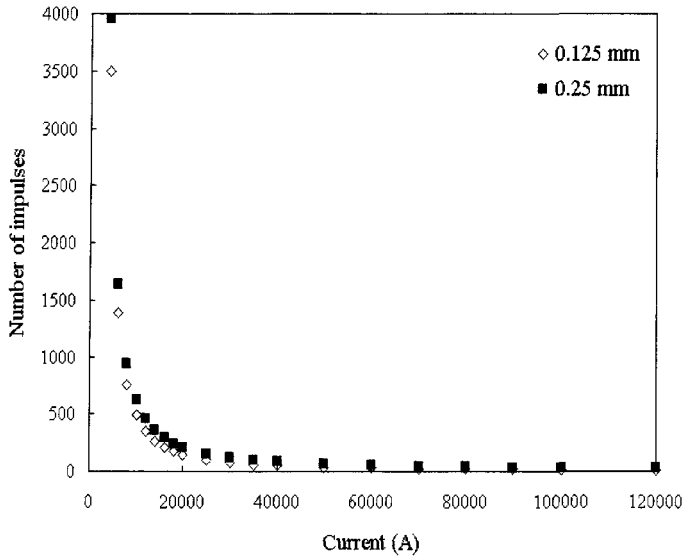

Figure 5.6 Number of impulses obtained with different shedding conditions

5.1.7 Effect of mesh quality and differential modulus of the EFD model

In the following section, the influence of different model parameters on the precision of numerical calculation is analyzed. Note that small time steps are required during calculations in order to resolve the very short impulse durations. Also, the EFD is the most precise for a differential modulus value of 1/6, in which case the truncation error becomes lowest [45]. Consequently, the differential modulus should be adjusted to this value. However, the only way to keep the time steps small is to decrease the differential modulus, M, due to limitations in the mesh quality. The extremely fine mesh results in time- and memory- expensive calculations. The main disadvantage of explicit schemes is that the mesh size and the time step are not independent from each other.

The calculations have been made with three different model set-ups, A, B and C for the simulation case already introduced in the previous section. The following sets of model parameters were investigated:

- Set-up A: Differential modulus, M_c, is 1/8. The mesh size is 0.1 mm in the conductor, and 0.125 mm in the ice sleeve.
- Set-up B: Differential modulus, M_c, is 1/80. The mesh size is 0.25 mm in the conductor and 0.5 mm in the ice sleeve.
- Set-up C: Differential modulus, M_c, is 1/45. The mesh size is 0.25 mm in the conductor, and 0.5 mm in the ice sleeve.

The results of required shedding time are shown in Figure 5.7. The corresponding required number of impulses is presented in APPENDIX 2. The most accurate results from

the analyzed cases are obtained with set-up A, in which the differential modulus is the closest to the recommended value of 1/6. Case A is tested with differential modulus values of ½÷⅛, and no remarkable changes are found in the calculated results. It can be clearly seen from the comparison of results obtained with set-ups B and C that they give significantly different results from those obtained with set-up A. Obviously set-up C is more precise than B due to larger differential modulus. It can be concluded by comparing the results of the three set-ups that significant deviation of M from the recommended value could have a greater effect on the precision than as the mesh quality. A finer mesh results smaller time steps for the same value of differential modulus. Furthermore, the resolution of the current intensity distribution is finer as well.

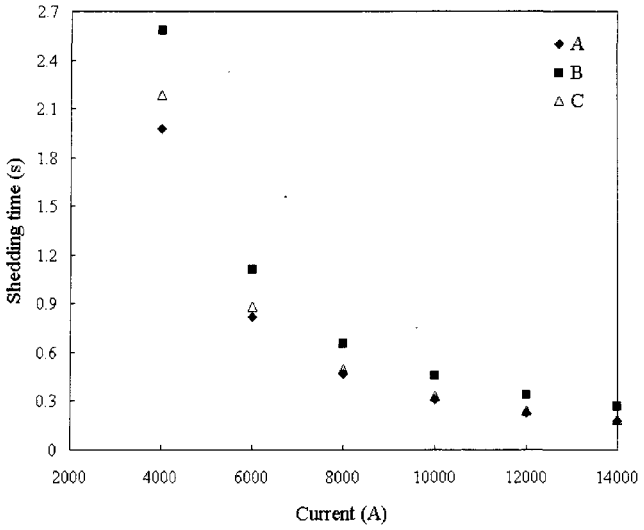

Figure 5.7 Shedding time obtained with different set-ups

5.1.8 Effect of equivalent frequencies of the impulse current

The impulse duration determines an equivalent frequency, as shown in Eq. 5.1-2. Naturally, the longer impulse duration supplies a lower equivalent frequency and a thicker

skin depth (see Table 5-1), where the greatest part of the Joule heat is generated in the conductor. Therefore, it is expected that the lower frequencies result in longer shedding time, and consequently more impulses are required to shed the ice. For the purpose of analyzing these effects, calculations were performed with following parameters:

- Ice thickness of 5 mm
- Air temperature of –5 °C
- Wind speed of 10 m/s
- Equivalent radial thermal conductivity of conductor: 7 W/mK
- Shedding condition established at 0.25 mm from conductor surface
- Mesh size of 0.1 mm in conductor and of 0.125 mm in ice sleeve
- Investigated equivalent frequencies: 318.3 Hz, 636.6 Hz, 1273.2 Hz and 3000 Hz

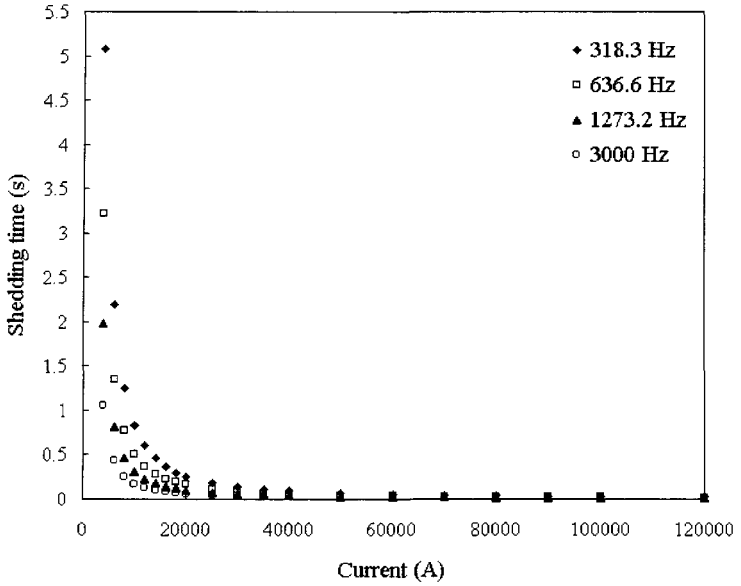

Figure 5.8 Required shedding time obtained for various equivalent frequencies

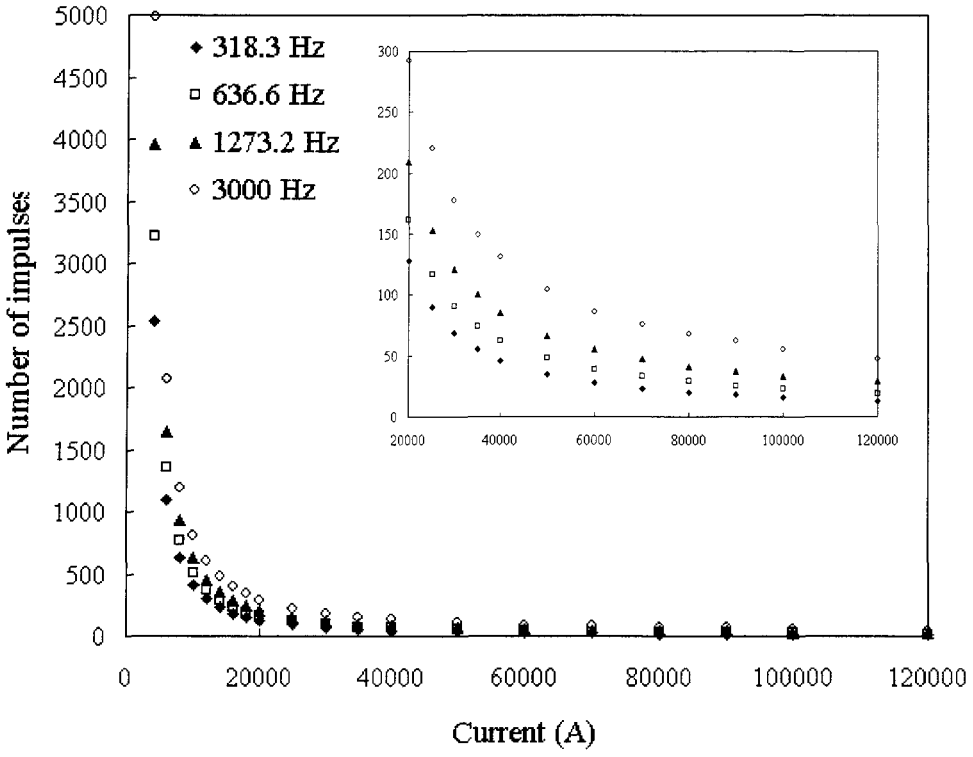

Figure 5.9 Number of required impulses obtained for various equivalent frequencies

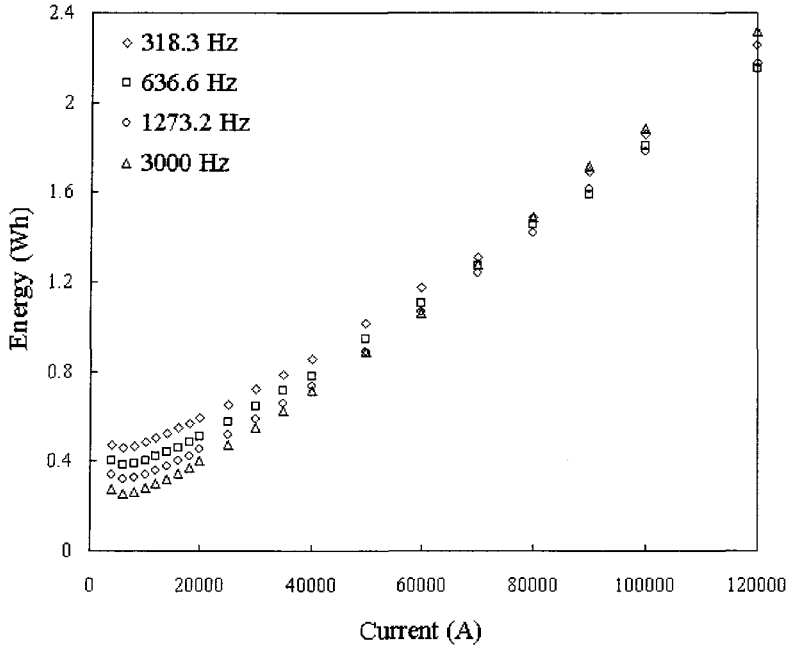

Figure 5.10 Required energy obtained for various equivalent frequencies

It is clearly shown in Figure 5.8 and Figure 5.9 that increasing the equivalent frequency and keeping the peak constant value results in shorter shedding time, but also in a greater number of required impulses. Naturally, the energy required to shed the ice increases with both number and duration of current impulses. Therefore, one may ask: What is the most economical set of equivalent frequencies and number of impulses?

The required energy is shown in Figure 5.10 for various equivalent frequencies. It can be seen that for each equivalent frequency there is an optimal peak current at which the required energy has a minimum value. This is a peak current of around 6000 A for the investigated simulation cases. It is also shown that for higher equivalent frequencies the minimum required energy is smaller. Therefore, from the energy conservation aspect the most convenient strategy is to apply the highest possible frequency with the optimum peak current in the conductor.At very high peak currents the required energy does not definitely decrease with increasing equivalent frequency. For example at peak currents of 100 000 A the required energy is the lowest for 1273.2 Hz, while at peak currents of 120 000 A the lowest value is obtained for 636.6 Hz.

Consequently, it can be realized that for each peak current there is also an optimum equivalent frequency when the energy requirements have a minimum. The required number of impulses seems to be critical from the view of practical use. The number of impulses is smaller for lower frequencies under same peak current. Therefore, in the further study the 318.3 Hz equivalent frequency will be in the focus.

5.1.9 Temperature distribution in conductor-ice sleeve composite at various peak currents and shedding condition

The thermal conduction process, the influence of equivalent frequency and of peak current on the shedding time could be better understood by analyzing the temperature history of conductor-ice composites during Joule heating by impulse current. Therefore, in the following section the transient temperature distributions along the radius are analyzed at various peak currents and frequencies. The temperature distribution calculations are made for the same cases as in section 5.1.8 with various peak current values. The transient temperature histories of conductor-ice sleeve composite are shown in Figure 5.11÷Figure 5.14, which were obtained for equivalent frequency of 3000 Hz and for various peak values of impulse current. Recall, the conductor radius is 17.5 mm.

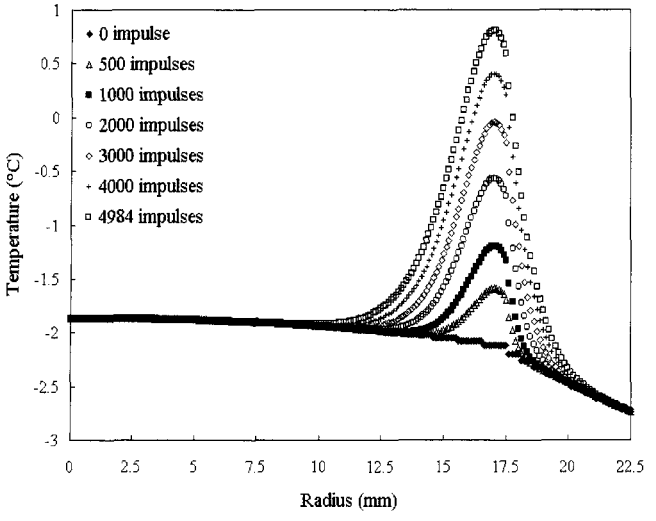

Figure 5.11 Temperature distribution at 3000 Hz and peak value of 4000 A

It is clearly shown that the impulse current of smaller peak value heats up a greater part of the conductor-ice composite. Also, part of conductor near the surface is warmer than

those of higher peak currents. These phenomenon leads to longer shedding time and consequently to a greater number of impulses.

At higher impulse peak values the temperature gradients are greater due to more intensive Joule heating. Surprisingly, the skin depth region could warm up to around 45 °C at high peak impulses of 100 000 A (see Figure 5.14).

By applying greater impulse peak currents could be more economical in shedding the ice from the conductor as the heating with small peak impulses, in which case a greater mass of conductor-ice composite is heated up. However, after particular peak values the difference between the heated mass is negligible (compare the temperature histories obtained for 50000 and 100000 A), but the average temperature of heated mass could be unnecessarily increased. Therefore, an economic peak value of impulses should be established for each set of equivalent frequency and atmospheric parameters in order to minimize the applied energy.

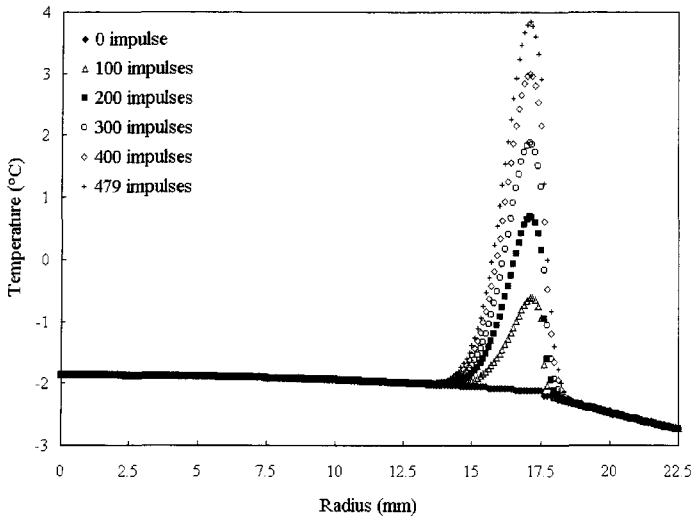

Figure 5.12 Temperature distribution at 3000 Hz and peak value of 14000 A

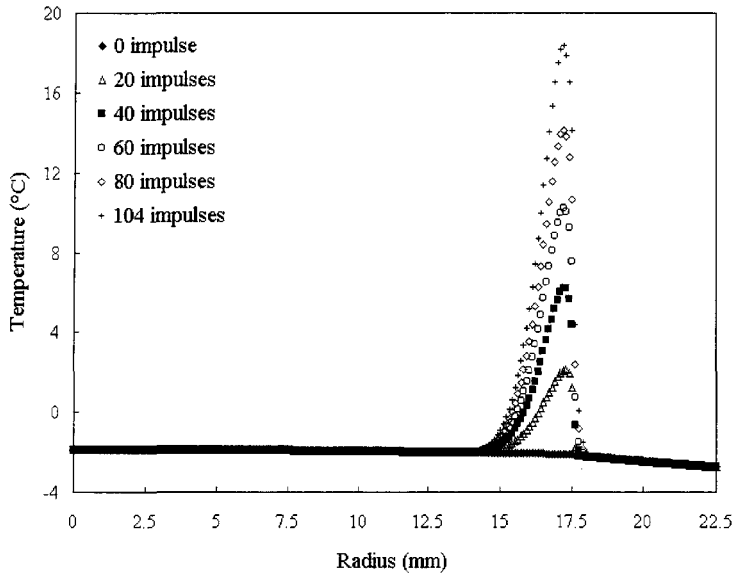

Figure 5.13 Temperature distribution at 3000 Hz and peak value of 50000 A

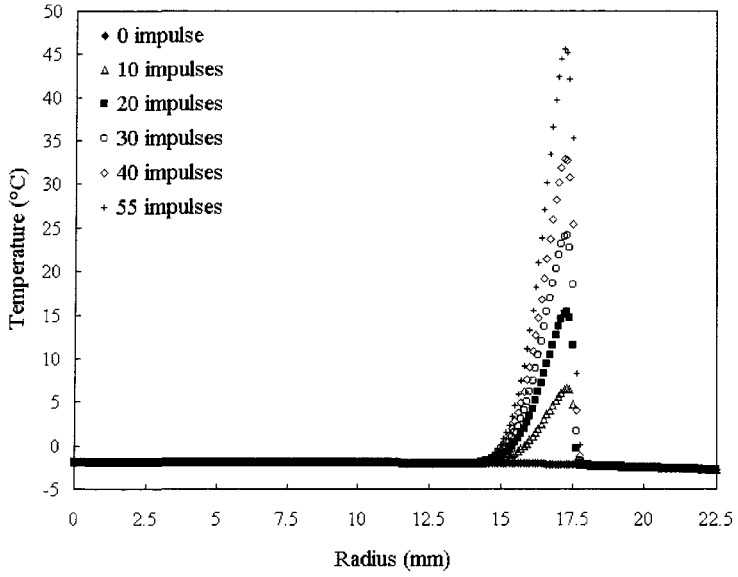

Figure 5.14 Temperature distribution at 3000 Hz and peak value of 100000 A

Figure 5.15 and Figure 5.16 show the temperature distributions of impulse heating with 318.3 Hz equivalent frequency. More temperature histories for various equivalent frequencies and peak currents can be found in APPENDIX 2. It can be seen that at lower

equivalent frequencies the heated mass of the conductor-ice composite is greater than at high frequencies. This is due to smaller current intensities and temperature gradients near the conductor surface.

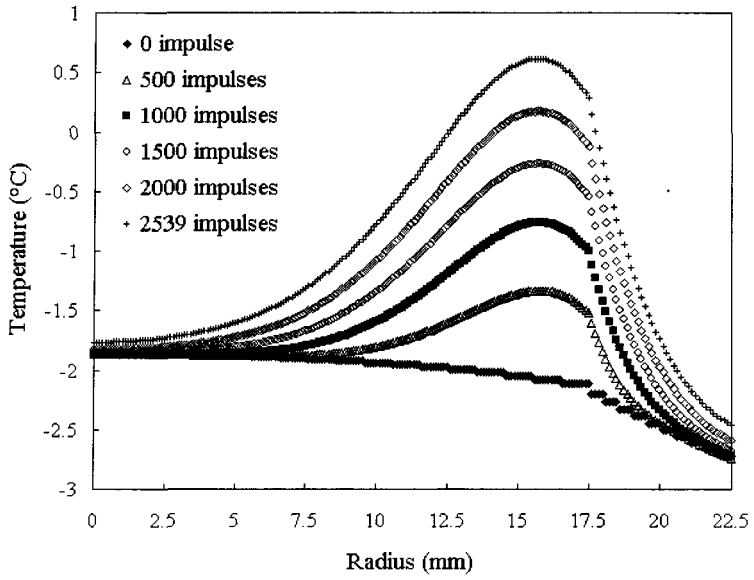

Figure 5.15 Temperature distribution at 318.3 Hz and peak value of 4000 A

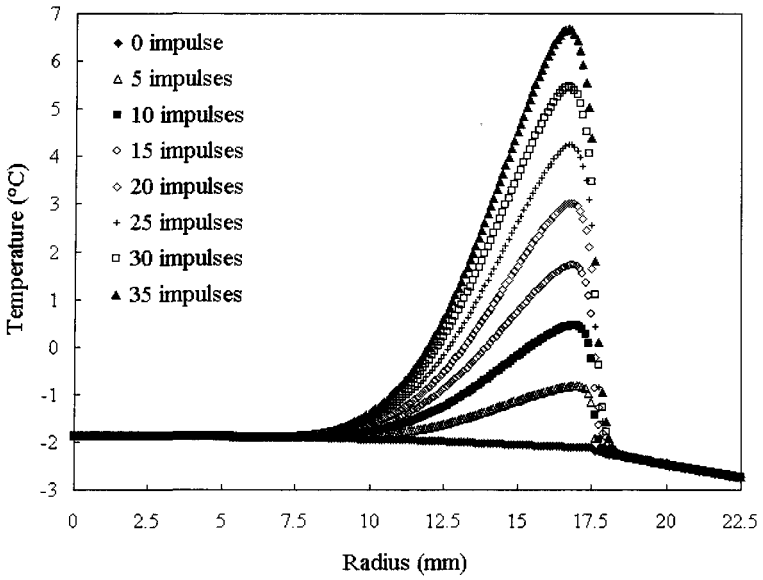

Figure 5.16 Temperature distribution at 318.3 Hz and peak value of 50 000 A

In the following section, a brief overview of the effects of equivalent frequency and peak current to the temperature distribution in the conductor-ice composite is presented.

If small peak current is applied into the conductor, then with increasing equivalent frequency (see also Figure 5.17):

- A smaller part of the conductor and ice layer is heated up
- The maximum temperature near conductor surface increases
- The temperature deeply inside the conductor section decreases
- Temperature gradients are greater in both ice and conductor
- The maximum value of temperature distribution moves toward conductor surface
- The outer ice sleeve surface temperature is lower

If high peak current is applied into the conductor, then with increasing equivalent frequency (see also Figure 5.18):

- A smaller part of the interior conductor is heated up, but this effect is less significant than for small peak currents
- The temperature of the conductor is inside section decreases significantly
- The maximum value of temperature distribution increases intensively
- Temperature gradients are greater in the conductor, but almost no significant changes can be observed in the ice sleeve temperature distribution

For the same equivalent frequency with increasing peak currents:

- A smaller part of the conductor and ice sleeve is heated up
- Temperature gradients and peak values of the temperature distribution are increase

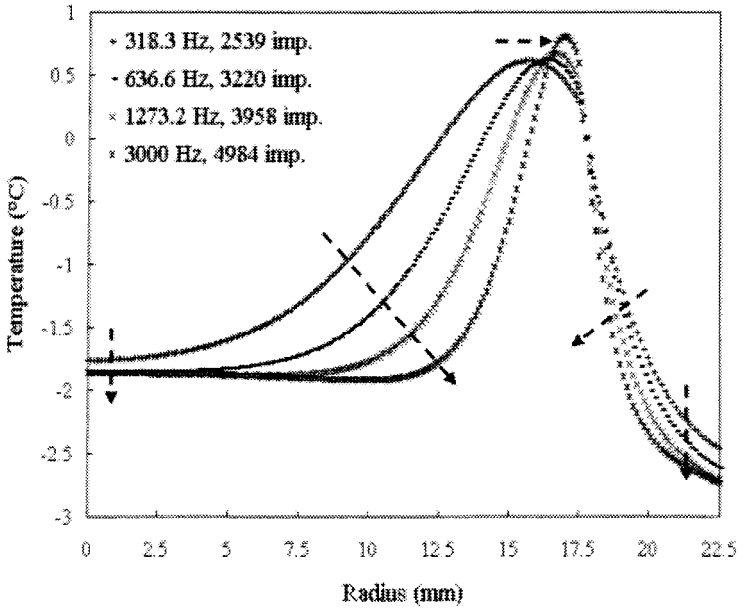

Figure 5.17 Temperature distribution after the last applied impulse of 4000 A peak current

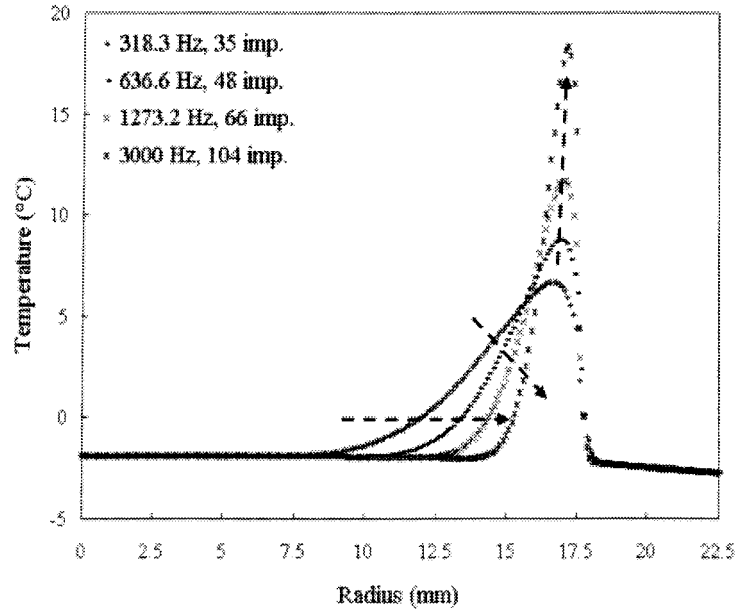

Figure 5.18 Temperature distribution after the last applied impulse of 50000 A peak current

5.1.10 Effect of wind velocity

It is easy to realize that the wind speed may influence the temperature of ice sleeve, and consequently the shedding time and the required energy. The strongest influence of this parameter is analyzed in the following section. Calculations have been made with parameters already presented in section 5.1.8 with an equivalent frequency of 318.3 Hz and under wind speeds of 5, 10 and 20 m/s. The result of these calculations is shown in Figure 5.19. It can be seen that there is no significant effect of wind velocity on shedding time or on the required number of impulses. The differences between calculated required number of impulses obtained under various wind speeds completely disappears at applied peak currents greater than 8000 A for the case investigated.

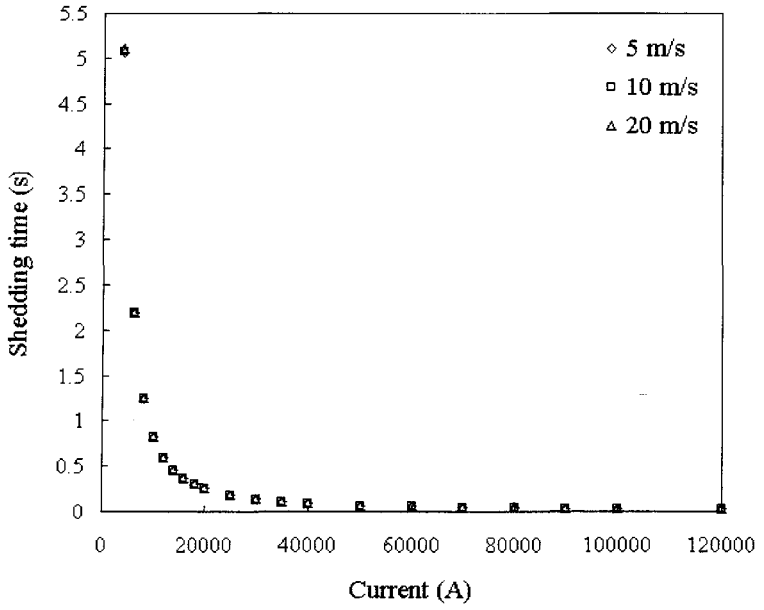

Figure 5.19 Required shedding time under various wind speeds

It seems to be one of the main advantages of the impulse current heating technique that the required shedding time is not sensitive to the wind velocity. It means that if the peak

current is correctly chosen, then the same electric energy is required to remove the ice sleeve in wind speed conditions under 5 m/s as wind speed conditions under 20 m/s.

5.1.11 Effect of equivalent thermal conductivity

The intensity of heat conduction in the conductor is determined by an equivalent thermal conductivity. As seen in Chapter 9, the radial equivalent thermal conductivity also depends on several parameters, including contact pressures between strands. In this section, the influence of this parameter on the shedding time is examined. It is expected that the shedding time will decrease with increasing equivalent thermal conductivity, since the heat conduction is more intensive. The calculations were made with the following set of parameters:

- Ice thickness of 5 mm
- Air temperature of –5 °C
- Wind speed of 10 m/s
- Shedding condition defined at 0.25 mm from conductor surface
- Differential modulus of EFD model: 1/8 in conductor, 1/29 in ice sleeve; exceptions are the calculations with 14 W/mK, where M_c is 1/3 and M_s is 1/22
- Mesh sizes of 0.1 mm in conductor and of 0.125 mm in ice layer
- Equivalent frequency of 318.3 Hz
- Equivalent radial thermal conductivities: 2 W/mK, 7 W/mK and 14 W/mK

The results of the required shedding time are presented in Figure 5.20 for various radial thermal conductivities. The corresponding number of impulses can be found in APPENDIX 2. It is clearly shown that generally, the greater equivalent thermal conductivities decrease the shedding time if enough large peak currents are applied. However, at smaller peak currents the greater equivalent thermal conductivity does not necessarily mean shorter shedding time as it is seen from Figure 5.20. Hence, there is an optimum equivalent thermal conductivity for which the shedding time and the required number of impulses is the smallest under the same peak current applied.

Figure 5.21 and Figure 5.22 show the temperature distribution after the shedding condition is reached near the conductor surface. The temperature history of these cases is also presented in APPENDIX 2. At a great peak current of 50000 A, there is no significant difference in the heated mass of the conductor with different equivalent thermal conductivities. However, the temperature gradients and the peak temperatures are greater for lower thermal conductivities, because less liberated heat is conducted away. At small applied peak current of 4000 A, the heated mass increases with increasing thermal conductivities. The temperature gradients and the peak temperatures are greater for lower thermal conductivities as in the case of large applied peak currents.

Finally, it can be concluded that the required shedding energy is less for conductors of higher radial thermal conductivity under significant peak currents.

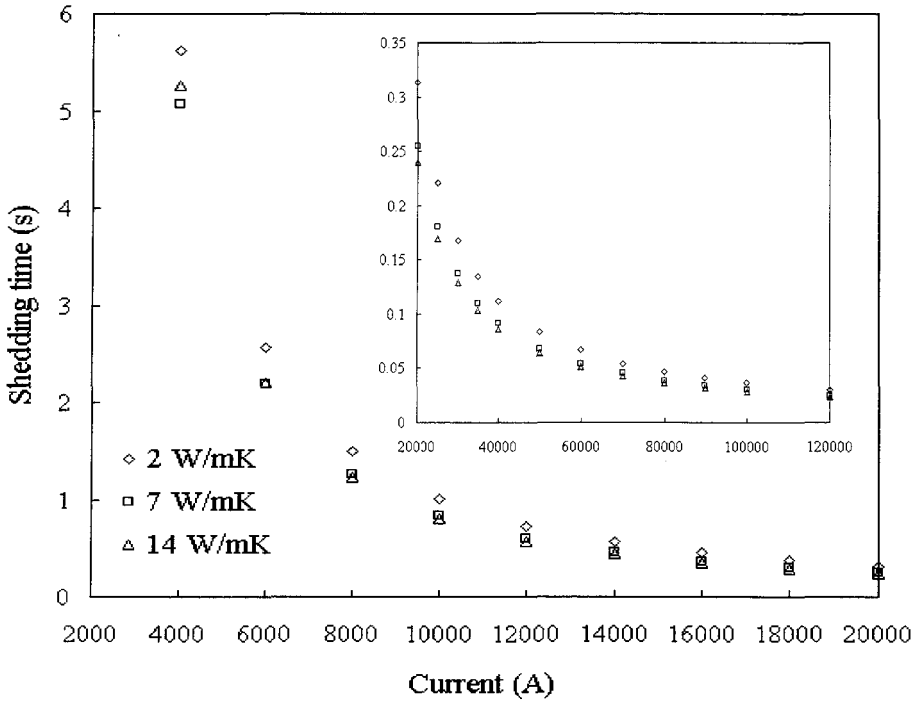

Figure 5.20 Shedding time versus peak current for different radial thermal conductivities

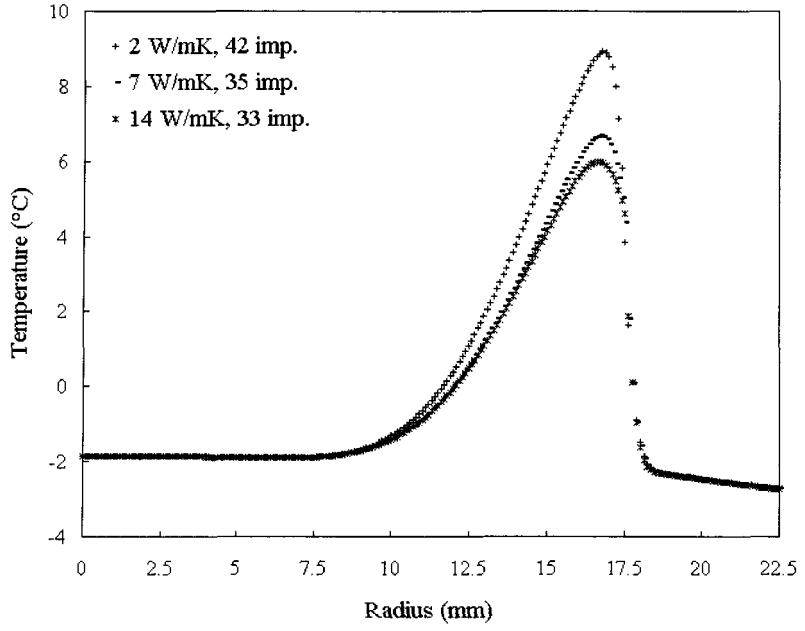

Figure 5.21 Temperature distribution after last applied impulse with different conductor thermal conductivities and 50000 A peak current in the conductor

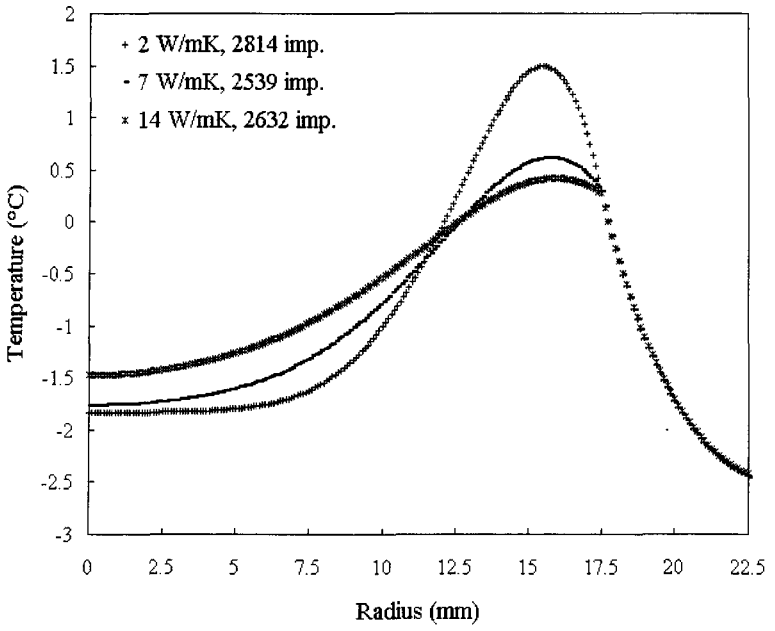

Figure 5.22 Temperature distribution after last applied impulse with different conductor thermal conductivities and 4000 A peak current in the conductor

5.1.12 Effect of ice thickness

The impulse heating technique could be applied after ice accumulation or at any time during the accretion process. It is well known that the thicker ice layer (larger diameter) increases the convective heat transfer from the surface. Furthermore, the thermal resistance due to heat convection decreases, while thermal resistance due to heat conduction increases with increasing ice thickness. Hence, one may ask: Which is the more economical strategy to interrupt the accretion process? Is there an optimal ice thickness which requires a minimum number of impulses? This is analysed in the following section for the following set of model parameters:

- Air temperature of –5 °C

- Wind speed of 10 m/s
- Shedding condition defined at 0.25 mm from conductor surface
- Differential modulus of EFD model: 1/8 in conductor and 1/29 in ice sleeve
- Equivalent radial thermal conductivity of 7 W/mK
- Mesh sizes of 0.1 mm in conductor and 0.125 mm in ice
- Equivalent frequency of 318.3 Hz
- Studied ice thicknesses: 2 mm, 5 mm and 8 mm

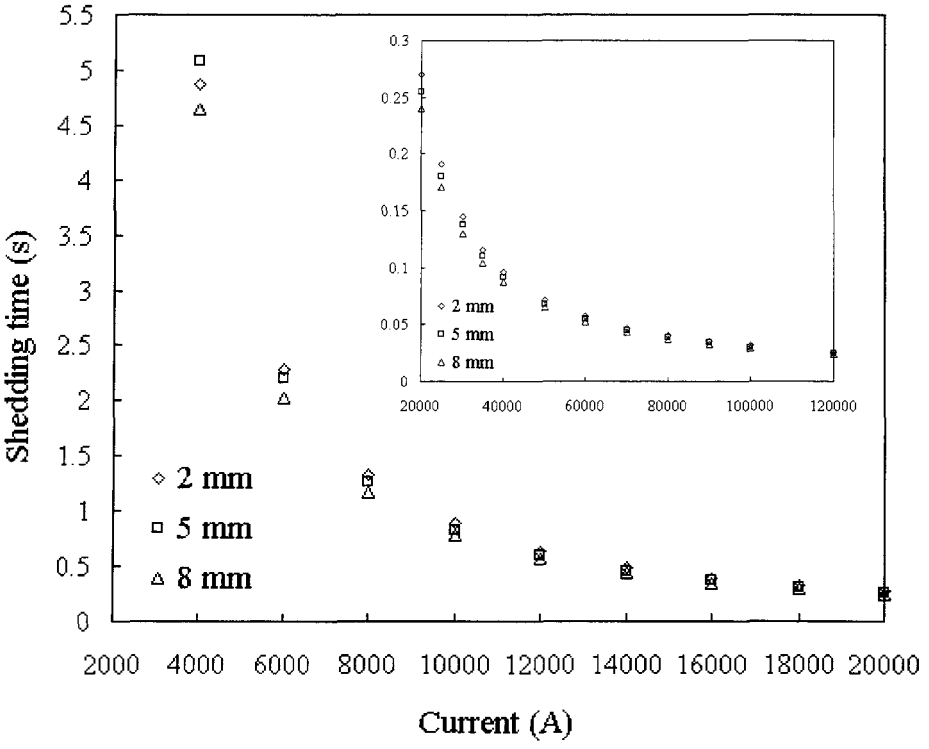

Figure 5.23 Required shedding time for various ice thicknesses on the conductor

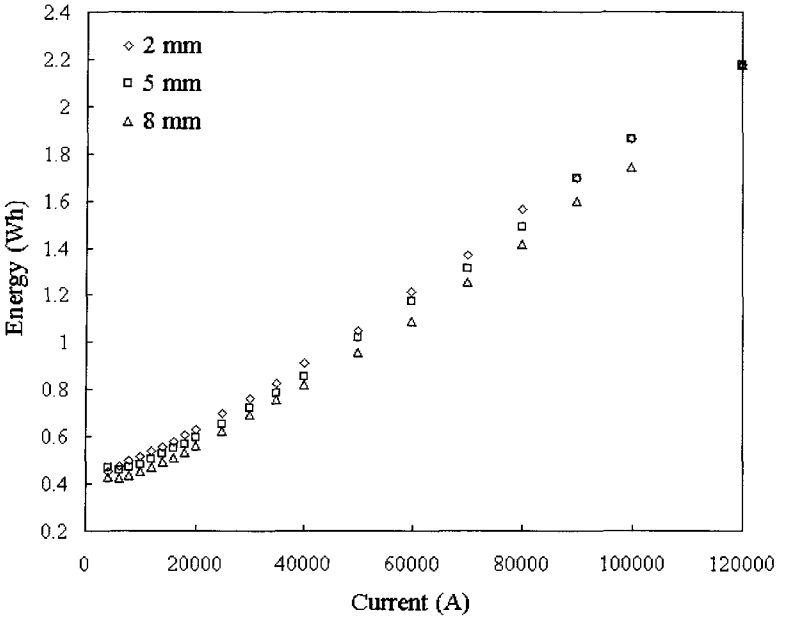

Figure 5.24 Required energy for various ice thicknesses on the conductor

It can be concluded from Figure 5.23 that generally, the increasing ice thickness reduces the shedding time as well as the required number of impulses. The only exception is at the relatively small peak value of 4000 A. In this case the 2 mm ice thickness requires less shedding time and energy than for an ice layer 5mm thick. The effect of ice thickness on the impulse number diminishes with higher peak currents in the conductor. It can be concluded that the most economical strategy is to allow the maximum ice thickness to accumulate on the conductor at which the conductor still does not turn and then remove the ice layer by Joule heating with impulse current. The temperature distribution obtained for various ice thicknesses is shown in APPENDIX 2. It is clear from Figure 5.24 that for each ice thickness an optimal impulse current exists, in which case required energy has minimum value.

5.1.13 Effect of air temperature

Naturally, under colder airflow conditions the initial temperature of the ice layer is lower also, before the Joule heating is applied. Obviously, the required shedding time increases with decreasing air temperature for the same peak current flow in the conductor. The influence of the air temperature is investigated for the following parameters:

- Wind speed of 10 m/s
- Shedding condition defined at 0.25 mm from conductor surface
- Differential modulus of EFD model: 1/8 in conductor, 1/29 in ice sleeve for -5 °C; ¼ in conductor and 1/15 in ice sleeve for -8 °C and -10 °C air temperatures
- Equivalent radial thermal conductivity of 7 W/mK
- Mesh size of 0.1 mm in conductor and of 0.125 mm in ice
- Equivalent frequency of 318.3 Hz
- Ice thicknesses of 5 mm
- Studied air temperatures: –5, -8 and -10 °C

The calculation results are shown in Figure 5.25÷Figure 5.27. It is shown that the air temperature has a significant influence on the shedding time as well as on the required energy. In order to diminish the effect of air temperature a high peak current should be applied.

There is also an optimum peak current for which the energy required to shed the ice has minimum value. This optimum value increases with decreasing air temperatures. For example, at an air temperature of -5 °C, the peak current of 6000 A is the optimum value, while at -8 °C and -10 °C approximately 12 000 A and 14 000 A are the optimum peak currents.

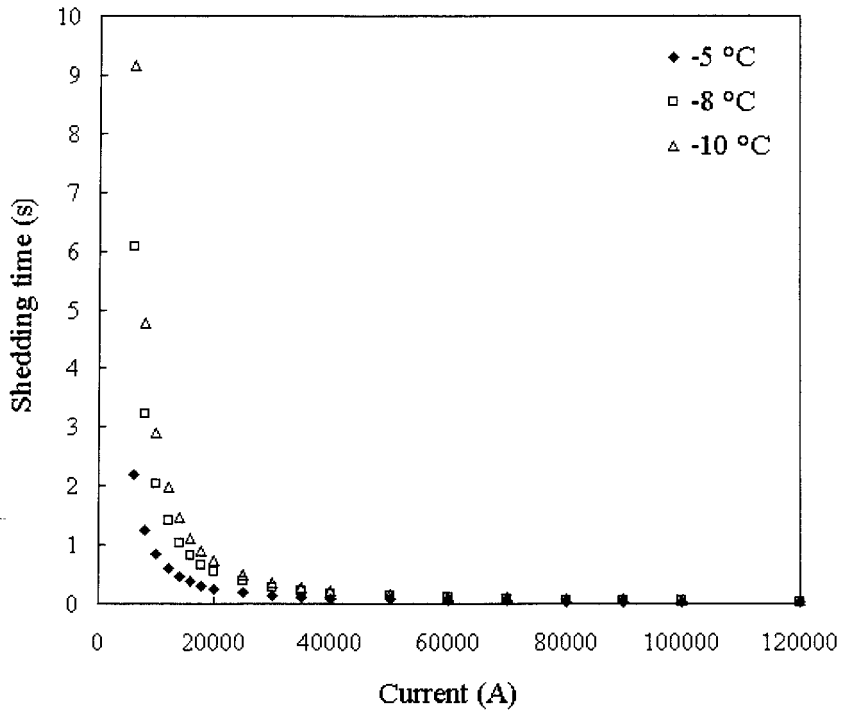

Figure 5.25 Required shedding time for various air temperatures

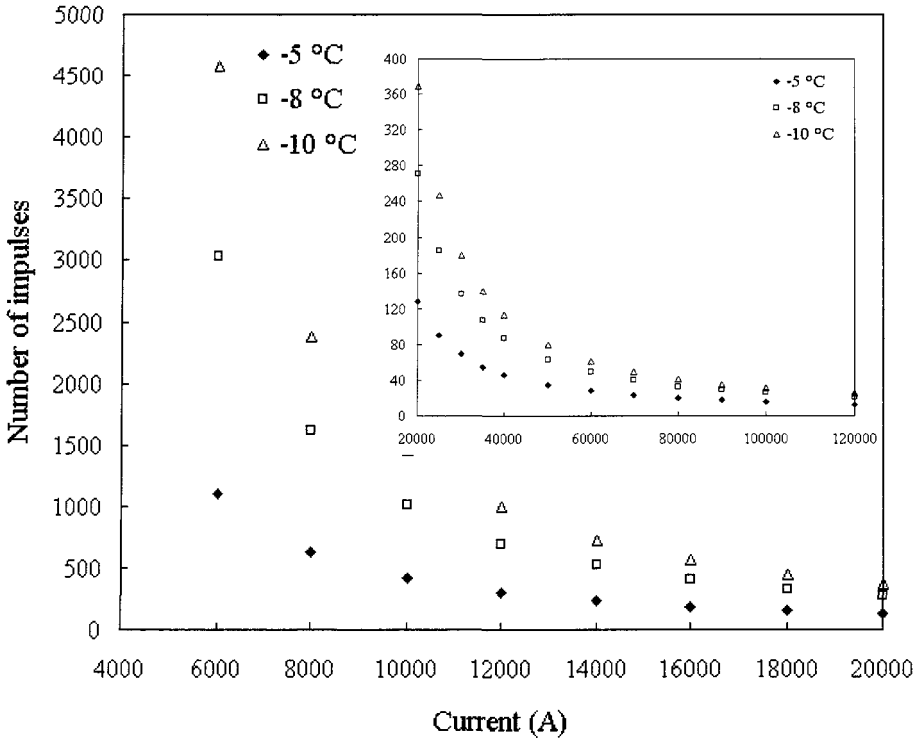

Figure 5.26 Required number of impulses for various air temperatures

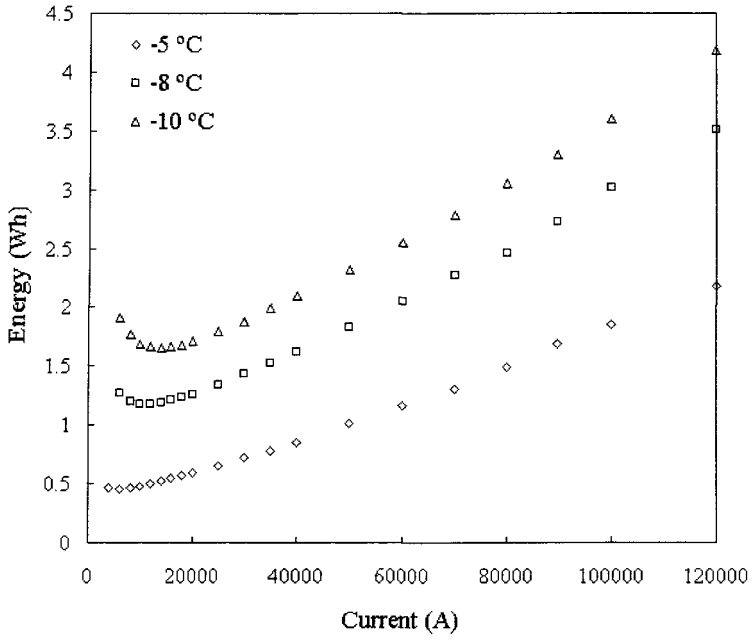

Figure 5.27 Energy required to shed the ice layer for various air temperatures

5.2 De-icing of partially ice-covered conductor by 60 Hz current heating

An alternative possibility for conductor Joule heating is to increase the nominal ac current in the conductor. Furthermore, the nominal ac current can be increased before, during or after ice storms. Remember, the ice prevention technique was related to increased nominal current applied before and maintained during the icing event (see Chapter 4). The present technique covers the cases when the nominal current is increased after an ice layer has already developed on the windward side of conductor, but the conductor still does not rotate due to the torque of the ice. In the following section, the current and energy requirements for the present heating technique are investigated under various current and atmospheric parameters.

The model presented in the previous section was used mainly for calculations. The calculation procedure is very similar to that of impulse current heating. In the present case it simplifies, since current distribution due to impulses and the steady state are not calculated. Most of the calculations were made assuming a compact aluminium cylinder of 17.5 mm external radius. Finally, a stranded conductor represented by an equivalent thermal conductivity as well as a steel cored conductor is investigated.

5.2.1 Effect of electric current magnitude

First, the influence of electric current magnitude on the shedding time and required energy is studied. The calculations are performed with the following parameters:

- ice thickness of 5 mm

- air temperature of -5 °C
- wind velocity of 10 m/s
- equivalent thermal conductivity of the conductor: 222 W/mK

The shedding time and the required energy are calculated with different values of electric current in the conductor. The results are shown in Figure 5.28 and Figure 5.29. It is shown that increasing the electric current in the conductor results in shorter shedding time and required energy. Therefore, the most economical de-icing technique of the non-rotating conductor is to apply the greatest amount of current possible.

The calculated minimum current (asymptotic solution) is 1086.8 A under actual meteorological conditions. The current values after infinite time tend to this value that still can trigger ice melting under the given atmospheric conditions.

Temperature history distributions obtained with various electric currents in the conductor are shown in Figure 5.30÷Figure 5.32. It can be seen that at higher currents much more heat is conducted into the ice layer from the conductor than is taken away at outer ice surface by airflow. A higher current flow in the conductor generates a greater temperature drop across the ice sleeve. At the conductor-ice interface the temperature gradient is determined by heat flux from the conductor that is produced by internal Joule heating.

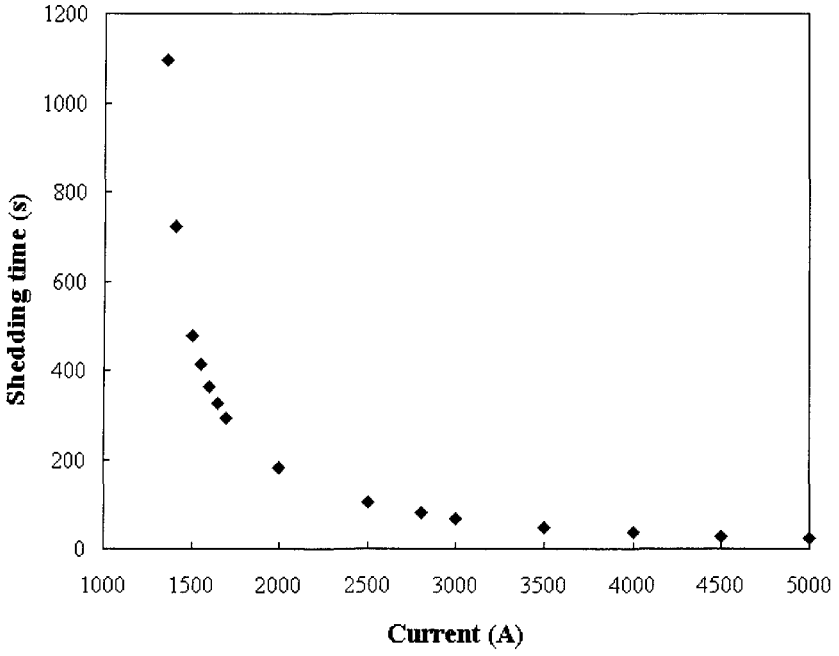

Figure 5.28 Required shedding time versus electric current in conductor

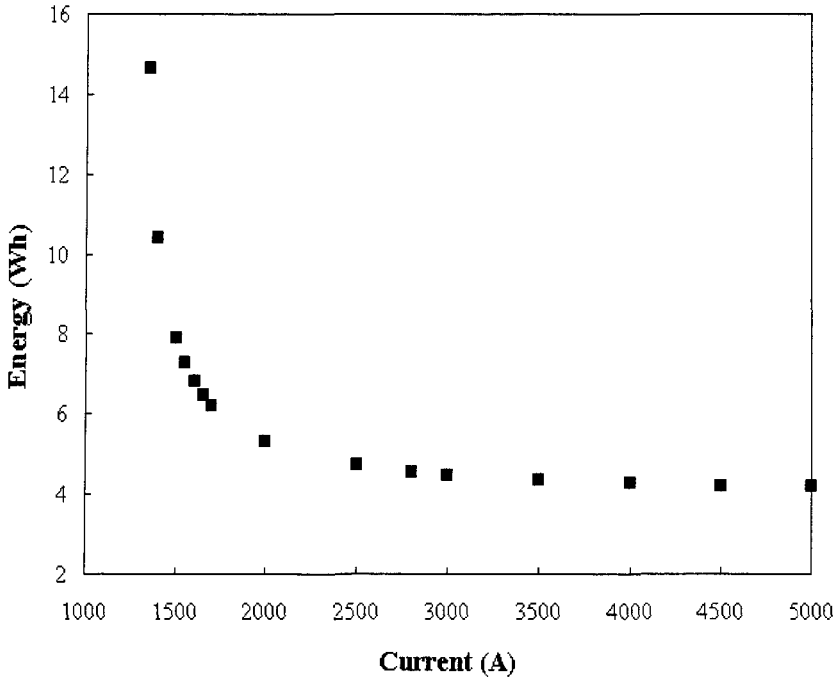

Figure 5.29 Energy required to shed ice layer versus electric current in conductor

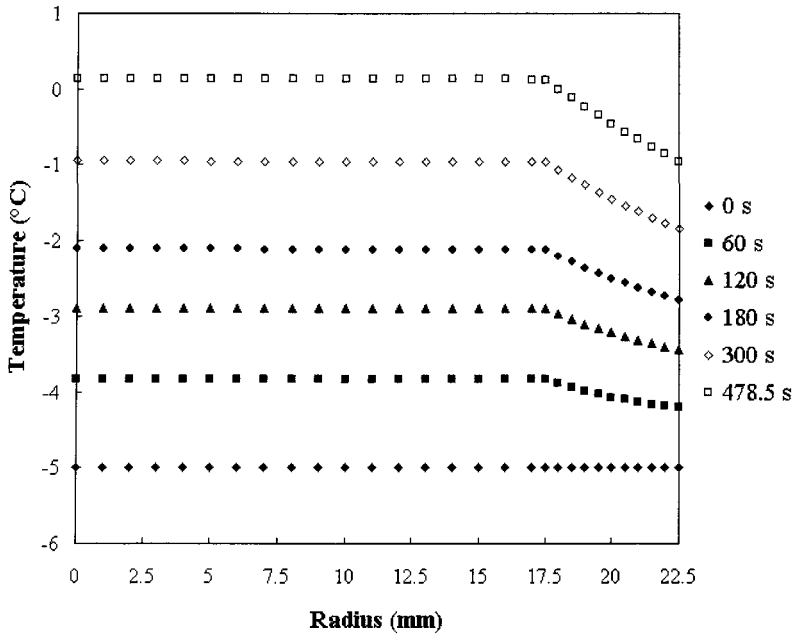

Figure 5.30 Temperature distribution at 10 m/s wind speed, -5 °C air temperature, 5 mm ice thickness and 1500 A current in the conductor

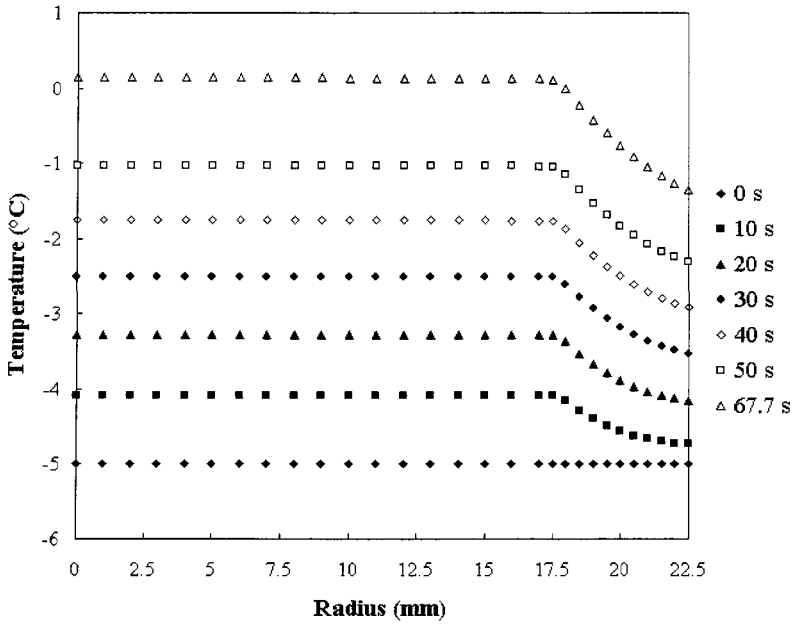

Figure 5.31 Temperature distribution at 10 m/s wind speed, -5 °C air temperature, 5 mm ice thickness and 3000 A current in the conductor

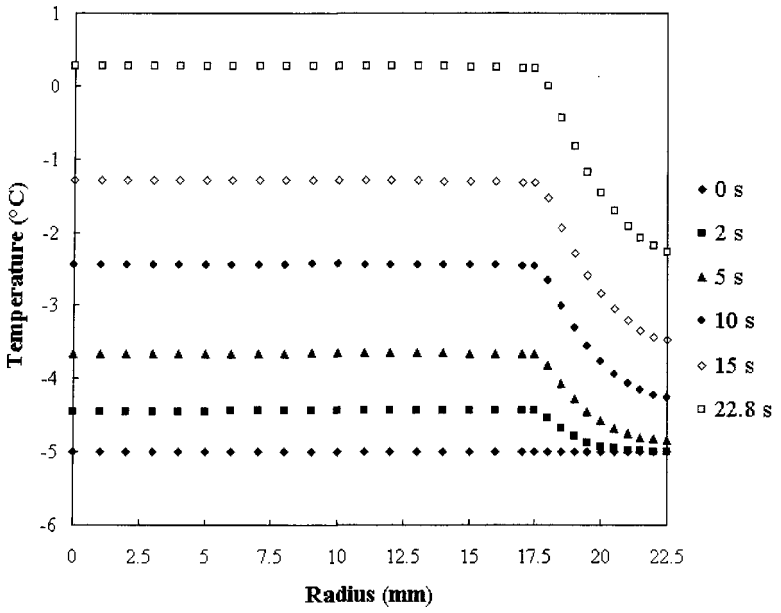

Figure 5.32 Temperature distribution at 10 m/s wind speed, -5 °C air temperature, 5 mm ice thickness and 5000 A current in the conductor

5.2.2 Effect of wind velocity

In the following section, the effect of wind velocity is analyzed on the required shedding time and energy. For the purpose of this analysis the previous simulation case is repeated under higher wind speeds, namely at 20 m/s and 30 m/s. The results of computation are shown in Figure 5.33 and Figure 5.34. Obviously, the shedding time and the required energy to shed all ice are greater under higher wind speeds than in moderate conditions. However, the required energy and melting time rise are negligible, if the applied current is high enough (greater than 3000 A in our case). Therefore, it can be concluded again that the most economical de-icing strategy is with the highest applicable current in the conductor.

The minimum current (asymptotic solution) from the analytical steady state calculations, which can still trigger ice melting with an air temperature of -5 °C and ice thickness of 5 mm is 1087, 1178 and 1227 A under wind velocities of 10, 20 and 30 m/s respectively.

The temperature distributions are presented in APPENDIX 3 for various cases. It is shown that the higher wind velocity causes a greater temperature drop across the ice sleeve. However, the change in the temperature distribution due to wind velocity is not essential at higher applied current (by comparing simulation cases of 3000 A with different wind speeds).

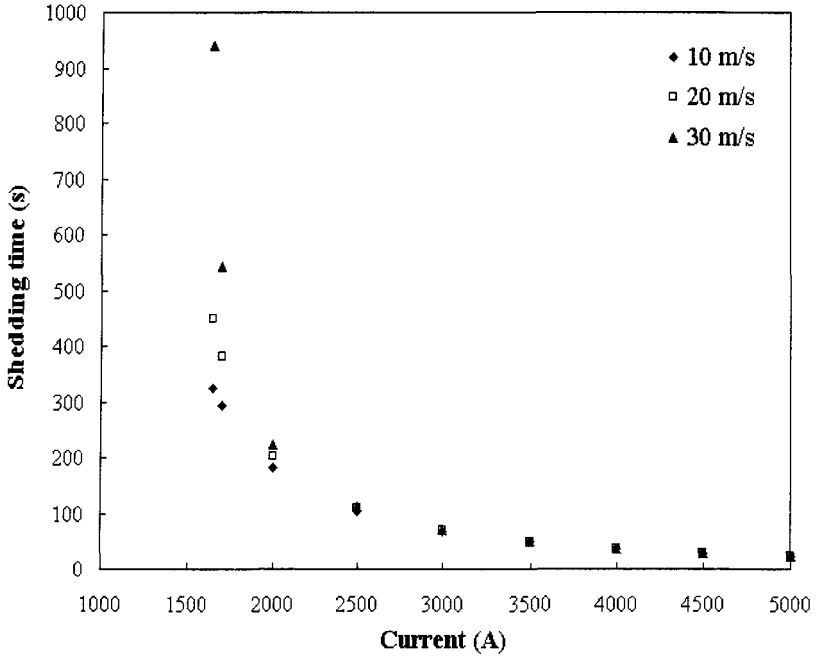

Figure 5.33 Shedding time versus electric current in conductor at various wind speeds

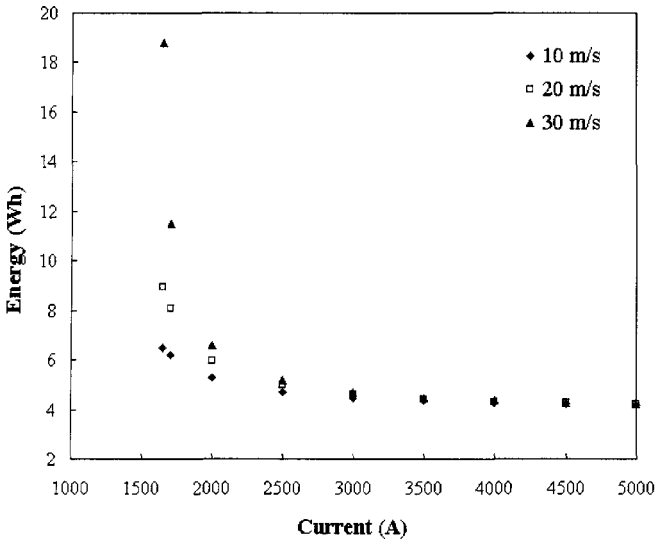

Figure 5.34 Energy required versus electric current in conductor at various wind speeds

5.2.3 Comparing ice shedding by AC and DC current heating from energy economic aspect

It is well known that the dc electric resistance of the conductor is smaller than the corresponding apparent ac resistance. Consequently, in the latter case the generated Joule heat is greater. The strongest influence of this effect is analyzed in the following section. Again, the calculations are performed with previously introduced parameters at 10 m/s wind velocity. The required shedding time and energy obtained with dc current are greater than for the corresponding nominal ac current (see Figure 5.35 and Figure 5.36). However, the differences in results with ac and dc currents are not significant at higher currents (approximately below 1 minute in present cases).

From an economical stand point there is not much difference whether ac or dc current is applied if the current value is high enough. Also, there is no noticeable difference in

temperature distribution in the conductor between cases with applied ac or dc current. Uniform, constant temperature distribution is observed along conductor radius due to the high thermal conductivity of aluminium.

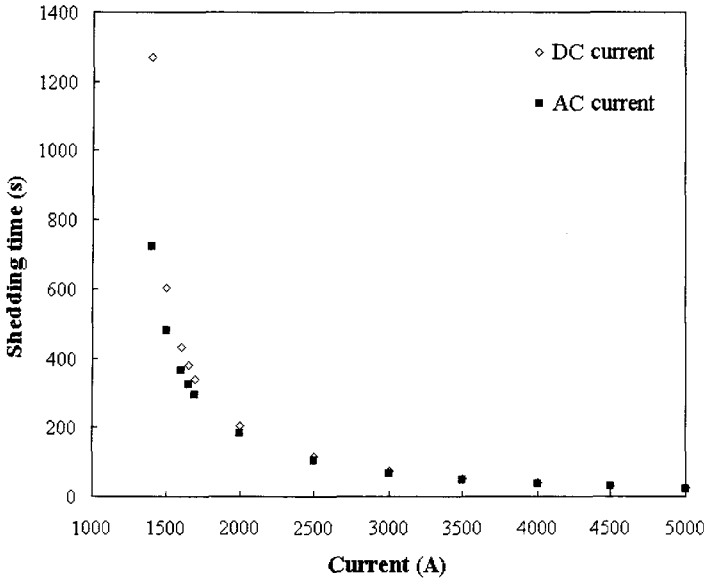

Figure 5.35 Shedding time versus ac and dc electric current in conductor

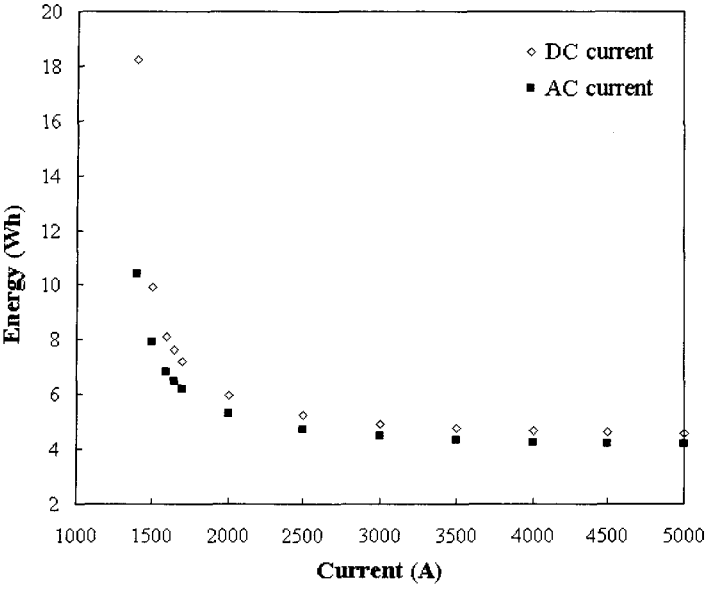

Figure 5.36 Energy required versus ac and dc electric current in conductor

5.2.4 Effect of equivalent thermal conductivity

It has been mentioned that the intensity of heat conduction in the stranded conductor is determined by an equivalent thermal conductivity. It is expected that the shedding time will be longer for smaller equivalent thermal conductivities. The strongest of this effect is analyzed using calculations obtained with following set of parameters:

- ice thickness of 5 mm
- air temperature of -5 °C
- wind velocity of 10 m/s
- equivalent thermal conductivity of 7 W/mK

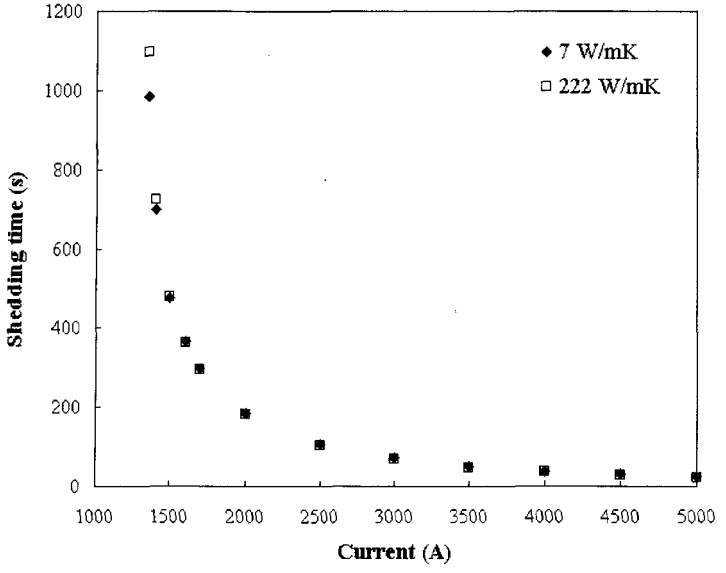

Figure 5.37 Shedding time versus electric current for different equivalent radial thermal conductivities

It is seen in Figure 5.37 that the shedding time is generally shorter with the conductor thermal conductivity set to 7 W/mK than with 222 W/mK (for solid aluminium) at low

currents in the conductor. The contrary is observed at higher currents, when the thermal conductivity of 7 W/mK requires more energy to shed the ice than with a pure aluminium conductor. However, the deviation in the shedding time obtained with thermal conductivities of 7 and 222 W/mK is not significant at higher currents in the conductor. The corresponding required energy and temperature distribution in conductor-ice composite is shown in APPENDIX 3.

5.2.5 Effect of air temperature

For impulse current heating, it was shown that the air temperature may have a significant influence on both shedding time and required energy. This influence is presently analyzed for ac current heating. For this purpose calculations have been made using the following parameters:

- ice thickness of 5 mm
- wind velocity of 10 m/s
- equivalent thermal conductivity of 222 W/mK
- air temperatures of -5, -10, -15 and -20 °C

Obviously, the shedding time and the required energy to remove the ice layer are greater for lower temperatures. It can be seen from Figure 5.38 and Figure 5.39 that the air temperature has a greater influence on results than any other investigated parameter so far. It can be concluded once again that the differences in required energy and shedding time under various air temperatures are smaller with increasing electric current. The increasing

rate of shedding time and energy with decreasing applied current is more intensive at lower temperatures. The history of temperature distributions at various air temperatures can be found in APPENDIX 3.

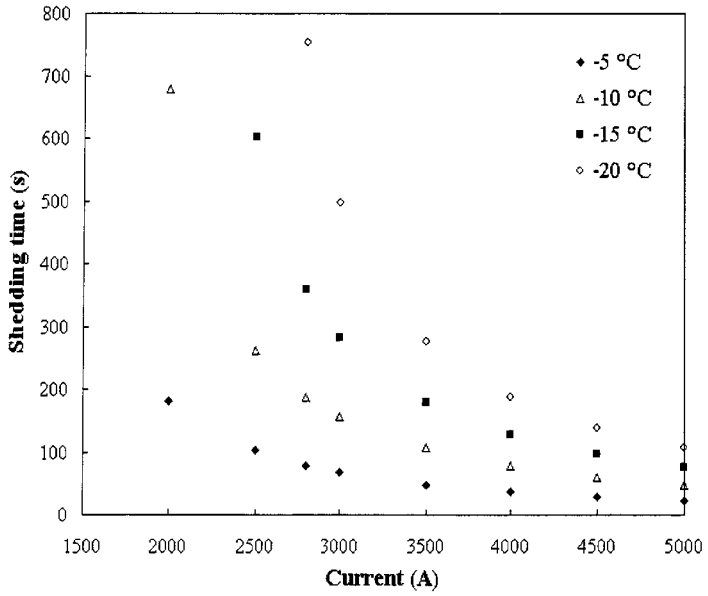

Figure 5.38 Shedding time versus electric current under various air temperatures

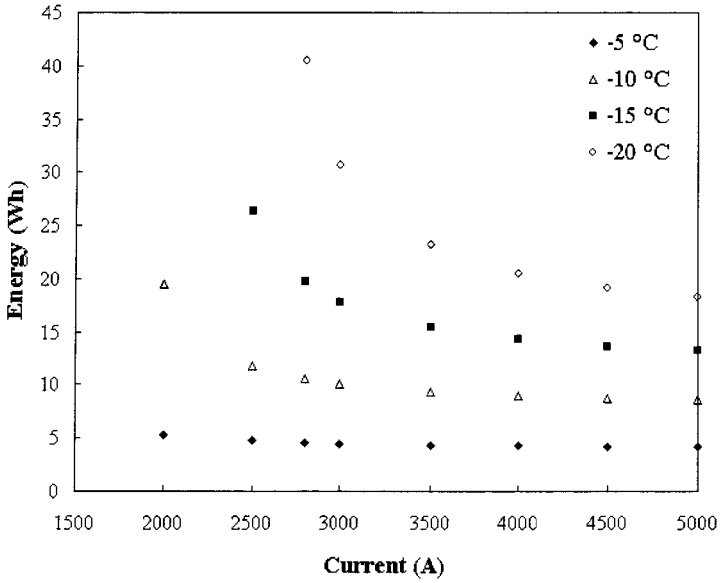

Figure 5.39 Required energy versus electric current under various air temperatures

5.2.6 Effect of ice thickness

In the following section, the influence of ice thickness on required shedding time and energy is analyzed briefly. The computations were performed with parameters presented in the previous section at air temperature of -5 °C and ice thicknesses of 2, 3, 5, 10 and 15 mm. The results are shown in Figure 5.40 and Figure 5.41. The shedding time and energy increases with increasing ice thickness. The contrary was observed for impulse heating, where the thicker ice required less energy to de-ice. The differences in both shedding time and energy are greater for lower currents in the conductor. It can also be observed from the temperature distribution (see APPENDIX 3) that with increasing ice thickness the heated mass of ice layer increases too. Therefore, from an economical stand point the preferable technique is to leave an ice layer of 1÷2 mm to accumulate, then to increase the current in order to remove the thin ice layer. This process should be repeated until the unfavourable conditions no longer exist.

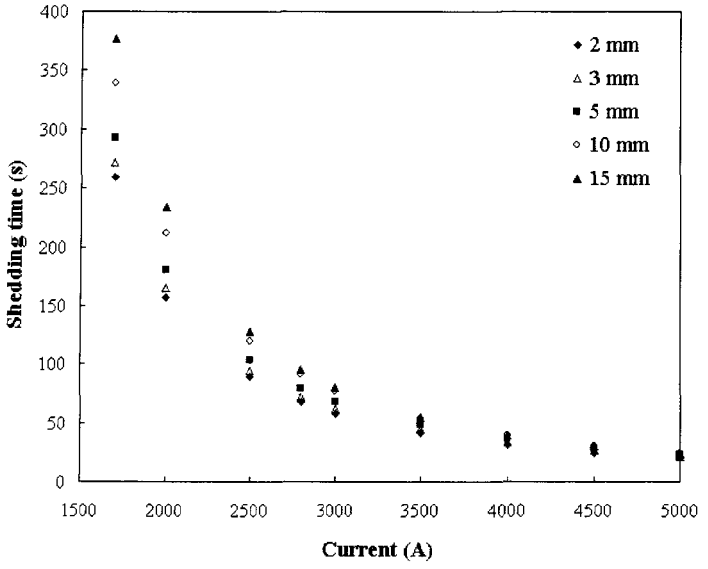

Figure 5.40 Shedding time versus electric current under various ice thicknesses

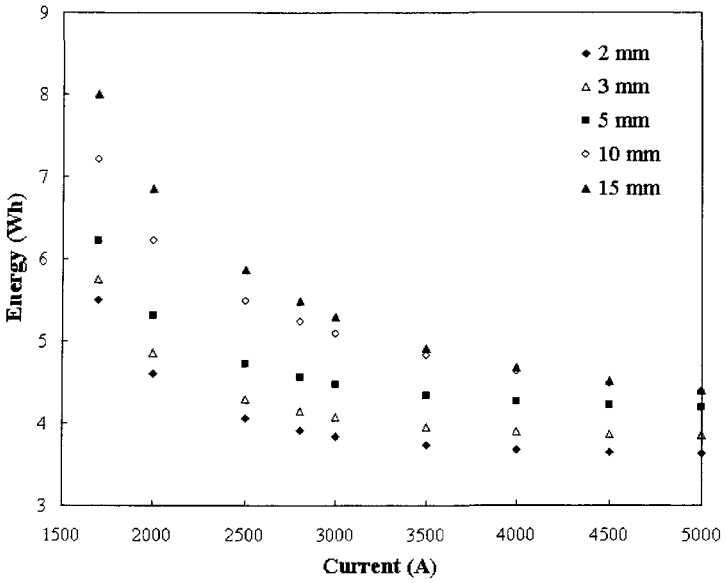

Figure 5.41 Required energy versus electric current under various ice thicknesses

5.2.7 Steel cored model results

Until now, the steel core was neglected in order to simplify and speed up the calculations. In the following section, the influence of this assumption is studied. The finite difference method has been extended to incorporate the steel core, which leads to a more complex model which is ready for more realistic simulations. During the computations, a steel core of 7.6 mm diameter is assumed with an equivalent thermal conductivity of 15 W/mK. The calculations have been made for an air temperature of -5 °C, 10 m/s wind speed and ice thickness of 5 mm. The results are shown in Figure 5.42 and Figure 5.43.

The steel core in the ACSR conductors increases the shedding time and the required energy, due to its thermal capacity and due to no current flow in the core. The differences between the results obtained by models with and without a steel core are more significant

at lower currents. The temperature distribution is different under various current values as shown in Figure 5.44÷Figure 5.46.

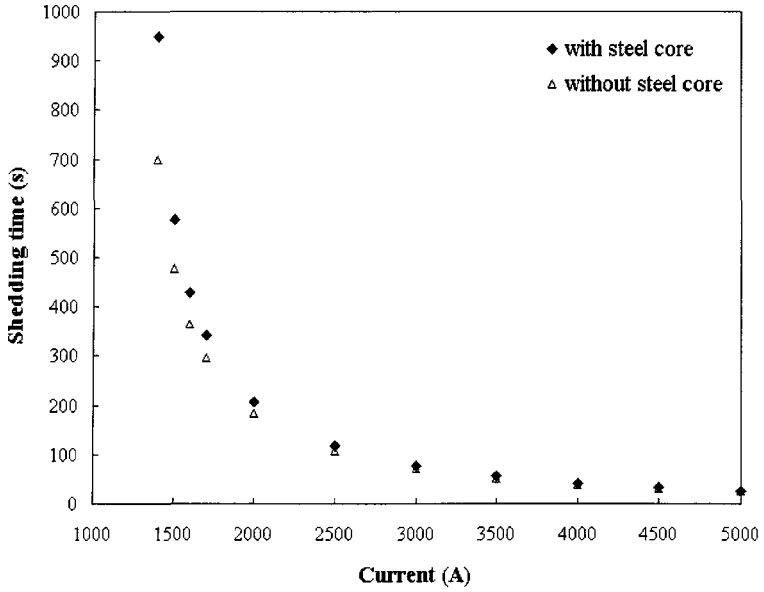

Figure 5.42 Shedding time versus electric current obtained by models with and without a steel core

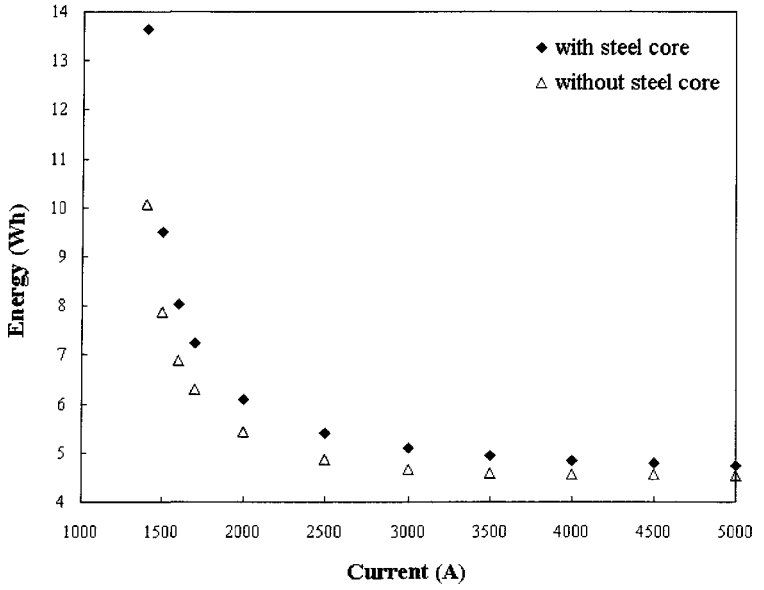

Figure 5.43 Required energy versus electric current obtained by models with and without a steel core

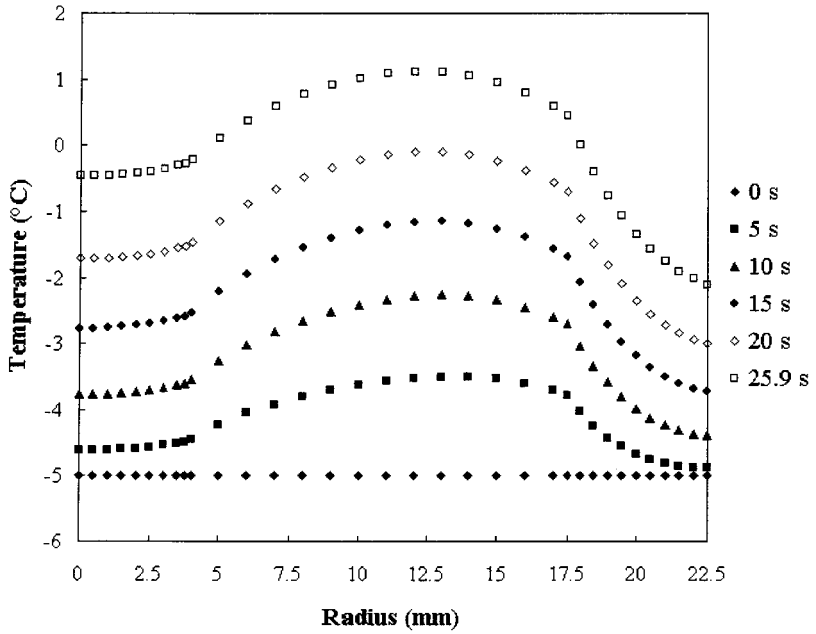

Figure 5.44 Temperature distribution at 5000 A

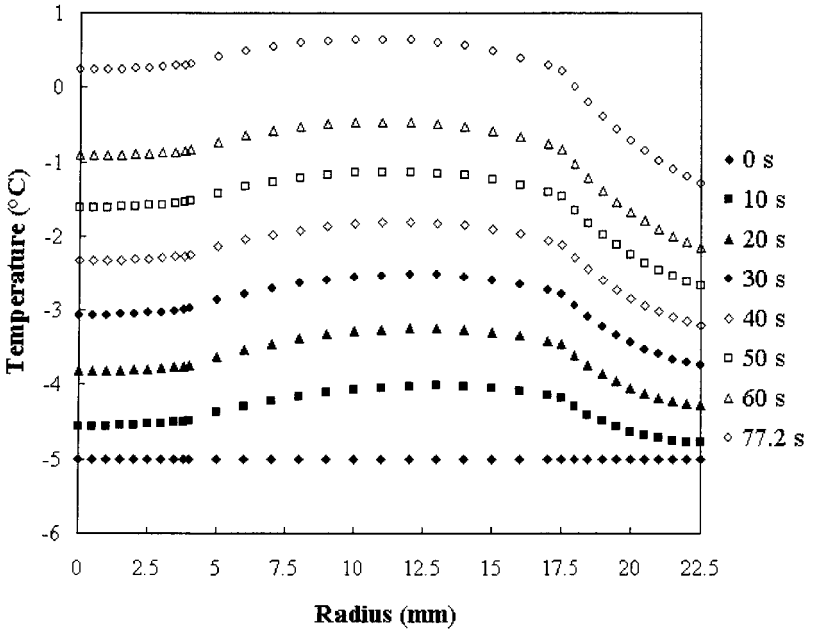

Figure 5.45 Temperature distribution at 3000 A

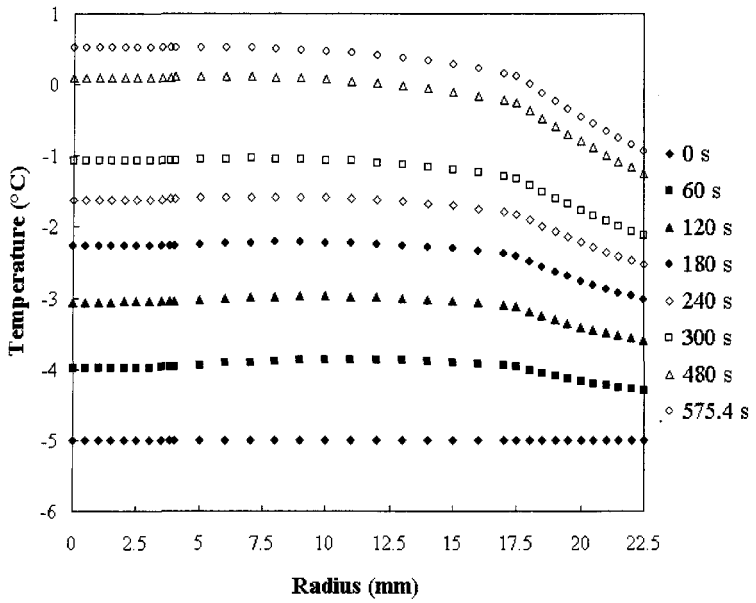

Figure 5.46 Temperature distribution at 1500 A

With higher current in the conductor, the aluminium outside warms up very fast, and a certain amount of heat is conducted in the core and a lesser amount of heat is conducted in the ice sleeve due to its smaller thermal conductivity. With decreasing current the shedding time increases, which allows the equalization of the temperature gradients. After enough time, there is no more temperature gradient in the steel core.

5.3 Comparing the impulse current heating with 60 Hz, ac current heating

The two techniques based on the electrical heating method due to the Joule effect are compared with each other from the standpoint of required energy. The comparison is made for the following set of parameters:

- Air temperature of –5 °C
- Wind speed of 10 m/s
- Shedding condition at 0.25 mm from conductor surface
- Radial equivalent thermal conductivity of the conductor: 7 W/mK
- Equivalent frequency of 318.3 Hz
- Ice layer thickness of 5 mm

Table 5-2 Results obtained with different heating techniques

Current (A)	Shedding time (s)					Energy (Wh)				
	60 Hz	318.3 Hz	636.3 Hz	1273.2 Hz	3000 Hz	60 Hz	318.3 Hz	636.3 Hz	1273.2 Hz	3000 Hz
2000	184.55	-	-	-	-	5.417	-	-	-	-
2500	106.44	-	-	-	-	4.882	-	-	-	-
3000	70.68	-	-	-	-	4.668	-	-	-	-
3500	50.98	-	-	-	-	4.582	-	-	-	-
4000	38.88	5.077	3.220	1.979	1.058	4.56	0.472	0.405	0.341	0.273
6000	-	2.196	1.355	0.820	0.438	-	0.460	0.384	0.318	0.255
8000	-	1.255	0.770	0.467	0.254	-	0.467	0.387	0.322	0.262
10000	-	0.829	0.510	0.312	0.172	-	0.482	0.402	0.336	0.278
12000	-	0.599	0.370	0.229	0.128	-	0.502	0.420	0.355	0.298
14000	-	0.458	0.286	0.178	0.102	-	0.524	0.440	0.376	0.321
16000	-	0.366	0.230	0.145	0.084	-	0.547	0.463	0.400	0.346
18000	-	0.302	0.191	0.121	0.071	-	0.569	0.486	0.424	0.373
20000	-	0.255	0.162	0.104	0.062	-	0.595	0.509	0.451	0.400

The results are shown in Table 5-2, where the currents represent the increased value of nominal 60 Hz, ac current, and the impulse peak value for impulse current heating. Note that the 60 Hz results are determined with shedding condition prescribed at 0.5 mm, while in the case of impulse heating it is determined at 0.25 mm from the conductor surface. However, the magnitude of differences shows clearly the advantages of impulse heating.

Finally, as a general rule, it can be concluded that applying a high current with high frequency may save some of the energy required to shed the ice from an electrical conductor.

Impulse heating

Briefly, it can be concluded that the increasing value of impulse amplitudes is decreasing significantly the shedding time. The higher equivalent frequency and radial thermal conductivity, warmer air temperature and thicker ice layer also decreases the required shedding duration. It seems to be one of the main advantages of the impulse current heating technique that the required shedding time is not sensible on the wind velocity. For each equivalent frequency and air temperature there is an optimal peak current at which the required energy has a minimum value. It can be also concluded that the most economical strategy is to allow the maximum ice thickness to accumulate on conductor at which the conductor still not turns and then removing the ice layer by Joule heating with impulse current.

Raised nominal current heating

Briefly, from energy economical aspect the preferable ac current heating technique is to leave just thin ice (e.g. 1÷2 mm) to accumulate on the conductor, and then removing it by increasing the nominal current. From economical aspect there is no much difference whether ac or dc current is applied if the current value is enough high. The air temperature has stronger influence on required energy than any other investigated atmospheric parameter. It can be concluded again that the most economical de-icing strategy is with highest applicable current in the conductor.

CHAPTER 6

DE-ICING OF ROTATING CONDUCTORS BY JOULE HEATING

Certain overhead power lines conductors are able to rotate when ice accumulates on them. As a consequence of this rotation, the accreted ice layer has an almost perfectly cylindrical shape. Naturally, this ice sleeve should be removed before reaching a critical mass in order to prevent damages to or even breakdown of the power lines. The candidate focuses on the Joule heating technique again as one of the de-icing techniques with the most potential. The previous models were concerned with reaching the melting conditions and did not include the phase change. However, in the present case the ice should be melted, and so an additional model/approach is required. Hence, one may ask: What is the required current or energy for complete ice removal? What is the optimal Joule heating strategy?

This chapter deals with the determination of the current required to completely remove the ice layer, which depends on a number of parameters including conductor electrical resistance, air temperature, ice thickness, and as convective heat transfer.

6.1 Experimental study

The aim of the experimental study was to determine the required electric current and energy for complete ice removal, which validates the theoretical approaches. Additionally,

the experimental study contributes to the better understanding of the melting process on Joule heated conductors.

Generally, the measurements were performed in two main steps. First, the ice layer was accreted on the rotating test conductor. Second, the electrical current was applied in the conductor in order to shed the ice by Joule heat. Both parts of the study were performed in the CIGELE refrigerated wind tunnel. The same experimental rig was used that was previously described in detail.

During the ice accretion process the meteorological conditions are continuously monitored and registered. The atmospheric parameters are acquired in a similar manner as during ice prevention measurements described previously in detail. Measured parameters during ice accretion are as follows:

- Wind velocity
- Air temperature
- Average ice layer diameter
- Relative and absolute humidity
- Flow rate, water and air pressure in nozzles

The LWC of air/water spray flow were obtained from [25] and [26] for the corresponding water and air pressure settings in the nozzle. The median volume diameter (MVD) of 51.18 μm was estimated using the correlations found in [29].

The ice layer was accreted on the continuously rotating conductor of 2 rpm. This resulted in a relatively symmetrical ice sleeve around the conductor under the given atmospheric conditions. In all cases, transparent glaze ice was produced on the conductor. A typical ice sleeve accreted on the rotating conductor is shown in Figure 6.1. For more information about the ice accumulation procedure consult APPENDIX 4.

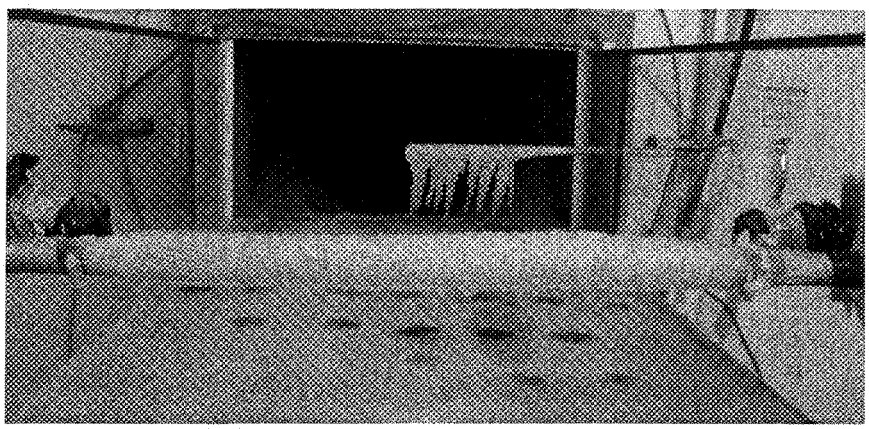

Figure 6.1 Accumulating glaze ice on rotating conductor

The parameters required to determine the electrical heating of the test conductor were collected beside the atmospheric parameters during the ice melting process. The measured and/or adjusted parameters during electrical heating were as follows:

- Electric current in conductor
- Voltage drop on the conductor and attachments
- Wind velocity of free stream
- Temperature of airflow
- Relative and absolute humidity of air

- Ice surface temperature by infrared camera
- Time duration of the ice shedding

The conductor connections were frequently monitored by an infrared camera. It was possible to estimate the strength of the parasite heating from the attachments toward the ice covered conductor from the images taken. A typical infrared measurement is shown in Figure 6.2. As a result, no significant parasite heat generation was found at the ends of the test conductor.

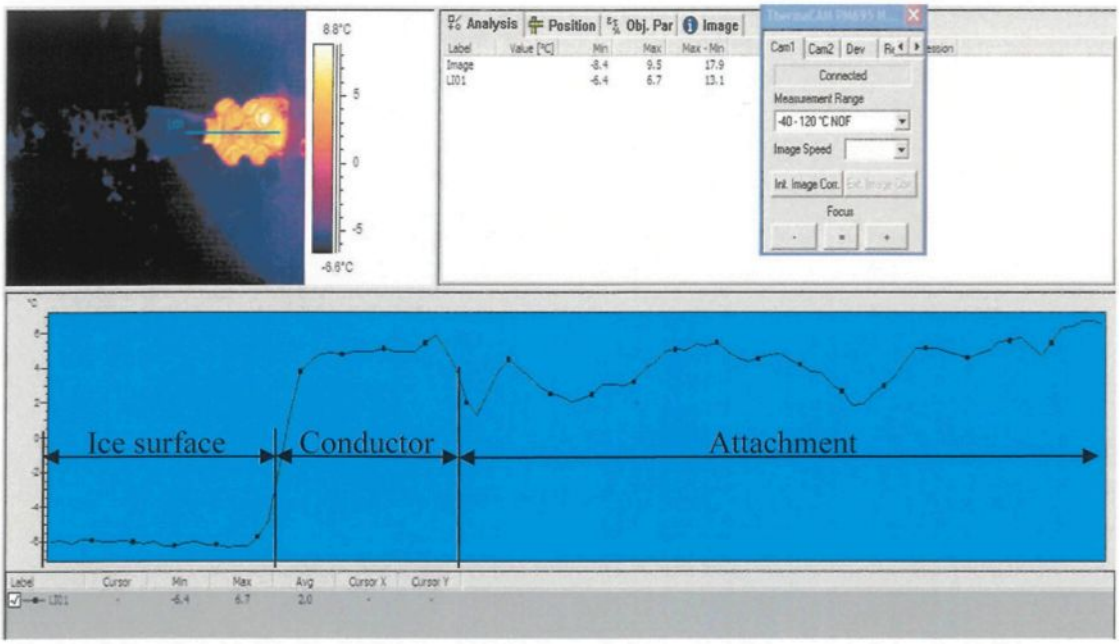

Figure 6.2 A typical infrared camera measurement of temperature distribution near the conductor attachment

6.1.1 Determination of minimum current

It has already been mentioned that the ice melting does not occur even after an infinite time if the current flow in the conductor does not pass the critical/minimum value.

Obviously, the value of minimum current, which is able to trigger ice melting, strongly depends on the meteorological conditions. It is almost mission impossible to measure the minimum/critical current exactly, since in this case one should measure over an extremely long period. For this reason the candidate defined the minimum current at the value, when the first water droplets were observed under a transparent glaze ice sleeve within 30 minutes of starting the electrical heating. In order to determine the minimum current as precisely as possible, the electric current in the test conductor was increased in very small increments. In most cases the measurements were repeated several times. The first attempt was a pioneering test aiming to discover the range of minimum current under the given atmospheric conditions.

6.1.2 The ice melting process on electrically heated conductor

The following is a short overview of the melting process triggered and maintained by inner Joule heating. It is based on observations during experimental work in the wind tunnel.

Obviously, the ice melting starts at the ice-conductor interface due to a Joule heated conductor. As a first effect, the adhesive force disappears from the conductor-ice interface and the first molten droplets appear. These molten droplets are running down in the "V" inter-strand channels toward the bottom of ice core due to gravity. The water is collected at the lowest location inside the ice core. Various ice melting scenarios may be observed, depending on the atmospheric conditions and on the amount of electric current in the

conductor. These scenarios are shortly overviewed in the following section with supporting figures about the melting mechanism.

The melting intensity is relatively slow when a small electric current flows in the conductor, relative to the convective cooling of airflow. In consequence, the collected water, which is heated by the conductor, has enough time to make a hole through the ice layer. In this way hollow icicles grow (see Figure 6.3). After a while these icicles are so long that the water has enough time to cool down and to freeze. Additionally, icicles attached to the ice layer act as cooling fins. This stops the further run-off of water from the ice cover. Consequently, the water looks for new places where it can break out (see Figure 6.3). However, during the melting process the bottom water layer becomes thicker, which increases the radial conductive thermal resistance. Thus, less heat is conducted in this direction. Finally, the molten water layer at bottom of ice core refreezes due to the intensive outer convective cooling. This is shown in Figure 6.4 a.

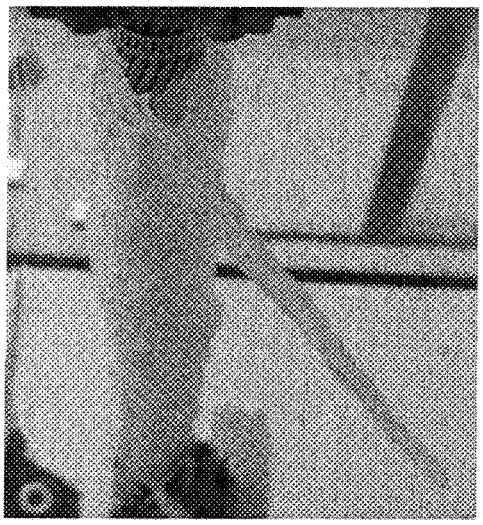

Figure 6.3 Icicle growing from runoff of water

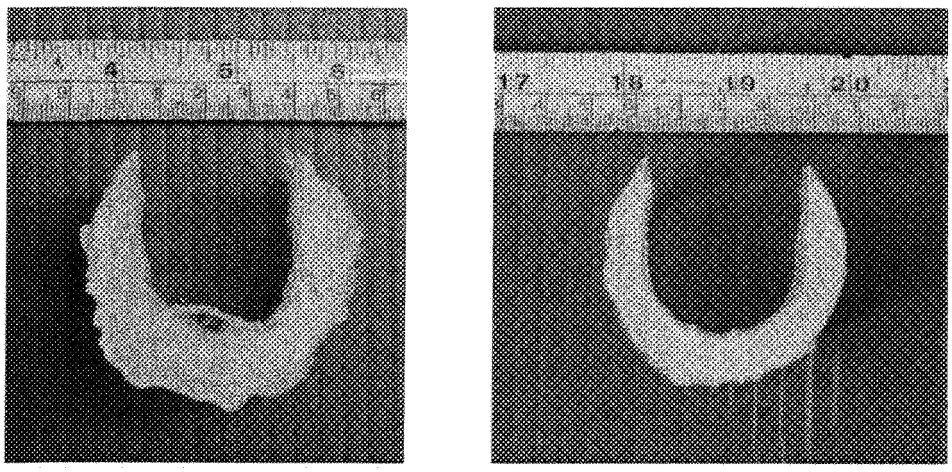

a. b.

Figure 6.4 Cross-sections of the removed ice sleeve obtained under the same atmospheric conditions. a.) Electric current of 2003 A; b.) Electric current of 3107 A

The melting surface propagation is rapid when the Joule heating due to electric current in the conductor is more significant than the outer convective cooling. There is not enough time for either the icicles to grow or the water layer captured at bottom of the ice sleeve to freeze because of the intensive inner heating. Generally, just the part of ice sleeve above the conductor and the ice in the vicinity of the conductor is molten. The cross-section of the removed ice layer with intensive inner heating is shown in Figure 6.4 b. APPENDIX 4 introduces different forms of the removed ice sleeve under various electric current and atmospheric conditions. In both cases, the ice sleeve detaches, when its upper section above the conductor is totally molten. The moment of ice core detachment is presented in Figure 6.5.

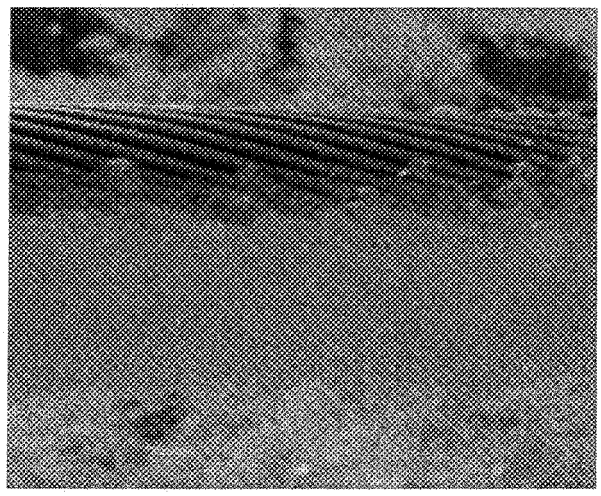

Figure 6.5 Moment of ice sleeve's detachment from conductor

The liquid layer increases the thermal resistance between the conductor and the ice layer, because the thermal conductivity of the water (melted ice) is about four times lower than that of the ice. This liquid layer has a non-uniform thickness around the conductor and as a result, its thermal resistance is non-uniform as well. Furthermore, there is also an air and/or water vapour filled gap between the conductor and ice (see Figure 6.6), which also influences the ice melting. Naturally, if there are macroscopic ruptures in the structure of ice sleeve then the vapour or the water can run out. In this case it is replaced by air. The intensity of the heat transfer varies around the ice layer. First, the local heat transfer coefficient varies at the external surface; secondly the liquid layer has a non-uniform thickness at the inner surface. The non-uniform ice thickness also influences the melting rate. Thinner ice follows the variation of the external air temperatures faster. Also the heat and mass transfer coefficients change with decreasing ice thickness that accelerates the rate of ice shedding at the places where the ice is thinner. In addition, the thermal resistance due

to conduction increases with increasing external radius, while the resistance due to convection decreases. Consequently, the total thermal resistance has a minimum value.

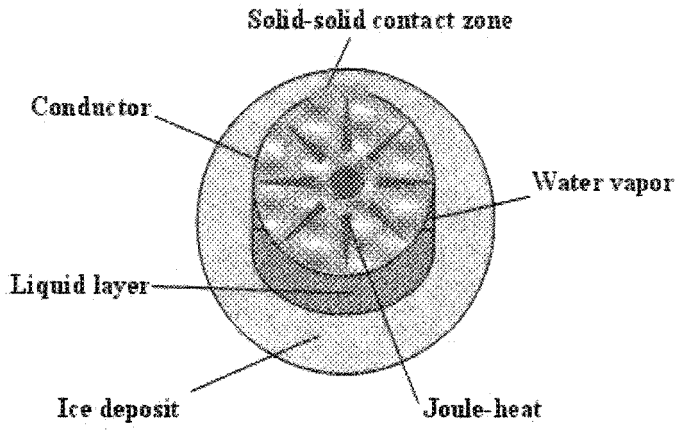

Figure 6.6 Melting at the inner surface of the ice deposit

6.2 Simple theoretical models

Generally, two main periods can be distinguished during the shedding of the ice sleeve by Joule heating. The first, transient period is from the start of the Joule heating until reaching the melting conditions at the conductor-ice interface. The second melting period consists of the complete melting of the ice sleeve. The phase change starts when the melting condition is reached. Consequently, the total shedding period and the corresponding required energy can be calculated simply as the sum of the two periods mentioned.

The transient period can be calculated using the finite difference method as presented in the previous sections. The melting period could be obtained from analytical solutions. Two

different approaches for calculating the melting period are presented briefly in the following section. Both approaches neglect what happens with the molten water layer.

6.2.1 Constant resistance model

The aim of this model is to calculate the time and energy required to shed the ice from an electrical conductor by Joule heating after the conditions of melting are reached at the interface of conductor and ice layer. The model is restricted to the following assumptions:

- The temperature of ice-conductor interface is 0 °C
- The ice sleeve melts just above the conductor
- The conductive thermal resistance is constant around the conductor during melting
- The effects due to the water layer are neglected

The above assumptions fit better the cases, when the inner Joule heating is more dominant than the outer convective cooling. The first assumption is a good approximation of the real melting process. Naturally, at the beginning of the phase change process the ice melts everywhere around the conductor. Then a molten water layer forms eccentrically around the conductor due to gravity. Therefore, the thermal resistance of heat conduction around the conductor is not uniform. It increases with increasing water layer thickness, since the thermal conductivity of water is approximately four times less than that of ice. Consequently, in the course of time almost all the heat generated is conducted away through the upper part of the ice layer above the conductor.

It is also assumed that the generated Joule heat, which is not conducted away through the ice layer, is contributing to the melting. Finally, the overall energy balance can be written as

$$Q_j \Delta t - E_l = Q_{cd} \Delta t \qquad \text{Eq. 6.2-1}$$

where Q_j is the generated Joule heat in the conductor (W), E_l is the latent energy of ice (J), Q_{cd} is the heat conducted through ice sleeve (W) and Δt is time duration (s). The parameterized form of Eq. 6.2-1 is as follows:

$$I^2 R_{ac,c} L \cdot \Delta t - \rho \cdot l \cdot V_{melt} = 2k_i L\pi \frac{T_0 - T_s}{\ln(R_i / R_c)} \cdot \Delta t \qquad \text{Eq. 6.2-2}$$

where T_s is the average temperature of ice surface (°C), T_0 is the melting temperature (°C), R_i and R_c are the radii of the ice sleeve and the conductor (m), respectively, and V_{melt} is the volume of melted ice (m^3).

The temperature of the ice layer surface exposed to wind is just rarely measured. Practically, during ice storms the surface temperature data are not available. Therefore, it should be expressed as a function of the air temperature and free stream velocity.

The heat conducted through the ice layer is taken away by heat convection as it is formulated by Eq. 6.2-3.

$$2k_i L\pi \cdot \frac{T_0 - T_s}{\ln(R_i / R_c)} = 2R_c \pi L h \cdot (T_s - T_a) \qquad \text{Eq. 6.2-3}$$

where h is the average heat transfer coefficient (W/m^2K), and T_a is the air temperature (°C).

Expressing the ice surface temperature, T_s, from Eq. 6.2-3, and substituting it into Eq.6.2-2:

$$\left[I^2 R_{ac,c} L + \frac{T_0 - T_a}{\frac{\ln(R_i / R_c)}{2k_i L\pi} + \frac{1}{2R_i \pi L h}} \right] \Delta t = \rho \cdot l \cdot V_{melt} \qquad \text{Eq. 6.2-4}$$

Note that in the denominator the sum of the convective and the conductive thermal resistances is present. The convective heat transfer coefficient can be calculated from the correlation of Achenbach for rough surfaces. It is shown in CHAPTER 7.

The required time, $t_{melt}= \Delta t$, to melt the ice sleeve above the conductor can be calculated using Eq. 6.2-4. Finally, the corresponding required energy for complete de-icing is found from Eq. 6.2-5.

$$E_{shed} = I^2 R_{ac,c} L \cdot (t_{melt} + t_{transient}) \qquad \text{Eq. 6.2-5}$$

where $t_{transient}$ is the duration of the first, transient period (s) that can be calculated using the finite difference method.

6.2.2 Melting surface propagation model

The present relatively simple analytical approach has been created in order to improve the previous constant resistant model. The advantage of this model is that it accounts for variations of the conductive thermal resistance in time, since the ice layer thickness is continuously decreasing during melting. The problem of the propagation of the melting surface above the conductor is solved in one-dimension. As before, it is assumed that the ice melts just in the region above the conductor.

The energy balance at the melting interface of ice and conductor is formulated in differential form as shown by Eq. 6.2-6:

$$q_j dt = \rho l \cdot dr + \frac{k_i}{r}(T_0 - T_s) \cdot dt \qquad \text{Eq. 6.2-6}$$

where r is the location of the melting surface (m), and q_j is the generated heat flux (W/m^2).

The energy balance at the ice-air interface is as follows:

$$k\frac{T_0 - T_s}{r} = h \cdot (T_s - T_a) \qquad \text{Eq. 6.2-7}$$

The following form is obtained after expressing T_s from Eq. 6.2-7, and writing in Eq. 6.2-6:

$$q_j dt = \rho l \cdot dr + \frac{T_0 - T_a}{\frac{1}{h} + \frac{r}{k_i}} \cdot dt \qquad \text{Eq. 6.2-8}$$

A new variable, y, is introduced in order to solve Eq. 6.2-8:

$$y = q_j hr + q_j k_i - k_i h(T_0 - T_a) \qquad \text{Eq. 6.2-9}$$

Writing Eq. 6.2-8 with the new variable, we have:

$$dt = \frac{\rho \cdot l}{q^2 h} dy + \frac{\rho \cdot l}{q^2} k(T_0 - T_a)\frac{1}{y} dy \qquad \text{Eq. 6.2-10}$$

Finally, the required melting time (t_{melt}) after solving the above differential equation is expressed as shown by Eq. 6.2-11.

$$t_{melt} = \frac{\rho l}{q^2}(R_i - R_c) + \frac{\rho l k_i}{q^2}(T_0 - T_a) \cdot \ln\frac{R_i qh + qk_i - k_i h(T_0 - T_a)}{R_c qh + qk_i - k_i h(T_0 - T_a)} \qquad \text{Eq. 6.2-11}$$

Afterwards, the melting time is obtained the corresponding required energy to remove the ice sleeve can be calculated using Eq. 6.2-5.

6.3 Experimental and mathematical results

The validation of analytical models with measurements is necessary, since both models contain certain assumptions. Thus, in the following section the two analytical approaches are compared with each other as well as with the experimental results. Ice density of 870 kg/m^3 and ice thermal conductivity of 2.2 W/mK were considered in the calculations.

6.3.1 Validating analytical calculations

6.3.1.1 The first series of validation

The first series of validations were made in order to investigate the predictive power of analytical approaches with various electric currents in the conductor. Hence, measurements were performed under similar atmospheric conditions and different applied electric currents.

In the first step of experimental validation, the ice was accumulated on a rotating (2 rpm) Carillon type conductor in wind tunnel. The appropriate atmospheric conditions of accumulation are shown in Table 6-1.

Table 6-2 shows the atmospheric parameters measured during the melting process in the wind tunnel. It also contains the calculated required energy needed to melt the ice from the conductor using Eq. 6.2-5. In the following section, these values are compared with those obtained from analytical approaches (see Figure 6.8).

Table 6-1 Atmospheric parameters measured during ice accumulation in wind tunnel

N°	Wind speed (m/s)	Air temperature (°C)	LWC* (g/m^3)	MVD* (μm)	RH (%)	Duration (min)	Ice diameter (mm)
1.	9.7	-9.8	5.791	51.18	93	30	49.1
2.	9.7	-9.9	5.791	51.18	92	30	49.3
3.	9.9	-9.9	5.92	51.18	92	30	49.4
4.	9.9	-9.7	5.92	51.18	92	30	50.0
5.	9.6	-9.9	5.727	51.18	95	30	49.3

* Obtained from [25], [29] and [26].

Table 6-2 Atmospheric and current parameters during ice melting with calculated energy

N°	Wind speed (m/s)	Air temperature (°C)	RH (%)	Current (A)	Shedding time (min)	K_t	K_s	Calculated Energy (Wh)
1.	9.9	-9.7	88	1505^m	119.00	1.007	1.037	159.56
2.	9.5	-9.7	92	2003	36.40	1.008	1.037	86.53
3.	10	-9.9	92	2217	19.75	1.010	1.037	57.63
4.	9.9	-10	93	2660	11.25	1.010	1.037	47.26
5.	10	-10	92	3107	8.00	1.010	1.037	45.85

Superscript *m* designates the measured minimum current required to trigger ice melting.

The durations of both periods, transient and melting, obtained from experimental study and mathematical calculations are compared in Figure 6.7. Note that the shedding time is the total time required to remove the ice sleeve from the conductor after the Joule heating is started. As aforementioned, the transient time period is calculated using the finite difference model, which has been previously presented. It is clearly seen from the comparison of the two analytical approaches that the propagation model regularly

underestimates the constant resistance approach. On one hand, the time duration obtained by the melting surface propagation approach is a function of conductive thermal resistance, which continuously decreases during melting. In consequence, the propagation of the melting interface slows down. On the other hand, the propagation model is one-dimensional; Hence, just the heat conduction in radial direction is considered in the thermal balance, which results in more heat converted into phase change. The latter assumption has a stronger influence on the time duration than the former, since the propagation model underestimates the constant resistance approach. The measurements are in agreement with experimental results at higher current flow in the conductor. With decreasing electric current the deviation between measured and calculated results increases, but they still agree relatively well.

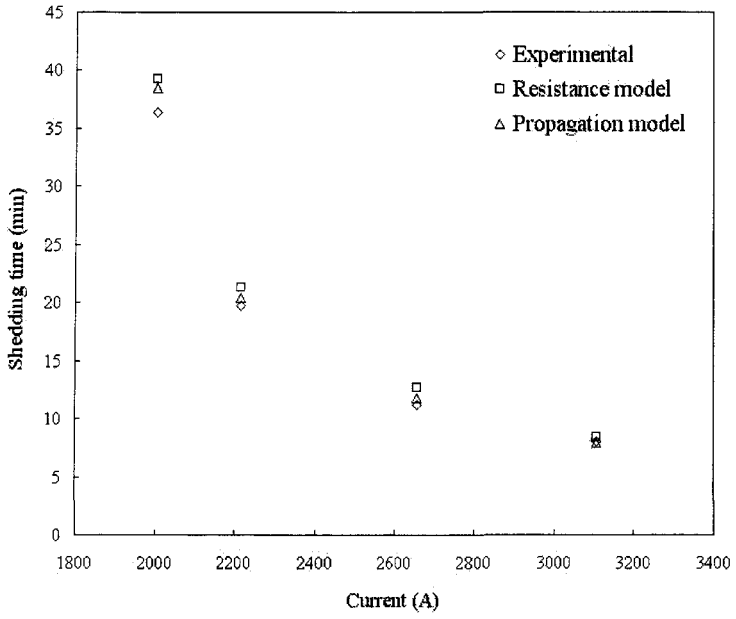

Figure 6.7 Experimental and analytical results of total shedding time. Validation cases obtained for wind speeds in a range of 9.5÷10 m/s, air temperature of -9.7÷-10 °C and ice diameter in range of 49.1÷50 mm, using Carillon test conductor.

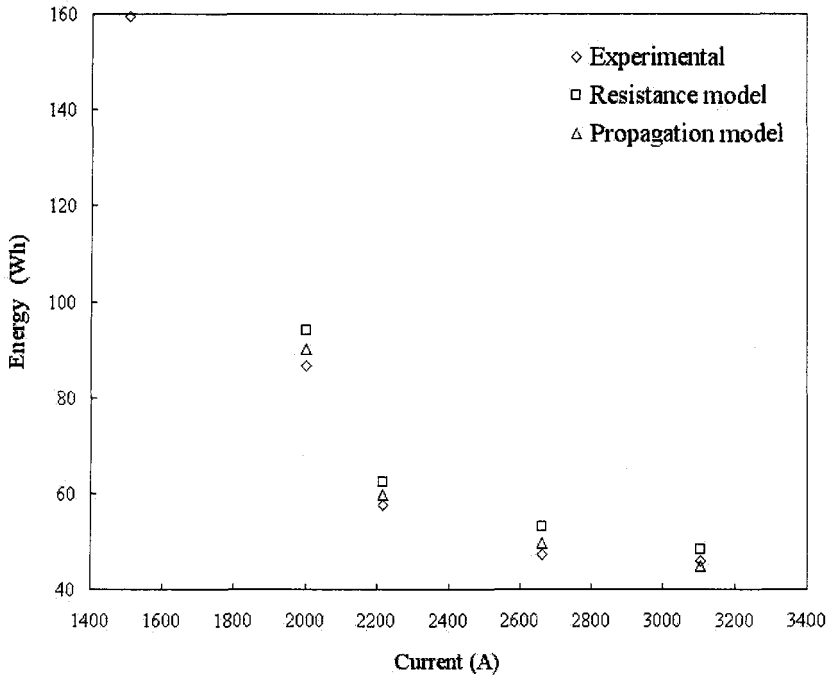

Figure 6.8 Experimental and analytical results of energy required to remove ice sleeve. Validation cases obtained for wind speed in range of 9.5÷10 m/s, air temperature of -9.7÷ -10 °C and ice diameter in range of 49.1÷50 mm, using Carillon test conductor.

6.3.1.2 The second series of validation

The second series of validations was performed to investigate the predictive power of the analytical approaches at different air temperatures and ice thicknesses. The measurements and the corresponding calculations were made at different air temperatures and ice thicknesses.

Figure 6.9 shows that the melting surface propagation model underestimates the constant resistance model once again. A larger difference can be observed between the two analytical approaches when thicker ice covers the conductor. It is shown in Figure 6.9 that the measurements accord better with the results obtained with the propagation model than

with the constant thermal resistance approach. However, both approaches slightly overepredict the measurements. Consequently, complete removal is more than assured when using the model for outdoor line de-icing.

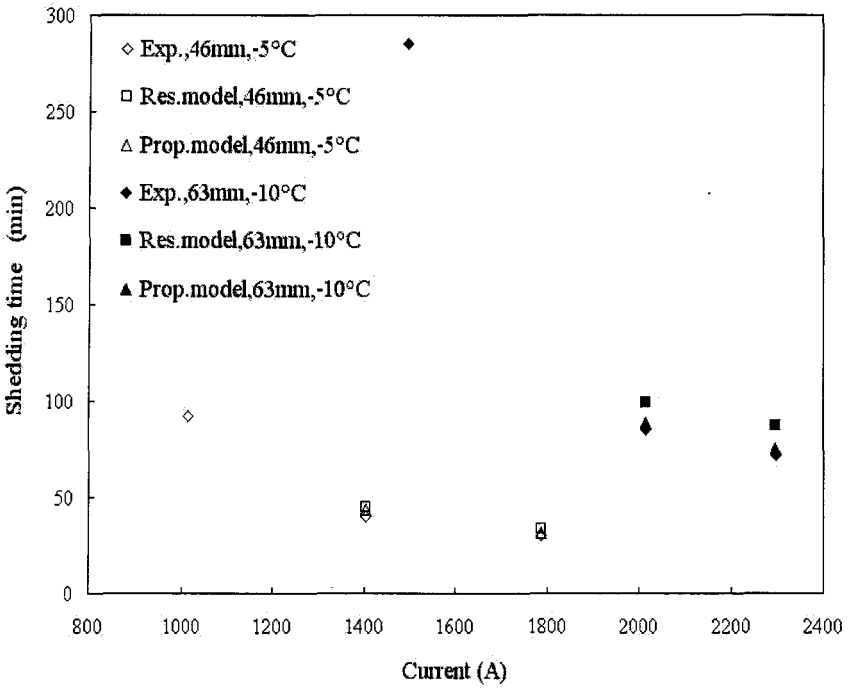

Figure 6.9 Shedding time obtained with analytical models and experimental study for Carillon type conductor. Wind speed was in the range of 6.5÷10 m/s; -5 °C and -10 °C cover air temperatures in the ranges of -4.3÷-4.5 °C and -9.5÷-9.8 °C, respectively.

6.3.2 Effect of electric current and ice sleeve diameter

In the following section, the time and corresponding energy requirements for different ice thicknesses with various electric current flows in the conductor are analyzed. The investigations are performed for the ice melting period (phase change part). The transient (pre-melting) period and the corresponding energy requirement are not included in the present analysis. Figure 6.10 and Figure 6.11 show the obtained melting time and

corresponding energy necessary to remove the ice sleeve from Joule heated conductor after the melting conditions are reached, using the constant resistance model. It is clear that the required melting time decreases drastically with increasing electric current. The decreases in the corresponding required energy are less intensive. However, one can save energy during ice shedding by applying the greatest available/possible electric current in the line conductor. Naturally, the required time and energy increases with the ice thickness. The thicker ice gives greater thermal insulation, but also a larger mass of ice needs to be melted in order to shed the ice sleeve from the conductor. The required melting time is obtained by using the propagation model as shown in Figure 6.12. It can be seen again that the propagation model underestimates the results obtained with the constant resistance model.

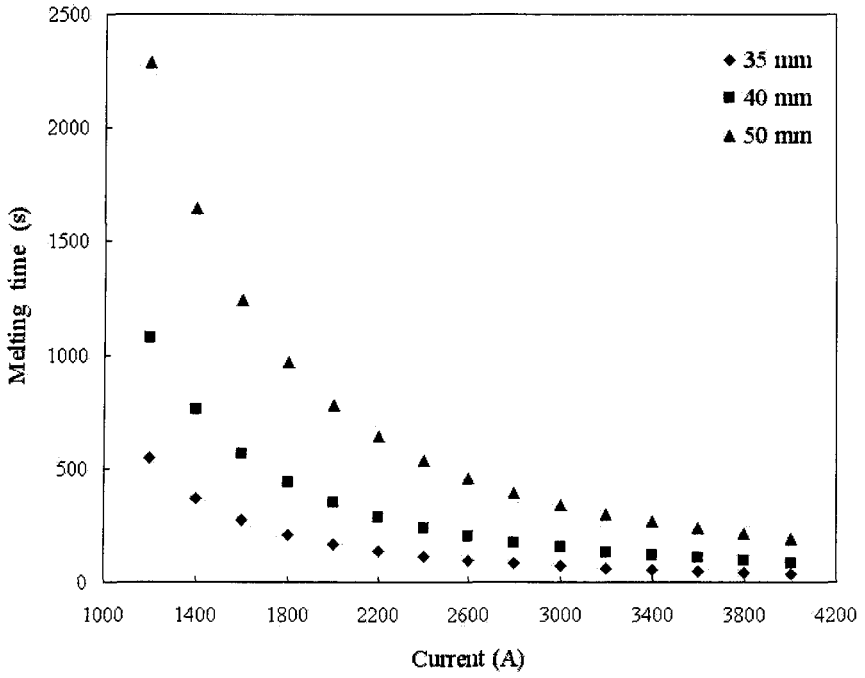

Figure 6.10 Effect of ice sleeve diameter on melting time, results obtained with the constant resistance model for Carillon type conductor

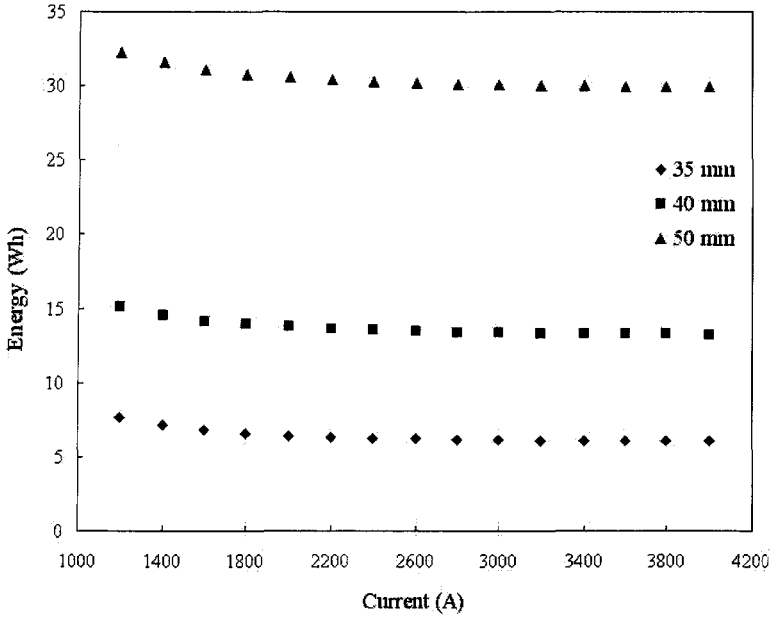

Figure 6.11 Effect of ice sleeve diameter on melting time, results obtained with the constant resistance model for Carillon type conductor

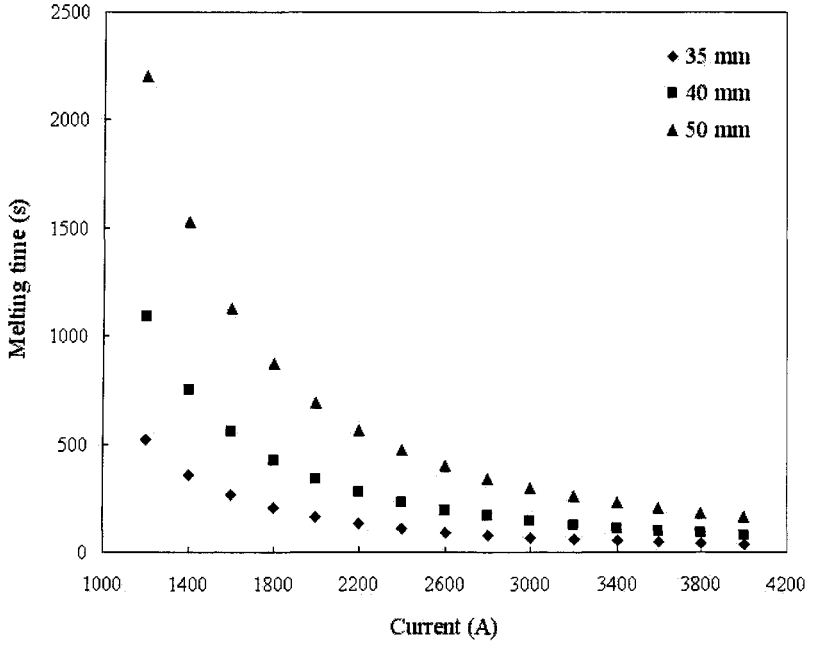

Figure 6.12 Effect of ice sleeve diameter on the melting time, results obtained with the propagation model for Carillon type conductor

6.3.3 Effect of wind speed

In the following section, the effect of wind velocity on the melting duration was analysed at two different ice layer diameters (35 and 40 mm). The calculations were performed using the melting surface propagation approach.

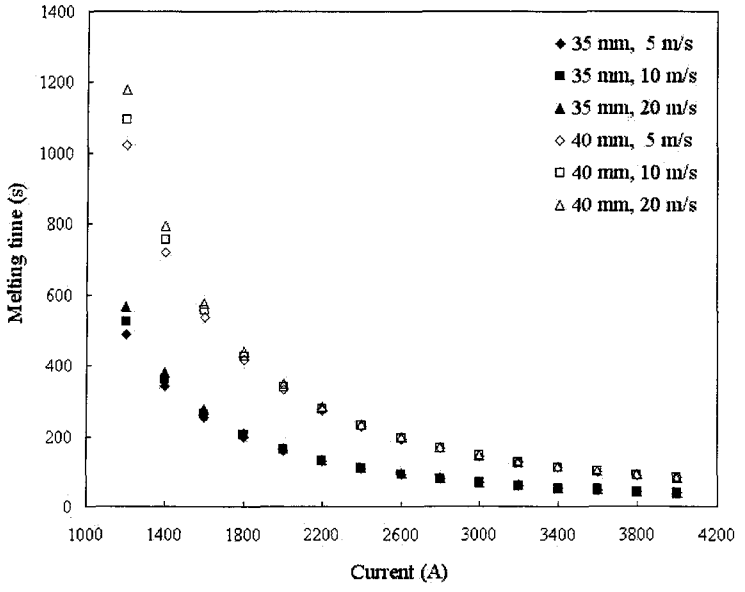

Figure 6.13 Effect of wind speed on melting time obtained with propagation model at -5 °C air temperature for Carillon type conductor

The results are presented at various wind velocities in Figure 6.13. A long melting duration can be observed at higher wind speeds. It is interesting that the wind speed has almost no effect on the melting duration, when high currents are used for de-icing. Consequently, it is possible to save some energy by applying the highest available/possible electric current in the conductor.

CHAPTER 7

FLOW AND HEAT TRANSFER AROUND A CONDUCTOR

7.1 Introduction

Heat transfer coefficients obtained from wind tunnel measurements are presented and compared with certain available literature data obtained by other researchers, as well as a short overview of the theory about fluid flow past cylinders together with the most common correlations in the relevant literature.

It is of great importance to calculate the heat taken away by the wind from the power line conductors. The convective heat transfer around electrical conductors plays a significant role in the thermal balance of power lines. For example, it is included in the formulations used for thermal ratings and in ice prevention calculations. In this study both, experimental study and numerical simulations were performed in order to predict the local and overall HTC around helically stranded conductors.

The local and overall HTC can be determined:

- from experiments (e.g. traditional electrical heating method, optical method)
- from numerical calculations (e.g. using finite volume, finite differences, finite element methods).

7.2 Flow and heat transfer around a single circular cylinder (theoretical overview)

It is well known that the convective heat transfer is strongly influenced by the flow field developed around the object of interest. Therefore, the flow field around a circular cylinder will be discussed in the following section. Detailed explanation of velocity, pressure and temperature distribution around a cylindrical object, can be found in the relevant literature, where fundamental explanations are available (e.g. [22], [28], [40], [43], and [53]). This discussion is restricted to the flow field around a single, smooth circular cylinder in a cross-flow of air.

7.2.1 Characteristics of flow past a circular cylinder

Different characteristics of the flow field could be observed depending on the range of the Reynolds number. These characteristics of the flow field help the explanation of the convective heat transfer distribution around the cylinder. Note that Reynolds number (Re) could be interpreted as the ratio of inertia and viscous forces.

In the range of $Re<1$, the inertia forces are negligible compared to the viscous forces. The boundary layer near the cylinder surface is developed along the perimeter in viscous flow. The flow field is steady and it has two symmetry lines (the same as the geometrical symmetry lines of the cylinder). It is very similar to a potential flow field. There are two stagnation points, a front stagnation point (also called as *forward stagnation point*) at 0°

and a rear stagnation point at 180°. In the stagnation point the velocity is zero, and it has maximal value at 90°.

If the Reynolds number is approximately 1÷2, then the flow field loses the symmetry perpendicular to the flow direction. The rear stagnation point separates into two parts and moves closer to first stagnation point symmetrically to the axis in the flow direction. The flow is in a steady state.

At Reynolds numbers higher than 2, the laminar boundary layer separates before reaching the rear stagnation point due to increased inertia forces. The flow is still steady and symmetrical. Two "separation bubbles" occupy the space liberated by the laminar layer separation. The separation point moves toward the first stagnation point with increasing Re numbers, and this leaves more space for larger bubbles. At Re ≈ 40, the separation occurs at 120° [53].

The stability of the two separation bubbles ends in a range of Re numbers above 40. Alternating vortices roll up periodically from the cylinder surface. In the wake two, inversely rotating vortices can be observed. The flow of these alternating vortices in the wake shows a certain regularity. This flow is called in the literature as Kármán vortex train or Kármán vortex street after the great Hungarian scientist Tódor von Kármán. The flow is not steady any more and it is not symmetrical. The separation of the laminar boundary layer moves from 120° closer to the first separation point with increasing Reynolds numbers.

In flows characterized with Re numbers in the range of $5 \cdot 10^3 \div 2 \cdot 10^5$, the boundary layer is still laminar, but the separation location essentially does not change with increasing Re numbers [22], [62]. In practice, it remains around 80°÷83° [53].

At critical Re numbers in the range $2 \cdot 10^5 \div 5 \cdot 10^5$, the laminar boundary layer "separates" near 107°, but it transforms almost immediately to turbulent, which reattaches to the cylinder surface [53]. This turbulent boundary layer finally detaches between 95° and 140° [62].

At supercritical Re numbers greater than $5 \cdot 10^5$, the boundary layer becomes turbulent before the detachments occur. Once again, the separation point moves toward the first stagnation point with increasing Re numbers [53]. The wake with vortices is formed downstream from the cylinder, where the flow is highly irregular [22].

In practice, the range of flow velocities around overhead power line conductors is above Re numbers $5 \cdot 10^3$. This is especially true during storms. Therefore, the investigation is limited to this range of airflow. The airflow could arrive on the cylinder at different angles relative to the conductor's longitudinal axis. The present analysis is restricted to cases when the airflow's direction is perpendicular onto the cylinder's longitudinal axis.

7.2.2 Heat transfer coefficient distribution around circular cylinders

In the relevant range of airflow, two main zones of the flow field could be distinguished depending on the characteristics of the flow: the boundary layer flow on the windward side and the irregular flow in the wake on the leeward side of the cylinder. Note that the

convection heat transfer is strongly influenced by the nature of the developed boundary layer.

In the stagnation point, the local heat transfer coefficient has a maximum value, since there the boundary layer thickness is zero. The temperature gradient across the boundary layer is increases with increasing layer thickness, which results in a lower rate of convective heat transfer (decreasing HTC). At the boundary layer separation point, the local heat transfer coefficient has a minimum value. From the separation point toward the rear stagnation point the convective heat transfer increases. At low Re number flows the convective heat transfer is more intensive on the boundary layer flow part than on conductor surface in the wake [53]. At higher Re numbers (near Re numbers of $5 \cdot 10^4$ by [17]) this tendency is inversed; the convective heat transfer is greater in the wake.

The local HTC distribution is slightly different in the critical and supercritical ranges of flow ($Re \geq 2 \cdot 10^5$). The convective heat transfer is increased by the turbulent boundary layer reattachment in the critical range or by the transition from laminar to turbulent layer in the supercritical range of flow. The local heat transfer coefficient distribution around the cylinder perimeter has two local minimum values, at the boundary layer transition point and at the turbulent boundary layer separation point.

A large number of correlations for convective heat transfer calculation around circular cylinder is offered, which are based on experimental studies by various researchers. This is briefly overviewed in the following chapter.

7.3 Literature overview of HTC correlations around a single circular conductor

This section is concerned with a brief overview of certain available literature data and correlations for convective heat transfer calculations around a single circular conductor. Unfortunately, a complete overview of all existing relevant international literature is impossible. Generally, the correlations for convective heat transfer calculation have been obtained from experimental study and only rarely from the numerical simulations.

The literature overview has been done for the following reasons:

- To compare the experimentally obtained overall HTC values with results obtained by other researchers for stranded conductor or cylinders with roughness.
- In order to compare the numerical predictions of local HTC distribution (calculated in the following chapter) with numerical and experimental results obtained for smooth circular cylinders by other authors. The recalculation of this trivial case numerically allows the estimation of the strength of HTC predictions around a stranded conductor using a commercial CFD code.

7.3.1 Measured local and overall HTC correlations for smooth circular cylinders

The following is not a complete overview of the available literature, since this thesis is not strictly related to smooth circular cylinders, but rather with stranded conductors. It has been done for the purposes of comparison with numerically predicted heat transfer coefficients. However, these correlations can be used for perfectly symmetrical ice sleeves.

7.3.1.1 Overall HTC results

One of the most detailed literature overviews of the overall HTC of circular cylinders, where numerous correlations are listed, is the work of Morgan [41]. The following is just a selection of most widely known and more recently used correlations, which refers to airflow (Pr $\approx$ 0.7) in the subcritical range (Re $\leq 10^5$). All correlations are based on experimental study under different conditions, which are introduced in detail in the appropriate literature.

Typically, the overall HTC is presented in the following form:

$$Nu_{mean} = C \cdot \mathrm{Re}^m \cdot \mathrm{Pr}^n \qquad \text{Eq. 7.3-1}$$

where m and n are the powers of Reynolds (Re) and Prandtl (Pr) numbers respectively. The proposed value of powers by researchers is different due to measurements taken under different conditions. This is discussed in detail in the following section.

Other researchers propose to separate the above equation into two or three parts depending on the heat transfer mechanism along the perimeter (laminar boundary layer, turbulent boundary layer and wake flow). For example, such a correlation is offered by [55]. Some others suggest using a correlation which covers a wide velocity range (e.g. Churchill and Bernstein).

Table 7-1 Correlations for overall heat transfer coefficients

Authors	Correlations	Range of Re	Pr	Re-marks
Churchill and Bernstein*	$0.3+\frac{0.62Re^{0.5}\,Pr^{1/3}}{\left[1+(0.4/Pr)^{2/3}\right]^{1/4}}\left[1+\left(\frac{Re}{282000}\right)^{5/8}\right]^{4/5}$	-	Re·Pr>0.2	
Hilpert (found in [22])	$0.193\cdot Re^{0.618}\cdot Pr^{1/3}$	$4\cdot10^3\div4\cdot10^4$	≥0.7	at T_f
	$0.027\cdot Re^{0.805}\cdot Pr^{1/3}$	$4\cdot10^4\div4\cdot10^5$		
Zhukauskas [62]	$0.25\cdot Re^{0.6}\cdot Pr_f^{0.38}\cdot(Pr_f/Pr_w)^{0.25}$	$10^3\div2\cdot10^5$	0.7÷500	at T_f
	$0.22\cdot Re^{0.6}$	$10^3\div2\cdot10^5$	Air, 0.7	
Sanitjai and Goldstein [55]	$0.446\cdot Re^{0.5}\cdot Pr^{0.35}+0.528((6.5e^{Re/5000})^{-5}+(0.031\,Re^{0.8})^{-5})^{-1/5}Pr^{0.42}$	$2\cdot10^3\div10^5$	0.7÷176	q=cts., Tu of 0.3%
Whitaker [60]	$(0.4\cdot Re^{0.5}+0.06\cdot Re^{2/3})\,Pr^{0.4}(\mu_f/\mu_w)^{1/4}$	$1\div10^5$	0.67-300	at T_f

* Correlation found in [22] and [53], but mistyped in [55].

7.3.1.2 Local HTC distributions

The overall HTC is used in the overall heat balance of the cylinder for the purpose of calculating an average temperature value. In order to calculate the surface temperature distribution, one uses the local HTC values, usually obtained from previous measurements. These local distribution characteristics are briefly reviewed in the following section.

Figure 7.1 shows the local Nu number distribution for smooth circular cylinder past air at different Reynolds numbers. These results are based on experimental study obtained by Zapp, Giedt, Schmidt and Wenner. Note that presented values in the figure are estimations from those found in literature. However, they confirm the theory introduced in previous

section. Zapp has reported turbulence intensity of about 0.9% in his measurements [28], and this was probably the case in the measurements of Giedt and Schmidt-Wenner also.

Martinelli, Guibert, Morrin and Boelter presented the local Nu number from front stagnation point to 80° based on the measurements of Schmidt and Wenner [28], as follows:

$$Nu = 1.14 \cdot \mathrm{Pr}^{0.4} \cdot \mathrm{Re}^{0.5}(1-(\alpha/90)^3) \qquad \text{Eq. 7.3-2}$$

The above equation simplifies for air with a Prandtl number of 0.74 as [28]:

$$Nu = 1.01 \cdot \mathrm{Re}^{0.5}(1-(\alpha/90)^3) \qquad \text{Eq. 7.3-3}$$

These correlations could be used for flows, where the free stream turbulence is less then 1%.

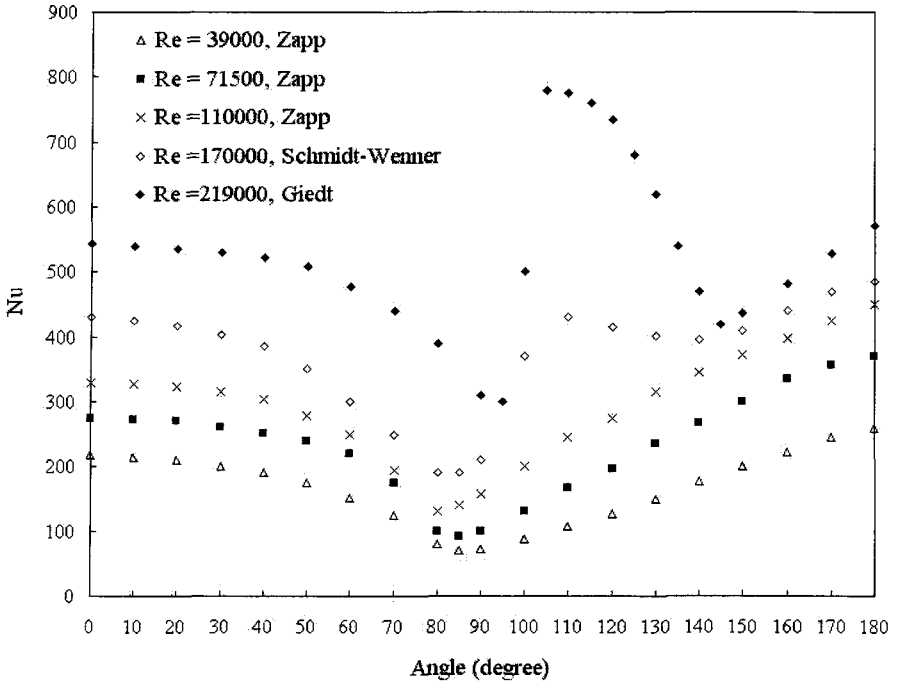

Figure 7.1 Local Nu number distribution around smooth circular cylinder at different Re numbers (Results reconstructed from [17], [28] and [53])

Figure 7.2 shows the local Nu number in a smaller range of Reynolds numbers (32000÷45300) also obtained by various authors. It is evident that these distributions may differ significantly from each other depending on the author. Obviously, the authors performed the experimental studies under different conditions. These influencing parameters/effects are overviewed in the following section.

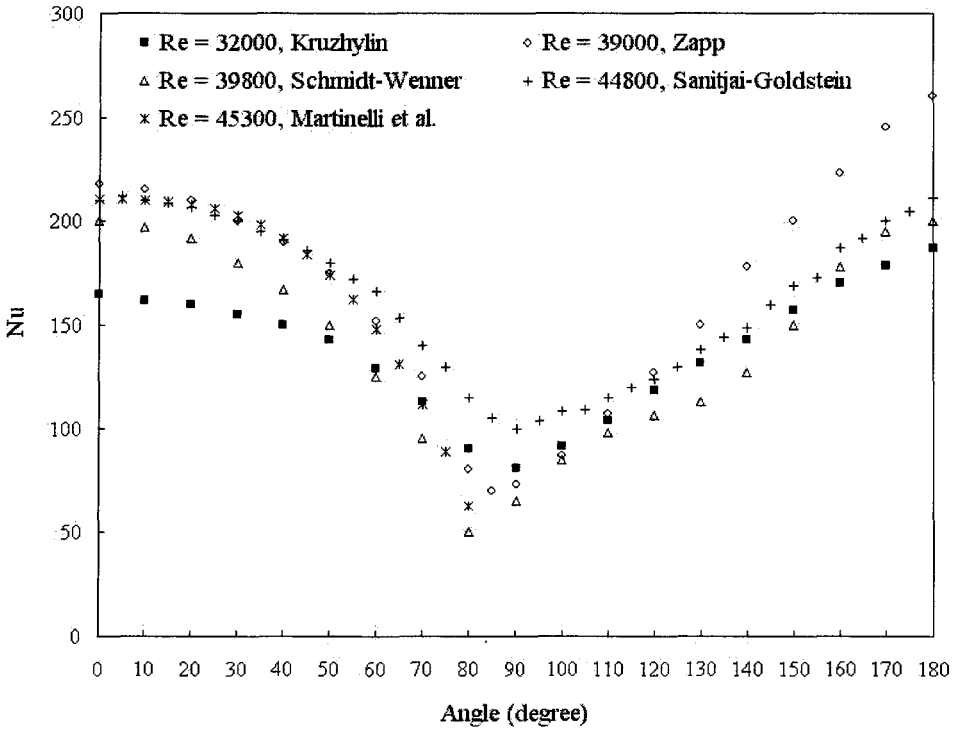

Figure 7.2 Local Nu number distribution around smooth circular cylinder at Re numbers in the range of 32000÷44800 (Results reconstructed from [17], [28] [53], [55], and [62])

7.3.2 Accuracy and limitations of experiments; influencing factors of HTC

For the comparison of HTC obtained by various authors, it is necessary to understand the effect of influencing factors/parameters coming from the different experimental or numerical setups. The HTC results obtained by different authors may differ from each

other by 10÷20%, but in some cases the differences may reach even 50% or more. The reason is that the experiments are influenced by numerous effects. Basically, the following phenomena have an influence on HTC [48], [53]:

- Turbulence intensity of the free stream
- Boundary conditions applied to the cylinder surface
- Tunnel blockage effect
- Length-diameter ratio of test cylinder
- Direction of heat transfer
- Influence of natural convection on forced convection during experiments
- Surface roughness/quality(protrusions)

Note that the HTC also depends on other parameters, including fluid properties, which vary with temperature in the thermal boundary layer. In the following section, the above-mentioned influencing factors are briefly reviewed.

7.3.2.1 Effect of tunnel blockage

During experiments the HTC is measured in a tunnel of a finite cross-section, which differs from theoretical/mathematical models where generally the domain around the cylinder is infinite. The cross-section of airflow decreases with increasing cylinder diameter/tunnel height (D/H) ratio. Consequently, the velocity of free stream increases, which increases the convective heat transfer as well. Certain authors offer a correction formula in order to account for this effect on HTC. The corrections are made to the Re

number as the tunnel blockage directly influences the fluid velocity. Reference [53] did a detailed literature overview on the influence of the tunnel blockage effect, from which the following can be concluded:

- The greater tunnel blockage (higher D/H) increases the local HTC on the windward side of the cylinder. Therefore, the overall HTC increases too [53].
- The boundary layer separation point moves toward rear stagnation point with increasing D/H ratio (kinetic energy of the boundary layer is greater).
- The Re number based on the velocity of the total cross-section should be corrected with correction formulas offered by the relevant literature (e.g. [53]) as a function of different D/H ratios.

Therefore, the experiments should provide a higher local HTC distribution on the front part of the cylinder and greater overall HTC as the mathematical predictions of infinite D/H ratio.

7.3.2.2 Effect of turbulence intensity of free stream

Generally, the theoretical/mathematical calculations of HTC around the cylinder take into consideration the inlet airflow of zero turbulent intensity. However, the free stream airflow in the experiments already has a turbulent intensity of a certain level. The effect of turbulent intensity (Tu) of free stream flow has stronger effect at higher Re numbers [53]. This effect was analysed by different authors and a good overview can be found in [53]. Figure 7.3 shows the effect of turbulence intensity of the free stream on the convective heat transfer obtained from measurements by Zapp.

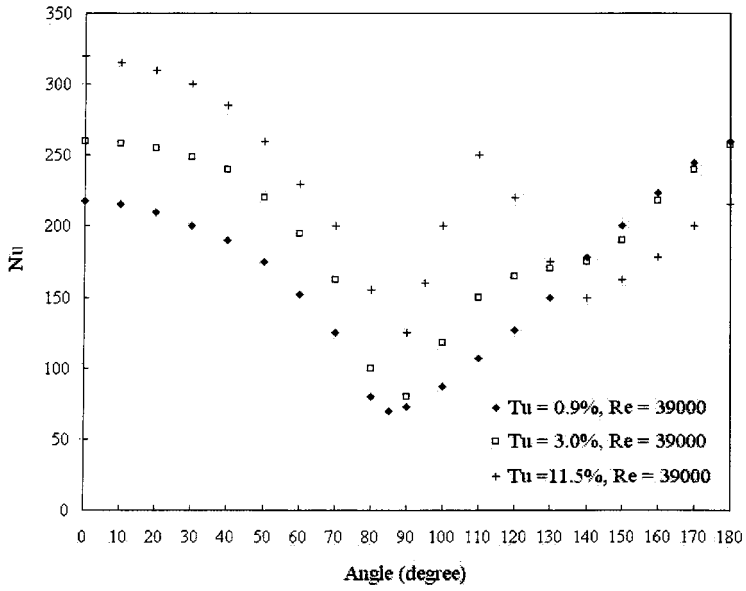

Figure 7.3 Local Nu number distribution around cylinder past airflow at different turbulent intensities and Reynolds number of 39000 (Results reconstructed from [28])

The following can be concluded from the overview in [53]:

- The turbulence intensity has an effect in particular on the local HTC at windward side of the conductor. The greatest influence is at the front stagnation point.
- The effect of free stream turbulence intensity is not evident on the conductor surface after boundary layer separation.
- The local HTC and the overall HTC both increase along the laminar boundary layer with increasing Tu.
- The critical Re number decreases with increasing Tu.
- Certain researchers offer a correlation to take into consideration the effect of Tu on the local and overall HTC for airflow. However, these correlations/correction

factors should be used with attention, because Nu numbers obtained in this manner may differ from each other by 30÷40%.

7.3.2.3 Boundary conditions applied to the cylinder surface

The HTC around the cylinder can be determined for the applied boundary conditions of the first (constant surface temperature) and the second kinds (constant heat flux on the surface). The obtained results from two different conditions differ from each other. For example, in an airflow with Re numbers in the 3000÷9000 range the HTC is about 10÷20% greater at constant heat flux than at constant surface temperature [6]. The difference between the theoretical calculations obtained with two different kinds of boundary conditions on the boundary layer covered surface part is about 30% [62]. The convective heat transfer is also influenced by the heat flux direction. Reference [62] reports that HTC is greater with heating than with cooling.

7.3.2.4 Effect of cylinder length/diameter ratio

In theoretical calculations, the cylinder length/diameter (L/D) is infinite. Therefore, the temperature and velocity distribution around the cylinder is two-dimensional. In experimental investigations the L/D ratio is finite, although the two-dimensional conditions could be achieved with compensation heating of cylinder ends. In practice, the Nu number does not essentially change, if L/D>4 [53].

7.3.2.5 Effect of natural convection on forced convection

Generally, natural convection is always present in HTC measurements in a certain order of magnitude. Its influence is more essential at fluid flows of low Re numbers. The

influence of natural convection on the forced convection is not negligible if Gr/Re^2 is greater than one [53]. Our investigations are restricted for wind speeds above 0.5 m/s (generally, for overhead conductors, this corresponds to Re numbers around 1000), in which case natural convection is negligible.

7.3.2.6 Effect of surface roughness

Surface roughness has an effect on convective heat transfer only at greater Reynolds numbers. On rougher surfaces, the critical Re number is decreasing [53]. In next section this effect is overviewed.

Consequently, it can be concluded that the aforementioned effects/influencing factors generally increase the convective heat transfer during the experiments. This means, that the experimentally determined HTC should normally be greater than that obtained from theoretical/numerical calculations.

7.3.3 Literature overview of HTC around rough and stranded cylinders

It is known that the surface of power line conductors is not smooth. It consists of twisted, cylindrical strands which cause serious non-uniformities on the surface. Therefore, one could ask whether the HTC correlations obtained for smooth circular cylinders can be used for stranded conductors? Various researchers have analyzed the effect of surface roughness or protrusions on convective heat transfer. It was concluded that it has very little effect if the protrusion is not higher than the laminar sublayer in the boundary layer. On the other hand, when roughness is present in the buffer layer, then it makes the boundary layer turbulent. Consequently, the convective heat transfer increases locally.

One of the first studies on this subject was the experimental study performed by Schmidt and Wenner [28]. They analyzed the effect of wires 1.5 mm in diameter attached to a smooth cylinder's surface. Two interference wires were placed at 77.5° from the stagnation point symmetrically on a smooth circular cylinder of 100 mm diameter [28]. The effect of this artificial non-uniformity on local convective heat transfer distribution is shown in Figure 7.4.

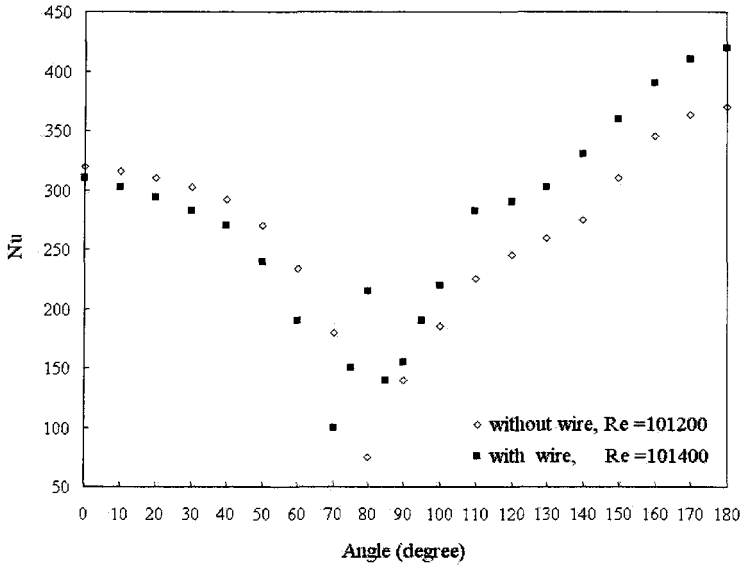

Figure 7.4 Effect of surface non-uniformity on local Nu number distribution in cross-flow of air; the interference wire is attached at 77.5° (Results reconstructed from [28])

It is evident from Figure 7.4 that the Nu number has a local maximum, where the interference wire is placed and on its both side the distribution has a local minimum value. Reference [28] explains this phenomenon with the boundary layer transition from laminar to turbulent caused by the wire, since the same was observed on a smooth cylinder surface when the boundary layer transition occurred (see Figure 7.1). Surprisingly, Schmidt and

Wenner reported that there was just a slight difference in overall Nu numbers obtained with and without interference wire.

The forced and natural convection from bare stranded electrical conductors (used for power lines) was studied by Morgan [40]. The studied conductors, characterized byroughness ratios in the 0.042÷0.366 range, were exposed to airflow of a Reynolds number in the 140÷47 000 range. The effect of surface quality and of yawing the wind was analyzed in details. It was found that the stranding has a negligible effect on the overall HTC for Reynolds numbers in the 140÷2000 [40] range. On the other hand, the stranding influences convective heat transfer at higher wind speeds, where the overall Nu number increases with increasing roughness ratio at constant a Re number [40]. It was also established that the "critical" Reynolds number (Re_{crit}) is related to the roughness ratio (H_r/D) as [40]:

$$\mathrm{Re}_{crit} = 130/(H_r / D) \qquad \text{Eq. 7.3-4}$$

Therefore, the stranding has a remarkable effect on the convective heat transfer (greater than 1%) in the flows, which are in a higher range than Re_{crit}. The increase in the Nu numbers for stranded conductors related to smooth cylinders is expressed in [40] as follows:

$$\frac{\Delta Nu}{Nu_{smooth}} = 0.01 + 0.0335\left(\frac{\mathrm{Re}_{smooth} - \mathrm{Re}_{crit}}{\mathrm{Re}_{crit}}\right)^{1.072} \qquad \text{Eq. 7.3-5}$$

It was not clear in which range of airflow that the above equation is valid and what the range of surface roughness is exactly.

When analyzing the yawing effect, [40] reports that the convective heat transfer is the most intensive in the case, when the bottom or top strands were normal to the flow (and not when the conductor axis is normal to the flow).

Unfortunately, in the available literature no local heat transfer distribution around stranded conductor was found, except that of Morgan [40] obtained at the small Re number of 2100.

7.4 Flow visualization around stranded conductor in wind tunnel

The flow field around a smooth circular cylinder was overviewed in section 7.2.1. It is expected that somewhat different flow characteristics are present in flow past a stranded, twisted electrical conductor; therefore, the focus of this section is these main characteristics. The initial assumption was that the flow past a stranded conductor is strongly three-dimensional due to the effect of "twisted" strands. Also, it is expected that the third component (along the longitudinal axis) is caused by twisted airflow.

A simple, easy-to-use flow visualisation technique is used in order to establish the flow behaviour around a stranded conductor. Very lightweight tufts/threats are attached onto the stranded surface, which can easily take the form of the flow. The positions of these tufts/threats are recorded using a high-quality camera.

The test conductor (code word Bersimis) was placed in the CIGELE wind tunnel perpendicular to the airflow. More than 1000 photos were taken from the threads attached to the leeward side of a stranded conductor at three different wind velocities, namely at 5,

10 and 20 m/s. First, observational tests were performed in order to find the ideal material (cotton or polymer, for example), length and number of threads for airflow visualization around a stranded conductor. In this section, just the most successful photos are presented.

7.4.1 Airflow at 5 m/s

Figure 7.5 shows that nearly all attached threads are in the cross-sectional plane at 5 m/s wind speed. The weaving of threads left and/or right is not significant. Consequently, the third/longitudinal velocity component is either not significant at low wind speed conditions or cannot be visualized using threads, since they are not sensitive enough to capture weak twisted effect at low wind speeds.

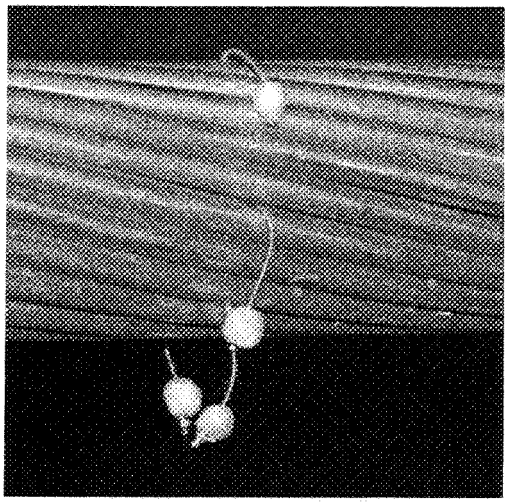

Figure 7.5 Tufts in leeward side, at the center of the test conductor exposed to 5 m/s wind speed

7.4.2 Airflow at 10 m/s

The threads occupy different locations in time at the leeward side of the stranded conductor. These positions are shown in Figure 7.6. It was observed that the position of

threads changes rapidly and it could be different related to conductor and to each other. This leads to the conclusion that the wake is chaotic and highly turbulent. However, certain signs of twisted airflow around the stranded surface can be seen (see Figure 7.6 a), since certain strands generally wave in the twisting direction of strands. In most of the cases, the thread attached to top of stranded conductor wave right according to the stranding, while thread at bottom of conductor inclines to left according to the appropriate twisting lay of strands. It can be observed from Figure 7.6 b.) that thread at 180° fit into the inter-strand channel at the leeward side of conductor. Therefore, one may assume a longitudinal velocity component of airflow in these channels.

Similar flow characteristics were observed at 20 m/s, just obviously more chaotic motion in the wake. The images taken from threads exposed to various wind speeds are presented in APPENDIX 5.

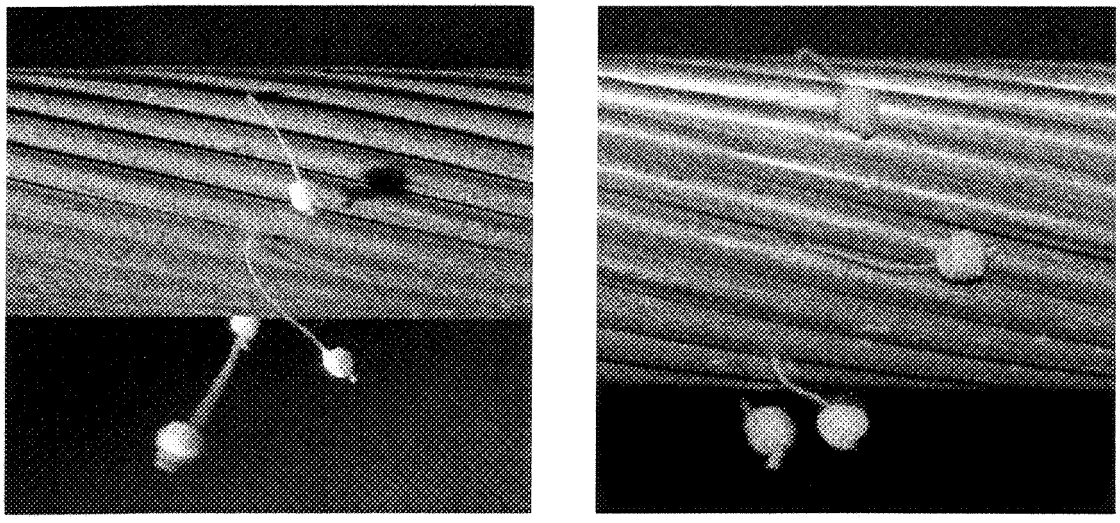

a.) b.)

Figure 7.6 Tufts in leeward side in different positions, at the center of the test conductor exposed to 10 m/s wind speed

7.5 Measuring the overall HTC around stranded conductor

7.5.1 Experimental rig and procedure

7.5.1.1 Test conductors

The effect of surface roughness on overall heat transfer coefficient was investigated on four specific types of ACSR conductors with circular cylindrical strands and concentric layers. These conductors are specified as A1/S1-468 (code word Drake), A1/S1-455 (with code word Condor), A1/S1-521 (code word Carillon), and A1/S1-1060 (code word Geant 5P), following the terminology of Canadian Standards Association [4]. For geometrical parameters of the conductors under study, see Table 7-2. The structure of these conductors is depicted in Figure 7.7 and Figure 7.8. The surface parameter, R, of the stranded conductors is defined in [42] as follows:

$$R = d_s / 2 (D_c - d_s) \qquad \text{Eq. 7.5-1}$$

where d_s (m) is the aluminium strand diameter and D_c (m) is the conductor's external diameter.

The geometrical parameters in Table 7-2 are the conductor's external diameter (D_c), the equivalent diameter (D_e), the strand diameter (d_s), the number of strands in the outer layer (m) and the surface parameter (R). Values of D_c and d_s are cited from [4]. Note that the surface geometry of both the Condor and Geant 5P conductors is the same, as they share a similar geometrical construction. It may also be observed from Table 7-2 that the Drake conductor has the roughest surface. The length of the conductor's test section was 850 mm. Their ends were welded and then machined to a cylindrical shape along 95 mm, in order to

assure the best possible contact surface between the conductor and the connectors, as well as to achieve a more regular current intensity distribution in the strands. Unfortunately, tension was lost in a few strands in the outer layers of the Carillon and Condor conductors during the preparation. Therefore, these two conductors have poorer contact between adjacent strands, which affect the regularity of the temperature distribution in the conductor. Additionally, they have a greater surface exposed to airflow. Consequently, the rate of convection heat transfer is more elevated for these conductors.

Table 7-2 Geometrical parameters of ACSRs

Code word	D_c	d_s	m	D_e	R
	mm	*mm*	-	*mm*	-
Carillon	30.48	3.98	20	43.78	0.0751
Condor	27.72	3.08	24	40.04	0.0625
Drake	28.11	4.44	16	39.96	0.0938
Geant 5P	45.00	5.00	24	65.00	0.0625

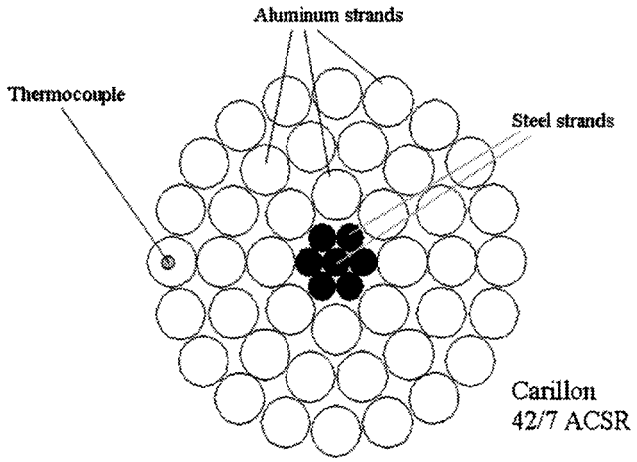

Figure 7.7 Cross-sectional view of 42/7 Carillon conductor with thermocouple installed in the stagnation point.

The thermocouple measuring the stagnation temperature was installed inside one of the outside strands in the middle of the conductor test section. The thermocouple's shielded wire was fit in a channel between the external strands.

7.5.1.2 Experimental setup and procedure

The experimental setup was rigged with a low voltage, high amperage transformer allowing for Joule heating the test conductor by sending alternating current through it. The effective current was measured by a current transformer installed in the circuit. The power line test conductor was installed in the test section of the CIGELE Icing Research Pavilion wind tunnel (see Figure 7.9), perpendicular to the direction of the airflow. The conductor connections were kept outside the wind tunnel in the thermally isolated room surrounding the test section. This room was cooled to the required temperature before each experiment, in order to keep the conductor connections as cold as possible and to reduce the thermal boundary layer in the wind tunnel test section, as well as the radiative heat loss from the conductor. The good connections are important in order to prevent the formation of parasite heat sources at the junctions. The connecting clamps were pressed against the ends of the conductor with four-four screws tightened as much as possible to ensure good contact. The voltage drop between the clamps at the ends indicates how good the contact is. An infrared camera was installed to monitor the surface temperature distribution along the test conductor and at the connector clamps. From the images taken, it was possible to estimate parasite heating and its effect at the mid-section of the conductor, where the thermocouple was located. As matter of fact, no significant parasite heat generation was found at the conductor ends.

The thermocouple installed in one of the outer strands was exposed to a strong magnetic field due to the alternating current flow in the conductor. In order to eliminate the noise captured by thermocouple, the wire's stainless steel shield was grounded and the connector box was isolated with a Faraday cage. Two other thermocouples were installed: one to monitor the air temperature in the wind tunnel, and the other to measure the temperature near to the conductor connections. All thermocouples were previously calibrated in crushed ice made of de-ionized water.

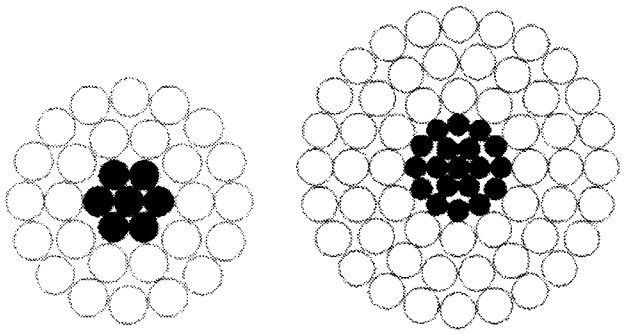

Figure 7.8 Structure of 26/7, two aluminium layer Drake and 54/19, three aluminium layer Geant 5P conductor.

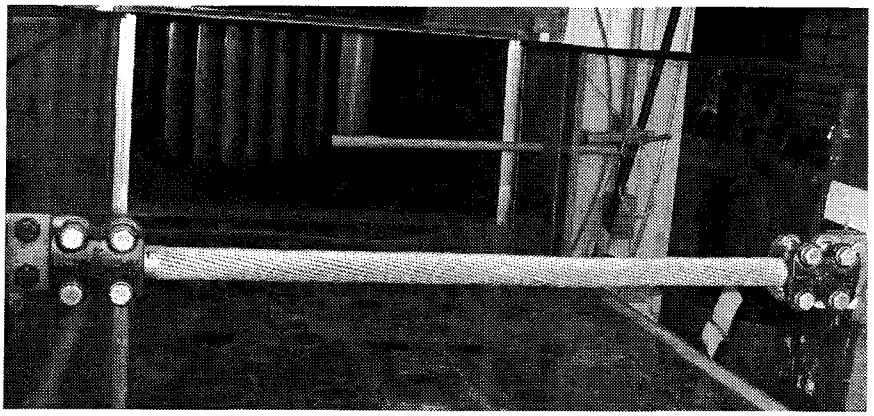

Figure 7.9 Test section of the line conductor installed in the wind tunnel

The cross-sectional dimensions of the wind tunnel test section were approximately 46x92 cm (18"x36"). The velocity field in the wind tunnel section under study was simulated for different free stream velocities and it showed quite a uniform distribution both horizontally and vertically [49]. The velocity field in the wind tunnel section under study was simulated for different free stream velocities. Figure 7.10 shows one of the simulations with the wind velocity distribution in a horizontal plane. It is evident that the velocity distribution in the test section (where the conductor was placed) is highly uniform, except for a thin boundary layer on the walls.

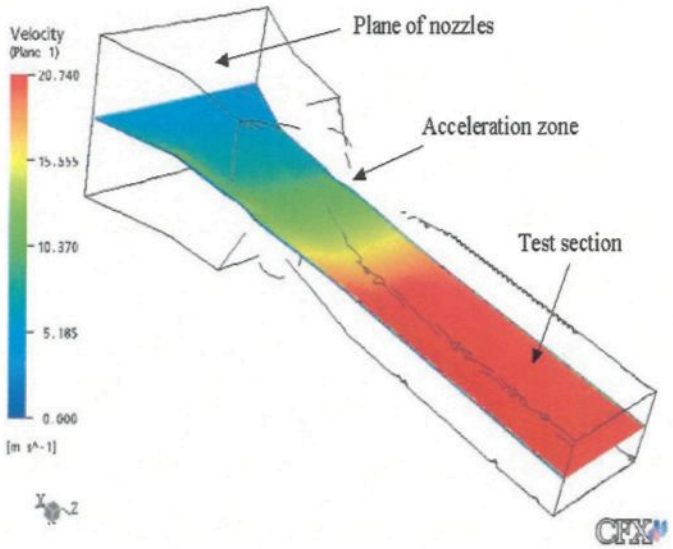

Figure 7.10 Airflow simulation of wind tunnel section using a CFD software (CFX-5.6).

During measurements, the appropriate wind speed was adjusted by controlling the fan speed and the wind speed was measured using a hand-held anemometer. Table 7-3 shows the estimated accuracy of all measured parameters during the experiments.

Table 7-3 Estimated accuracy of measured parameters

Measured parameter	Accuracy
Velocity of dry airflow	±2%
Load current below 2200 A	±2 A
Load current above 2200 A	±20 A
Temperature	±0.2 °C ÷ ±0.3 °C

7.5.2 Overall heat transfer coefficient

The overall HTC is evaluated for the investigated ACSR conductors in order to be able to calculate the minimum current required for preventing ice formation on a stranded surface. Therefore, an attempt was made to estimate the HTC for stranded conductors with different surface geometry. This estimation method is based on the heat balance (Eq. 7.5-2) of an electrically heated conductor under steady state, dry airflow conditions. Moreover, the HTC estimations were compared with certain empirical correlations found in the literature. In both cases, wind direction perpendicular to the conductor axis was assumed.

$$I^2 R_{ac,c} = h\ A\ (T_s - T_a) \qquad \text{Eq. 7.5-2}$$

The convection coefficient was calculated from Eq. 7.5-2 after both conductor surface and air temperatures were measured at constant current intensity. This calculation, as well as that of the Nusselt (Nu) and Reynolds (Re) numbers, was repeated under different wind velocities in the range of 5÷25 m/s. During these series, the air temperature was maintained around –10 °C, as can be seen in Figure 7.11. The air and the cable surface temperatures in

the wind tunnel were continuously registered (see Figure 7.11) and the average values of the steady state period were computed.

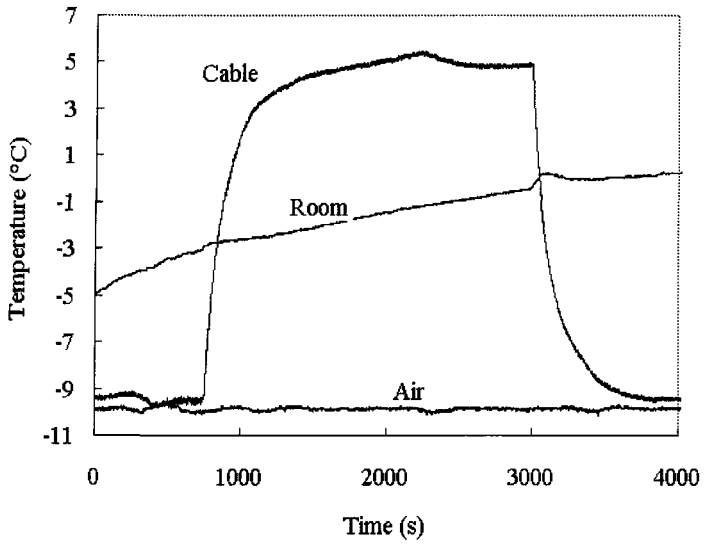

Figure 7.11 Registered temperature history during a typical test at 1900 A current in conductor and airflow velocity of 10 m/s

The results are plotted in Figure 7.12 for each analyzed conductor type. It can be clearly seen from Figure 7.12 that the Nu–Re correlations are nearly linear for all tested conductors in the airflow range under study. In Eq. 7.5-2, the A (m^2) is the surface exposed to the dry airflow that is calculated from the equivalent diameter of the stranded conductor. The HTC correlations for the Carillon type conductor are also presented in [49], where the conductor surface is obtained from the circumscribing diameter.

The conductor temperature measured at the stagnation point is assumed to be the average value for the whole circumscribing surface. This assumption is based on the high longitudinal thermal conductivity of ACSR conductors. As the outer strands are helically arranged around the adjacent layer, any strand is equally part of both the leeward and

windward side of the conductor in a length of lay. Indeed, no significant angular temperature variation around the conductor is reported in [46] and [47]. During these tests series, the air temperature was maintained around –10 °C. The conductor surface and the air temperatures in the wind tunnel were continuously registered. Finally, the average values of the steady state period were computed. Since the electrical resistance varies with temperature, different values of skin coefficient (k_s) were sampled at conductor working temperature during the evaluation of HTC from Eq. 7.5-3. These were in the range of 1.031÷1.037 for Carillon type conductors, 1.014÷1.015 for Condor, 1.010÷1.012 for Drake and 1.095÷1.103 for Geant 5P.

The maximal error of HTC measurements is also shown in Figure 7.12. They are below 4% for Drake and Condor type conductors, and below 5% for Geant 5P. For Carillon type conductors the measurement errors are higher, but below 13%. It has already been mentioned that some outer strands of Carillon and Condor type conductors lost their strength, probably letting air pass between them. This effect leads to relatively greater HTC and Nu numbers, as seen in Figure 7.12. Comparing the measurement results of Condor and Geant 5P (both with same surface geometry), a 16.5% rise in overall HTC due to strength loss is established. The overall Nu number can be parameterized as follows:

$$Nu = M\ Re^{z} \qquad \text{Eq. 7.5-3}$$

The coefficient M and exponent z are presented in Table 7-4. Figure 7.13 shows the measurement results for different test conductors, as well the correlations found in the literature [10], [13], [21], [35], and [38].

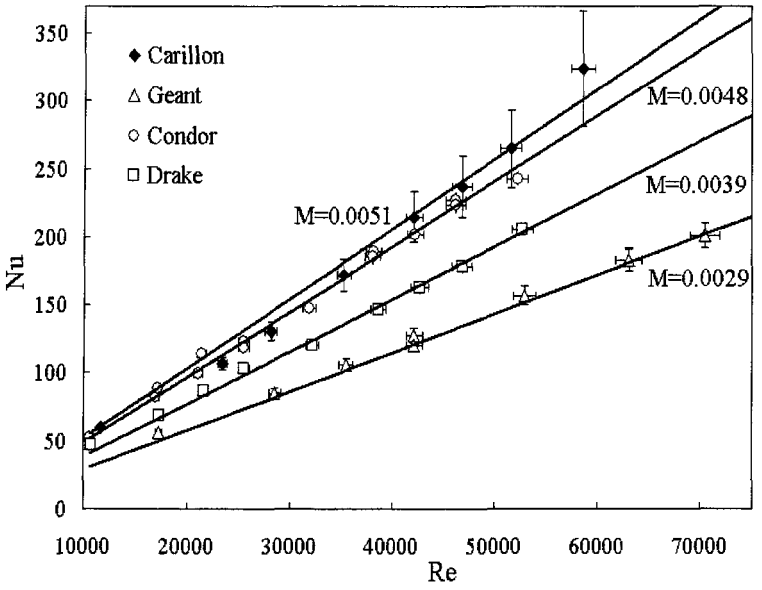

Figure 7.12 Nu number as a function of Reynolds number, measured for conductors of different surfaces. Wind direction assumed perpendicular to conductor axis.

Table 7-4 Constants of Eq. 7.5-3

Source	M	z	Re
Achenbach[b]	0.032	0.85	$7 \cdot 10^4$ - $9 \cdot 10^5$
Clem[c]	0.324	0.5	not reported
IEEE'93**	0.2396	0.60	$< 5 \cdot 10^4$
Carillon[d] (measured)	0.0051	1.00	10^4 - $7 \cdot 10^4$
Condor[d] (measured)	0.0048	1.00	10^4 - $7 \cdot 10^4$
Drake (measured)	0.0039	1.00	10^4 - $7 \cdot 10^4$
Geant 5P (measured)	0.0029	1.00	10^4 - $7 \cdot 10^4$

The empirical correlation of Achenbach [35] is very similar to that obtained for Condor type conductors around $7 \cdot 10^4$ Re number. Achenbach used a cylinder with 0.9 mm high roughness elements while the corresponding value is 1.54 mm (half of the strand diameter) for a Condor conductor. The 1993 IEEE standard [21] for calculating the current-

temperature relationship of bare overhead conductors suggests two equations for the calculation of the convective heat transfer rate (with superscript * and ** in Figure 7.13). At Re numbers below $2 \cdot 10^4$, the equations account for the measured results. However, at higher Re numbers, the measured values are underestimated by Clem and IEEE standards.

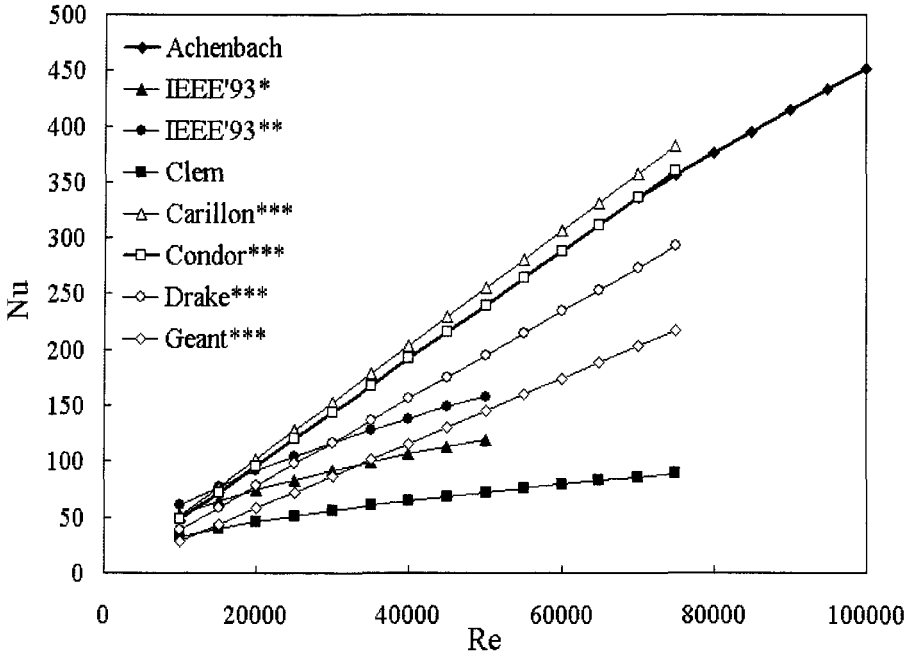

Figure 7.13 Nu numbers calculated in this study (with superscript ***) and those found in literature [10], [13], [21], [35], and [38], versus Reynolds number.

In conclusion, the overall heat transfer coefficient measurements are presented for four different ACSR conductor types. The Nu-Re correlations showed a linear relationship between the 10^4 and $7 \cdot 10^4$ Reynolds numbers. The measurement results were compared with those found in the literature. It can be also concluded that the strength loss of ACSR conductors gives a higher heat convection rate projected to the same heat transfer surface.

CHAPTER 8

NUMERICAL PREDICTION OF CONVECTIVE HEAT TRANSFER COEFFICIENT AROUND A SMOOTH CIRCULAR CYLINDER AND STRANDED ELECTRICAL CONDUCTOR

8.1 Introduction

This chapter deals with the numerical prediction of convective heat transfer around smooth, stranded, and twisted cylindrical conductors. Convective heat transfer coefficients obtained from numerical simulations are presented as well as they are compared with certain available literature data. A short overview of the possibilities of predicting heat transfer using numerical simulations is also presented.

The numerical analyses in this study are restricted to convective heat transfer around a single cylindrical conductor in a cross-flow of air. The conductor is fixed perpendicularly to the airflow (non-vibrating, non-rotating case). The wind velocity is high enough that the natural convection can be neglected. The effect of boundary conditions applied on the conductor surface, the computational domain size used, the applied turbulence model, the effect of stranded surface, and the influence of the free stream turbulence intensity on the HTC are investigated. At the end, brief qualitative and quantitative conclusions of the numerical analyses are presented.

The relevant literature offers a large number of correlations for local and overall HTC around cylinders. However, just a few of them discuss the effect of surface roughness on

HTC, and very few focus on the helically stranded conductors (e.g. [40]). Furthermore, the available works on stranded conductors are restricted to flows with low Reynolds numbers. Therefore, it was necessary to study the effect of helical strands on the conductor surface at greater Reynolds numbers.

8.2 Numerical predictions of HTC

The CFD (Computational Fluid Dynamics) codes are rarely used for heat transfer predictions, since fluid dynamic simulations require significant computer resources. Often the numerically calculated heat and mass transfers supply a different result than those obtained from experimental study [30]. Furthermore, the simulations were very unwieldy and computationally very expensive. However, with the developments in computer technology, specifically, significant improvements in turbulence models and in solution procedures for Navier-Stokes equations, the numerical simulation becomes an alternative to experimental correlations in predicting HTC. A brief historical overview of CFD codes and implanted turbulence models is available in [59].

In this study, a commercial CFD code, namely Ansys CFX-10.0, is used for numerical predictions of airflow and HTC around cylindrical conductors. This code is based on the finite volume technique.

8.2.1 Turbulence models

First, the flow field should be calculated correctly in order to predict the HTC around an object. Ansys CFX-10.0 provides a wide scale of both eddy-viscosity and Reynolds-stress turbulence models. Both are based on the Reynolds Averaged Navier-Stokes (RANS) equations. A detailed list is available in [2]. k-ε and k-ω are probably the two most popular and widely-used models to approximate the effect of turbulence. Both are categorized as of eddy-viscosity models [2]. In the k-ε model, the turbulent length scale is predicted from the ε-equation. This model offers relatively good accuracy, although it fails in certain simulation cases. Unfortunately, models based on the ε-equation over-predict the location and under-predict the amount of separation [2]. Note that the accurate simulation of boundary layer detachments under an adverse pressure gradient is one of the main problems in turbulence modelling [2]. An alternative solution is to use the ω-equation instead of the ε-equation, which predicts the length scale in adverse pressure gradient flows well. The theory and formulation of the k-ε and k-ω turbulence models are thoroughly introduced in the relevant literature (e.g. [39], [59], [61]). The main disadvantage of using the ω-equation is that it is very sensitive to the free stream outside the boundary layer [59].

It seems that the "ideal" solution is the hybrid model created from the previously mentioned turbulence models, which uses the advantages of these models. The SST (Shear-Stress-Transport) model uses the strong points of the k-ε model away from the wall, and those of the k-ω near the wall [59]. The combination is created with a blending function (F1), which is equal one near the surface (activating the Wilcox model) and zero in the rest of the flow (activates k-ε model) [59]. The blending function depends on the wall distance,

which is calculated by additional equations [2]. The detailed formulation is presented in [59]. Figure 8.1 shows the blending function in the flow around a circular cylinder. Another implementation in the SST model is the upper limit for the turbulent shear stress in the boundary layer. This limiter helps to eliminate the build-up of turbulence in stagnation regions of blunt objects [59]. Reference [2] introduces the SST model as that which gives precise predictions of the location and the amount of boundary layer separation under adverse pressure gradients. This is true only if the strict grid requirements of this model are met.

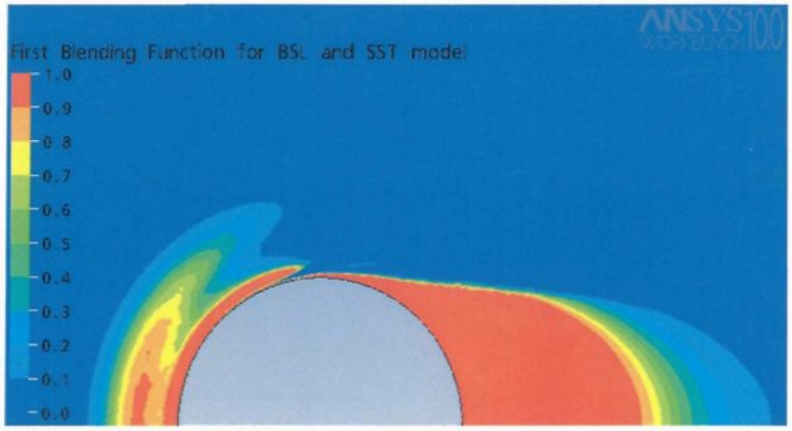

Figure 8.1 Distribution of blending factor (F1) using SST model around smooth circular cylinder (at Reynolds number of 41 028)

8.2.2 Near wall treatment

The treatment of equations near the wall is also an important part of the HTC calculations, since it has a significant influence on the boundary layer development (including boundary layer separation) [59]. Generally, the boundary layer contains three regions: viscous sublayer, defect layer and log layer [61]. In the vicinity of the wall is the *viscous sublayer* (also called the laminar layer), where the molecular viscosity affects

significantly the momentum and heat transfer [2]. Here, the flow is laminar. The *logarithmic layer* (log layer) is at the outer part of boundary layer. In the log layer both the molecular viscosity and the turbulence are important [2]. Between the viscous and log layer is an overlap region called the *defect layer* (also called the buffer layer), where turbulence dominates the mixing process [2]. The velocity in this sublayer is scaled with the distance from the wall. The velocity profile as a function of wall distance is described with a logarithmic function. This function is called "log law of the wall" or just "law of the wall" in the literature [2], [61]. The velocity in the defect layer is determined from the "velocity-defect law", also called "Clauser defect law" [61]. For more details about the law of the wall formulation see [61].

In most cases, one of the two most popular methods for the near-wall treatment is applied, namely wall-functions or low-Re number model, which are used to complete the turbulence models.

Wall-functions use the theory of logarithmic profile region of the boundary layer. The viscosity-affected sublayer is defined with empirical formulae. This method assumes that the near wall grid is located in the fully-turbulent region of the boundary layer [59]. This criteria supplies strict sensitivity to the near-wall meshing, especially in the case of flows with a small Re number. Furthermore, the boundary layer should be sufficiently resolved (at least 10 nodes), but the standard wall functions deteriorate on very fine grids [59]. The **scalable wall functions** solve this problem and they may be applied on extremely fine grids, since their grid sensibility is reduced. There is no need to resolve the boundary layer very precisely, since the logarithmic wall function is applied to model the boundary layer.

This does not affect the validity. It just reduces the quantity of information in the boundary layer. The theory of this approach is explained in detail in [59].

The low-Re number model is based on different damping factors. In the vicinity of the wall it requires very fine mesh length scales perpendicular to the wall. The boundary layer should be resolved with at least 15 nodes [2]. General grid requirements are $y^+<2$ (y^+ is the dimensionless distance from wall) for mesh independent solutions, which leads to a large number of nodes near the wall [2]. With the low-Re number model, the boundary layer transition is provoked by the wall damping functions [2]. Reference [2] reports that this approach is not sensitive enough to different influencing factors, including free-stream turbulence, boundary layer separation and pressure gradients. Ansys CFX recommends using the full Transition model instead of the low-Re number model for calculating boundary layer transition.

The automatic near-wall treatment includes an algorithm, which shifts between the viscous sublayer formulation (low-Re number model) and wall functions depending on the mesh density [59]. Consequently, this near-wall treatment is less sensitive to the mesh density than wall-functions or low-Re number model. This means that the resolution requirements are reduced compared to the low-Re number model, without a loss in accuracy [2]. However, in order to reduce the errors caused by automatic shift from one model to another, the boundary layer should be resolved with at least 10 nodes [2]. Different users found that ω-equation models worked well with the automatic near-wall treatment model. The numerical predictions of HTC were obtained using SST and k- ω models with automatic wall treatment, in the following section.

Using a full **Transition model** for boundary layer transition is advised by Ansys CFX in order to capture the influence of turbulence intensity of the free-stream and that of the separation [2]. It involves two additional equations, one for intermittency and one for momentum thickness Reynolds number. Reference [2] mentions that the transition model has been validated together with the SST model for a wide range of transitional flows. However, the sources of these validation reports were not mentioned in [2]. Only one validation report was found concerning heat transfer predictions using the SST model for internal flows, natural convection and impinging jets. The grid requirements for this model are relatively strict (y^+ should be approximately one [2]). At very low y^+ (below 0.001) the transition location moves downstream, since the specific turbulence frequency is a function of first grid point height [2]. Conversely, the transition moves upstream if y^+ is higher than 8 [2]. The mesh independent solution could be obtained with y^+ values between 0.001 and 1, and with an expansion factor in the range from 1.05 to 1.1 [2]. The solution is independent from the streamwise grid resolution if there are at 75÷100 grid points in the streamwise direction [2]. Note that rough wall treatment is included in CFX-10, but it is only a beta feature [2].

8.3 Numerical results in the relevant literature

The fact that CFD codes are only rarely used to predict the heat transfer coefficient (HTC) has already been mentioned. To the candidate's knowledge, literature [30] is one of the latest studies about predicting HTC around smooth circular cylinder in cross-flow using

CFD. The calculations in [30] are based on the k-ε turbulence model used with both standard wall function and low-Re number models. Certain parts of these numerical calculations are reproduced in Figure 8.2. The two-dimensional calculations are performed for a circular cylinder 100 mm in diameter in airflow in a range of 0.5÷5 m/s. Thermal boundary conditions of first kind were applied on the cylinder surface. The inlet turbulence intensity varied in a range of 1.5÷40% [30]. In most cases the boundary layer was resolved equally into 15 layers of 0.5mm×0.5mm grid size. Finally, the cylinder surface was divided into 1280 elements [30].

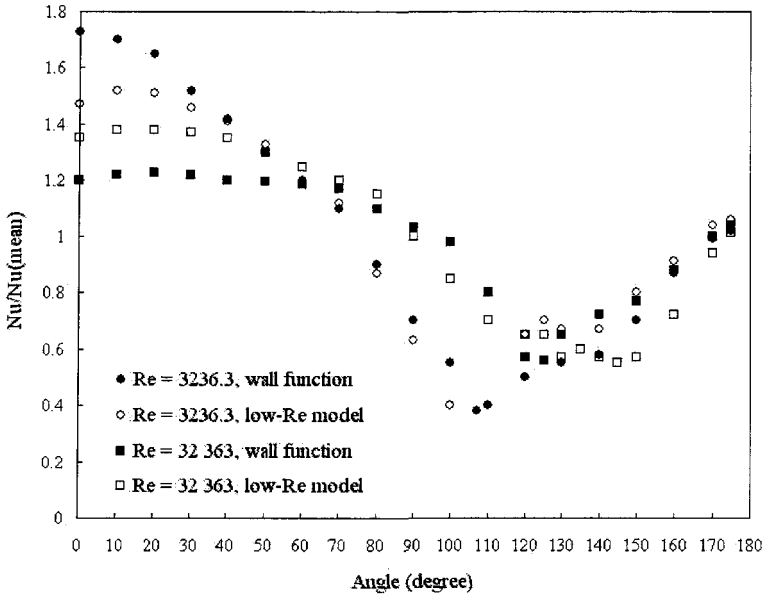

Figure 8.2 Relative Nu number along the circular cylinder perimeter obtained from numerical calculations. The above results are reproduced from [30], where the actual turbulence intensity value is not clear.

Reference [30] has studied the HTC prediction capability using the k-ε turbulence model coupled with standard wall function at low wind speed (1 m/s) and low inlet turbulence intensity (1.5%) in order to minimize the distortion effect due to the actual

turbulence formulation. It was found that in this case the numerical calculations overestimate the experimentally obtained overall Nu numbers by about 45%, while this difference was in a range of 37÷225% for higher wind velocity and turbulence intensity [30]. The calculated location of boundary layer separation was in a range of 110÷120°, instead of 80÷85° as measured by various authors (already discussed in section 7.2.1).

Generally, Wolfshtein's low-Re number model better approximates the experimental results than when the wall functions are used [30]. The numerical results of the overall Nu number were closer to experimental values, but differences were still observed between them up to 45% [30]. Increased velocity moved the boundary layer separation more downstream (130÷140°) from the experimental value (see Figure 8.2).

Reference [30] suggests the use of a low-Re number model instead of wall functions for convective heat transfer predictions, since the distortion of the k-ε turbulence model near the wall can be compensated for with implemented damping functions. This model was found to predict with relative accuracy the overall HTC at Re numbers in a range of 5000÷40 000, if the turbulence intensity was high. Unfortunately, the model does not correctly describe the local HTC distribution around a circular cylinder (see Figure 8.2). First, the separation of boundary layer occurs late (far from the measured location). Secondly, the distribution of HTC in the wake flow is not in agreement with the experimental studies of various researchers.

8.4 Numerical calculation of HTC around a smooth cylinder by CFX-10.0

First, a trivial case (flow and heat transfer around a smooth cylinder) is modelled, in order to asses the predictive power of numerical simulations using Ansys CFX. It has already been mentioned that Ansys CFX is a commercial CFD code based on finite volume technique. An important issue in the accurate HTC prediction is the correct formulation of the physical model and the use of an appropriate mesh for the given problem. On the one hand, refining the mesh does not mean that the accuracy of the result improves [59], although the calculation time could increase significantly. On the other hand, the results should be independent from the grid. For this purpose, a grid sensitivity analysis is necessary for each numerical simulation.

8.4.1 Preliminary simulations – brief conclusions

More than 100 simulation cases were investigated with different meshes and physical problem sets. The most important conclusions of these simulations are described briefly in the following section.

A. Dimensions of the simulation domain

Can HTC around a smooth cylinder be calculated in a two-dimensional domain? The same physical problem was repeated in a domain with third dimension of 0.1, 0.5, 6 and 30 mm. The result was that, no remarkable difference was observed. Furthermore, simulations were made with 1, 5 and 12 elements in a third direction. It was found that the number of elements in the third direction had no influence on the solution either. Consequently, in

order to save computational time and memory resources, one-element-thick mesh is used in simulations, where the physical problem is the same in the third direction everywhere.

The two-dimensional flow field around a smooth cylinder is symmetrical along the axis for the investigated Re numbers, which contains the stagnation points. Consequently, the velocity, temperature and pressure fields are identical on both sides of the axis. Therefore, just one-half of the symmetrical, two-dimensional domain is simulated in order to save further computer resources. Figure 8.3 shows the simulation domain of the symmetrical problem.

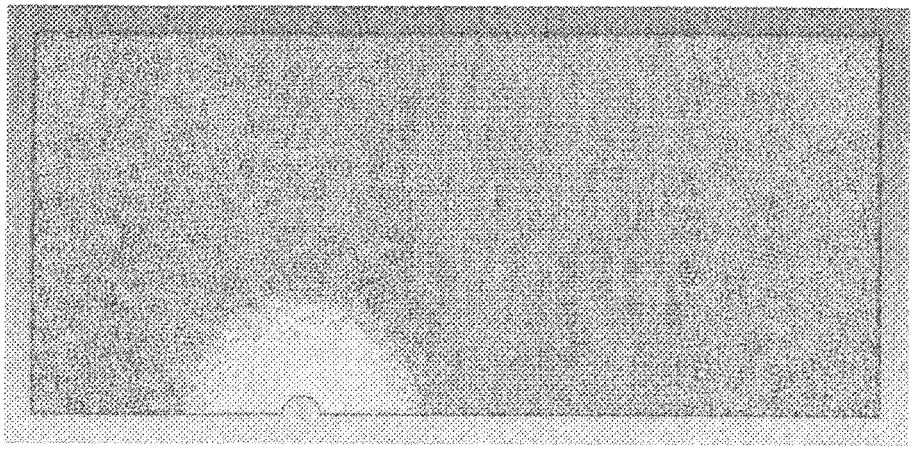

Figure 8.3 Mesh of simulation domain

B. First prism height

The first prism height near the wall is one of the critical mesh parameters, which should be correctly set to obtain accurate solutions for boundary layer separation problems using the SST turbulence model. The directives to set this parameter are given in section 8.2.2 for different wall functions. The first prism height scales with the y^+ dimensionless distance from the wall. Ansys CFX uses this parameter to judge in which region of the fluid domain

wall functions should apply and in which region Reynolds Averaged Navier-Stokes (RANS) equations should apply.

The value y^+ should be around 1, but always greater than 0.001 and lower than 2 for the SST turbulence model used with low-Re wall function [2]. This restriction assures that the first grid is placed in the laminar sub-layer of the boundary layer. For example, for simulating an airflow of 20 m/s around a circular cylinder 35 mm in diameter, the prism height of 0.003 mm was found to be too small, but 0.006 mm and 0.008 mm had already given a "correct" solution. In the following simulations, the first prism height of *0.008 mm* is used.

C. Assuring high level of accuracy

In order to obtain high accuracy calculations all normalized RMS (root mean square) and MAX (maximal) residuals were kept below 10^{-5}. Generally, this condition was reached with steady state simulation after 200 iterations. Further decreasing of the residuals had no visible influence on the solutions. However, in some cases, to reach the required residual level more quickly, the simulation was run in transient mode with an adaptive time scheme. The normalized residuals at level of 10^{-3} have influence primarily on the results in the region after the separation point. The overall flow balances were always far below 0.1%.

D. Domain mesh size

Certain differences were observed between the local HTC distribution on the lower- and upper half of the cylinder's surface when a coarser mesh was applied to the simulation domain. However, the adequate improvements (for obtaining mesh independent solution)

of the mesh in the entire simulation domain led to an extremely large number of nodes. In extreme cases, a computational time of around 3 days was reached. In order to overcome this problem, two different mesh regions were defined in addition to the boundary layer inflations. A finer mesh was applied around the cylinder in the circle of 1.5D (D is the cylinder diameter), and the coarser mesh was used in the rest of the simulation domain (a mesh size of 5 mm was found adequate). The transition between two different mesh regions was defined with an element expansion factor of 1.1 (the consecutive elements grow by approximately 10%).

E. Choosing the simulation timestep

Generally, the timestep has a strong influence on the convergence of numerical calculations. The very small timestep results in extremely slow convergence. Contrary, the large timestep leads to "bouncy" or non-convergent simulations [2]. A small timestep can be estimated as less than 1/3 of the smallest length/velocity ratio during the simulation [2]. During the simulations the Auto Timestep option was combined with Maximum timescale, in order to start the simulation with a computed conservative timestep for ensuring convergence, which is continuously recalculated after 5 iterations until the user-defined maximum value is not reached.

8.4.2 Problem definition

The geometry of the simulation domain

The airflow around a smooth circular cylinder *35 mm in* diameter (D) was simulated in a two-dimensional domain (the third dimension is one element thick). As aforementioned,

just one-half of the fluid domain is simulated due to symmetric flow field as shown in Figure 8.3. The plane containing the cylinder's axis and the two domain sides that are perpendicular to the third direction are treated as symmetry planes. The inlet is 7D, while the outlet is 15D away from the centre of cylinder. The upper domain side (which closes the fluid domain) is 10D far from the cylinder center, and it is treated as a free-slip wall. The distance of this wall from the cylinder has an influence on the fluid flow, which is known as tunnel blockage in the literature. This effect was introduced in section 7.3.2 and it is analyzed in section 8.4.4.

Physical definition

The SST (Shear Stress Transport) turbulence model, which was introduced in a previous section, was applied with Automatic wall function. The equations are solved with the Second Order Backward Euler scheme. The gravity force was not included in the mathematical model. The viscous work term was incorporated in the Total Energy heat transfer model without any radiation being considered.

Boundary conditions at the inlet:

- Airflow of 20 m/s
- Air temperature of 273 K
- Small turbulence intensity of 0.1%; dynamic and turbulent viscosity ratio (μ/μ_t) of 1

Boundary conditions on the cylinder surface:

- No-slip, smooth wall

- Heating with constant heat flux of 2000 W/m^2

Boundary conditions at the upper wall:

- Free slip condition (wall shear stress, the velocity normal component is zero)
- Air temperature of 273 K

The pressure outlet boundary condition was applied at the exit of the fluid domain.

Initial conditions:

- Air velocity 20 m/s (in direction of cylinder axis)
- Air temperature of 273 K
- All other initial parameters are calculated automatically by Ansys CFX

Air is considered as ideal gas with the following properties:

- Specific heat: 1004.4 J/kgK
- Thermal conductivity and dynamic viscosity are defined as a function of temperature based on the tabulated data found in [43].

The local heat transfer coefficient is determined from the following equation:

$$h(\alpha) = \frac{q}{T_w - T_a} \qquad \text{Eq. 8.4-1}$$

where q is the constant heat flux on cylinder surface (W/m^2), T_w is wall temperature (K) and T_a is the air temperature of the free stream (K).

The Nu number based on cylinder diameter is calculated from the local heat transfer coefficient (h) as follows:

$$Nu(\alpha) = \frac{h(\alpha) \cdot D}{k_a} \qquad \text{Eq. 8.4-2}$$

where k_a is the thermal conductivity of air (W/mK) at the temperature of free stream.

Estimating turbulence intensity at the stagnation point

The turbulence intensity (Tu in the following study) value prescribed at the inlet decreases toward the cylinder depending on the inlet eddy viscosity ratio (μ/μ_t) [2]. The local Tu downstream from the inlet can be estimated with the following formula [2]:

$$Tu = \sqrt{Tu_i^2 \left(1 + \frac{3 \cdot \rho \cdot V \cdot x \cdot \beta \cdot Tu_i^2}{2 \cdot \mu \cdot (\mu_t / \mu)}\right)^{-\beta^*/\beta}} \qquad \text{Eq. 8.4-3}$$

where Tu_i is the prescribed turbulence intensity at the inlet, V is the free-stream velocity (m/s), x is distance from the inlet (m), μ_t/μ is eddy viscosity ratio (in our case 1), and β and β^* are constants for SST model with values of 0.09 and 0.0828, respectively. Here is a short estimation for Tu at the stagnation point using the following parameters:

- $\rho = 1.2$ kg/m^3
- $V = 20$ m/s
- $x = 6.5D = 0.2275$ m
- $\mu = 1.71 \cdot 10^{-5}$ m^2/s
- $\mu_t/\mu = 1$

- $Tu_{inlet} = 0.001$

Turbulence intensity of *0.00098* is obtained at the stagnation point using Eq. 8.4-3. This represents a very low turbulence level.

Initial conditions

All simulations were started from the same initial conditions, and calculation was stopped when the maximum residuals of all equations were in the magnitude of 10^{-5}. This level of residuals was reached in most of the cases within 200 iterations.

8.4.3 Mesh independent solution, assuring mesh quality

It has already been mentioned that a sufficient resolution of the simulated domain is necessary for an accurate solution. Three different mesh regions were in the simulation domain in order to obtain a grid-independent solution in some acceptable simulation times. The grid independent solution is established by comparing the results of the two finest grids of each mesh region. These mesh regions are discussed in the following section.

Region 1: Inflated prismatic mesh elements were used to adequately resolve the boundary layer near the surface of the cylinder (see Figure 8.4 and Figure 8.5). These thin elements are able to capture the high-pressure gradients near the wall. The mesh is regularly structured. Generally, the inflation mesh quality is controlled by adjusting three parameters: thickness of elements, Δy, number of prismatic layers, N, and elements' expansion factor, E.f. It has already been mentioned that in the case under study, it is very important to keep y^+ around 1. It was found in the preliminary simulations that the

expansion factor should be in the range of 1÷1.2 and the first prism height near the wall of 0.008 mm is adequate.

In order to obtain good quality mesh, it is also important to have a smooth transition between Region 1 and Region 2. It is shown in Figure 8.4 that prismatic elements near the tetrahedral grid have unit aspect ratio (height equal to base length). During the meshing process, this transition is always examined.

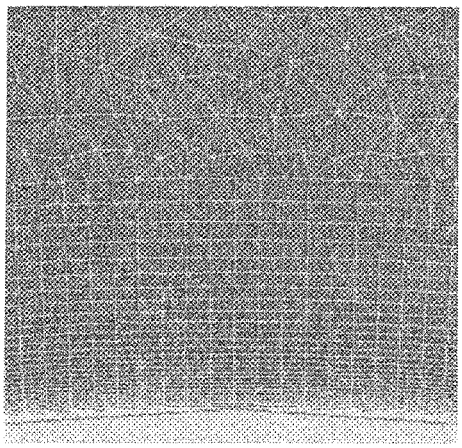

Figure 8.4 Prismatic elements near the wall

Region 2: fine mesh around inflated layers needs to be applied on the upper and lower half-part of the cylinder (see Figure 8.5) to obtain the same solution. The mesh is unstructured, which is characterized by maximum element size (s), expansion factor, and radius of influence. The element size beyond the radius of influence grows with the expansion factor away from the conductor surface until it reaches the background mesh size (this is defined in Region 3). The expansion factor should be set between 1 and 1.5 for adequate transition. It was concluded from the preliminary results that a radius of influence of 1.5D seems to be sufficient.

Region 3: the unstructured mesh is characterized by the same parameters as in Region 2. The main difference from Region 2 is that the mesh length scale should be set to the coarsest value used anywhere in the domain. A maximum mesh size of 5 mm was found adequate in preliminary calculations. This value was used by the mesher (CFX-Mesh) when it created triangles on the surfaces and a tetrahedral grid in the volume of the domain.

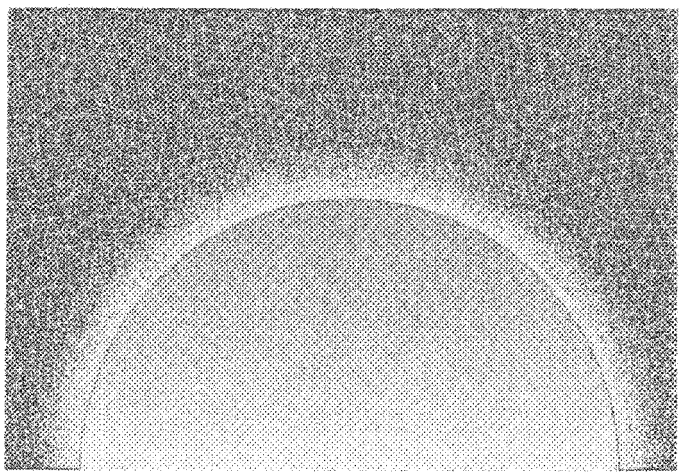

Figure 8.5 Mesh around the cylinder surface

The influence of certain mesh parameters should be analyzed to assure a correct and mesh independent solution. Therefore, the mesh parameters are refined, one by one, in each region, in order to analyze their influence on the numerical result. This is discussed in the following section.

A. Number of inflated layers

It has already been mentioned that adequately resolving the boundary layer is one of the key factors in predicting HTC. Generally, two criteria should be met. Both the first node distance from the wall and a minimum number of nodes in the boundary layer depend on the applied wall function. In the preliminary simulations, it was found (see section 8.4.3)

that the first prism height of 0.008 mm is a good value to obtain y^+ around 1 on the cylinder surface for the simulation case defined in the previous section. Figure 8.6 shows a typical y^+ distribution on the circular cylinder surface obtained with simulations using the SST model.

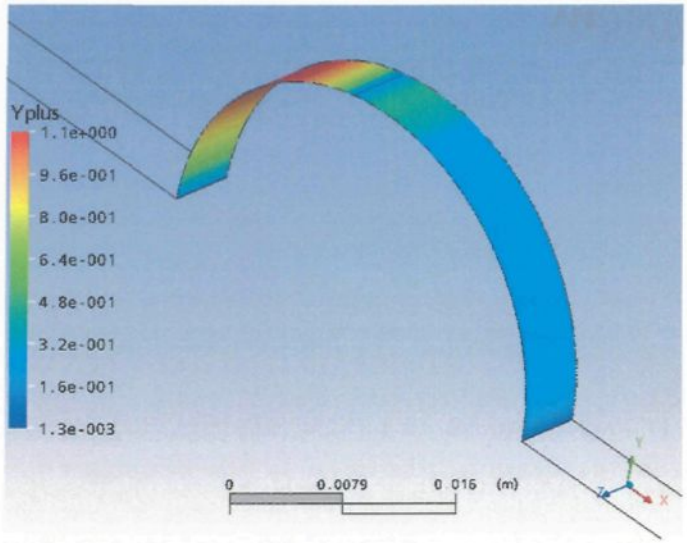

Figure 8.6 Dimensionless distance of first node (y^+) on the cylinder surface. Simulation obtained for free stream velocity of 20 m/s, Tu=1% and turbulent ratio is 1 at the inlet using the SST model.

The numerical results obtained with three different boundary layer meshes were compared. All simulations were performed for the problem introduced in detail in the previous section. One difference between the three grids is in the number of prismatic layers and expansion factors. Figure 8.7 shows the difference in the local Nu number distribution along the half perimeter of the circular cylinder. It is evident that increasing the number of prismatic layers from 20 to 28 improved the results. However, adding further layers (N=33) has a negligible effect on the calculated Nu number. Consequently, resolving the near wall region with about 28 prismatic layers was adequate. Note that the variation of

number of prismatic layers is in the range of 20÷33 and has no effect on the Nu results at the laminar boundary layer part. The differences in results appear immediately after the separation point (where the Nu number has minimum). Little difference was also observed downward in the wake (see Figure 8.7).

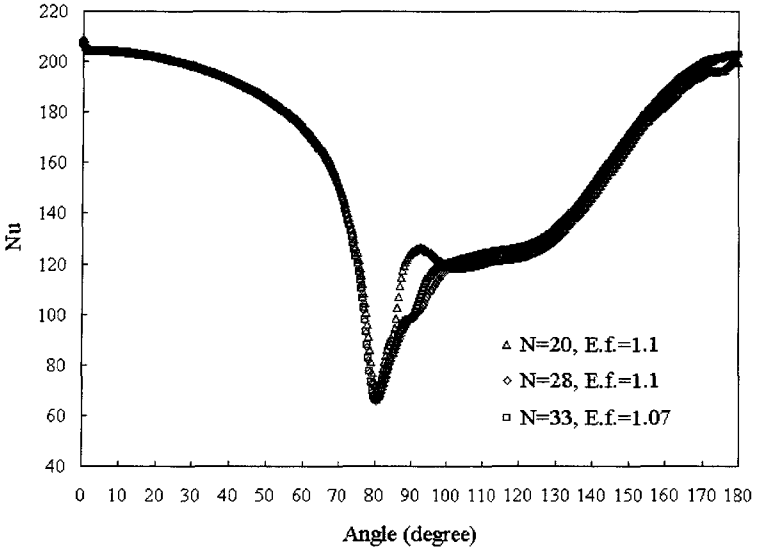

Figure 8.7 Effect of a number of prismatic layers on the solution

B. Mesh size in Region 2

In this section, the influence of the grid size in Region 2 is analyzed. For this purpose, the numerical results obtained with three different grid sizes are compared. It was observed from the preliminary simulations that improving the mesh quality around the prismatic layers significantly influenced the numerical results. Refining the mesh around the cylinder in circle of 1.5D was sufficient. The physical definition of the flow problem is identical, which was already introduced in detail in section 8.4.2. The boundary layer is resolved into 28 prismatic layers with expansion factor of 1.1.

Figure 8.8 shows that the Nu number distribution along the half perimeter of the circular cylinder obtained with the 0.5 mm and 0.25 mm grid sizes in Region 2 are identical. However, the Nu numbers obtained with a coarser grid size of 1 mm differ from finer grids on the leeward side of the cylinder. Finally, it can be concluded that a grid size of 0.5 mm in Region 2 supplies a mesh independent solution. All further refinements in the mesh have no effect on the numerical solution.

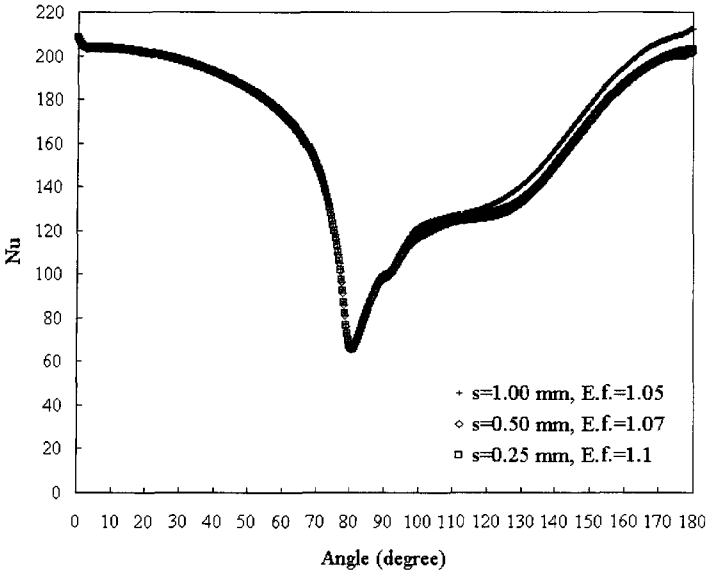

Figure 8.8 Effect of mesh size in Region 2 of the solution

C. Number of elements along the conductor perimeter

The resolution of the cylinder surface also has significant influence on the numerical solution. Obviously, the results improve with an increasing number of elements along the perimeter of the cylinder. In order to analyze the power of this influence, results are compare that were obtained with three different grid resolutions. The physical problem and the geometry problem is the same as presented in section 8.4.2. The boundary layer is

resolved with 28 inflation layers and y^+ is always lower than 1.1. A grid size of 0.5 mm is used in Region 2.

The comparison of results is shown in Figure 8.9. The element sizes analyzed were 0.1, 0.05 and 0.035 mm, which correspond to 513, 1025 and 2049 element numbers along the half perimeter of the cylinder, respectively. The grid on the cylinder surface resolved its perimeter into equal parts. The results obtained with different grid resolutions showed differences in the region after the separation point. Increasing the number of elements from 513 to 1025 lead to a more realistic Nu number distribution. Surprisingly, further increment in the element number supplied less accurate simulation results. The reason is probably that the smaller element size along the perimeter leads to a high elements aspect ratio in the inflated layers near Region 2. Naturally, this could be avoided by refining the mesh in the boundary layer and Region 2 drastically, which results in extremely expensive mesh generation and simulation time.

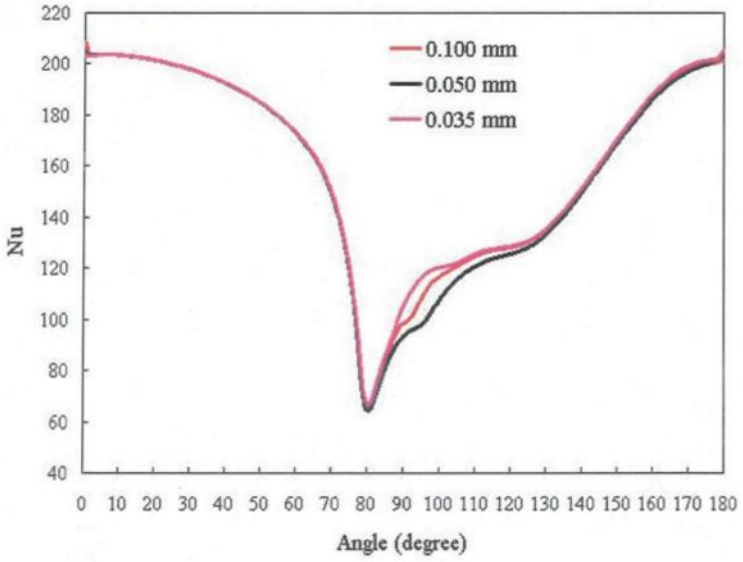

Figure 8.9 Effect of grid size on the cylinder surface

Briefly, a grid resolution of 1025 elements along the half-perimeter of cylinder supplies a quite acceptable Nu distribution. Therefore, further numerical simulations were calculated with 0.05 mm grid resolution on the cylinder surface.

8.4.3.1 Conclusions

The minimum grid requirement, to obtain mesh independent solution with less expensive computational time, are as follows:

- Inflated prismatic layers in the boundary layer: N=28, E.f.=1.1 and Δy_1=0.008 mm.
- Mesh resolution on the cylinder surface: 0.05 mm (1025 elements on the half perimeter).
- Region 2: grid size of 0.5 mm, E.f.=1.07, radius of influence around cylinder is 52.5 mm.
- Region 3: grid size of 5 mm, E.f.=1.1.

All of the following numerical calculations of flow around a smooth circular cylinder are calculated for the mesh described with the above parameters.

8.4.4 Domain size independent solution

The distance between the cylinder surface and the boundary walls (inlet, outlet and free slip wall) also influences the flow and temperature field around the cylinder. If the top side of domain is very close to the cylinder then the tunnel blockage affects the HTC distribution around the cylinder perimeter. This effect was introduced in section 7.3.2.

Also, the cylinder should be placed far enough from inlet and outlet in order to exclude the interference with the boundary conditions prescribed there.

In order to obtain results, which are not influenced by where the boundary conditions are prescribed, three different domain sizes are analyzed. The geometrical description of the analyzed domain is presented in Table 8-1.

Table 8-1 Geometrical parameters of analyzed domains

Domain	**Distance from inlet**	**Distance from outlet**	**Domain height**
Domain 1	4D	8D	5D
Domain 2	7D	15D	10D
Domain 3	10D	20D	15D

The numerical calculations are performed for the physical problem defined in section 8.4.2 and for the domain mesh described at the end of section 8.4.3. As aforementioned, all simulations were started from the same initial condition. The maximum residuals of all equations were below $2 \cdot 10^{-5}$. The numerical results of velocity-, pressure- and temperature distributions are presented in Appendix 7.1.

The previous section showed a dissimilar velocity distribution was obtained, but there was no remarkable difference in temperature field of the analyzed domains. Let us see briefly how this results in the convective heat transfer. The Nu number distribution along the half-perimeter of the cylinder is shown in Figure 8.10. It is evident that the Nu numbers obtained in Domain 1 are greater than in Domains 2 and 3, which relatively well accords with each other. This is due to increased velocity and turbulence level of the flow caused

by the tunnel blockage effect. The Nu number distribution in Domains 2 and 3 differ from each other just in the region after the boundary layer separation. However, this difference was found to be negligible when related to the increased computational time for Domain 3. Therefore, in the following section the simulation in Domain 2 is used (as in previous cases).

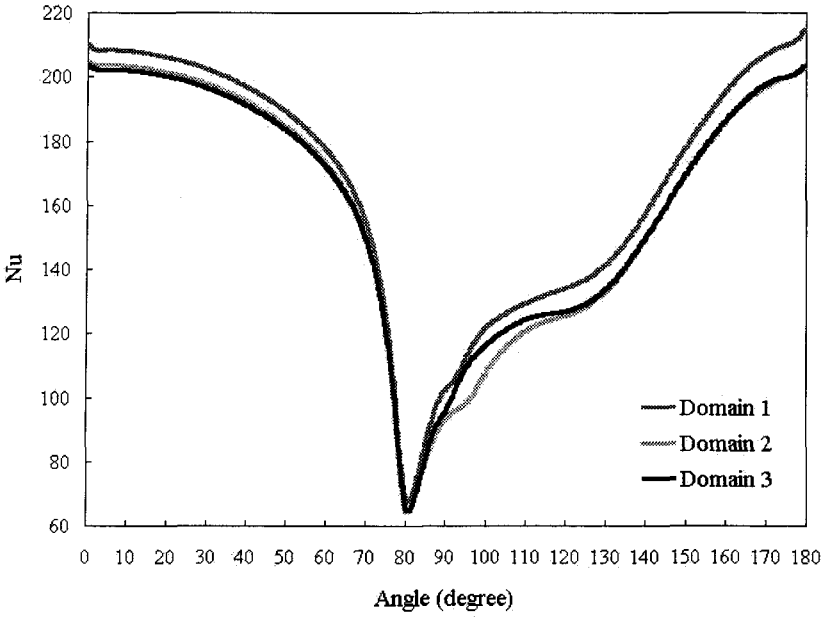

Figure 8.10 Effect of distances from the boundaries on Nu number distribution

8.4.5 Analyzing different boundary conditions on the cylinder surface

The applied boundary condition on the cylinder surface also influences HTC distribution. This effect is briefly described in section 7.3.2. The following section of the study investigates how Ansys CFX can capture this physical phenomenon as well the sensitivity of HTC numerical results on prescribed thermal boundary conditions on a cylinder surface. For this purpose, boundary conditions of the first and second kind are

compared and the effect of heat flux direction was analyzed (cooling and heating). All simulations were performed at 20 m/s free stream velocity in Domain 2. The mesh of the simulation domain and the physical problem definition is the same, discussed previously in detail. The following boundary conditions are applied on the cylinder surface:

- Boundary condition of the second kind, heating: heat flux of 2000 W/m^2.
- Boundary condition of the second kind, cooling: heat flux of -2000 W/m^2.
- Boundary condition of the first kind: constant temperature of 288 K (15 °C).

The numerical results obtained with the boundary conditions described above are introduced and briefly analyzed in the following section.

Note that in temperature plots where the range of variable is mentioned, the lowest and the highest coloured values cover the range of variable below and above, respectively. This is valid for all numerical plots in this chapter.

A. Heating with constant heat flux of 2000 W/m^2

Note that previous numerical simulations correspond to this thermal boundary condition applied on the cylinder surface. Figure 8.11 shows the temperature distribution around a circular cylinder, the surface of which is heated with constant heat flux. Obviously, the air is warmer in the thermal boundary layer near the surface and it cools down toward the free stream. The isotherms of the boundary layer and of wake flow show similarities to isotherm plots found in literature that are obtained from measurements (e.g. [53]).

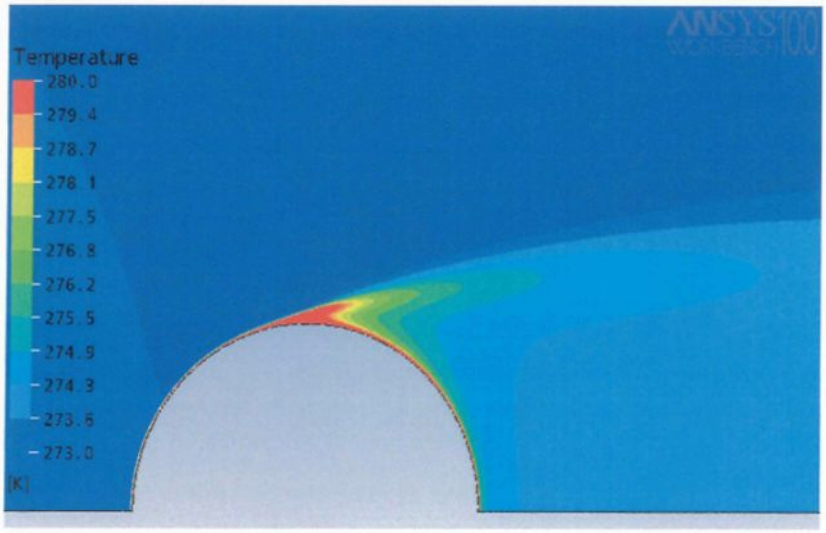

Figure 8.11 Temperature distribution around circular cylinder surface heated with constant heat flux of 2000 W/m^2 (plot in range of 273÷280 K)

B. Cooling with constant heat flux of 2000 W/m^2

Temperature distribution obtained with constant heat flux cooling shows the similar characteristics to that obtained with constant heating. Naturally, there are certain differences from the previous case since both thermal conductivity and dynamic viscosity vary slightly with the air temperature. Figure 8.12 shows the temperature of the conductor surface. The highest temperature is in the stagnation point, since there the boundary layer thickness is zero. The surface temperature decreases toward the separation point due to growth of the boundary layer thickness. It is coldest in the region of boundary layer separation. Downstream the surface temperature increases due to increased turbulence level in the wake (increased convective transport).

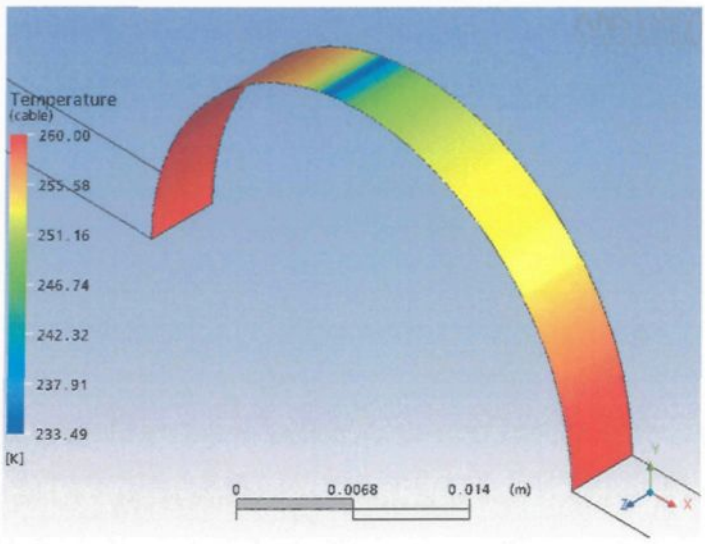

Figure 8.12 Temperature of cylinder surface at constant cooling of 2000 W/m^2

C. Constant temperature prescribed on cylinder surface (T=288 K)

The numerical result obtained with a boundary condition of the first kind (constant temperature) is shown in Figure 8.13. The main difference from the previous cases seems to be in the boundary layer separation zone by comparing Figure 8.13 with Figure 8.11. The temperature gradients in the boundary layer on constant surface temperature are smaller than gradients above constant heat flux surface.

Finally, we compare the Nu number distributions (along the half-perimeter of cylinder) obtained with different applied boundary conditions. The comparison is presented in Figure 8.14. It is shown that the heat transfer is more intensive from the cylinder surface with constant heat flux than that of constant temperature. This is in accord with theory and measurements performed by other authors. The phenomenon has already been discussed in section 7.3.2. It was mentioned that the difference between results obtained with two different kind of boundary condition is about 30 % in reference [62]. The same Nu number

is obtained in the stagnation point under the first and second kinds of boundary condition, since there the boundary layer thickness is zero.

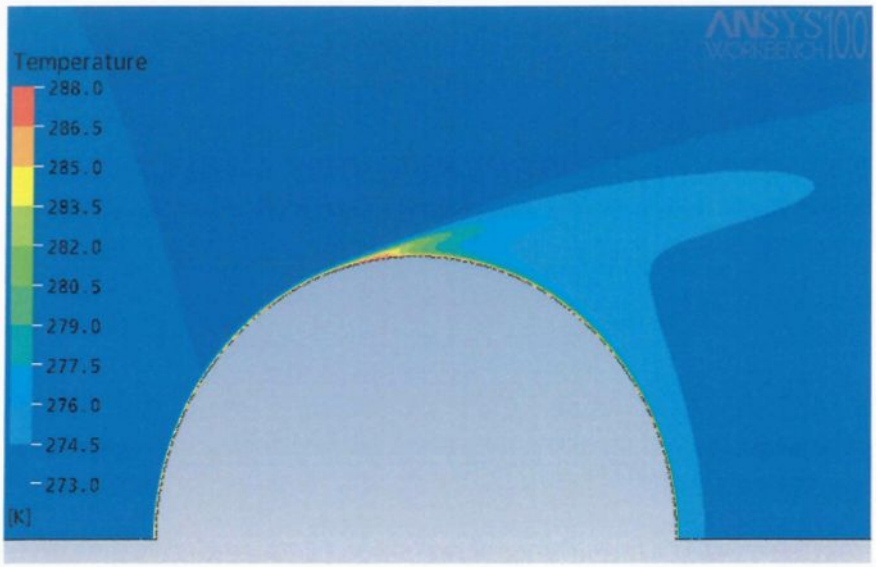

Figure 8.13 Air temperature distribution around cylinder at constant temperature of 288 K

Reference [62], based on experimental results, reports that HTC is greater for a heated surface than for a cooled surface. Consequently, the difference in Nu distribution obtained with Ansys CFX for heating and cooling with constant heat flux is a great challenge to explain, since the results in Figure 8.14 show the contrary. Note that during the numerical calculations, the dynamic viscosity and thermal conductivity of air were determined as a function of temperature. Both properties decrease with temperature (with different intensity), which results in thicker thermal and velocity boundary layers.

In the following simulations the constant heat flux heating was applied, since it approached the case of the overhead conductor best.

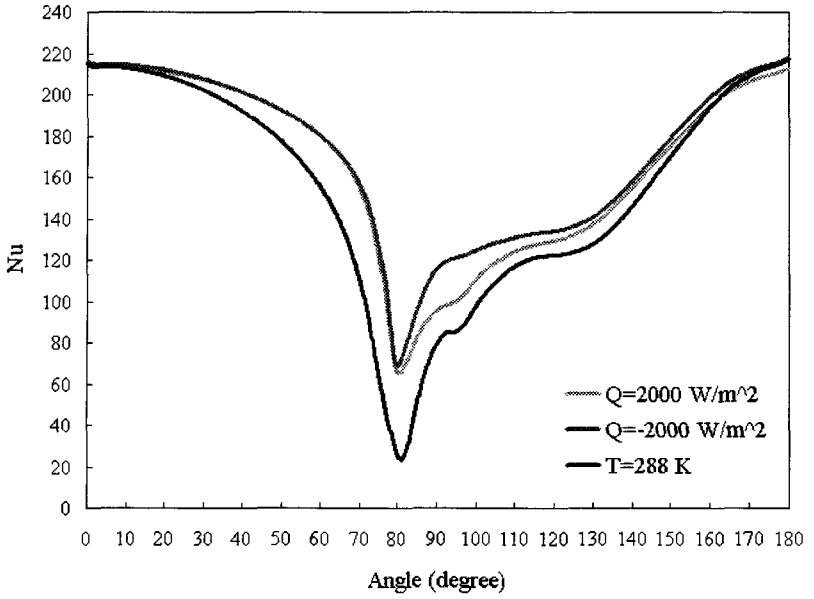

Figure 8.14 Nu number distribution around the cylinder perimeter obtained for different prescribed thermal boundary conditions

Short conclusions

- Numerical predictions of HTC, for two different kinds of boundary conditions, are in agreement with the theoretical solutions and measurement obtained by other authors. However, it seems that Ansys CFX fails the in prediction of HTC around cylinder cooled with constant heat flux.

- The thermal boundary condition of constant heat flux (heating) prescribed on the surface corresponds to the case of the electrically heated conductor. Therefore, the following simulations are calculated for this kind of boundary condition.

8.4.6 Analyzing the effect of turbulent intensity (Tu) of free stream on flow and convective heat transfer around a circular cylinder

The effect of turbulence intensity on the convective heat transfer has already been discussed briefly in section 7.3.2. In the following section, the SST model's (implemented in Ansys CFX) sensitivity on the turbulence intensity (Tu) is analyzed. In Ansys CFX, the Tu of free stream can be prescribed at the inlet, which decreases downstream of the flow. The rate of Tu decreasing is expressed in Eq. 8.4-3, introduced in section 8.4.2. Figure 8.15 shows the Tu as a function of distance from the inlet at 20 m/s free stream velocity for different inlet turbulence levels. The cylinder stagnation point is 0.225 m from the inlet.

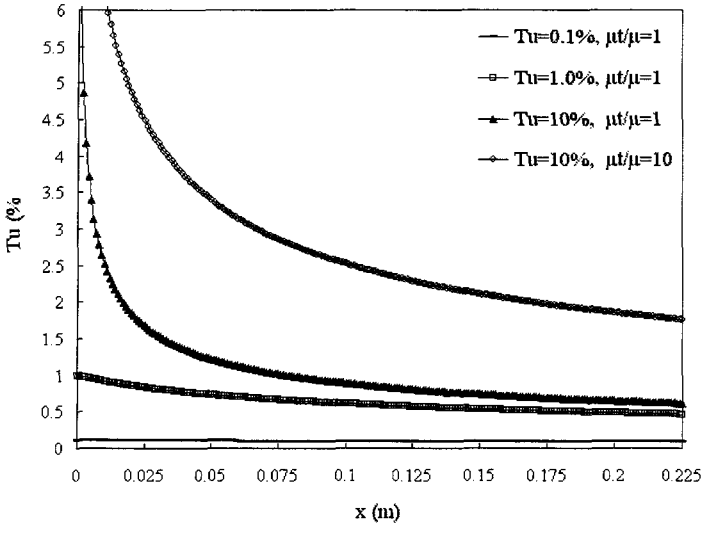

Figure 8.15 Tu as a function of distance from the inlet, in the case of 20 m/s air velocity and viscosity ratio of 1.

Numerical results obtained with four different turbulences set at the inlet are compared and analyzed. The following inlet turbulences are set: turbulence intensities of 0.1%, 1% and 10% applied with a viscosity ratio of 1, as well as 10% turbulence intensity with a

viscosity ratio of 10. These inlet turbulences decrease to turbulence intensities at stagnation points of 0.098%, 0.464%, 0.61327% and 1.76%, respectively. Note that inlet turbulences with unit viscosity ratio represent a low level of turbulences, and the research shows, their intensity values are in the same range near the cylinder.

Figure 8.16 shows the Nu number distribution around a cylinder obtained at different turbulence levels. First, it is shown that the convective heat transfer (and Nu number also) increases with increasing turbulence level of the flow. The differences are mainly observed in the boundary layer separation zone. The Nu numbers obtained at low turbulence level differ just slightly from each other in the region of boundary layer flow. In this boundary layer zone, in the flow of higher turbulence intensity (Tu=1.76%) the convective heat transfer intensity is more elevated (greater Nu). This tendency is inversed in the wake flow, where the Nu number is greater for the flow of lower inlet turbulence level. The reason is that after the separation point the turbulence kinetic energy of higher inlet turbulence is below the kinetic energy of the wake of smaller inlet turbulences. The turbulence kinetic energy distribution around the circular cylinder at different turbulence levels is presented in Appendix 7.2. It is shown in Figure 8.16 that higher turbulence intensities increase the heat transfer rate in the region of boundary layer detachment as well as the separation point relocates afew degrees downstream. It can be concluded that at higher Tu values the reattachment of turbulent boundary layer occurs at a lower Re number. The experimental measurements made by other researchers showed the same phenomena, but at higher turbulence intensities as in the cases currently under analysis. Therefore, it seems that the

SST model is overly sensitive on turbulence level of the free stream. For more numerical results obtained at different turbulence levels consult Appendix 7.2.

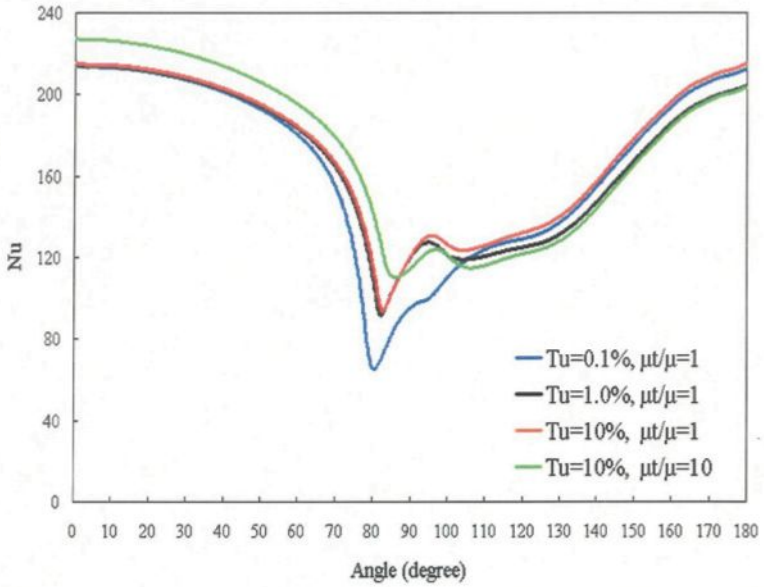

Figure 8.16 Nu number distribution around smooth cylinder at 20 m/s free stream velocity with different turbulence intensities (obtained with SST model)

8.4.7 Comparing different turbulence models

The way the turbulences are modelled is one of the key elements of predicting HTC using numerical simulations. The following section compares the three most recommended eddy-viscosity models for boundary layer separation problems, namely, the k-ω, SST and SST with Transition models.

It has been mentioned that the k-ω model predicts the length scale for boundary layer separation problems well, but it has a strong sensitivity to free stream flow. The SST model should give an accurate result for the onset and amount of flow separation of under adverse pressure gradient [3]. The capability of the SST model to model boundary layer separation

due to adverse flow near wall is shown in Appendix 7.3. Generally, the Transition model is used with turbulence models (presently SST) in order to improve their capability to predict boundary layer separation and to capture the influence of different factors (for more details see [2]). From the existing transition transport models the two equation model (the intermittency and the transition onset Re number equations) is implemented [3]. Note that this model has strict grid requirements, which should be met for correct use (for more details consult [2]).

The numerical results obtained by using different turbulence models are presented in Appendix 7.4. Simulations were performed for the physical problem in Domain 2 and with the mesh parameters already presented in sections 8.4.2 and 8.4.3, respectively. Furthermore, the predicted Nu number distributions obtained using the aforementioned three turbulence models are shown in Figure 8.17. Naturally, the surface temperature distribution (presented in Appendix 7.4) around the cylinder perimeter shows the same characteristics as the Nu number distribution.

Note that the k-omega turbulence model calculates more moderate convective heat transfer than the SST model on the conductor surface in wake flow. Probably, this is related to the fact that the calculated turbulence kinetic energy level of the wake flow is lower using the k-omega model instead of the SST model (see Appendix 7.4). It can also be seen that the SST model used with the Transition model is either overly sensitive to the free stream or just does not solve the region after boundary layer separation correctly. Finally, it can be concluded that the SST turbulence model without the Transition model predicts the convective heat transfer most closely to the measurement results from the available

turbulence models. Note that the SST model is used with low-Re wall function, where the wall damping functions trigger the boundary layer transition [2].

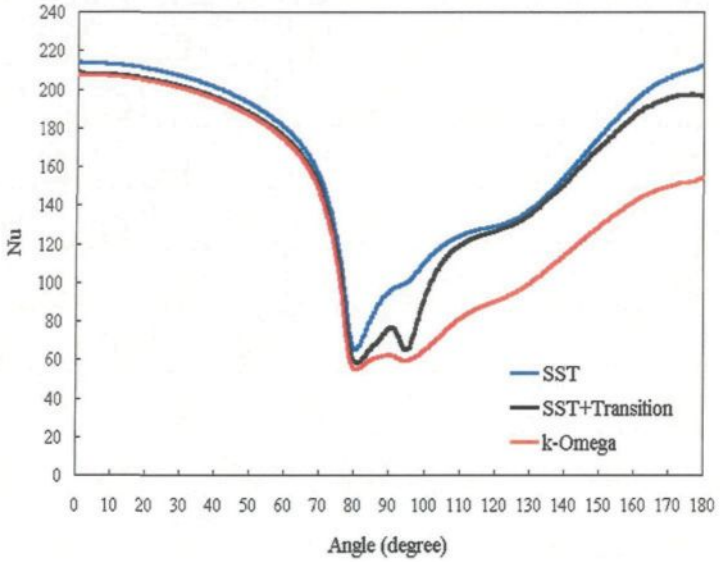

Figure 8.17 Nu number distribution obtained by using different turbulence models

It is shown in Figure 8.17 that almost all analyzed models correctly predict the location of boundary layer separation, contrary to what was observed with the k-ε turbulence model presented in section 8.3. Furthermore, the HTC distribution in the wake is much closer to experimentally observed characteristics as obtained in [30]. Consequently, the numerically calculated overall HTC is less different from the measured one. Note that the numerically predicted Nu number is *165.28* simply using the SST turbulence model with Automatic wall function at Re number of 45300.

The flow field characteristics around a circular cylinder are not the main focus of this work. However, it could be helpful to answer how accurately the actual simulation model approaches the physical phenomena. Additionally, the accuracy of the flow field strongly

influences the predicted convective heat transfer. Appendix 7.3 presents these flow characteristic including boundary layer separation, streamlines around cylinder, flow in wake and boundary layer flow. These results are obtained using the SST turbulence model with low-Re number wall formulation. Probably the most interesting part is how the adverse flow near the wall causes the boundary layer separation, since this phenomenon seems to be the most challenging task for turbulence models. Note that different turbulence models predict relatively well convective heat transfer, but they become confused in the separation zone. Once again, the SST turbulence model predicts the convective heat transfer the most accurately of the available turbulence models.

8.5 Numerical calculations of HTC around a 2D stranded conductor

In this section the effect of a stranded surface on flow field and on convective heat transfer is analysed. The conductor is not twisted, since only the influence of the surface non-uniformity (stranded surface) is investigated. Therefore, the computational domain is two-dimensional, and the geometrical parameters are similar as those used in Domain 2 for a circular cylinder. The flow symmetry to stagnation line could not be assumed (as for a smooth circular cylinder), since the flow around stranded conductors can to become unstable.

The meshing procedure of the simulation domain is strongly based on the optimized grid of the smooth cylinder simulation. The numerical results obtained with those optimized mesh parameters are already validated and have shown the potential to correctly resolve the

fluid domain for the given physical problem. Grid distortion was carefully avoided around the stranded surface during the meshing procedure. For this reason, the mesh near the surface was carefully analyzed during the grid generation. The grid near the stranded surface is shown in Figure 8.18. Consult Appendix 7.5 for more details about the simulation domain mesh.

The geometry of stranded conductors

The two-dimensional stranded conductor has an outer diameter of 35.17 mm. This value is very close to the diameter of the investigated smooth circular cylinder. The outside of the conductor consists of 20 strands with a diameter of 4.7 mm.

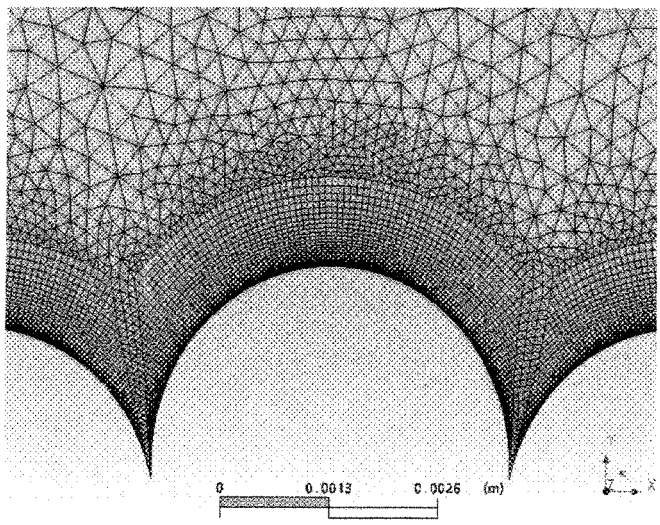

Figure 8.18 Mesh near stranded surface

Mesh parameters

As for the circular cylinder, the domain mesh can be divided into three regions. These regions were generated using the following parameters:

- Inflated prismatic layers for the boundary layer: N=28, E.f.=1.07 and Δy_1=0.008 mm.
- Mesh resolution of stranded surface: 0.05 mm (1025 elements on half perimeter).
- Region 2: grid size of 0.5mm, E.f.=1.08, influence radius around conductor is 52.5 mm.
- Region 3: grid size of 5 mm, E.f.=1.1.

The mesh generated around the stranded surface must meet the requirement that y^+ is in the range of 0.001÷2. This is proven in Figure 8.19.

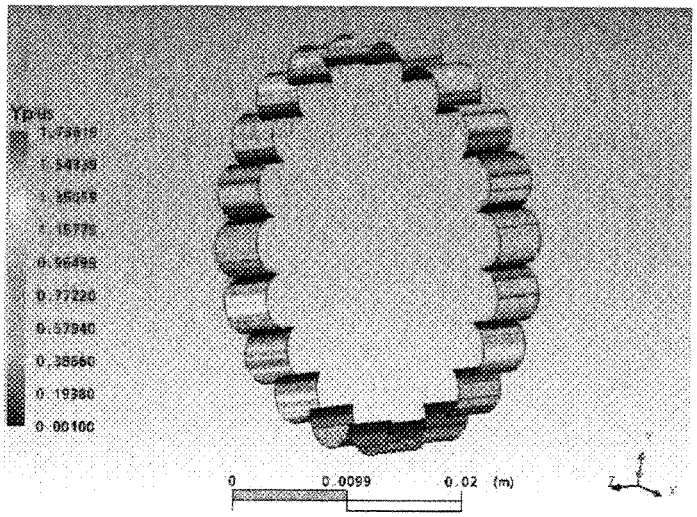

Figure 8.19 y^+ distribution around stranded conductor at 20 m/s using the SST model

The physical problem definition is the same as for the smooth circular cylinder as described in section 8.4.2. Consequently, the 20 m/s free stream velocity now corresponds to a Reynolds number of 45520 based on outer diameter, which just slightly differs from

that of the circular cylinder simulation. This simulation case is presented in the following section.

Note that the same simulation was also repeated for a smaller stranded conductor. This case corresponds to a Reynolds number of 41028 at 20 m/s free stream velocity. The numerical results of this simulation are presented in Appendix 7.6.

8.5.1 Flow and convective heat transfer around stranded conductor at Reynolds number of 45520

The simulation was run in transient mode, which was started from the initial guess obtained from a very short (20 iteration steps) steady simulation. The results of transient simulations were continuously analyzed and the consecutive results were compared. The transient simulation was considered to reach the steady state when the consecutive results correspond to each other in a certain range. The main steps of this comparison procedure based on velocity and corresponding temperature distribution are presented in Appendix 7.6. The velocity and temperature fields obtained at 0.005 s transient time slightly differ from those at 0.0018 s. The differences between consecutive time steps disappear after 0.005 s transient time, since no remarkable differences were observed after comparing with results obtained at 0.007 s. The finale velocity and temperature distributions are shown in Figure 8.20 and Figure 8.21.

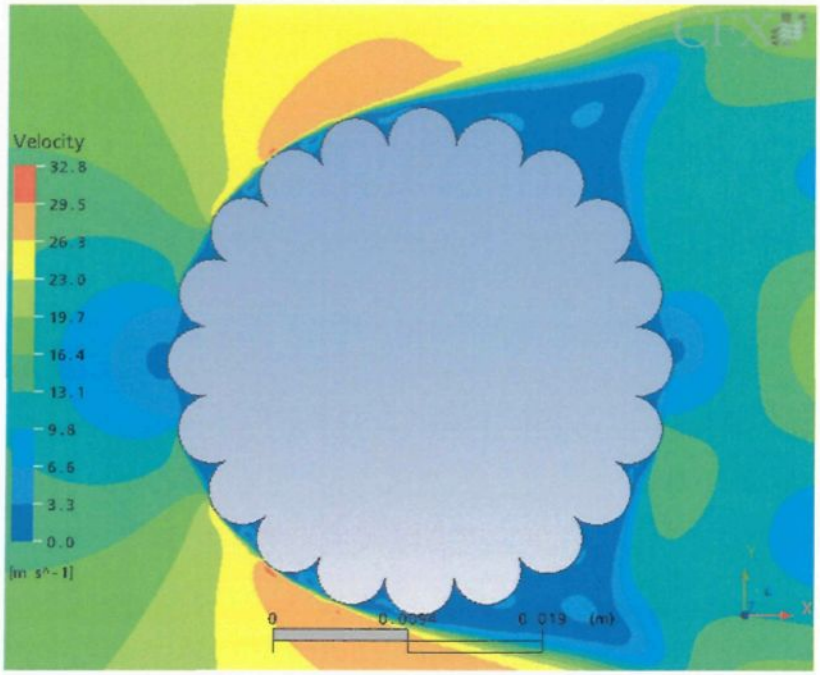

Figure 8.20 Velocity distribution of airflow around stranded conductor after 0.007 s transient simulation time

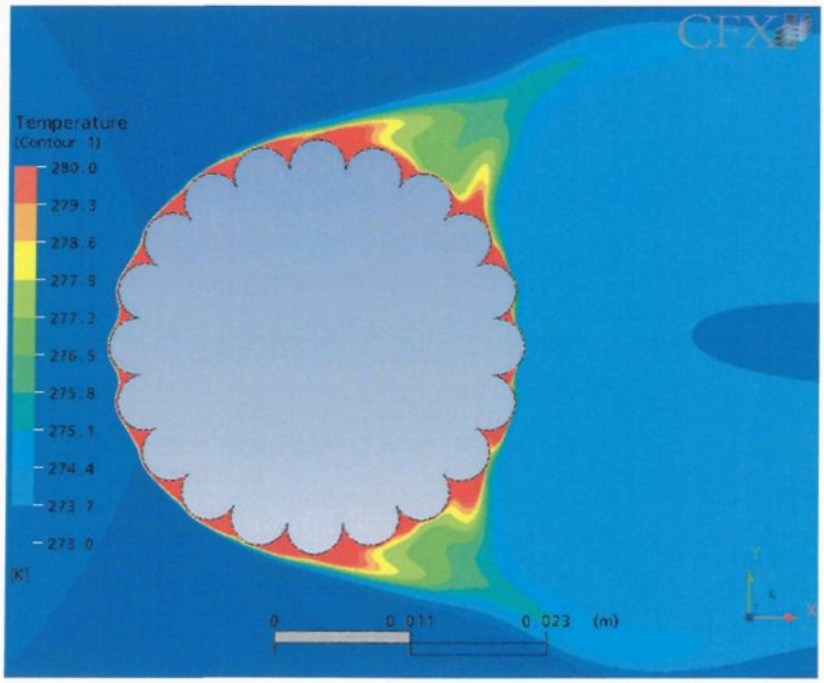

Figure 8.21 Air temperature distribution near stranded surface after 0.007 s

Figure 8.20 demonstrates that the velocity is very slow in the "V" channels between adjacent strands. Consequently, the air is warmest in these channels (see Figure 8.21) and the conductor surface temperature also has a maximum value here (see Figure 8.23). However, low intensity swirls can be observed in surface channels, which are separated from the main boundary layer flow. The direction of swirling flow in surface channels depends on their position along the perimeter. In the front part of the cylinder, from the stagnation point (at 0°) to the boundary layer separation (near 90°, see Figure 8.22), the swirling flow in channels takes a similar form. It is simply a detached eddy from the main stream (see Appendix 7.6). From strand six (at 90°), there are two (in one case three) eddies/swirls rotating inversely to each other. These airflows in the channels are covered in detail in Appendix 7.6.

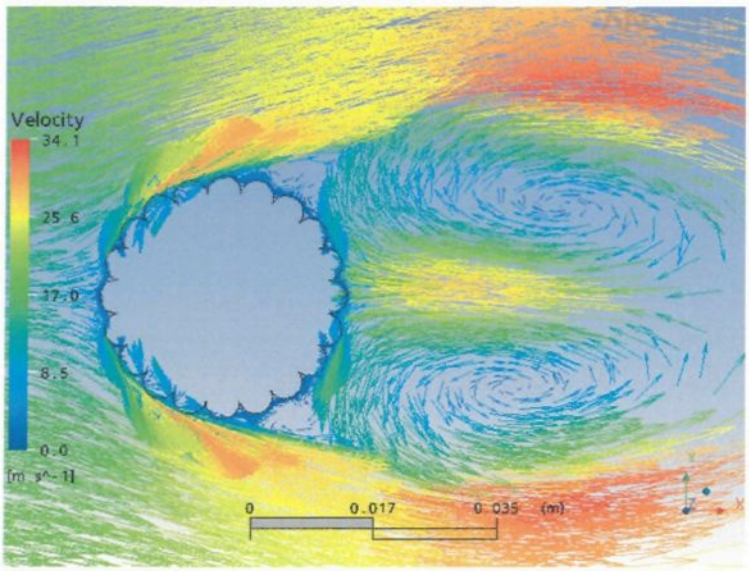

Figure 8.22 Flow field around stranded conductor (2D vector plot)

The thickness of the thermal boundary layer varies along the perimeter of the conductor. Obviously, its thickness is at its maximum at the contact point of adjacent

strands and is thinnest near the top of each strand. The absolute maximum thickness of the thermal boundary layer is observed just after the boundary layer separation (see Figure 8.21).

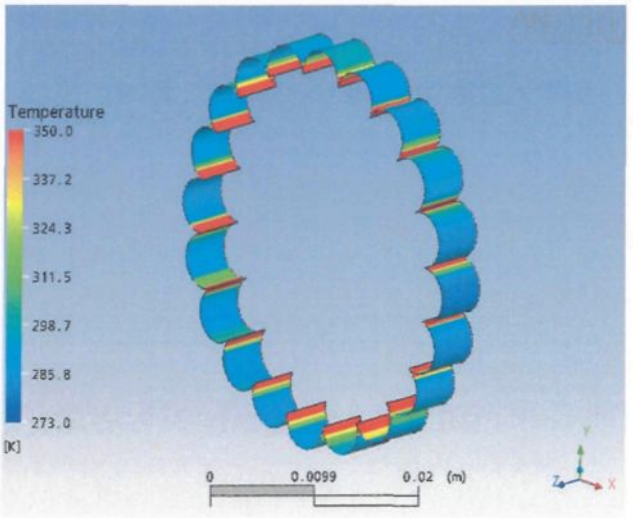

Figure 8.23 Temperature of stranded conductor surface after 0.005 s transient time in a range of 273÷350 K

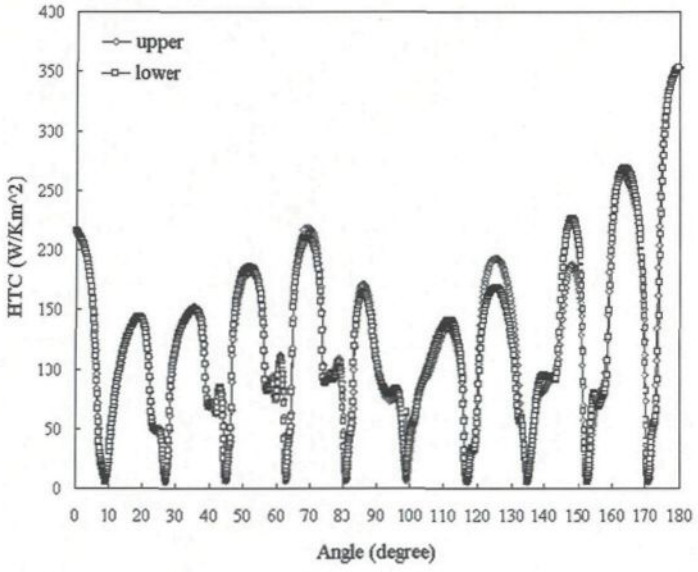

Figure 8.24 Heat transfer coefficient distribution around lower and upper part of stranded conductor at Re number of 45 520 (zero degree is in stagnation point)

The heat transfer coefficient (HTC) is predicted from Eq. 8.4-1 and the Nu number distribution from Eq. 8.4-2 (as for circular cylinder). The HTC distribution around the upper and lower half-perimeters is shown in Figure 8.24. Certain differences may be observed in the comparison of two HTC distributions.

The main difference occurs at strands eight and nine (if the first strand is in the stagnation point) located in region of 120÷150°. The HTC is higher on strand eight in the upper half than on the same strand in the lower half of the conductor. The opposite happens on strand nine, where HTC is higher on the lower part than on the upper half-perimeter (see Figure 8.24). In the following section, the Nu number distribution on the upper half-perimeter is analysed.

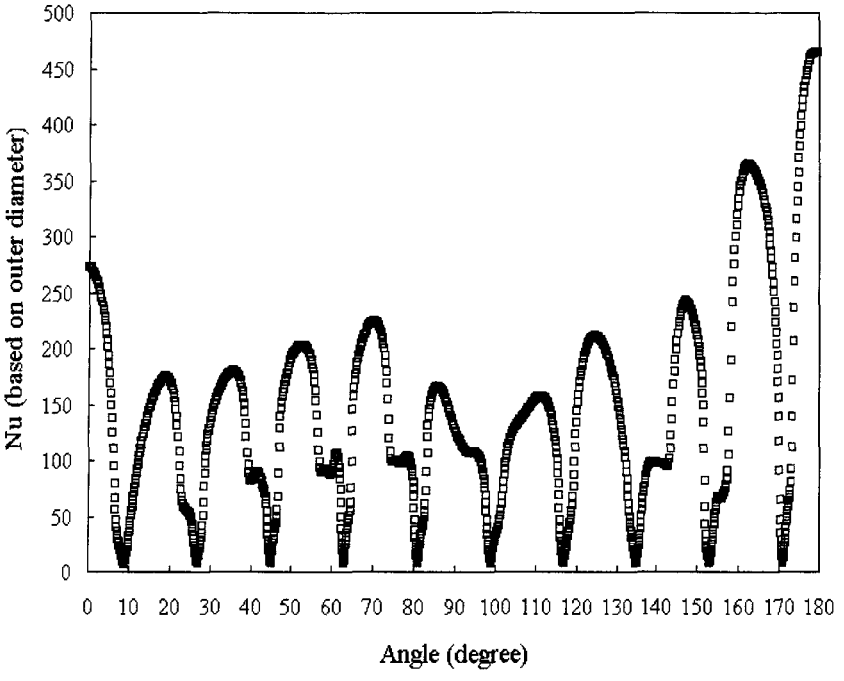

Figure 8.25 Nu number (based on conductor outer diameter of 31.7 mm) distribution around upper part of stranded conductor surface at Re number of 41 028

Figure 8.25 shows the Nu number distribution around the upper half-perimeter of the stranded conductor at a Reynolds number of 41028. The distribution characteristics are the same as shown in Figure 8.24; the differences are just in values of the Nu numbers. It is shown that the convective heat transfer shows periodic characteristics; the periodicity is after each strand. The local maximum values are near the top of strand, since there the thermal boundary layer thickness has a local minimum. The Nu number decreases toward the contact point with the adjacent strand due to decreasing velocity, and afterwards it increases until the top of the next strand. The distribution between two adjacent strands is not symmetrical at the point of contact due to recirculation in the channel. However, this non-symmetrical form shows certain regularities depending on the direction of swirls. Note that the largest local Nu is at the location of the rear stagnation point.

Surprisingly, the calculated overall Nu number based on the outer diameter is *164.59* at Re number of 45520. This value is almost the same as that obtained for smooth circular cylinder (overall Nu of *165.28*). It is well known that the surface roughness increases the convective heat transfer in both external and internal flows, since the flow becomes more turbulent. This can be observed near the top of each surface strand. However, in our case the air seems to get trapped in the surface channels. Naturally, this decreases the convective heat transfer rate. Probably, these two adverse phenomena affect the overall heat balance with the same intensity in airflow at a Re number of 45520.

8.5.2 Stable and non-stable flow fields at Re number of 41028

Occasionally, for the identical simulation case (physical definition, grid and geometry) different numerical solutions can be obtained depending on the initial conditions. As aforementioned, numerical simulations were performed for a stranded conductor of 31.7 mm at 20 m/s free stream velocity. These calculations were obtained in two different manners. In both cases, the simulations were first run in steady mode to obtain an initial guess for transient calculations. In one case, the steady simulation was made in 17 iteration steps, while in other case it was in 77 iterations. The conclusion was that in steady state mode the convergence of equations cannot be reached, contrary to simulations of flow around a circular cylinder.

Therefore, the simulations were calculated in transient mode with Adaptive time scheme. The transient numerical schema showed good convergence, and finally all residuals were below $2 \cdot 10^{-5}$ with imbalances less than 0.1%.

The calculation performed with short steady simulation results in an almost perfectly symmetrical flow field. The corresponding temperature field is shown in Figure 8.26. More numerical results and details of this simulation case are available in Appendix 7.7. Surprisingly, the numerical results obtained from simulation started from long steady iteration are quite different. Figure 8.27 shows the obtained non-stable temperature distribution; for more numerical results of this simulation case see Appendix 7.8. The main difference between the two cases is in the wake flow. The obtained non-stable flow field shows the characteristics of Karman's vortex flow, but without periodicity of boundary

layer separation. It seems that the separated boundary layer from the lower half dominates on the separation from other half. This dominating behaviour is present in the steady solution, which is obtained by comparing the consecutive transient results.

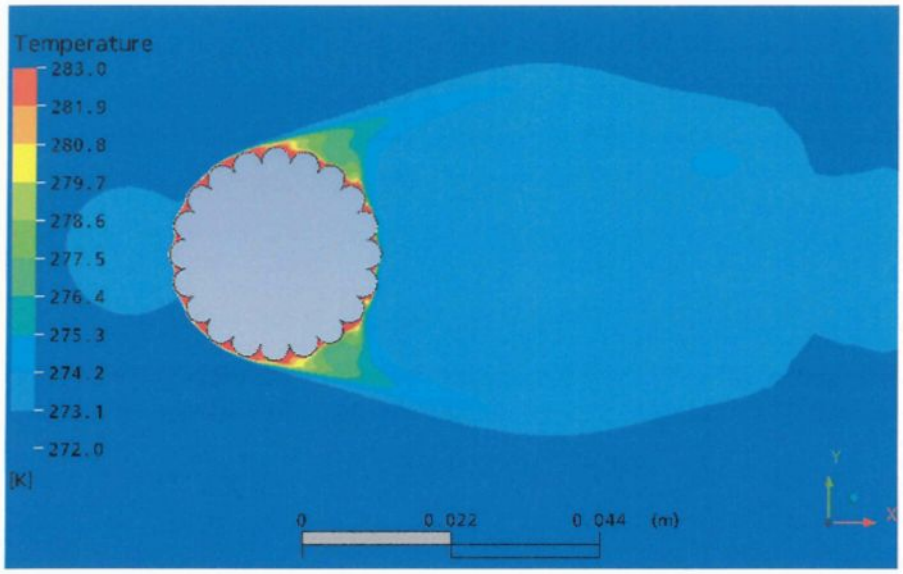

Figure 8.26 Air temperature of stable flow around stranded conductor in range 272÷283 K

Obviously, the non-stable flow field is obtained due to an "irregular" initial guess obtained from long non-converging steady simulation. However, this "irregular" initial guess could approach the outside flow field around overhead conductors. Consequently, it is interesting to study how this unstable solution works out in the convective heat transfer. The local convective heat transfer distributions for both cases are presented in Appendix 7.7 and Appendix 7.8. The conclusion after comparing the two convective heat transfer distributions is that the only remarkable difference in the characteristics is at the rear stagnation point. Additionally, the calculated overall Nu number is somewhat greater for stable flow *(Nu of 146.7)* as that obtained for non-stable flow *(Nu of 138.2)*.

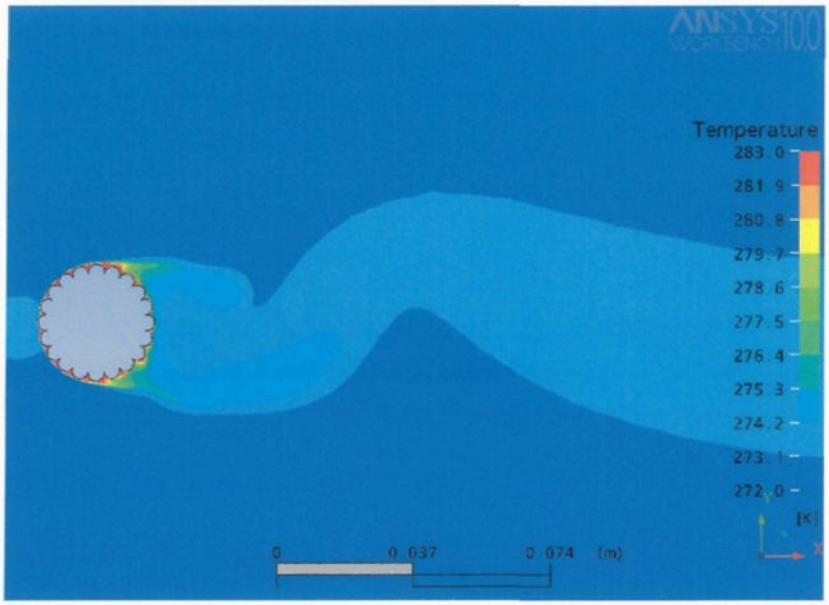

Figure 8.27 Air temperature distribution of non-stable flow around stranded conductor in range of 272÷283 K

In short, the flow field around a stranded surface is very sensitive to the initial condition, and the non-stable results correspond probably better to outside wind conditions.

8.6 Numerical predictions of HTC around twisted, stranded cable

The overhead conductors of power lines are not just stranded, but twisted along their length. This means that in reality the airflow around the conductor is three-dimensional. This chapter consist of a quantitative analysis of the effect of twisted, stranded surface.

8.6.1 Numerical calculation

Obviously, the computational domain should be three-dimensional (contrary to the previous simulations) in order to capture the twisting effect (see Figure 8.28). This leads to a computational domain with an extremely large amount of nodes, if the meshing is performed with the previously optimized parameters for the correct prediction of HTC. Generally, the previous two-dimensional simulations required around $1.7 \cdot 10^5$ elements. If the same mesh parameters are applied to a three-dimensional domain, the thickness of which is equal to one lay length, then approximately 10^8 elements are obtained. Solving the mathematical model on this grid of extremely large elements requires very powerful computer resources (for example, more processors connected in parallel with extremely large memory capacity, which is not available to the candidate. Additionally, even with very powerful resources the computational time would be very expensive.

However, numerical results can also be obtained on poorer mesh, which can help to analyze the characteristics of the flow field around a stranded, twisted conductor (without predicting the convective heat transfer). Therefore, qualitative numerical results could be obtained with a single processor computer as well. It was analyzed that the given numerical

simulation could still be solved on the mesh containing $2 \cdot 10^6$ elements with existing computer resources.

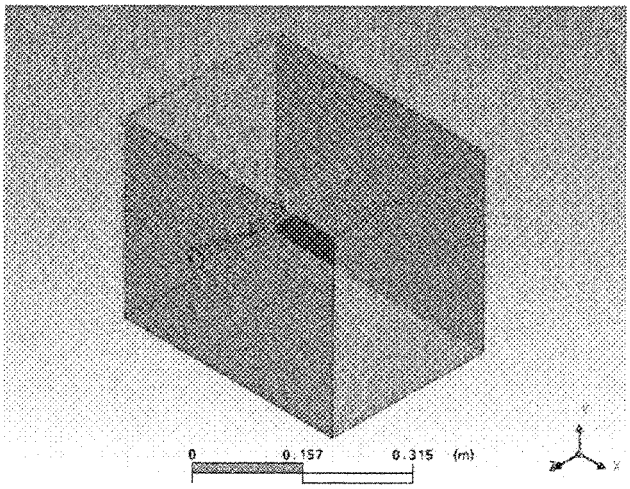

Figure 8.28 Computational domain of airflow around twisted conductor

Domain mesh

Two mesh regions are defined in the computational domain. The size of background hexagonal elements is maximum 7 mm. The fluid domain near the conductor surface is also refined with hexagonal grid. The size of the refined elements on the stranded surface is 1 mm, which increases toward the background mesh with a factor of 1.2 (20%). Figure 8.29 shows the domain mesh near the stranded surface and the transition between two mesh regions.

Physical problem definition

The physical problem definition is very similar to the previously described simulation cases. The SST turbulence model was used together with Automatic wall function, which were solved with the Second Order Backward Euler scheme. The gravity force and

radiation heat transfer were not considered during the simulation. The Total Energy heat transfer model was used, in which a viscous work term is incorporated. The materials properties are the same as in previous numerical calculations. The following boundary conditions apply.

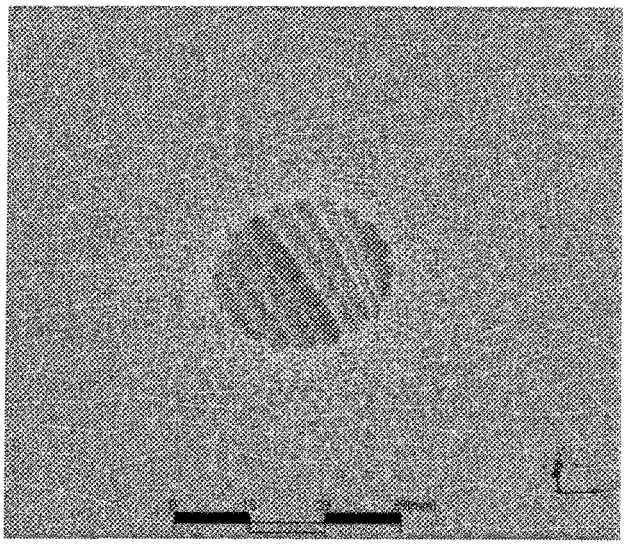

Figure 8.29 Increased mesh density near stranded surface

Boundary conditions at the inlet:

- Airflow of 20 m/s
- Air temperature of 273 K
- Small turbulence intensity of 0.1%, dynamic and turbulent viscosity ratio (μ/μ_t) of 1

Boundary conditions on cylinder surface:

- No-slip, smooth wall
- Heating with constant heat flux of 2000 W/mK^2

Boundary conditions at upper wall:

- Free slip condition (wall shear stress and the velocity normal component is zero)
- Air temperature of 273 K

Boundary conditions on side walls (containing conductor sides):

- Free slip condition
- Adiabatic wall

The pressure outlet boundary condition was applied at the exit of fluid domain.

The simulation was run in transient mode, which started from an initial guess obtained from steady calculation. The maximal residuals (MAX) of each equation were below $4.6 \cdot 10^{-5}$, generally in a magnitude of 10^{-7} after a simulation time of 40 hours.

8.6.2 Numerical results, flow field characteristics

In the following section, the three-dimensional flow characteristics are discussed. It is expected that the flow field around a twisted-stranded conductor is in some manner also "twisted", since the airflow follows the form of surface. This phenomenon cannot be observed on the windward side of the flow, but on the leeward side just after the boundary layer separation. This is shown in Figure 8.30 through Figure 8.32. On the windward side, the inertia forces govern the flow path since the velocity is high enough. Here the frictional forces are negligible to inertia forces. The velocity decreases on the leeward side, and therefore the inertia forces also decrease. Consequently, the frictional forces are not negligible in this part of conductor and the streamlines follow the form of the surface.

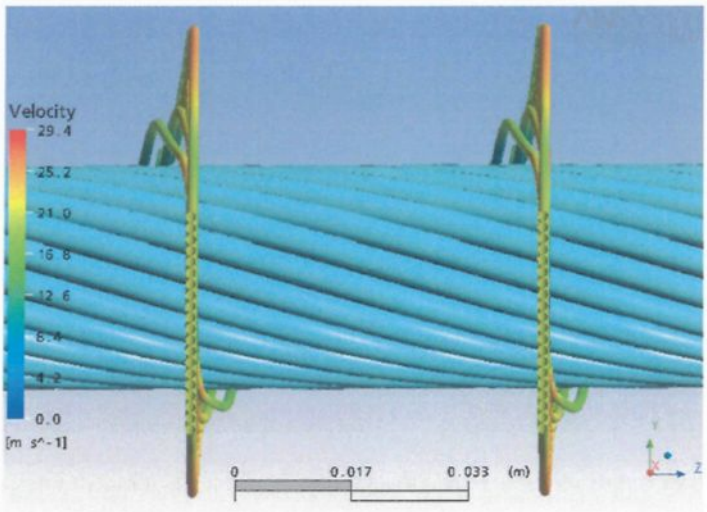

Figure 8.30 Streamlines at windward side of the conductor

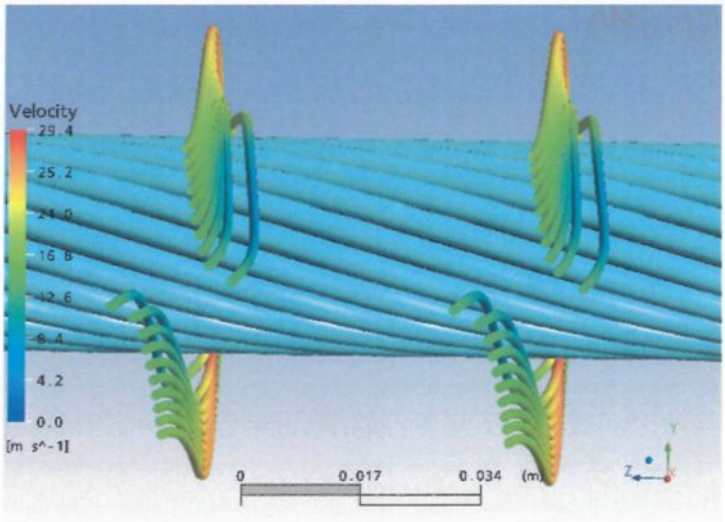

Figure 8.31 Streamlines at leeward side of the conductor

Figure 8.31 and Figure 8.32 show clearly that the streamlines lean out of the opposite direction on top and bottom of conductor, depending on the actual twisting direction. The same phenomenon was demonstrated with the tuft visualization technique in section 7.4 as well as in APPENDIX 5. Consequently, the flow characteristics obtained from numerical simulations are in agreement with the experimental observations.

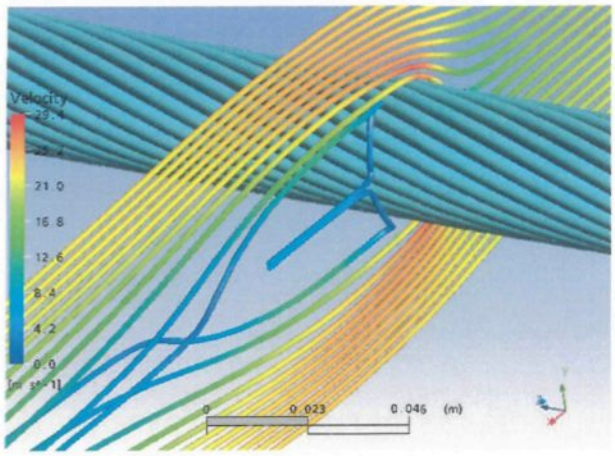

Figure 8.32 Streamlines at leeward side of the conductor

Figure 8.33 and Figure 8.34 show the calculated velocity and temperature fields around the twisted conductor in the center plane of the calculation domain. Certain differences may be observed from results obtained in two-dimensional simulations. First, the maximum of the velocity field is lower in the case of 3D calculation (28.5 m/s) than for 2D (32 m/s). Second, both the velocity and thermal boundary layer thicknesses seem to be thicker on the top of strands.

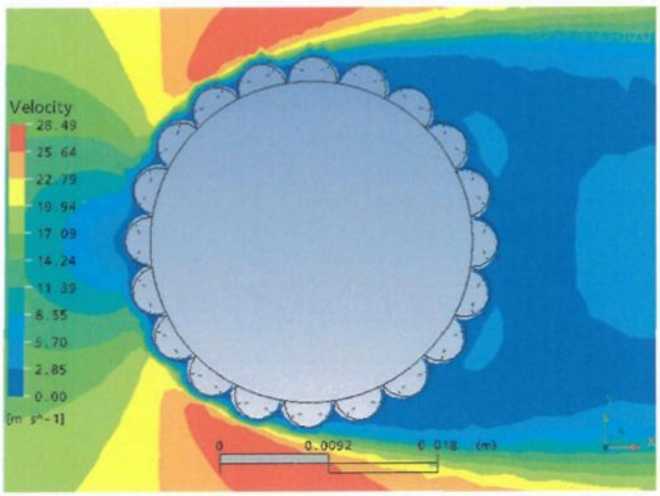

Figure 8.33 2D velocity field around twisted conductor in center plane of domain (z=0.15m)

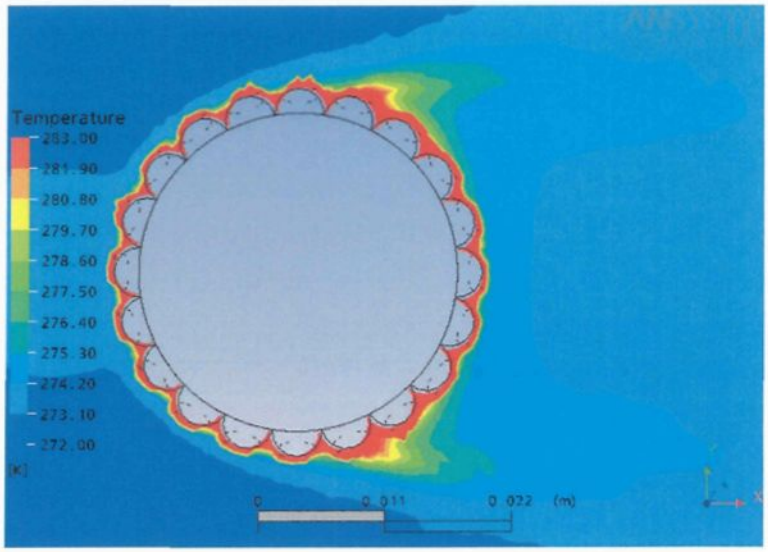

Figure 8.34 Temperature distribution of air in range of 272÷283 K (z=0.15 m)

8.7 Comparing the convective heat transfer results

This section is a brief overview and comparison of convective heat transfer coefficient proposed by both the candidate and other researchers obtained through different methods and probably under different conditions.

8.7.1 Overall HTC results for smooth conductors

Table 8-2 shows the overall Nu numbers obtained from correlations proposed by certain researchers as well as those calculated from numerical simulations performed by the candidate. The different results are compared to the numerically predicted overall Nu obtained for low turbulence intensity (appr. 0.1%) airflow past a smooth circular cylinder surface of constant heat flux (using SST turbulence model). This reference case is denoted with superscript * in Table 8-2. The difference is defined as follows:

$$\Delta = \frac{Nu - Nu^*}{Nu^*} \qquad \text{Eq. 8.7-1}$$

where Nu* is the overall Nu number of the reference case.

It is shown in Table 8-2 that generally the numerical results overpredict the overall Nu number compared to experimental results obtained by other researchers. The only exception is that obtained using the k-omega turbulence model, but this value was obtained from local HTC distribution, which differs significantly from experimental observations after boundary layer separation occurs.

The correlation proposed by Sanitjai and Goldstein [55] is one of the most recent (in Table 8-2). This is a correlation developed from the local heat transfer data, while previous correlations are based on the overall heat transfer measurements. This correlation supplies the greatest Nu number from all those based on the experiments. Obviously, the difference comes from how precisely the local heat transfer distribution is measured. Sanitjai and Goldstein [55] used eight thermocouples to measure the surface temperature, and they got greater Nu number than if they had used just one. Consequently, one may ask: Will the overall Nu number increase if the surface temperature is measured in more points along the perimeter? Probably yes, but the decreasing rate will be smaller with increasing measurements along the perimeter. This is approved by the numerical calculations, where the cylinder half-perimeter is resolved on 1025 calculation points. The result is a higher Nu number and the difference is just 4.5% between them (see Table 8-2). This difference is smaller than that between overall Nu obtained from one and eight surface temperature measurements. Naturally, we should recognize also that a 4.5% difference between

experimentally and numerically obtained Nu numbers may arise from an influencing effect during the measurements (see section 7.3.2) and/or from approximations of turbulence models as well as numerical residuals (see section 8.2).

Table 8-2 Overall Nu numbers at Reynolds number of 45 300

Author	Method	BC	Tu (%)	Δ (%)	Nu_{mean}
Churchill and Bernstein	Experimental	-	-	-21.9	129.2
Hilpert	Experimental	-	-	-18.8	134.2
Sanitjai and Goldstein	Experimental	q=cts.	0.3	-4.10	158.6
Whitaker	Experimental	-	-	-15.4	139.9
Zhukauskas	Experimental	-	<1	-17.2	136.8
Candidate*	Numerical, SST model	q=cts.	0.1	0	165.3*
Candidate	Numerical, SST model	T=cts.	0.1	-7.2	153.5
Candidate	Numerical, SST model	q=cts.	1.76	+4.5	172.7
Candidate	Numerical, k-ω model	q=cts.	0.1	-16.4	138.2

It is also seen from Table 8-2 that the numerically calculated Nu numbers for higher turbulence intensity of free stream and applied boundary condition of the first kind on the cylinder surface are in agreement with theoretical and experimental studies. Namely, turbulence intensity increases the convective heat transfer, while the overall Nu number is smaller for constant temperature surface as for constant heat flux.

It can be concluded that numerical predictions of the overall Nu number around smooth circular cylinders are in agreement with measurements and are recommended for developing correlations for a wide range of airflow.

8.7.2 Overall HTC for stranded conductors

In the previous section it was shown that the numerical predictions accord well with measurements for smooth circular cylinders. In the following section, the numerical and experimental Nu numbers obtained by the candidate for stranded conductors are compared. Furthermore, these values are compared to those calculated with equations 5.3-4 and 5.3-5. The experimental values are calculated at the appropriate Reynolds number from the correlations that is based on the experimental study. During the measurements and numerical simulations the free stream turbulence intensity was below 0.1%. The comparison is presented in Table 8-3.

It can be seen that the numerical and experimental overall Nu numbers are quite different. These differences may come from various reasons. First, as aforementioned, the experimental results obtained with Carillon and Condor conductor supply greater convective heat transfer, since these test conductors lost their strength and let air pass between adjacent strands. Secondly, the correlation offered by V.T. Morgan is probably not very accurate in this range of Reynolds numbers and for this type of "roughness". It was not clear from [41] how the correlation was obtained, but it seems to be developed from measurements with different stranded conductors of various roughness ratios basically at Reynolds number in a $100 \div 2 \cdot 10^4$ range.

Table 8-3 Overall Nu numbers for stranded conductors in cross-flow of air

Author	Method	Conductor	H_r/D	Re number	Nu_{mean}
V.T. Morgan	Experimental	Beaumont	0.078	41 028	242.9
Candidate	Experimental	Carillon	0.0751	41 028	209.2
Candidate	Experimental	Condor	0.0625	41 028	196.9
Candidate	Experimental	Geant 5P	0.0625	41 028	119.0
Candidate	Experimental	Drake	0.0938	41 028	160.0
Candidate	Numerical	Beaumont	0.078	41 028	146.7 (138.2*)
V.T. Morgan	Experimental	Bersimis	0.077	45 520	271.7
Candidate	Experimental	Carillon	0.0751	45 520	232.2
Candidate	Experimental	Condor	0.0625	45 520	218.5
Candidate	Experimental	Drake	0.0938	45 520	177.5
Candidate	Experimental	Geant 5P	0.0625	45 520	132.0
Candidate	Numerical	Bersimis	0.077	45 520	164.6

* Non-stable solution.

Comparing the rest of results, it can be concluded that the overall Nu number increased with surface roughness or surface non-uniformity. However, it should be noted first that the experimental results obtained by the candidate are calculated from one single temperature measurement in the stagnation point. Secondly, the numerical predictions were made for stranded, but not twisted conductors. Therefore, the third-dimensional effect (twisted flow) is not included in numerically obtained convective heat transfer.

More experimental and numerical work is required in order to formulate a more general correlation, in which the roughness ratio of a stranded surface is included; furthermore, it is valid in a wide range of Reynolds numbers.

8.7.3 Convective heat transfer distribution on smooth circular cylinder surface

In this section the convective heat transfer distributions obtained by numerical calculations and experimental work are compared. This is analyzed under thermal boundary conditions of the first and second kinds. The comparison is shown in Figure 8.35.

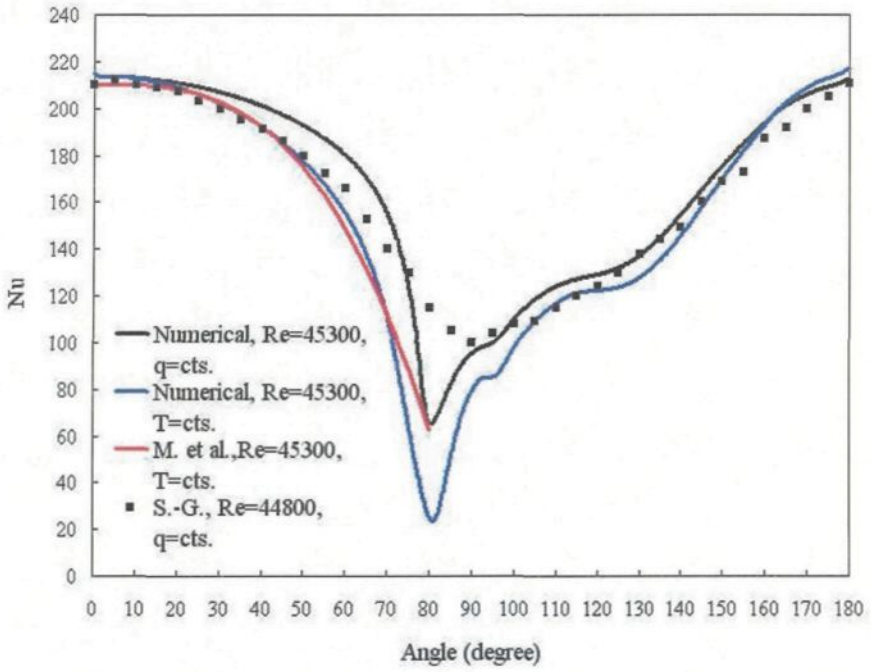

Figure 8.35 Nu number distribution along half-perimeter of smooth circular cylinder

It is shown in Figure 8.35 that the experimental results overpredict the numerical calculations in the region of boundary layer separation for both boundary conditions. The reason is probably that, in this region, the Nu number distribution shows the highest degree of variation. Naturally, the measurements resolve the perimeter more coarsely, with two orders of magnitude more than the numerical calculations. The temperature measurement in a surface point represents the temperature of its near vicinity, and not the temperature of an infinite small point. Note that in the case of boundary conditions of the first kind, the

measurements and numerical simulation results accord extremely well with each other. The difference between numerical calculations and measurements (found in literature) is more noticeable, but it is within an acceptable range. This difference may arise from various reasons, including influencing factors during experiments (see section 7.3.2), describing the turbulence with mathematical models, numerical residuals, small variations in Reynolds numbers and smaller number of temperature measurements along the perimeter. Briefly, the numerical calculations accord well with the experimental convective heat transfer results.

CHAPTER 9

EQUIVALENT RADIAL THERMAL CONDUCTIVITY OF OVERHEAD CONDUCTORS

It is well known that the ACSR conductor contains aluminium and steel strands, with air gaps (channels) between circular strands. The heat conduction in stranded conductors is quite complex due to its heterogeneous structure. Air gaps hinder heat conduction, and contact surfaces between strands increase thermal resistance. However, this problem can be reduced to heat conduction in a single, homogeneous material by introducing a new transport coefficient, namely the equivalent thermal conductivity. It is interesting to note that it is also known as "apparent", "resultant" or "effective" conductivity in the literature. [27]. In this study, the term "equivalent" is used.

The equivalent thermal conductivity was established from an experimental study performed in the CIGELE wind tunnel. It was also estimated by adapting different theoretical models offered by various researchers as well as conductivity models developed by the candidate. Furthermore, a qualitative analysis was performed based on analogy with electric conductivity.

9.1 Structure of overhead conductors

First, a brief introduction is necessary in order to better understand the heat conduction in stranded conducters. Different types of electrical conductors are used on the overhead

transmission lines. This study deals with aluminium conductors, steel reinforced (ACSR), with round wire and concentric layers.

Geometry of conductors

Basically, the stranded conductors are comprised of concentric layers of helically laid strands. The best use of space of the circle area is when six wires are placed around the center wire (king wire) [14]. Consequently, in most cases the steel core of ACSR conductors contains 7 stainless steel strands. In each aluminium layer, theoretically 2π (6.28), more strands can be placed than in the layer below [14]. In practice, of course, only 6 additional strands can be found in the adjacent layers. Consequently, the conductor cross-section has six axes, which divide the cross-section into identical symmetrical elements. The diameter of the stranded conductor depends strongly on the number and diameter of strands. It is calculated with Eq. 9.1-1 for non-twisted conductors and with Eq. 9.1-2 for twisted conductors [14].

$$D = \frac{d}{\sin(\pi / n)} + d \qquad \text{Eq. 9.1-1}$$

$$D_{twisted} = \frac{n \cdot d}{3} + d \quad , \qquad \text{Eq. 9.1-2}$$

where n is the number of strands in the conductor and d is the strand diameter (m).

Porosity of the stranded conductors

The porosity is one of the significant factors influencing thermal conduction in the stranded conductor. In the following equation, the estimation of the porosity of circular stranded conductors is briefly introduced. The porosity is defined as the ratio of the air gaps

volume to the total volume (air and solid). Therefore, it can be written for one unit length of conductor as follows:

$$P = \frac{A - A_s}{A} = 1 - \frac{A_s}{A} \qquad \text{Eq. 9.1-3}$$

where A is the cross-sectional area of the conductor (m^2) and A_s is area of the strands in the cross-section (m^2). By connecting the centers of any three neighbouring circular strands, an equilateral triangle is obtained (with good approximation), which contains air gap and circular sectors. The estimated porosity of this section, which could be assumed for the whole conductor, is as follows:

$$P = 1 - \frac{\pi}{2\sqrt{3}} = 0.093$$

Contact surfaces in the stranded conductor

The adjacent strands of the same layer are in contact with each other along helical lines. Additionally, each strand has contact with other strands from the neighbouring layers. These point contacts expand into ellipses, and the line contacts into strip contacts because of the bearing forces acting upon them [18]. The tensions of the strands of each layer cause them to embrace the layer below with a certain amount of pressure [18]. This pressure results in friction between strands.

9.2 Measuring the equivalent thermal conductivity

The aim of this experimental study is to obtain a good estimated value of the equivalent thermal conductivity of stranded conductors. The experiments consist of Joule heating of

the test conductor with a known current intensity. Thereby, the equivalent thermal conductivity can be estimated by measuring the steady state temperature at two points along the radius of the conductor. The generated thermal energy as well the geometrical data are known. The experimental results were evaluated for two cases: i) Uniform heat generation in the conductor, and ii) Considering the skin effect.

9.2.1 Experimental setup

An experimental rig was built using a low-voltage, high amperage transformer to heat a section of the conductor. A test rig was installed in the refrigerated wind tunnel in order to cool the conductor surface to avoid extreme warming of the conductor, which would lead to the melting of the aluminium or damage to the sensors. It was important to have good connections (attachments) at the ends of the conductor; otherwise, additional heat sources were created, supplying parasite heat flow in the conductor. The voltage drop at the two sides of the attachment indicated the quality of the contact. The surface temperature distribution along the length of the conductor and at the connections was monitored by infrared camera. From the images taken, it was possible to estimate the magnitude of the parasite heating and its effect at the middle of the conductor section, where the thermocouples were placed.

Three T type thermocouples (Omega Compact Transition Joint Probes) were installed in the conductor strands. Stainless-steel shielded and grounded thermocouples were used to measure the temperature in order to prevent noise capture. One thermocouple was installed in the stainless-steel strand in centre of conductor. Another one was placed in the

aluminium strand of the first layer (beside the steel core), and the third one was in the aluminium strand of the third, surface layer (see Figure 9.1). More details about the installation of the thermocouples can be found in APPENDIX 9. The diameter of the thermocouple head is 0.5 mm (see Figure 9.2), and the socket nominal diameter is 1 mm, in which the sensors are fixed. The thermocouples are at the middle of the conductor section, in the center of the aforementioned strands (see APPENDIX 9).

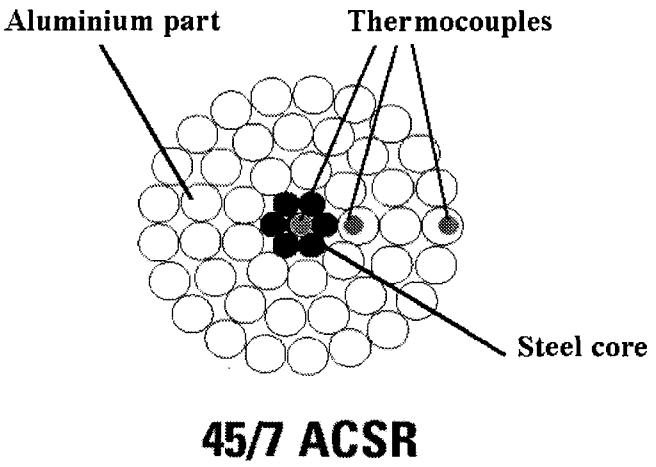

Figure 9.1 Cross-section of the Bersimis conductor with installed thermocouples

A thermocouple is installed in the steel core for the purpose of indicating (or not) the electrical current flow in this part of the conductor. As a result, during all tests the temperature was the same (within the measurement accuracy) as that measured in the first layer. This means that there is no considerable current flow in the steel core, which is in agreement with the approved standard used in practice. Note that the resistivity of steel is an order of magnitude higher than that of aluminium. Thereby, it is a good approximation, not considering current flow in the core.

The high amperage current flow in the conductor produced a significant magnetic field in the vicinity of the experimental rig. This phenomenon created a high level of noise for the temperature measurement. Hence, the extension wires were installed with great care and the connector box was placed in the grounded Faraday cage in order to avoid such noise. As a result, the built-in sensor (in the connector box) responsible for the cold-junction compensation was well isolated.

Figure 9.2 Head of the thermocouple (microscope view)

In our case the thermocouples measured in the low range of temperature. The requirement of the present experimental study is to measure a temperature difference of a few degrees Celsius. Normally, the accuracy of the thermocouple measurements is around ±1 °C, which is relatively high in comparison with the measured temperature difference of this magnitude. The thermocouples were selected with great care and were paired with the appropriate channel (and extension wire) in order to improve the accuracy.

One of the greatest challenges during the installation of the thermocouples was how to close the stranded conductor. What was the original force that was used to twist the

strands? The conductor was twisted to have a good contact between the strands without exceeding the limit of plastic deformation.

9.2.2 Temperature distribution in the conductor with uniform thermal energy generation

First, the temperature distribution in cylindrical conductors should be established in order to evaluate the equivalent thermal conductivity from the experimental data. The heat conduction equation with thermal energy generation in a cylindrical coordinate system for constant thermal conductivity reduces to Eq. 9.2-1 [22]:

$$\frac{1}{r}\frac{d}{dr}\left(r\frac{dT}{dr}\right)+\frac{q}{k}=0 \qquad \text{Eq. 9.2-1}$$

where r is the radius (m), T is the temperature (K), q is the volumetric heat source (W/m^3) and k is the thermal conductivity (W/mK).

First, for the sake of simplicity, uniform heat generation in the electrical conductor is assumed. Hence, the q is independent from the r radius. After solving Eq. 9.2-1 by the appropriate mathematical procedure, the general form of the temperature distribution is obtained:

$$T=-\frac{q}{4k}\cdot r^2+C_1\cdot\ln r+C_2 \qquad \text{Eq. 9.2-2}$$

where C_1 and C_2 are constants of integration. These constants are obtained from the boundary conditions, which are presented in the following sections.

9.2.2.1 Neumann condition at the interface of steel core and aluminium outside

Boundary conditions of the second kind (also called Neumann conditions) are applied at the interface of the steel core and the aluminium outside. Namely, zero heat flux is prescribed at the interface, since no significant electrical current flow is assumed in the steel core. This assumption has been previously discussed; thus, the temperature of the stainless steel core is constant along the radius in steady state (see Figure 9.3).

The appropriate Neumann condition:

$$\left.\frac{dT}{dr}\right|_{core} = 0 \quad \text{, at } r=r_c \qquad \text{Eq. 9.2-3}$$

Applying the Neumann condition to Eq. 9.2-3 before as well as after integration:

$$0 = -\frac{q}{2k} r_c + \frac{C_1}{r_c} \qquad \text{Eq. 9.2-4}$$

$$C_1 = \frac{q}{2k} r_c^{\,2} \qquad \text{Eq. 9.2-5}$$

Hence, the appropriate form of Eq. 9.2-2:

$$T = -\frac{q}{4k} \cdot r^2 + \frac{q}{2k} \cdot r_c^{\,2} \cdot \ln r + C_2 \qquad \text{Eq. 9.2-6}$$

9.2.2.2 Dirichlet condition at the conductor outer surface

Boundary conditions of the first kind (also called Dirichlet conditions) are applied at the outer surface of the conductor, and constant temperature is prescribed. This temperature is measured by a thermocouple placed in one of the outer aluminium strands. The applied Dirichlet condition is as follows:

$$T = T_s, \text{ at } r=r_s \qquad \text{Eq. 9.2-7}$$

where T_s is the conductor surface temperature and r_s is the outer surface radius.

Hence, Eq. 9.2-7 can be written in the following form:

$$T_s = -\frac{q}{4k} \cdot r_s^{\,2} + \frac{q}{2k} \cdot r_c^{\,2} \cdot \ln r_s + C_2 \qquad \text{Eq. 9.2-8}$$

Expressing the constant of integration from the above equation:

$$C_2 = T_s + \frac{q}{4k} \cdot r_s^{\,2} - \frac{q}{2k} \cdot r_c^{\,2} \cdot \ln r_s \qquad \text{Eq. 9.2-9}$$

The final form of the temperature distribution is obtained after substituting the constants of integration into Eq. 9.2-6.

$$T(r) = T_s + \frac{q}{4k} \cdot \left(r_s^{\,2} - r^2\right) + \frac{q}{2k} \cdot r_c^{\,2} \cdot \ln \frac{r}{r_s} \qquad \text{Eq. 9.2-10}$$

The volumetric heat generation, q, can be calculated, if I electrical current passes through the cylinder, as follows:

$$q = \frac{Q}{V} = \frac{I^2}{S} \cdot \frac{R}{L} \qquad \text{Eq. 9.2-11}$$

where Q is the generated Joule heat (W), V is the volume, where the heat is generated (m^3), I is the electrical current (A), S is the cross-section (m^2) through the current passes (cross-section of the aluminium outside, without steel core) and R/L is the electrical resistance of the given length of the conductor (Ω/m).

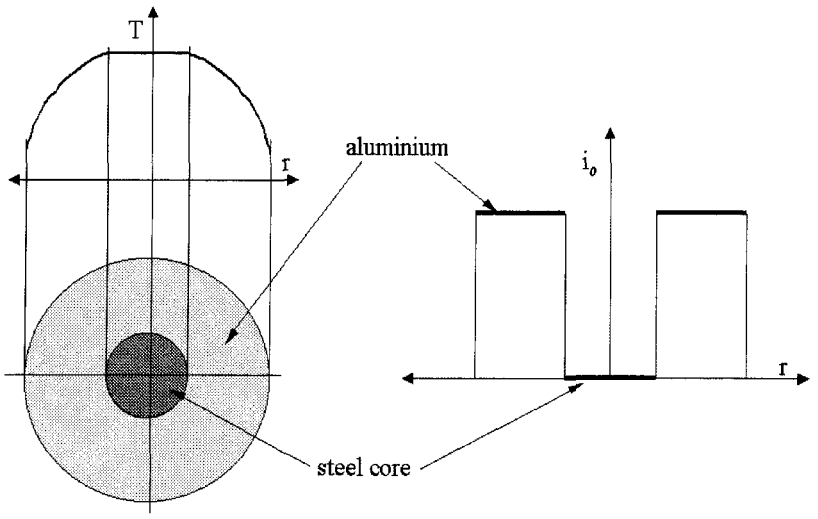

Figure 9.3 Apparent temperature distribution in conductor, in the case of uniform electrical current distribution in the aluminium strands without ac current in the steel core.

9.2.3 Evaluation of equivalent thermal conductivity assuming uniform energy generation

Writing Equation 9.2-10 at locations, where the thermocouples are placed and expressing the thermal conductivity, the result is:

$$k = \frac{q}{4(T_1 - T_2)}\left[\left(r_2^{\,2} - r_1^{\,2}\right) + 2r_c^{\,2} \cdot \ln\frac{r_1}{r_2}\right] \qquad \text{Eq. 9.2-12}$$

Equation 9.2-12 shows that thermal conductivity can be determined after both; the generated heat as well as the temperatures at locations 1 and 2 are known. The temperatures, T_1 and T_2, were measured by thermocouples placed in these locations.

Three measurements were performed with different nominal current in the conductor, namely 1789.4, 2659 and 3100.7 A. Naturally, the generated temperature difference

between locations 1 and 2 were different. Table 9-1 shows these temperature differences as well as the corresponding equivalent thermal conductivity.

Table 9-1 Experimental results assuming uniform heat generation

Applied current (A)	Measured temperature difference, T_1-T_2 (K)	Evaluated equivalent thermal conductivity (W/mK)
1789.4 (2000)	1.05	5.88
2659.0 (3000)	2.45	5.56
3100.7 (3500)	3.30	5.61

Note that in Table 9-1 the current values in parentheses are those before calibration of the CIGELE-S5000A transformer. After recognizing that the transformer control panel did not indicate the correct value of the electric current passing through the conductor, it was calibrated. Calibration curves are presented in APPENDIX 10. Unfortunately, the first evaluation was presented in [49] assuming electric current shown by control panel (values in parentheses). Naturally, the equivalent thermal conductivity obtained with higher current led to the greater value of 7.2 W/mK. Table 9-1 shows that the evaluated equivalent thermal conductivities from measurements with different current flow accord with each other. The estimated average value is *5.7 W/mK,* assuming uniform energy generation.

9.2.4 Temperature distribution in the conductor with non-uniform thermal energy generation

In the previous section, uniform heat generation due to constant electrical current distribution in the aluminium cross-section was analysed (see Figure 9.3). However, the

current distribution is not uniform when ac current passes in the conductor. It is well known that higher current density flows at the outer surface than in the interior of the conductor due to a skin effect. Consequently, the thermal energy generation is also non-uniform along the conductor's radius.

9.2.4.1 Electrical current distribution in conductor; skin effect

The electrical current distribution is required in order to assess the appropriate temperature field in the conductor assuming non-uniform thermal energy generation.

First, consider the nominal depth of penetration of the conductor. The thickness in which the current decreases to 1/e of its value at the surface (maximum current) is called penetration or skin depth [23], [56]. It can be calculated using Eq. 9.2-13 [8], [23] and [56].

$$\delta = \sqrt{\frac{\rho}{\pi \cdot f \cdot \mu}} \qquad \text{Eq. 9.2-13}$$

where ρ is the resistivity of conductor (Ωm), f is the frequency (Hz) and μ is the absolute magnetic permeability of the conductor (H/m). The absolute magnetic permeability is

$$\mu = \mu_r \cdot \mu_o$$

where μ_r is the relative magnetic permeability (-), which is, with good approximation, 1 for the paramagnetic materials such as aluminium. The free-space value, μ_0, is $4\pi \cdot 10^{-7}$ H/m.

Estimating the skin depth of the A1 conductor

The estimation is made for an electric current of 60 Hz frequency. The electrical resistivity of $0.028264 \cdot 10^{-6}$ Ωm is assumed for the A1 (CSA standard) aluminium conductor at 20 °C temperature [4]. The calculated skin depth is *0.01092 m* using

Eq. 9.2-13. This means that at 10.92 mm from the surface, the current decreases by 36.79% (1/e) of its surface value.

Current density distribution in a cylindrical conductor

The relevant literature gives a general solution for the current density distribution as a function of radius (see Eq. 9.2-14) [23].

$$i = i_m \cdot \frac{ber(\sqrt{2} \cdot r/\delta) + j \cdot bei(\sqrt{2} \cdot r/\delta)}{ber(\sqrt{2} \cdot r_s/\delta) + j \cdot bei(\sqrt{2} \cdot r_s/\delta)} \qquad \text{Eq. 9.2-14}$$

where i_m is the current intensity at the outer radius of the conductor (A/m^2), r_s is the surface radius (m), and δ is penetration depth (m). The denominations *ber* and *bei* are derived from words "Bessel function real" and "Bessel function imaginary", respectively [23]. These functions are plotted for different values of argument in APPENDIX 8.

The absolute value of Eq. 9.2-14 gives the magnitude of the current density as a function of radius and its angle gives the phase of current [23]. The estimated current intensity ratio at the steel core surface is *0.735* (i_c/i_m), obtained for A1 Bersimis conductor, 60 Hz current using Eq. 9.2-13. It means that 73.5% less current flows at the interface of the core and the outside as at the outer surface of the conductor.

Calculation of the electrical current distribution using finite element code

The electrical current distribution due to the skin effect in the cylindrical conductor is calculated using a commercial finite element code, Maxwell SV. Figure 9.4 shows the simulation result in the case of a 1 A nominal current applied in an A1 compact conductor.

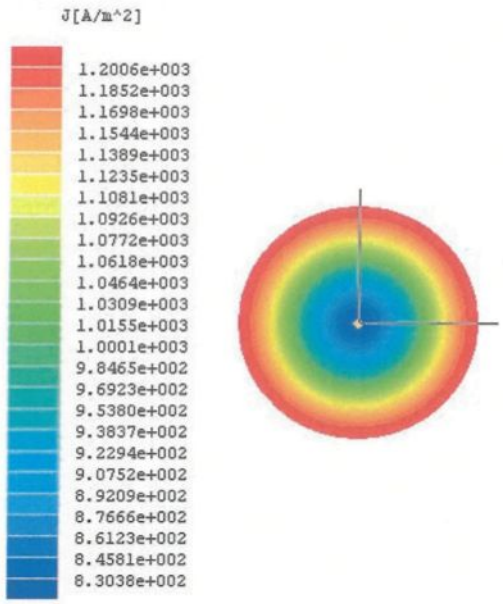

Figure 9.4 Current intensity distribution of 1 A nominal current flow in cylinder, obtained using Maxwell SV code

As previously shown, the current intensity distribution in a compact cylinder is described using a special form of the Bessel functions. However, it seems to be more convenient to approximate the current distribution with a polynomial of the third order. Hence, the current intensity, i, in the conductor can be described simply as a function of radius, as follows:

$$i = A \cdot r^3 + B \cdot r^2 + C \cdot r + D \qquad \text{Eq. 9.2-15}$$

where A, B, C and D are constant numbers.

9.2.4.2 Temperature distribution in the cylindrical conductor

Thermal energy generation is not uniform in the cylinder in which alternating current flows. The intensity of the non-uniform heat source in a point can be written as follows:

$$q(r) = i^2 \rho \qquad \text{Eq. 9.2-16}$$

The general form of the temperature distribution is obtained by following the same mathematical procedure, which was presented in detail in the previous section. The result is described in Eq. 9.2-17:

$$T(r)=\frac{\rho}{k}\left[A^2\frac{r^8}{64}+2AB\frac{r^7}{49}+(2AC+B^2)\frac{r^6}{36}+2(AD+BC)\frac{r^5}{25}+(2BD+C^2)\frac{r^4}{16}+2CD\frac{r^3}{9}+D^2\frac{r^2}{4}\right]+K_1\ln r+K_2$$

Eq. 9.2-17

where K_1 and K_2 are constants of integration. These constants can be obtained from the appropriate boundary conditions applied on the surfaces of the domain examined. As for similar problems in previous sections, the same mathematical process is followed.

Neumann condition applied at interface of core and outside

Constant (zero) heat flux is applied to an interface of steel core and aluminium outside, as follows:

$$\left.\frac{dT}{dr}\right|_{core}=0 \quad \text{, at } r=r_c$$

The K_1 constant of integration is expressed with Eq. 9.2-18, after the appropriate mathematical manipulation of Eq. 9.2-17 and the applied Neumann condition.

$$K_1=\frac{\rho}{k}\left[A^2\frac{r_c^8}{8}+2AB\frac{r_c^7}{7}+(2AC+B^2)\frac{r_c^6}{6}+(AD+BC)\frac{2r_c^5}{5}+(2BD+C^2)\frac{r_c^4}{4}+2CD\frac{r_c^3}{3}+D^2\frac{r_c^2}{2}\right]$$

Eq. 9.2-18

Inserting the constant of integration into Eq. 9.2-17:

$$T(r)=\frac{\rho}{k}\left[A^2\frac{r^8}{64}+2AB\frac{r^7}{49}+(2AC+B^2)\frac{r^6}{36}+2(AD+BC)\frac{r^5}{25}+(2BD+C^2)\frac{r^4}{16}+2CD\frac{r^3}{9}+D^2\frac{r^2}{4}\right]+$$
$$+\frac{\rho}{k}\left[A^2\frac{r_c^8}{8}+2AB\frac{r_c^7}{7}+(2AC+B^2)\frac{r_c^6}{6}+(AD+BC)\frac{2r_c^5}{5}+(2BD+C^2)\frac{r_c^4}{4}+2CD\frac{r_c^3}{3}+D^2\frac{r_c^2}{2}\right]\ln r+K_2$$

Eq. 9.2-19

Dirichlet condition applied at the outer surface

A constant temperature is prescribed at the conductor's outer surface as follows (Dirichlet condition):

$$T = T_s \text{, at } r=r_s$$

Applying the boundary condition to Eq. 9.2-19 and expressing the K_2 constant of integration:

$$K_2 = \frac{\rho}{k}\left[A^2\frac{r_s^8}{64}+2AB\frac{r_s^7}{49}+(2AC+B^2)\frac{r_s^6}{36}+2(AD+BC)\frac{r_s^5}{25}+(2BD+C^2)\frac{r_s^4}{16}+2CD\frac{r_s^3}{9}+D^2\frac{r_s^2}{4}\right]+$$
$$+\frac{\rho}{k}\left[A^2\frac{r_c^8}{8}+2AB\frac{r_c^7}{7}+(2AC+B^2)\frac{r_c^6}{6}+(AD+BC)\frac{2r_c^5}{5}+(2BD+C^2)\frac{r_c^4}{4}+2CD\frac{r_c^3}{3}+D^2\frac{r_c^2}{2}\right]\ln r_s + T_s$$

Eq. 9.2-20

The final form of temperature distribution is obtained after rewriting K_2 into Eq. 9.2-19.

$$T(r)-T_s = \frac{\rho}{k}\left(A^2\frac{r_s^8-r^8}{64}+2AB\frac{r_s^7-r^7}{49}+(2AC+B^2)\frac{r_s^6-r^6}{36}+2(AD+BC)\frac{r_s^5-r^5}{25}+(2BD+C^2)\frac{r_s^4-r^4}{16}+\right.$$
$$\left.+2CD\frac{r_s^3-r^3}{9}+D^2\frac{r_s^2-r^2}{4}+K_1\ln\frac{r}{r_s}\right)$$

Eq. 9.2-21

9.2.5 Evaluation of equivalent thermal conductivity assuming non-uniform thermal energy generation

Equation 9.2-21 describes the temperature distribution in the cylindrical conductor for non-uniform volumetric heat source. Note that the same thermocouples measure the temperature at locations r_1 and r_2 as in the previous case. The equivalent thermal conductivity can be expressed after the same mathematical procedure as for uniform energy generation. The final form is presented in Eq. 9.2-22.

$$k=\frac{\rho}{T_1-T_2}(A^2\frac{r_2^{\,8}-r_1^{\,8}}{64}+2AB\frac{r_2^{\,7}-r_1^{\,7}}{49}+(2AC+B^2)\frac{r_2^{\,6}-r_1^{\,6}}{36}+2(AD+BC)\frac{r_2^{\,5}-r_1^{\,5}}{25}+(2BD+C^2)\frac{r_2^{\,4}-r_1^{\,4}}{16}+$$
$$+2CD\frac{r_2^{\,3}-r_1^{\,3}}{9}+D^2\frac{r_2^{\,2}-r_1^{\,2}}{4}+K_1\ln\frac{r_1}{r_2})$$

Eq. 9.2-22

Table 9-2 shows the calculated equivalent thermal conductivity values for different applied currents assuming non-uniform Joule heat generation. Once again, it can be concluded that the measured results with different currents in the conductor are very close to each other. The average value of *3.5 W/mK* is considered a good estimation assuming non-uniform energy generation.

Note that evaluating the equivalent thermal conductivity, assuming non-uniform energy generation when ac current flows in the conductor is more realistic than simply using the temperature distribution with constant heat generation along the radius. The values obtained assuming non-uniform energy generation are lower than when constant heating is considered, since the non-uniform current distribution helps to obtain the same temperature difference between locations 1 and 2.

Table 9-2 Equivalent thermal conductivities assuming non-uniform energy generation

Applied current (A)	Measured temperature difference, T_1-T_2 (K)	Evaluated equivalent thermal conductivity, (W/mK)
1789.4 (2000)	1.05	3.63
2659.0 (3000)	2.45	3.43
3100.7 (3500)	3.30	3.46

9.3 Theoretical models of equivalent thermal conductivity

The literature offers certain theoretical models for estimating the equivalent thermal conductivity. A certain number of these models can be adapted to the heat conduction in stranded conductors. Additionally, certain theoretical models were constructed specifically for application with stranded conductors.

9.3.1 Riemann model

This is probably the simplest theoretical model. The model does not account for heat conduction in the air gaps between the strands. Furthermore, the arrangement of strands is idealized. It is assumed that the cylindrical strands are arranged in regular columns and rows when using this model (see Figure 9.5). The challenge of using this model is to establish the contact radius "a" between strands.

Riemann proposed Eq. 9.3-1 for calculating the equivalent thermal conductivity of porous material [27].

$$\frac{k_e}{k_s} = \frac{1}{\frac{R}{a} + \frac{1}{\pi}\ln\left(\frac{2R}{a}\right)} \qquad \text{Eq. 9.3-1}$$

where k_e is the equivalent thermal conductivity (W/mK) and k_s is the thermal conductivity of the conducting solid (W/mK).

Estimating k_e for Bersimis conductor using the Riemann model

The aluminium strand diameter, 2R, of the Bersimis conductor is 4.57 mm and the thermal conductivity of aluminium, k_s, is 210 W/mK. The equivalent thermal

conductivities *1.81, 4.45 and 8.73 W/mK* were estimated by using Eq. 9.3-1, assuming contact radius of 20, 50 and 100 μm, respectively.

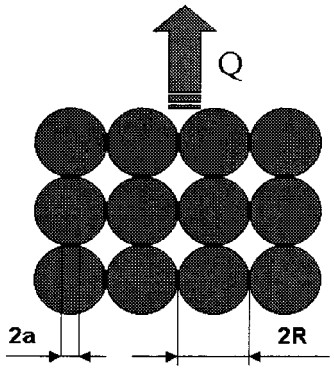

Figure 9.5 Arrangement of strands using the Riemann model

The equivalent thermal conductivity strongly depends on the contact radius, which is a function of contact pressure between strands. Figure 9.6 shows the possible equivalent thermal conductivities as a function of the contact radius. Obviously, the contact radius is smaller under weak pressure than when strands are firmly pressed together. Hence, the strength loss of conductors results in lower radial equivalent thermal conductivity.

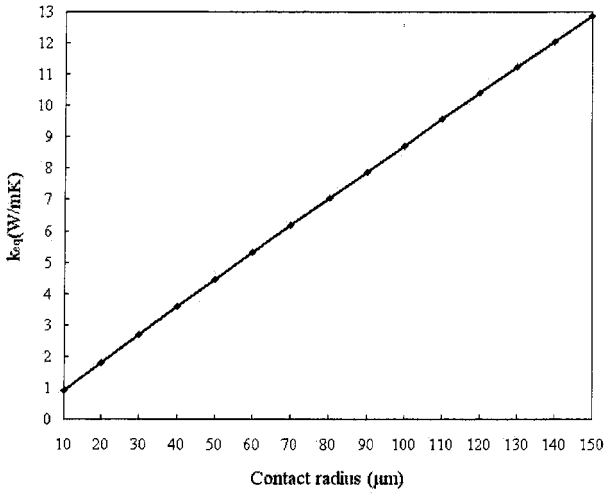

Figure 9.6 Equivalent thermal conductivity versus contact radius using the Riemann model

9.3.2 Zehner-Bauer-Schlünder model

The advantage of this model is that it takes into account the form of cells (air gaps) as well as the heat transfer between the solid particles (strands). The model was developed for packed spherical beds. However, it has now been adapted to stranded conductors by using a deformation factor (B), which describes the form of the cells. The deformation factor is defined by Eq. 9.3-2 [27].

$$B \approx 1.25\left(\frac{1-P}{P}\right)^{10/9} \qquad \text{Eq. 9.3-2}$$

Introducing a third, so-called "core" conductivity, k_{core} [27]:

$$k_{core} = \frac{2 \cdot k_g}{N}\left(\frac{B}{N^2} \cdot \frac{k_s/k_g - 1}{k_s/k_g} \cdot \ln\left(\frac{k_s}{B \cdot k_g}\right) - \frac{B+1}{2} - \frac{B-1}{N}\right) \qquad \text{Eq. 9.3-3}$$

$$N = 1 - B \cdot \left(\frac{k_g}{k_s}\right) \qquad \text{Eq. 9.3-4}$$

where k_s is the thermal conductivity of the conducting solid (W/mK), and k_g is the thermal conductivity of gas in pores (W/mK). The ratio of the equivalent thermal conductivity and conductivity of gas in pores (air between strands) is expressed by Eq. 9.3-5.

$$\frac{k_e}{k_g} = 1 - \sqrt{1-P} + \left(\frac{k_{core}}{k_g}\right) \cdot \sqrt{1-P} \qquad \text{Eq. 9.3-5}$$

Estimating equivalent thermal conductivity for Bersimis conductor

The following properties are used for the estimation:

- Porosity in the conductor (air gaps), P: 0.093
- Thermal conductivity of aluminium, k_s: 210 W/mK

- Thermal conductivity of air, k_g: 0.028 W/mK

The calculated deformation factor is B=15.7, and for the corresponding equivalent thermal conductivity *3.78 W/mK* is obtained. This value is very close to that obtained from measurements assuming non-uniform energy generation (3.5 W/mK).

9.3.3 Krischer model combined with contact resistance

The radial heat flow in stranded conductors could flow through the contact surfaces of strands, but also through interstitial air channels between strands. The main idea of the following section is to calculate the equivalent thermal conductivity from contact resistance coupled with thermal resistance of heat flow through air gaps. The Krischer Low Limit (KLL) model is used to calculate the resistance of heat flow through the air gaps and the aluminium. The contact resistance model represents the heat conduction through the contact surfaces. Finally, the equivalent thermal conductivity is obtained from the parallel connection of these two resistances (see Figure 9.7).

9.3.3.1 Krischer Low Limit model

The equivalent thermal conductivity of Krischer Low Limit model can be calculated as shown in Eq. 9.3-6.

$$k_{KLL} = \frac{k_s}{1 + P \cdot ((k_s / k_g) - 1)} \qquad \text{Eq. 9.3-6}$$

The k_{KLL}, calculated using Eq. 9.3-6 for the same case as presented in the previous section, is 0.3 W/mK. This thermal conductivity should be connected parallel to the contact

resistance between strands. The estimation of contact resistances between strands is the greatest challenge of using this simple model. This is discussed in the following sections.

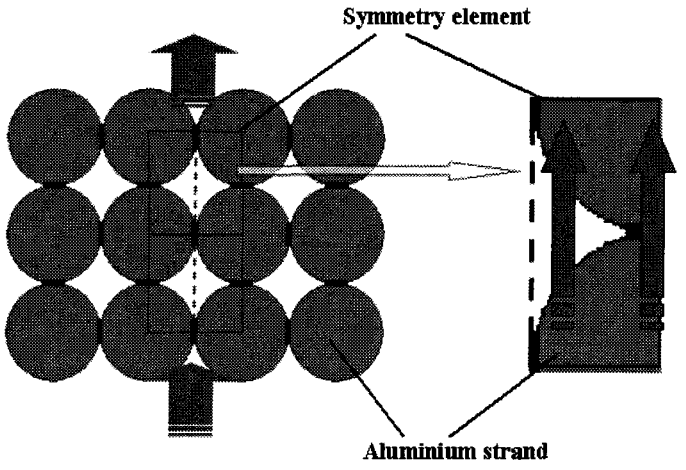

Figure 9.7 Heat flow in one half of the symmetrical element

9.3.3.2 Contact resistance between strands

The surface contact resistance can be approximated using the isothermal circular contact on a half space [44], assuming that the contact area is small in relation to the strand diameter. The isothermal contact resistance is expressed in Eq. 9.3-7.

$$R_c = 1/(4k_s a) \qquad \text{Eq. 9.3-7}$$

where a is the contact radius (m). The contact surface, between two inclined cylindrical strands from different layers crossing each other, can be approximated using the contact surface between two spheres. In this case the contact radius of the circular area is obtained from the Hertz relation for elastic contacts, as follows [11]:

$$a = \sqrt[3]{\frac{3N\left[\left(\frac{1-\nu_1^{\,2}}{E_1}\right)+\left(\frac{1-\nu_2^{\,2}}{E_2}\right)\right]}{8\left(d_1^{\,-1}+d_2^{\,-1}\right)}} \qquad \text{Eq. 9.3-8}$$

where N is normal force on strands (N), d is strand diameter (m), E is moduli of elasticity (Pa) and ν is Poisson's ratio (1). Subscripts 1 and 2 denote the upper and lower strands in contact, respectively. In the following section, the desired contact resistance between two aluminium strands of same diameter is being researched. In this case, Eq. 9.3-8 simplifies as shown by Eq. 9.3-9.

$$a = \sqrt[3]{\frac{3Nd\left(1-\nu^2\right)}{8E}} \qquad \text{Eq. 9.3-9}$$

In the symmetry element (cube of d length) there are two parallel connected contact resistances ($R_c/2$). By expressing the effective contact thermal conductivity (k_{ce}) from heat flow through the symmetry element, we have:

$$k_{ce} = k_s \frac{2a}{d} \qquad \text{Eq. 9.3-10}$$

Finally, the equivalent thermal conductivity is simply the sum of k_{KLL} and k_{ce} as shown in Eq. 9.3-11.

$$k_e = k_{KLL} + k_{ce} \qquad \text{Eq. 9.3-11}$$

Estimating the contact resistance and the equivalent thermal conductivity

The estimation is made for Bersimis conductors with the following parameters:

- Aluminium strand diameter (d) of 4.57 mm
- Poisson's ratio of aluminium (ν) of 0.33

- Elasticity moduli of aluminium (E): 70 GPa
- Thermal conductivity of aluminium: 210 W/mK
- Normal force acting on strands (N): 7.6 N (a typical value found in [12])

The calculated contact radius is 54.9 μm using Eq. 9.3-9, and the corresponding R_c contact resistance is 43.37 K/W. This results in 5.05 W/mK effective contact conductivity. Finally, the estimated equivalent thermal conductivity of the parallel connected model is *5.35 W/mK.*

9.3.4 Resistance network of radial heat conduction in stranded conductor

This model is based on the contact resistance between strands. The model does not incorporate the thermal resistance of aluminium, since it is negligible compared to the contact resistance. The symmetry element under analysis is 1/6 of the circular cross-section (see Figure 9.8). It is considered that each strand is in contact with adjacent strands in the same layer and with two strands in the layers both above and below. The contact resistance between strands in the same layer is $R_{l,}$ referring to line contact. The contact resistance between strands of different layers is $R_{p,}$ referring to point contact (the strands crossing each other at an angle). Figure 9.8 shows the contact thermal resistance network of a symmetry element.

Naturally, the contact resistance network shown in Figure 9.8 can be simplified. After several steps of transformations and necessary simplifications the equivalent resistance is obtained by the candidate as follows:

$$R_{\Sigma} = \frac{R_M \cdot R_p\left(R_p + 3R_l\right)}{4R_M R_l + R_p\left(R_p + 3R_l\right)} \qquad \text{Eq. 9.3-12}$$

$$R_M = \frac{R_p\left(R_p + 3R_l\right)}{2\left(2R_p + 3R_l\right)} + \frac{R_p\left(R_p + 3R_l\right)}{6\left(R_p + R_l\right)} = \frac{R_p\left(R_p + 3R_l\right)\left(7R_p + 9R_l\right)}{6\left(R_p + R_l\right)\left(2R_p + 3R_l\right)} \qquad \text{Eq. 9.3-13}$$

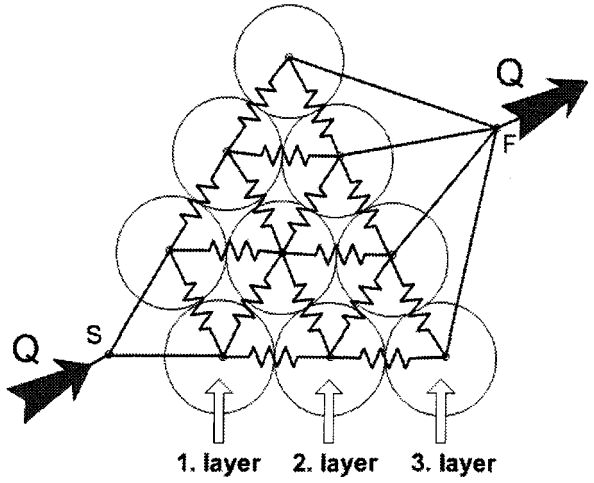

Figure 9.8 Resistance network of the symmetrical element

Estimating the equivalent thermal conductivity

An estimation was made to obtain the equivalent thermal conductivity with the same parameters that are used in the previous estimation for combined model. It was assumed that the R_L line contact resistance is half of the point contact resistance in order to simplify the quite complex R_{Σ} equivalent resistance. Hence, the obtained equivalent thermal conductivity from the heat flow through the cylindrical shape is *3.99 W/mK*.

9.4 Radial electric conductivity of stranded conductors

9.4.1 Analogy between electric and thermal conductivity

The radial electric current flow and the radial heat flow through a hollow cylinder are analog phenomena, as shown in Eq. 9.4-1 and Eq. 9.4-2.

$$I_r = \sigma \cdot \frac{2\pi L}{\ln(r_2 / r_1)} \cdot \Delta U \qquad \text{Eq. 9.4-1}$$

where σ is the electric conductivity (1/Ωm), ΔU is potential difference between the surfaces of the hollow cylinder (V), r_1 and r_2 are the inner and outer radius (m) of the hollow cylinder, respectively.

$$Q_r = k \cdot \frac{2\pi L}{\ln(r_2 / r_1)} \cdot \Delta T \qquad \text{Eq. 9.4-2}$$

where k is the thermal conductivity (W/mK), and ΔT is temperature difference between the surfaces of the hollow cylinder (K).

Therefore, from radial electric conductivity measurements certain qualitative conclusions can be made for radial thermal conductivity as well. The objective of these measurements was to analyse the radial conductivity under different applied radial contact pressures (or forces) acting on strands. The radial electric conductivity was measured, since it requires simpler and cheaper installation rig. The experimental study was performed in the CURAL laboratory with Mr. Mathieu Rouleau, where more than 20 tests were done.

9.4.2 Experimental rig

The ACSR conductor, code word Bersimis, was used during the experimental study. The length of the test conductor was 9.8 cm. The steel core of the conductor was replaced with a compact copper cylinder for the purpose of producing an equipotent surface (see Figure 9.9). The outer surface of the conductor was wrapped with thin copper sheeting. The copper core and sheet were connected to a dc current source in order to pass electric current in radial direction through strands. The current source was connected to copper sheeting with more than 20 wires in order to produce surface of the constant potential.

Two series of tests were realized with 15 A and 50 A currents passing in radial direction of a stranded cross-section. The electric potential difference was monitored continuously between strands of the first and the third layers. In the symmetry elements, three voltage drops (ΔU) were measured depending on the position of strands with connections A, B and C. This is shown in Figure 9.9. These three measurements cover all possible current flow possibilities through the symmetry element. In total, three symmetry elements (1, 2 and 3) of a possible six are used to measure the A, B and C voltage drops.

The measurements were repeated for different radial pressures between strands. The radial pressure was produced by adjusting the torque on four clamps belted around the copper sheet. The torque that was used to tighten the clamps was adjusted using a torque wrench. Unfortunately, the radial pressure could not be calculated from the adjusted torque on the screws. However, the qualitative relation between them was obvious; increasing the torque increases the radial pressure between the strands.

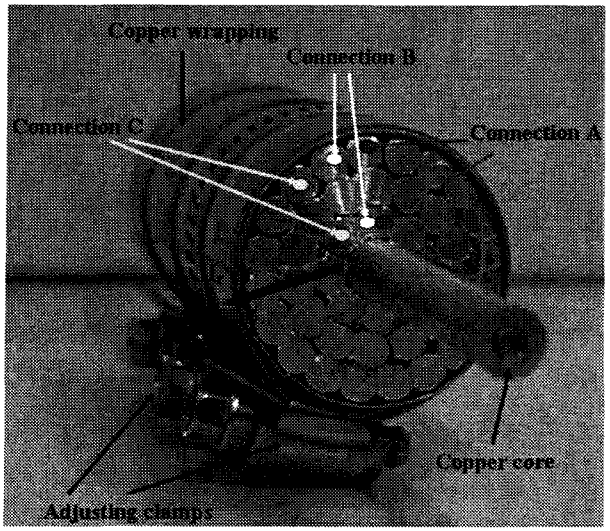

Figure 9.9 Experimental setup of radial electric conductivity measurement

9.4.3 Experimental results of radial electrical conductivity

Finally, the σ electric conductivity was calculated using Eq. 9.4-1 after the radial current flows and the potential differences ΔU were measured between strands in the first and the third (surface) layer. The results of the radial electrical conductivity measurements are shown in Figure 9.10 and Figure 9.11.

It is shown that the radial electric conductivity strongly depends on the measurement connections from which it is obtained. In certain extreme cases the difference could be 100% when comparing different connections (see Figure 9.11). However, it can be concluded that the radial conductivity increases with increasing contact pressure. The exceptions are cases 1A and 1B, in which the radial conductivity decreases with higher contact pressures. This probably occurs due to irregular rearrangements of these strands under a stronger deformation force. There are also certain strands (1C and 3B), which

indicate non-monotonic increasing of radial conductivity with increasing deformation force. This phenomenon is also due to "place arrangements" of strands. On the overhead power line conductors this is probably a more common phenomenon, since they are exposed to strong bending torque and in certain cases they have a strongly curved shape (inclination angle).

Generally, it can be concluded from these measurements that the radial conductivity (electric and thermal) increases with radial contact pressure, but the deformation force can periodically or persistently rearrange the strands, and thus the radial conductivity as well.

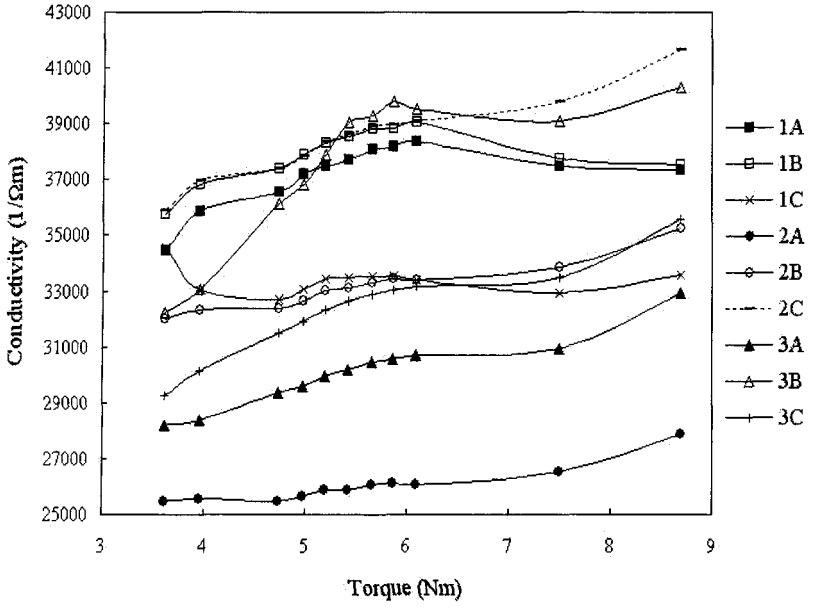

Figure 9.10 Radial conductivity measurements performed with 15A electric current

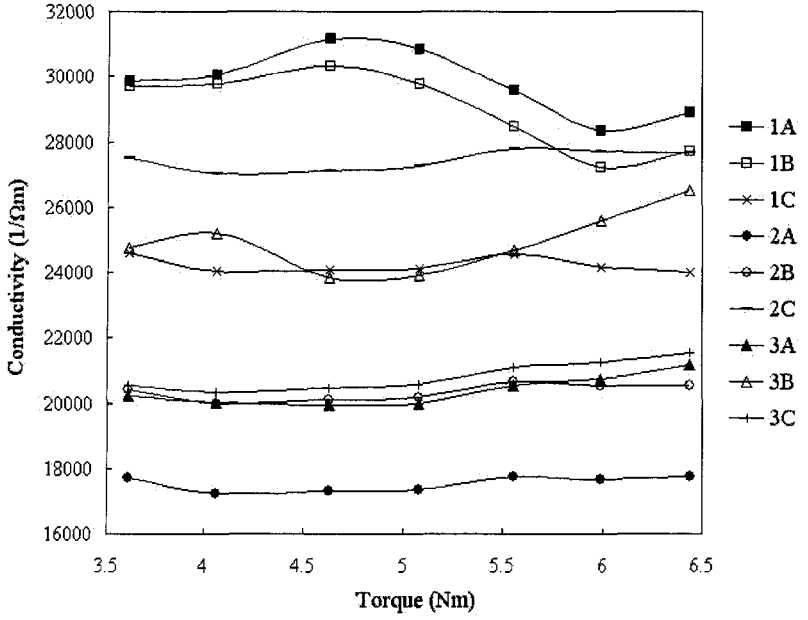

Figure 9.11 Radial conductivity measurements performed with 50 A electric current

9.5 Comparing equivalent radial conductivities

In the previous section, the radial equivalent thermal conductivity was estimated from experimental study as well as evaluated from various theoretical models. The estimated values with different methods are shown in Table 9-3. It can be concluded that both the experimental and theoretical results are in the range of 3.5 W/mK and 5.7 W/mK, which is an order of magnitude lower than that of the conducting solid (pure aluminium of 237.2 W/mK [58]). Consequently, the surface contact thermal resistance between the strands plays a very important role in the radial heat conduction for this type of conductor.

Table 9-3 Estimated equivalent thermal conductivities for Bersimis conductor

Method	Equivalent thermal conductivity, k_e (W/mK)
Experimental, considering skin effect	3.50
Experimental, with uniform heat generation	5.70
Theoretical, Riemann model	4.45
Theoretical, Zehner-Bauer-Schlünder model	3.78
Theoretical, Krischer Low Limit model combined with contact resistances	5.35
Theoretical, resistance network model	3.99

It was shown that the radial conductivity in stranded conductors is strongly linked to the contact pressure between strands (or on radial load). This effect is incorporated into the Riemann model (via contact radius), in both the combined model and the resistance network. These models supply greater radial conductivity than the Zehner-Bauer-Schlünder model, which does not account for contact pressure. However, the greatest challenge of using models that account for contact pressure is determining the radial load between adjacent strands. When these models are used, the estimated equivalent thermal conductivity depends strongly on the assumed radial load. The radial load depends on several factors including geometry parameters of conductor and axial load. Involving these parameters in the model greatly increases the complexity of the theoretical models. The equivalent thermal conductivity evaluated assuming skin effect gives a more realistic result, just as when it is calculated from uniform heat generation. It should be noted that the

experiments also involve the estimation of radial load, since after opening the test conductor for thermocouple installation the original twisting force was abandoned.

The radial electric conductivity measurements showed that the radial conductivity increases with contact pressure between adjacent strands, but the deformation force can periodically or persistently rearrange the structure, and thus the radial conductivity as well.

CHAPTER 10

CONCLUSIONS AND RECOMMENDATIONS

10.1 Conclusions

a) First, the melting conditions of ice layers accumulated on overhead conductors were analysed using the finite difference method. The ice melting conditions depend on many parameters, including conductor diameter, mean heat transfer coefficient, electric current, ice thickness, thermo-physical parameters of the ice and conductor, and ambient air temperature. In order to reduce the large number of parameters the melting conditions were examined in dimensionless form. The methodology was applied to identify those conditions that provoke the melting either at the inner or at the outer surface of the ice deposit.

b) A mathematical model was established to calculate the minimum energy required to prevent ice accumulation on overhead power line conductors, based on the Joule effect and taking into account different conductors and atmospheric parameters. Correction factors, taking into account water runback on the conductor surface, as well as deviation of the water layer from the thermal equilibrium state, were introduced for three stranded conductors. The product $\kappa_1 \cdot \kappa_2$, was estimated at 0.7 for the Geant 5P and Condor type conductors (both sharing the same surface geometry) and at 1.03 for the Drake conductor.

c) An experimental study was carried out to analyze the minimum current required to inhibit ice accretion on different power line conductors under a wide range of atmospheric conditions. The maximal error of the measurements, at less than 12%, was within an acceptable range for conductor types Condor, Drake and Geant.

d) The mathematical model, which was validated experimentally, can efficiently be used to calculate the minimum current required to prevent ice from accumulating on a single power line conductor under wide range of meteorological conditions.

e) The radial equivalent thermal conductivity was estimated from experimental study as well as being evaluated from various theoretical models. Both the experimental and theoretical results are in the range of 3.5 W/mK and 5.7 W/mK, which is two orders of magnitude lower than that of the solid aluminium of 237.2 W/mK.

f) It was shown that the radial conductivity in stranded conductors strongly depends on either the contact pressure between strands or on the radial load. This effect was incorporated in the Riemann model via the contact radius, in the combined model and in the resistance network also. These models supplied higher radial conductivity than the Zehner-Bauer-Schlünder model, which did not account for contact pressure.

g) The overall convective heat transfer coefficient measurements were presented for four different ACSR conductor types. The Nu-Re correlations showed a linear relationship between 10^4 and $7 \cdot 10^4$ Reynolds numbers. It was shown that the strength loss of ACSR conductors gave a higher heat convection rate projected to the same heat transfer surface.

h) The heat transfer coefficient distributions around the perimeter of stranded conductors and smooth cylinders, as well as the corresponding overall convective heat transfer were calculated from CFD simulations. The convective heat transfer around stranded surfaces shows periodic characteristics after each strand at the two different Reynolds numbers investigated 45 520 and of 41 028. Surprisingly, the calculated overall Nu number based on the outer diameter was *164.59* at Re number of 45 520. This value was almost the same as that obtained for the smooth circular cylinder (overall Nu of *165.28*).

i) A mathematical model was established, which calculated the current and energy requirements for de-icing of non-rotating conductors depending on the Joule heating technique and atmospheric parameters. In one technique the Joule heating is accomplished by superposed impulse current on nominal ac current. Another heating technique is based on the simple increasing of the ac nominal current. Both techniques can be used with different strategies depending on the time of interaction in the ice accretion process (during or after icing event). The current and energy requirements were analyzed under various current and atmospheric parameters. It was found that under modest icing event conditions the impulse heating could be more economical.

j) An experimentally validated mathematical model was developed to determine the shedding time and energy for de-icing of completely ice-covered conductor by Joule heating with increased nominal ac current. The effect of many influencing factors was investigated, including air temperature, ice thickness, electrical resistance of the conductor and the magnitude of increased current. This procedure is able to give a fast

estimation of the required Joule heat to totally remove the ice around the conductor as a function of the different influencing factors.

10.2 Recommendations for future research

General convective heat transfer coefficient correlations for bare stranded conductors

More experimental and numerical work is required in order to formulate a more general correlation for calculating the convective heat transfer from bare stranded overhead conductors. These correlations should be elaborated for various roughness ratio of stranded surface in wide range of Reynolds numbers. The methodology of measurements and numerical calculations were introduced in detail in the thesis.

General computerized procedure for current and required energy determination

A computerized procedure could be developed to support decision-making when a weather forecast is available to choose the most economical Joule heating method (de-icing or prevention), technique (type of applied electric current) and strategy (when to interact in accretion process) under given atmospheric conditions. Naturally, the comparison of energy consumption is only one factor in the decision-making process, the safety of the network, the availability of energy, and other factors need to be evaluated as well.

Effect of structure of the ice layer on the rate of shedding

It is well known that different types of ice with various ranges of porosity may accumulate the overhead conductors. In order to use the developed de-icing models for various types of ice accretions, it is necessary to assess their radial thermal conductivity. Therefore, an experimental procedure should be developed for determining the apparent thermal conductivity of various ice accretions. Finally, a theoretical sound equivalent conductivity model could be established on the available experimental data about the structure of different ice types.

CHAPTER 11

REFERENCES

[1] Aluminum Electrical Conductor Handbook, 3rd ed., the Aluminum Association, pp. 3.8-3.13, Washington, 1989.

[2] Ansys CFX-Solver, Release 10.0: Modelling. User Manual, 2005.

[3] Ansys CFX-Solver, Release 10.0: Theory. User Manual, 2005.

[4] Bare Overhead Cable. (2003, Nov.), Alcan Cable, Canadian Product Catalogue. [Online]. Available: http://www.cable.alcan.com.

[5] Bouamoul, A., "Étude expérimentale et théorique sur le processus de délestage par fonte de la glace accumulée autour d'un cylindre", Ph.D. thesis, Université du Québec à Chicoutimi, octobre 2002.

[6] Boulos, M.I. and Pei D.C.T., "Dynamics of heat transfer from cylinders in a turbulent air stream," International Journal Heat Mass Transfer, vol 17., pp.767-783, Pergamon Press, 1974.

[7] Bowman, F., "Introduction to Bessel functions", Dover Publications Inc., New York, 1958.

[8] Breuer, H., "SH atlasz, Fizika", (in hungarian), Springer Hungarica Kiadó Kft., Budapest, 1993.

[9] Çengel, Y.A., "Heat transfer: a practical approach", 2nd ed., New York, McGraw-Hill, 2003, pp. 130, 737, 868.

[10] Clem, J. E., "Currents Required to Remove Conductor Sleet," Electrical World, pp. 1053-1057, Dec. 1930.

[11] Collins, J.A., "Mechanical design of machine elements and machines," John Wiley and Sons, USA, 2003.

[12] Costello, G.A., "Theory of Wire Rope," Springer-Verlag, New York, 1990.

[13] Davidson, G.A., Donoho, T.E., Landrieu, P.R.H., McElhaney, R.T., Saeger, J.H., "Short-time thermal ratings for bare overhead conductors," IEEE Transaction on Power Apparatus and Systems, vol. PAS-88, no. 3, pp. 194-198, Mar. 1969.

[14] Dékány, L., Frank, E., "Acélkötelek", (in hungarian), Műszaki Kiadó, Budapest, 1963.

[15] Druez, J., Louchez, S., Bouchard, G. "Study of Ice Shedding Phenomenon on Cables," Proceedings of the Ninth International Conference of Offshore Mechanics and Arctic Engineering, pp. 143-148, 1990.

[16] Druez, J., McComber, P. "Ice Accretion and Shedding on Overhead Line Cables," Proceedings of the Seventh International Offshore and Polar Engineering Conference, Vol. II, pp. 647-655, 1997.

[17] Eckert, E.R.G., and Drake, R.M., "Analysis of heat and mass transfer", McGraw-Hill Book Company, New York, 1972.

[18] Electric Power Research Institute, "Transmission line reference book: wind-induced conductor motion", EPRI, pp. 154, Palo Alto, 1979.

[19] Finstad, K.J., Lozowski, E.P., and Gates, E.M., "A computational investigation of water droplet trajectories," Journal of Atmospheric and Oceanic Technology, vol.5, pp.160-170, Feb. 1988.

[20] Godard, S., "Mesure de gouttelettes de nuage avec un film de collargol," Bulletin de l'Observatoire de Puy de Dome, pp. 41-46, 1960.

[21] IEEE Standard for Calculating the Current-Temperature Relationship of Bare Overhead Conductors, Std. 738, 1993.

[22] Incropera, F.P., and DeWitt, D.P., "Fundamentals of Heat and Mass Transfer," John Wiley and Sons, 5th ed., New York, 2002.

[23] Johnson, W.C., "Transmission lines and networks," McGraw-Hill Book Company, pp. 58-80, New York, 1950.

[24] Karev, A.R., and Farzaneh, M., "Evolution of droplet size distribution in an icing wind tunnel," in Proc. of 10th IWAIS, Brno, Czech Republic, pp. 73, 2002.

[25] Karev, A.R., Farzaneh, M., and Kollár, L.E., "An icing wind study on characteristic of an artificial aerosol cloud. Part I: Cloud uniformity and accompanying droplet size distribution", submitted to Journal of Applied Meteorology.

[26] Karev, A.R., Farzaneh, M., and Mousavi, M., "Influence of non-uniformity of droplet size distribution on ice accretion", in Proc. of 10th IWAIS, Brno, Czech Republic, pp. 74, 2002.

[27] Kiss, L.I., "Thermo-physical properties in heat conduction", Lecture notes, Université de Liège, LTAS, 1996.

[28] Knudsen J.M. and Katz D.L., "Fluid dynamics and heat transfer", McGraw-Hill Book Company, New York, 1958.

[29] Kollár, L.E., Farzaneh, M., and Karev, A.R., "Modeling Droplet-Size Distribution near a Nozzle Outlet in an Icing Wind Tunnel," Atomization and Sprays, to be published.

[30] Kondjoyan, A., and Boisson, H.C., "Comparison of Calculated and Experimental Heat Transfer Coefficients at the Surface if Circular Cylinders Placed in a Turbulent Cross-flow of air," Journal of Food Engineering, vol. 34, Elsevier Science Ltd., Great Britain, 1998.

[31] Laforte, J.L., Allaire, M.A., Laflamme, J., "State-of-the-art on power line de-icing," Atmospheric Research, vol. 46, page 143-158, 1998. .

[32] Laforte J.L., and Phan, L.C., "Microstructure of ice accretions grown on aluminum conductors," Journal of Applied Meteorology, vol. 22, No. 7, pp.1175-1189, Jul. 1983.

[33] Langmuir, I., and Blodgett, K.B., "Mathematical investigation of water droplet trajectories," Collected works of Irving Langmuir, Pergamon Press, Oxford, pp. 335-393, 1945.

[34] Makkonen, L., "Estimating intensity of atmospheric ice accretion on stationary structures", Journal of Applied Meteorology, vol. 20, pp. 595-600, May. 1981.

[35] Makkonen, L., "Modeling of ice accretion on wires," Journal of Climate and Applied Meteorology, vol. 23, pp. 929–939, 1984.

[36] Makkonen, L., "Heat transfer and icing of a rough cylinder", Cold Regions Science and Technology, vol. 10, pp. 105-116, 1985.

[37] Makkonen, L., "Models for the growth of rime, glaze, icicles and wet snow on structures," Phil. Trans. Royal Soc. London A 358, pp. 2913–2939, 2000.

[38] McComber, P., Nguyen, D.D., et Druez, J., "Prévention par chauffage de la formation de givre de verglas sur les conducteurs cylindriques ou toronnés," Recherche Canadienne en Génie Mécanique, vol. 3, pp. 27-33, 1978.

[39] Mohammadi B., and Pirenneau O., "Analysis of the K-Epsilon Turbulence Model," Research in Applied Mathematics, John Wiley and Sons, 1994.

[40] Morgan, V.T., "The heat transfer from bare stranded conductors by natural and forced convectio in air," International Journal of Heat and Mass Transfer, vol.16, pp. 2023-2034, Pergamon Press, Great Britain, 1973.

[41] Morgan, V.T., "The Overall Convective Heat Transfer from Smooth Circular Cylinders," Advances in Heat Transfer, vol.11, Academic Press, New York, 1975.

[42] Morgan, V.T., "Thermal behaviour of electrical conductors", Taunton, Somerset, England, Research Studies Press, pp. 677-679, 1991.

[43] Munson, B.R., Young, D.F. and Okiishi, T.H., "Fundamentals of Fluid Mechanics," 4th Edition, John Wiley and Sons Inc., 2004.

[44] Ogniewicz, Y., and Yovanovich, M.M., "Effective conductivity of regularly packed sphereds: Basic cell model with constriction," AIAA 15th Aerospace Sciences Meeting, pp.209-228, Los Angeles, California, Jan. 1977.

[45] Ozisik, M.N., "Finite difference methods in heat transfer", CRC Press, Boca Raton, Florida, 1994.

[46] Personne, P., and Gayet, J.-F., "Prevention of wire icing by Joule heating," in Proc. of 3rd IWAIS, Vancouver, Canada, pp. 429-433, 1986.

[47] Personne, P., and Gayet, J.-F., "Ice accretion on wires and anti-icing induced by Joule effect," Journal of Applied Meteorology, vol. 27, no. 2, pp. 101-114, Feb. 1988.

[48] Péter, Zs., "Analysis of the ice shedding due to thermal mechanisms," Diploma Thesis, Budapest, Hungary, 2002.

[49] Péter, Zs., Farzaneh, M., and Kiss, L. I., "Power line conductor icing prevention by the Joule effect: parametric analysis and energy requirements," in Proc. of 11th IWAIS, Montréal, Canada, pp. 361-366, 2005.

[50] Péter, Zs., Farzaneh, M., and Kiss, L. I., "Assessment of the current intensity for preventing ice accretion on overhead conductors," IEEE Transactions on Power Delivery, in press, 2006.

[51] Phan, C.L., et Sévigny, A., "Recherche sut le dégivrage des lignes de transport d'énergie électrique", L'Ingénieur, pp. 3-8, Jul.-Aug. 1978.

[52] Poots, G., "Ice and Snow Accretion on Structures," Research Studies Press, Taunton, Somerset, England, 1996.

[53] Postásy, R., "Tranziens hőátadás vizsgálata optikai módszerekkel," PhD dissertation, Budapest, Hungary, 1988.

[54] Ražnjević, K., "Handbook of thermodynamic tables and charts", Hemisphere Publishing Corporation, 1976.

[55] Sanitjai S. and Goldstein R.J., "Forced convection heat transfer from a circular cylinder in crossflow to air and liquids", International Journal of Heat and Mass Transfer, vol.47, pp. 4795-4805, Elsevier Ltd., 2004.

[56] Seshadri S.R., "Fundamentals of transmission lines and electromagnetic fields," Addison-Wesley Publishing Company, Don Mills, Ontario, 1971.

[57] Stewart, R.E., Crawford, R.W., Donaldson, N.R., Low T.B., and Sheppard, B.E., "Precipitation and environmental conditions during accretion in Canadian east cost winter storms," Journal of Applied Meteorology, vol. 29, pp.525-538, Jul. 1990.

[58] Touloukian, Y.S., Powell, R.W., Ho, C.Y., and Klemens, P.G., "Thermal conductivity: metallic elements and alloys," The TPRC Data Series, Ifi-Plenum, New York, 1970.

[59] Vieser, W., Esch, T. and Menter, F., "Heat transfer predicctions using advanced two-equation turbulence models," CFX Validation Report (CFX-VAL10/1002), AEA Technology.

[60] Whitaker S., "Forced convection heat transfer correlations for flow in pipes, past flat plates, single cylinders, single spheres, and for flow in packed beds and tube bundles," AlChe Journal, vol. 18, No.2, pp.361-371, March, 1972.

[61] Wilcox, D.C., "Turbulence modeling for CFD," Second Edition, DCW Industries INC., pp. 540, La Canada, USA, 2000.

[62] Zhukauskas, A., "Heat transfer from a single tubes and banks of tubes in crossflow," Heat and mass transfer in boundary layer, vol. 2., pp. 843-865, Pergamon Press Inc., Oxford, 1972.

APPENDIX 1 WETTED SURFACE OF STRANDED CONDUCTOR

The wetted surface of stranded conductor in air/water spray flow is analysed in this section. Wind tunnel observations have been made in order to improve the knowledge about the wetted mechanisms such as runback droplets, water layer detachments and droplet flow in the inter-strand channels. Finally, different cases/classification are distinguished depending on the actual/corresponding physical processes occurred under various atmospheric conditions (wind speed and LWC).

Observatory tests have been performed in CIGELE wind tunnel on ACSR conductor with code word GEANT 5P. The conductor was placed perpendicular into the air/water spray flow. The tests were repeated under various sets of wind speed and LWC (precipitation rate). Large number of images was taken from the wetted surface, from which just the most successful are presented in the following section.

Wetted surface on windward side of conductor

Generally, water droplets are present on strands and in the inter-strand channels. However, continuous water layer is not observed on the windward surface of conductor under atmospheric conditions of investigations. At wind velocity of 20 m/s the water droplets are driven by airflow into the channels, where they are conducted either toward top or toward bottom of the conductor depending on the initial droplet location on the windward surface. The same process is observed at 30 m/s just much faster.

On windward surface below the stagnation point at 10 m/s wind speed, certain droplets may step out from the inter-strand channel and over cross/pass few strands before falling down at -90° (bottom of the conductor) due to gravity force. At higher wind speed of 20 m/s the droplets are conducted strictly in inter-strand channels below the stagnation point. At 30 m/s wind speed, probably, the water is forced under the outside strand layer. On windward surface above the stagnation point at wind speed of 20 m/s, certain droplets are taken away by the airflow. This was not observed at 10 m/s. At stronger wind velocity of 30 m/s, one part of the water layer is detached in this section of the surface.

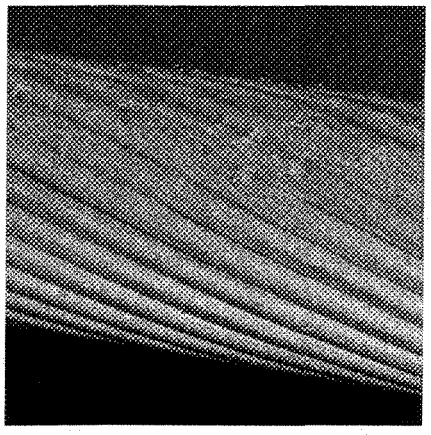

At 20 m/s wind speed and 6.6 g/m^3 of LWC

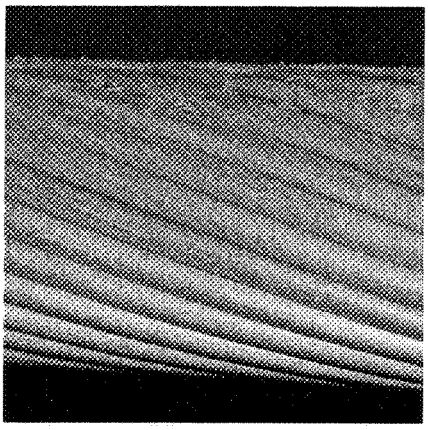

At 20 m/s wind speed and 8.5 g/m^3 of LWC

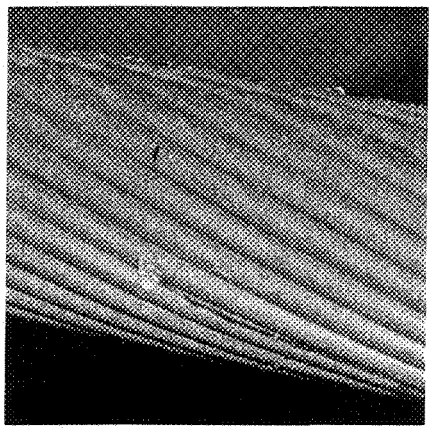

At 30 m/s wind speed and 5.3 g/m^3 of LWC

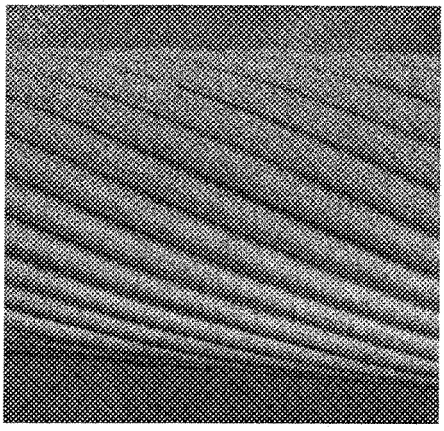

At 10 m/s wind speed and 5.6 g/m^3 of LWC

Water layer on the top of conductor

As it is was mentioned, certain water droplets from windward surface are conducted to the top of the conductor in inter-strand channels. A "top water layer" was developed in windward side around 80°÷85° at 10 m/s, and near 90° (top) at 20 and 30 m/s wind velocities. This water layer at top of conductor is not continuous along the length of conductor, except at extremely high LWC (it was observed at LWC of 8.5 g/m^3 and 20 m/s wind speed). One part of the "top water layer" is driven away by the airflow at stronger wind velocities of 20 and 30 m/s, while the rest of water layer runs toward the leeward side of conductor.

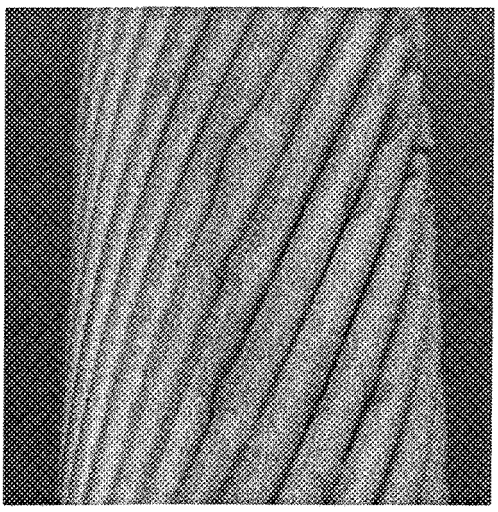

At 10 m/s wind speed and 5.6 g/m^3 of LWC

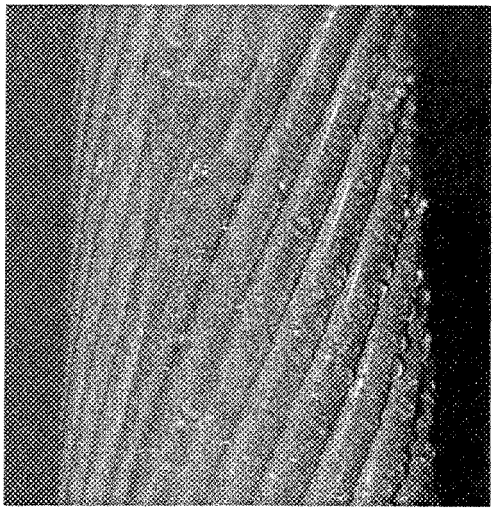

At 30 m/s wind speed and 5.3 g/m^3 of LWC

Water layer detachment at bottom of conductor

At bottom of conductor at higher wind velocities of 20 and 30 m/s, the water detachment occurs on the greater surface as in the case of 10 m/s wind speed (just near -

90°). The water layer detaches at higher wind velocities on the leeward side (appr. in section -90÷-95°).

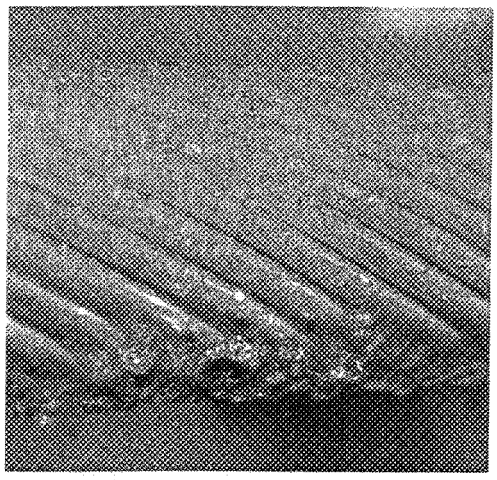

At 20 m/s wind speed and 6.6 g/m^3 of LWC

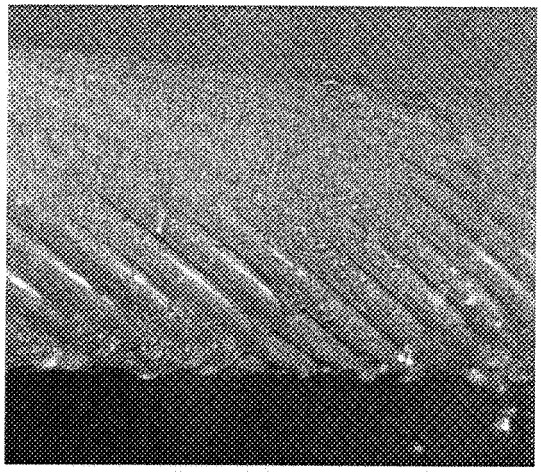

At 20 m/s wind speed and 8.5 g/m^3 of LWC

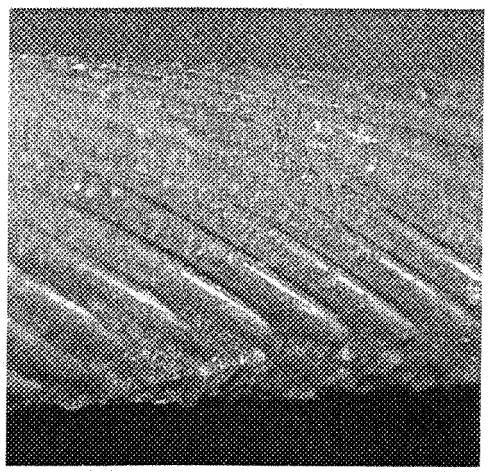

At 30 m/s wind speed and 5.3 g/m^3 of LWC

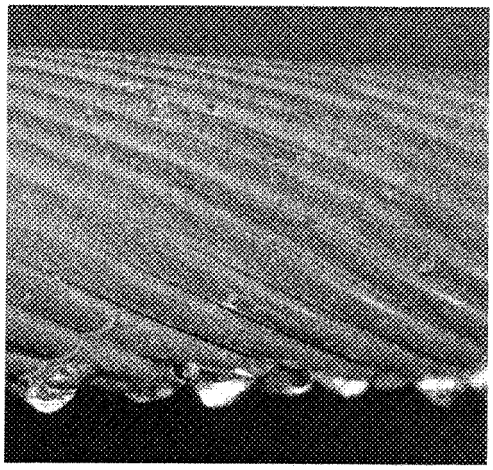

At 10 m/s wind speed and 5.6 g/m^3 of LWC

At 10 m/s wind speed, the water detachment at bottom of the conductor is mainly governed by the gravity force, while at 20 and 30 m/s the water layer detachment is influenced by aero-dynamical forces too (it detaches in the direction of the airflow). The

detached water layer at bottom of conductor collects also the runback water from leeward side as well as water droplets from the windward side.

Wetted surface on leeward side of the conductor

A certain part of the leeward surface is covered by the "stationary" water droplets caused by the by-pass water/air dispersed flow. At 20 and 30 m/s wind speed, water runback is observed from windward to leeward side. This was observed at 10 m/s wind velocity just rarely. Two kind of water runback can be distinguished depending on the droplet motion: "slow" and "fast" water runback. A so-called "fast" water runback is triggered by the water layer detachment at the top of the conductor. It rolls relatively fast cross the leeward surface. The "slow" droplet runback is conducted from the windward channel. It flows slowly, and it crosses the strands step by step. It rolls over one or two strands and then it continues to flow in surface channel. After a certain time, the droplet again steps out from the channel and it crosses one or more strands before flowing again in the channel. Finally, the runback water is detached with the water layer from the windward side at the bottom of conductor. At 30 m/s wind speed, the "stationary" sprays are much more frequent as the runback droplets. At 10 m/s wind speed the "stationary" sprays are not observed. Obviously, the amount of the observed "stationary" sprays increases with the LWC (comparing the cases of 6.6 g/m^3 and 8.5 g/m^3 at 20 m/s).

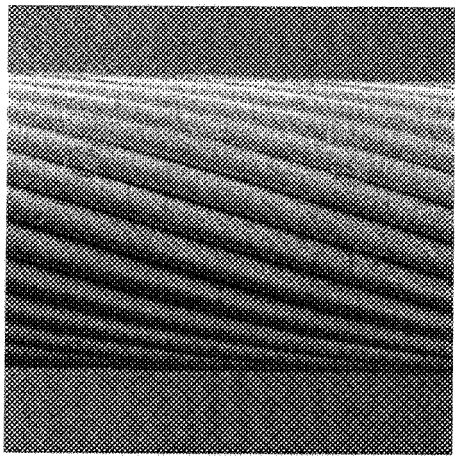

At 10 m/s wind speed and 5.6 g/m^3 of LWC

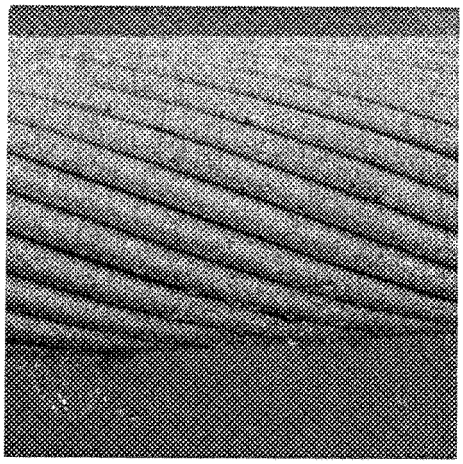

At 20 m/s wind speed and 6.6 g/m^3 of LWC

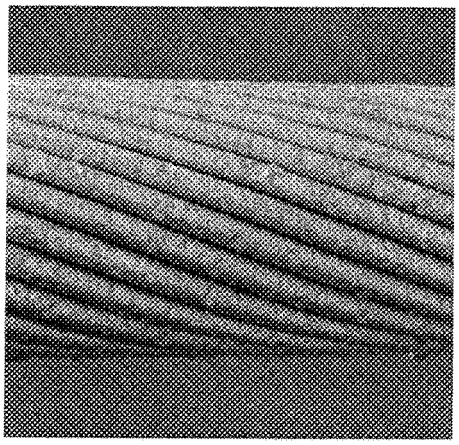

At 30 m/s wind speed and 5.3 g/m^3 of LWC

APPENDIX 2 DE-ICING OF NON-ROTATING CONDUCTORS BY IMPULSE CURRENT HEATING

Effect of geometry mesh and differential modulus of the EFD model

Results obtained for various model set-ups using parameters described in section 5.1.7.

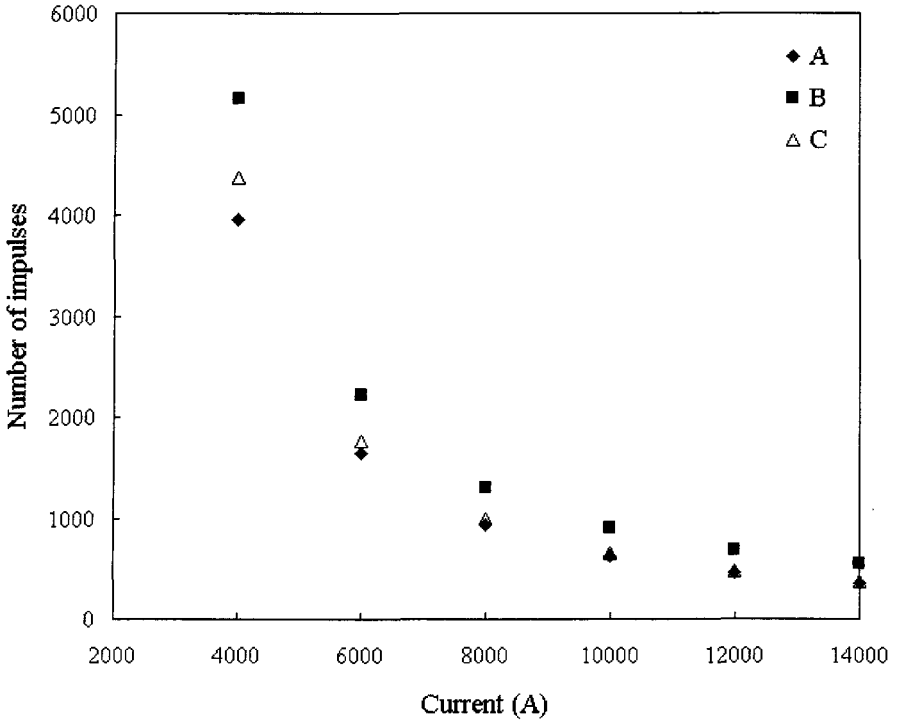

Number of required impulses obtained with different EFD model set-ups

Temperature distribution in conductor-ice sleeve composite at various peak currents and shedding condition

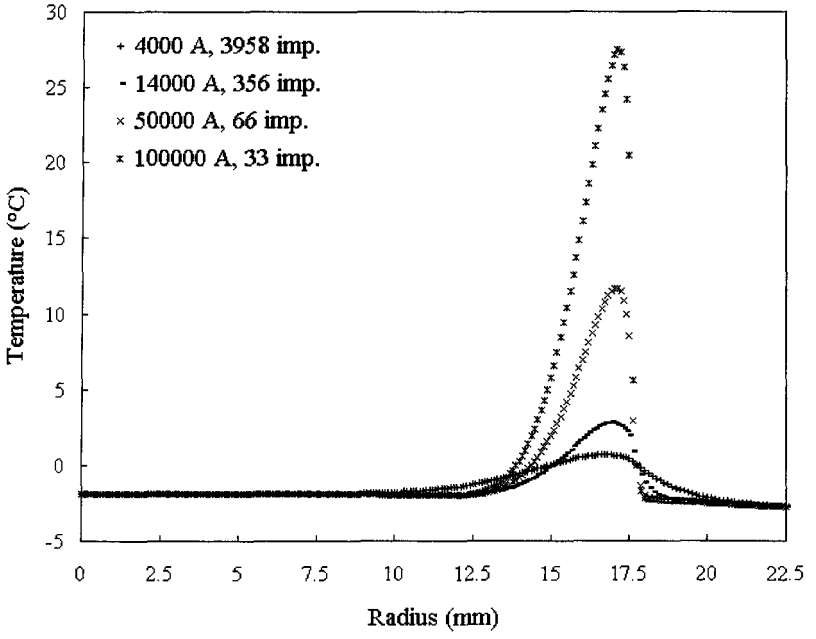

Temperature distribution after last applied impulse at1273.2 Hz

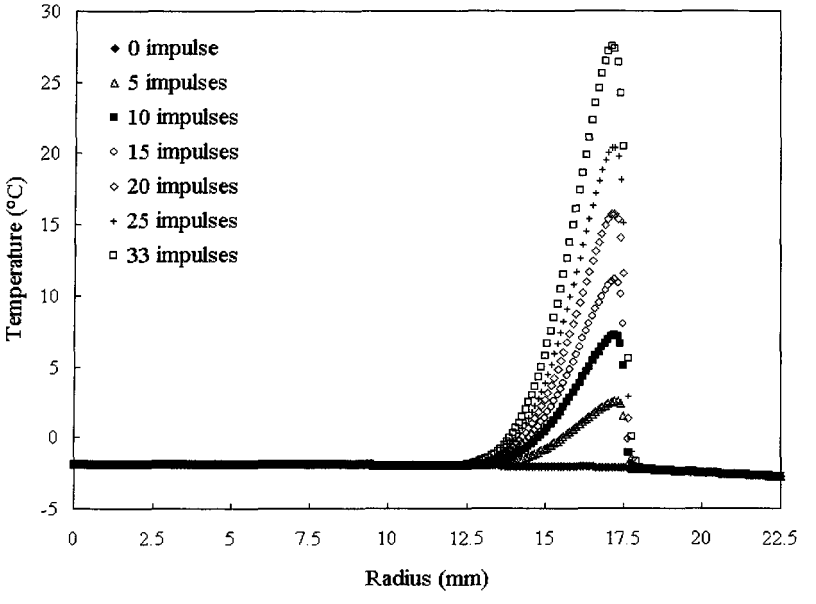

Temperature distribution at 1273.2 Hz and 100 000 A

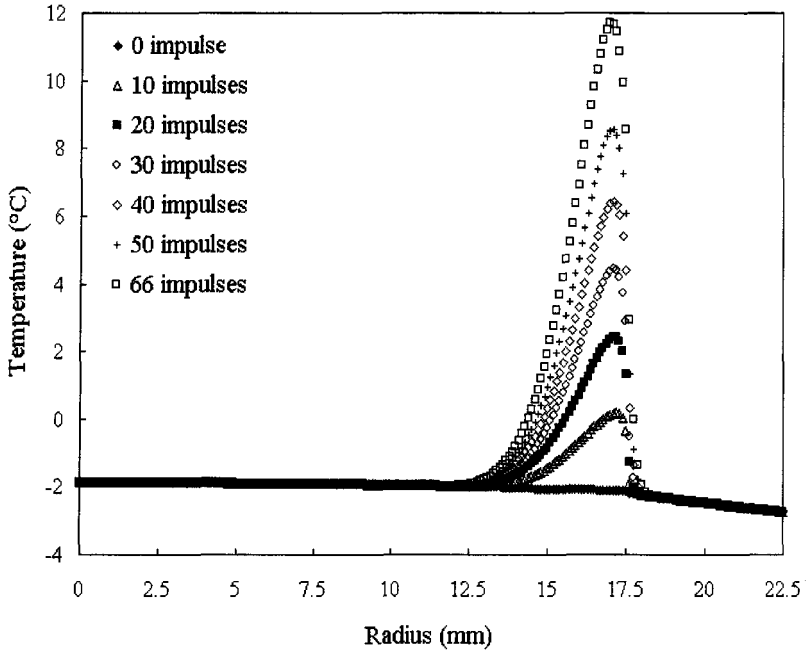

Temperature distribution at 1273.2 Hz and 50 000 A

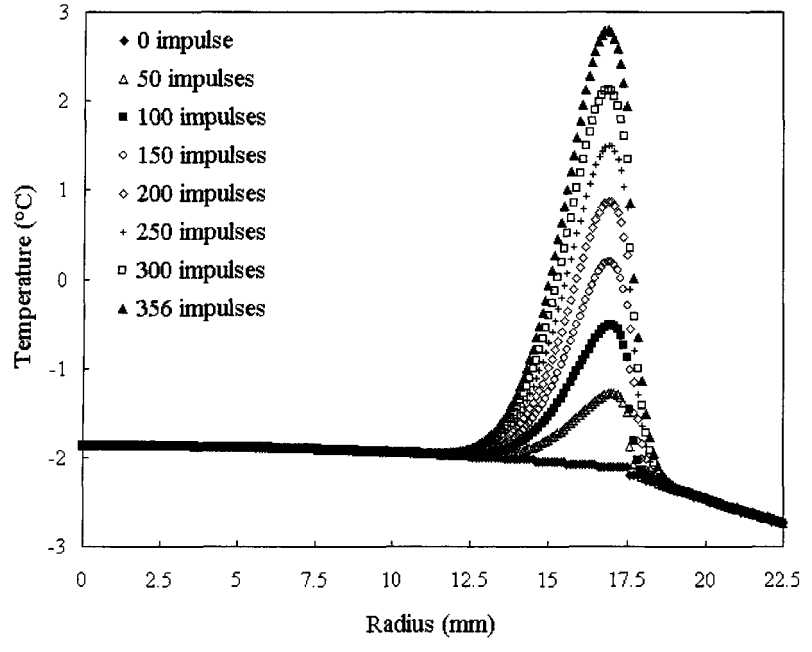

Temperature distribution at 1273.2 Hz and 14 000 A

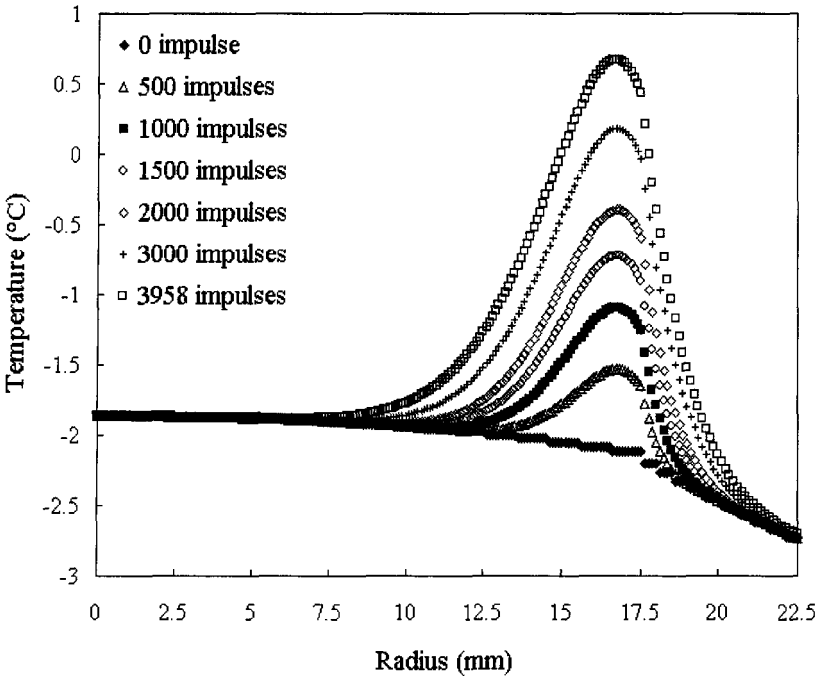

Temperature distribution at 1273.2 Hz and 4000 A

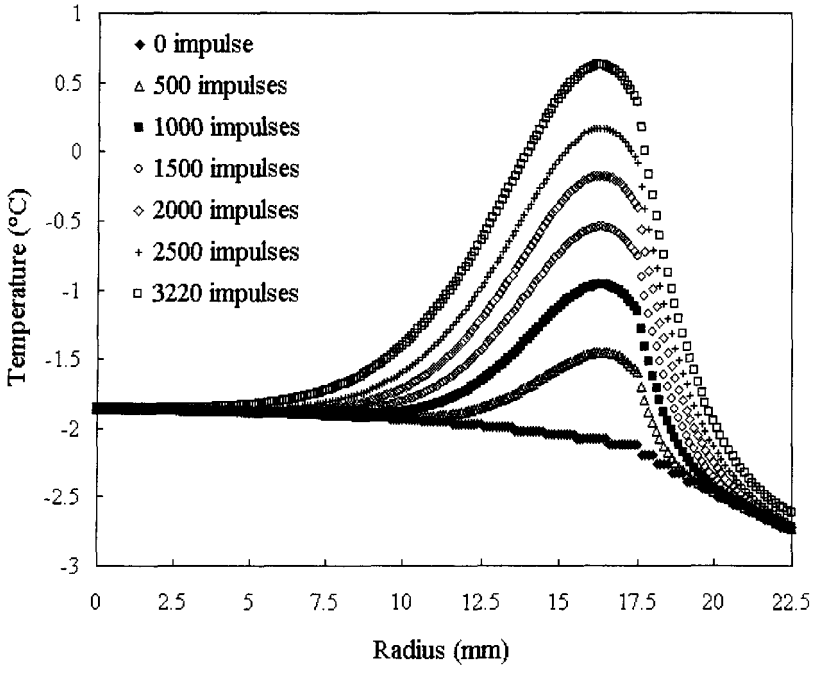

Temperature distribution at 636.6 Hz and 4000 A

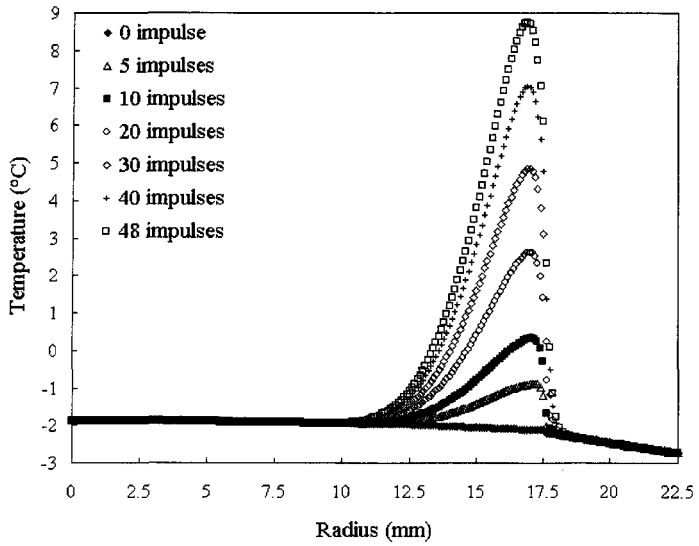

Temperature distribution at 636.6 Hz and 50 000 A

Effect of equivalent thermal conductivity

Simulation parameters described in section 5.1.11.

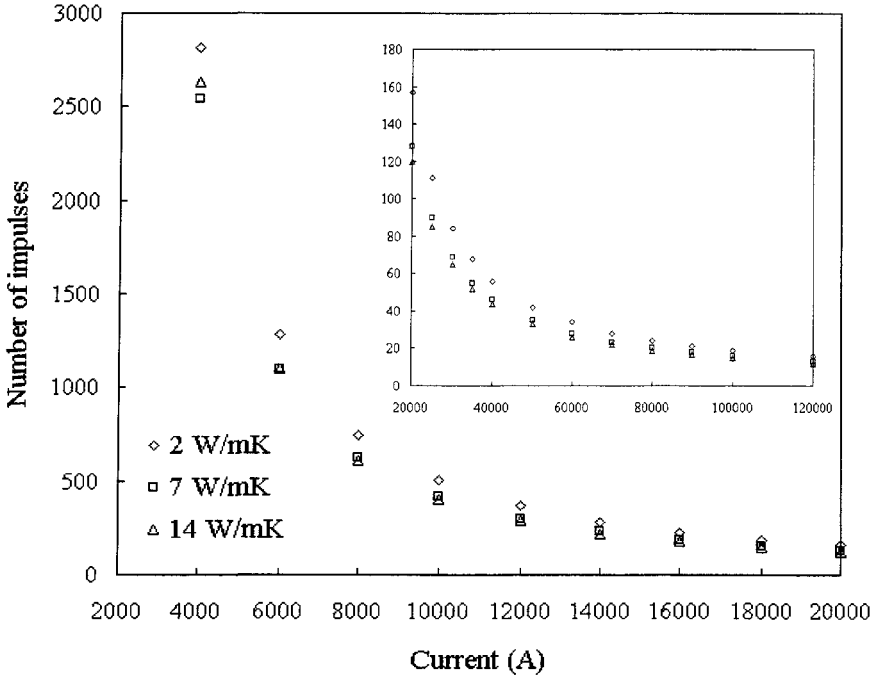

Number of impulses required to shed the ice layer from the conductor

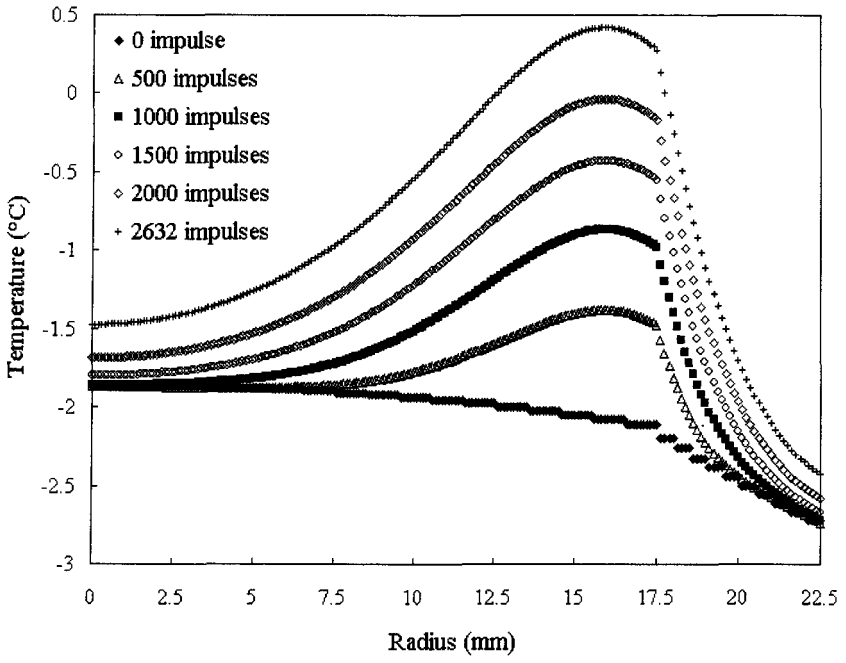

Temperature distribution at 318.3 Hz equivalent frequency, equivalent thermal conductivity of 14 W/mK and 4000 A peak current

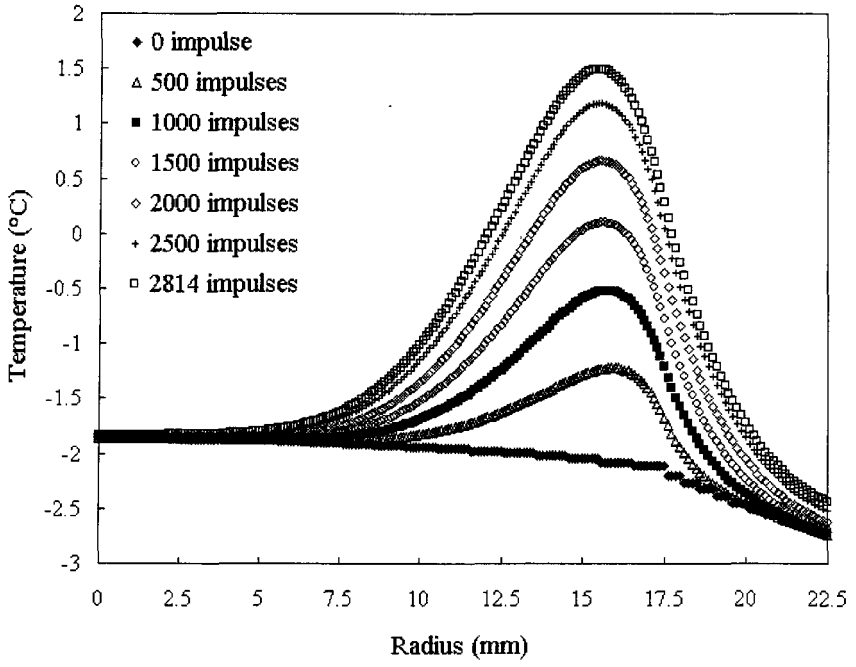

Temperature distribution at 318.3 Hz equivalent frequency, equivalent thermal conductivity of 2 W/mK and 4000 A peak current

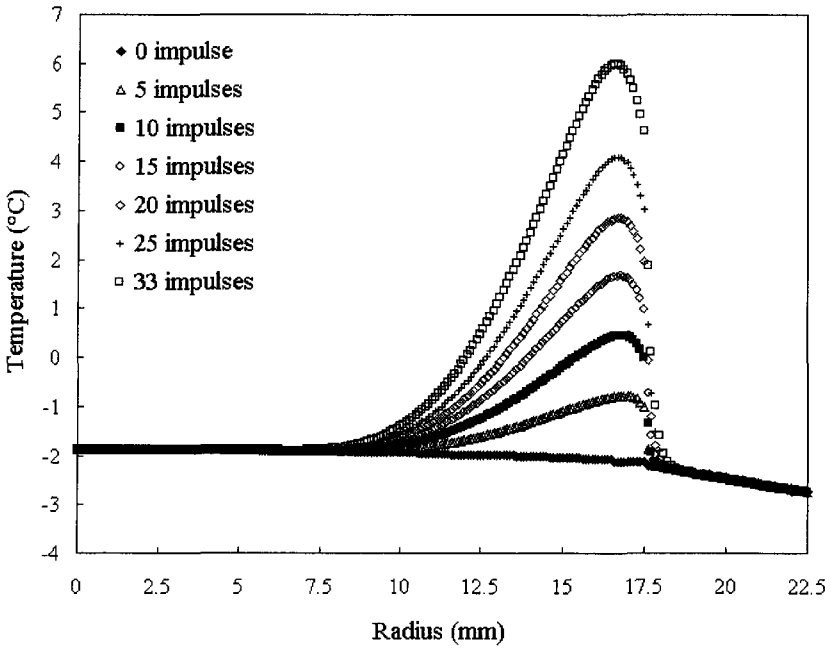

Temperature distribution at 318.3 Hz equivalent frequency, equivalent thermal conductivity of 14 W/mK and 50000 A peak current

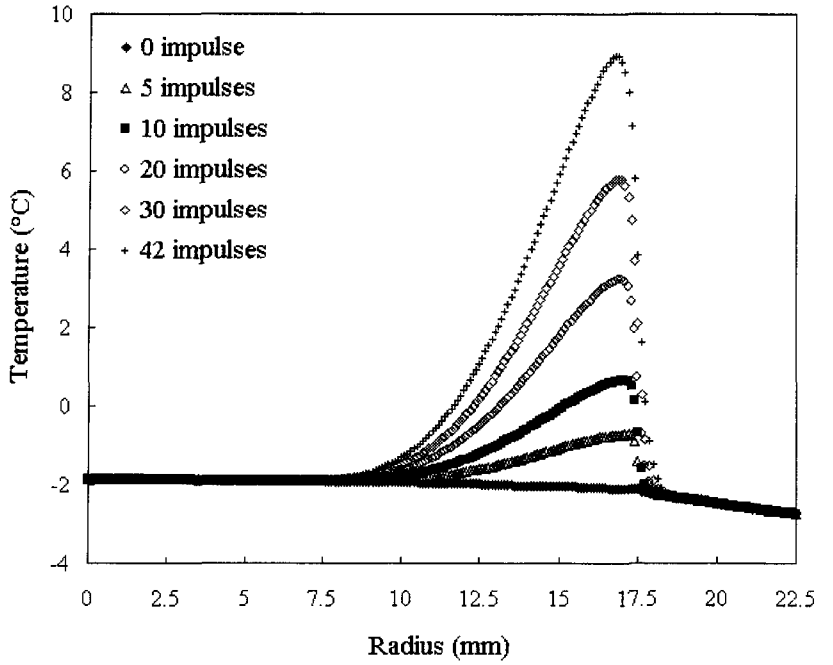

Temperature distribution at 318.3 Hz equivalent frequency, equivalent thermal conductivity of 2 W/mK and 50000 A peak current

Effect of ice thickness

Simulation parameters described in section 5.1.12.

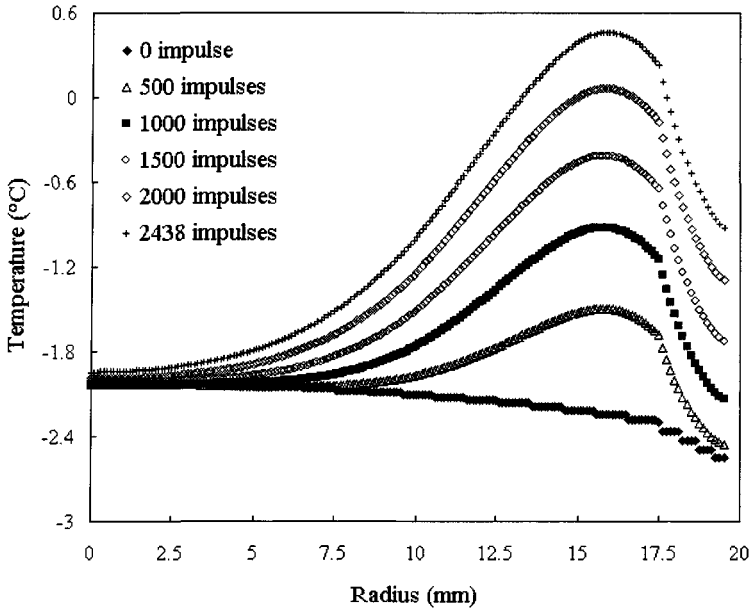

Temperature distribution with 2 mm thick ice and 4000 A

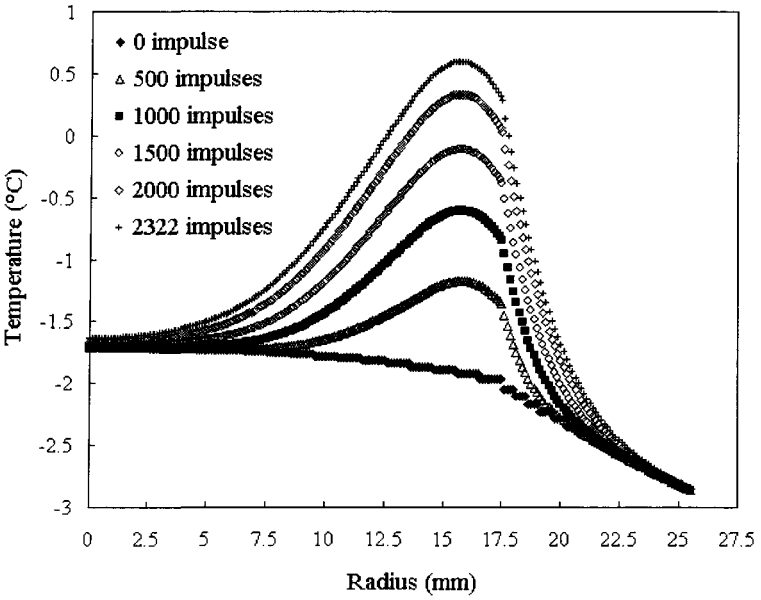

Temperature distribution with 8 mm thick ice and 4000 A

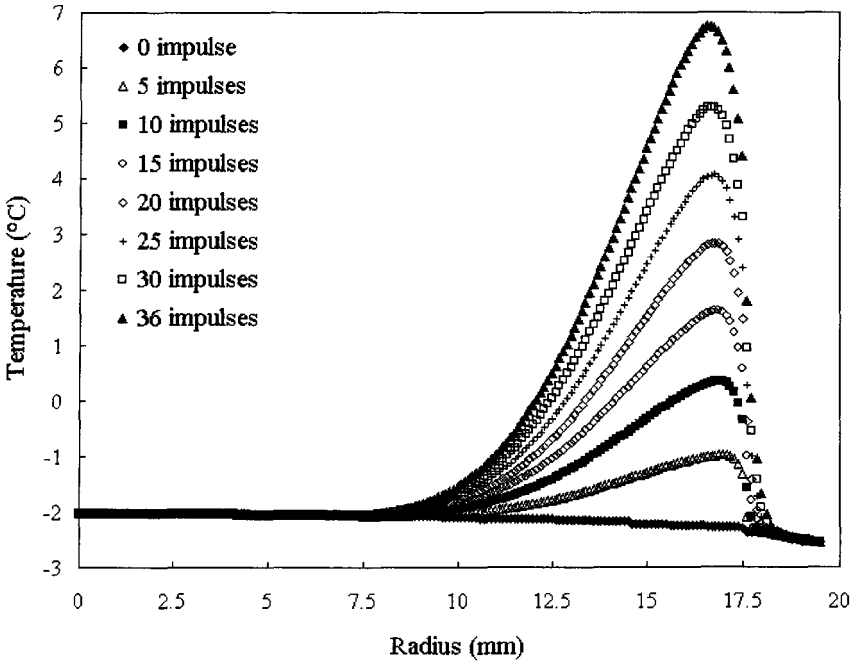

Temperature distribution with 2 mm thick ice and 50 000 A

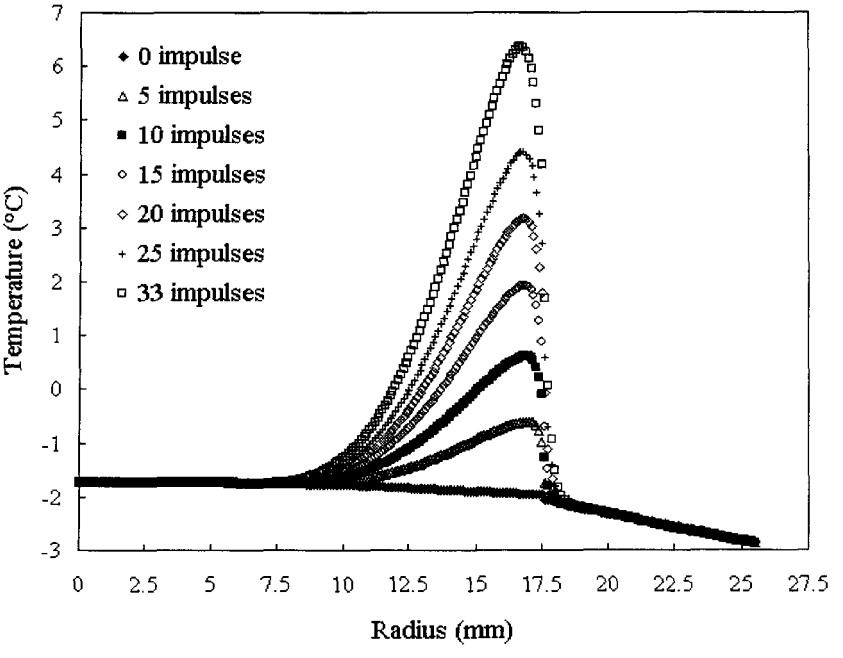

Temperature distribution with 8 mm thick ice and 50 000 A

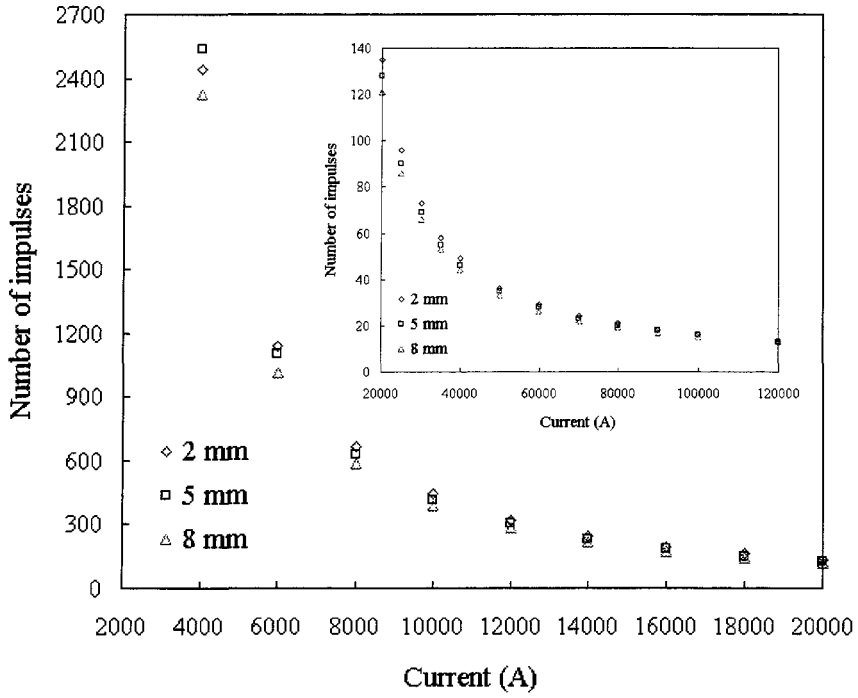

Required number of impulses for various ice thickness on the conductor

Effect of air temperature

Simulation parameters described in section 5.1.13.

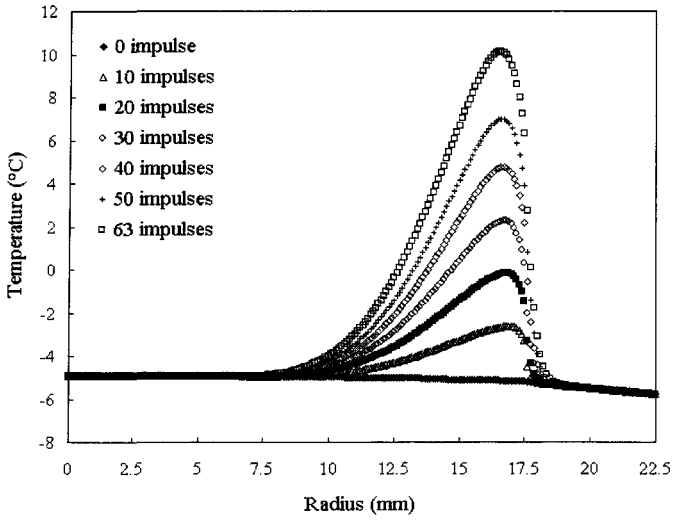

Temperature distribution with 50 000 A at -8 °C

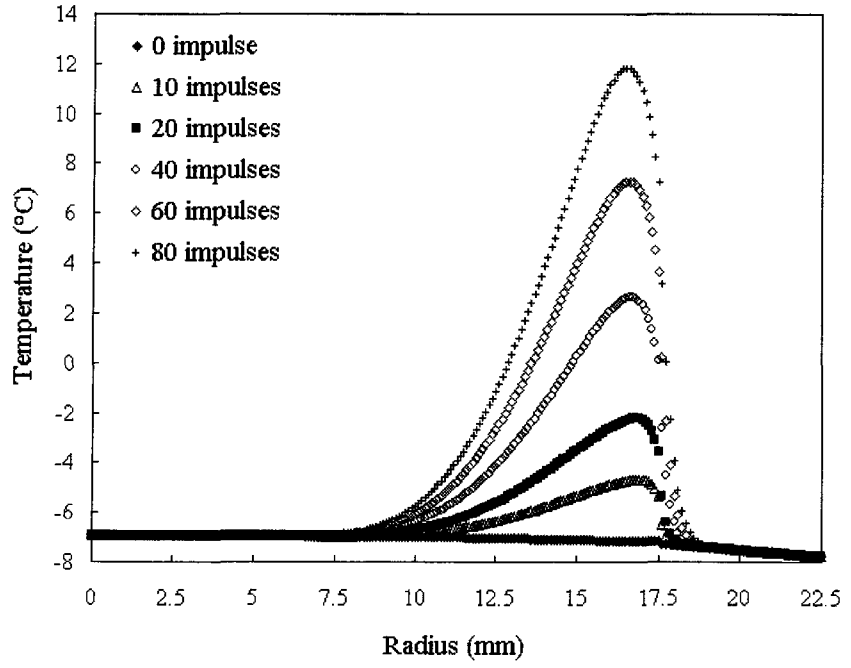

Temperature distribution with 50 000 A at -10 °C

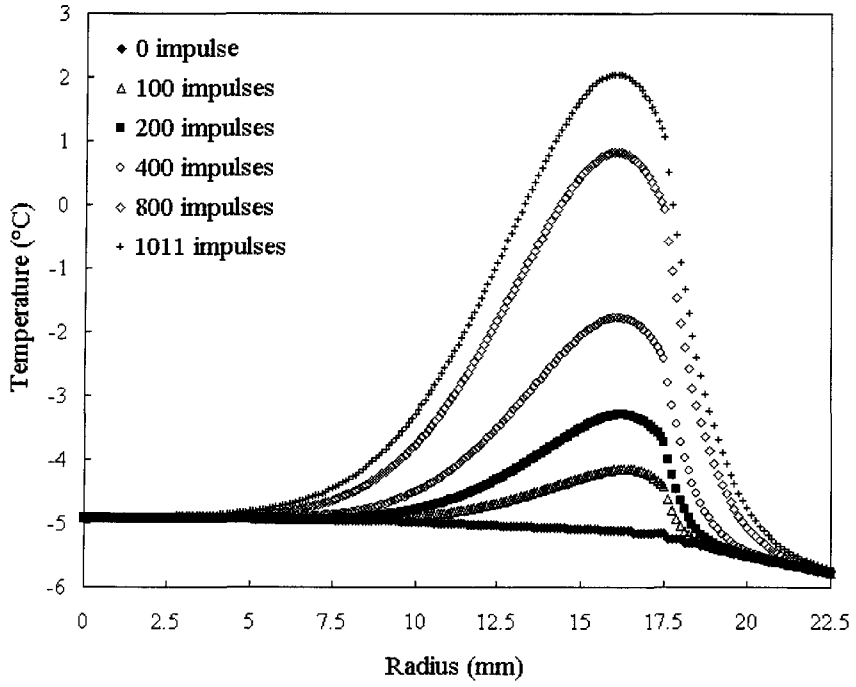

Temperature distribution with 10 000 A at -8 °C

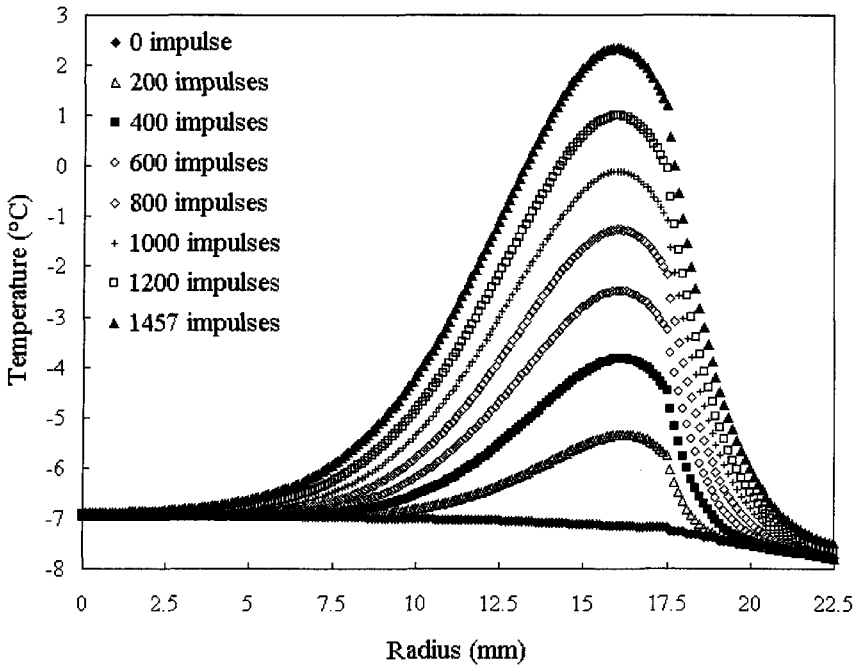

Temperature distribution with 10 000 A at -10 °C

APPENDIX 3 DE-ICING OF NON-ROTATING CONDUCTOR BY 60 HZ, AC CURRENT HEATING

Effect of wind velocity

Temperature distribution in conductor-ice composite under high currents

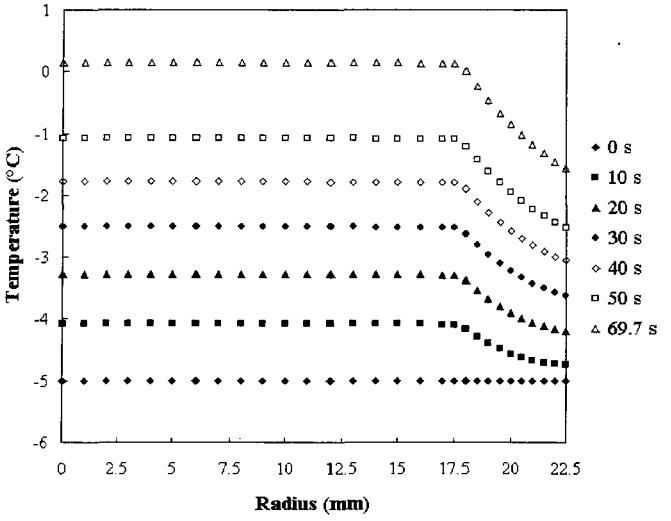

At 20 m/s wind speed, -5°C air temperature, 5 mm ice thickness and 3000A electric current

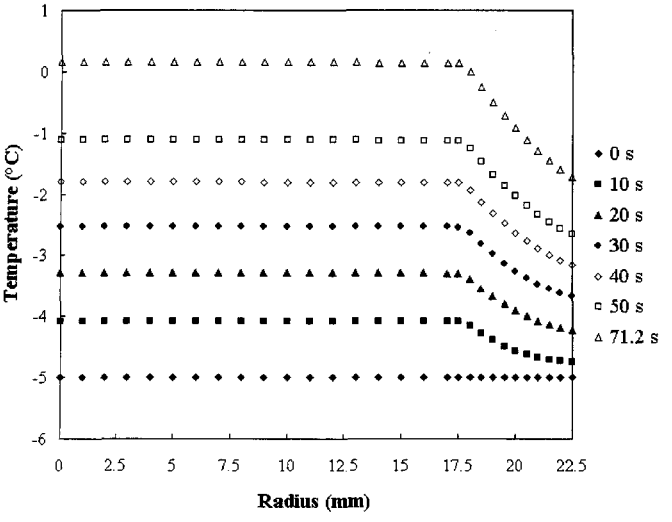

At 30 m/s wind speed, -5°C air temperature, 5 mm ice thickness and 3000A electric current

Temperature distribution in conductor-ice composite under low currents

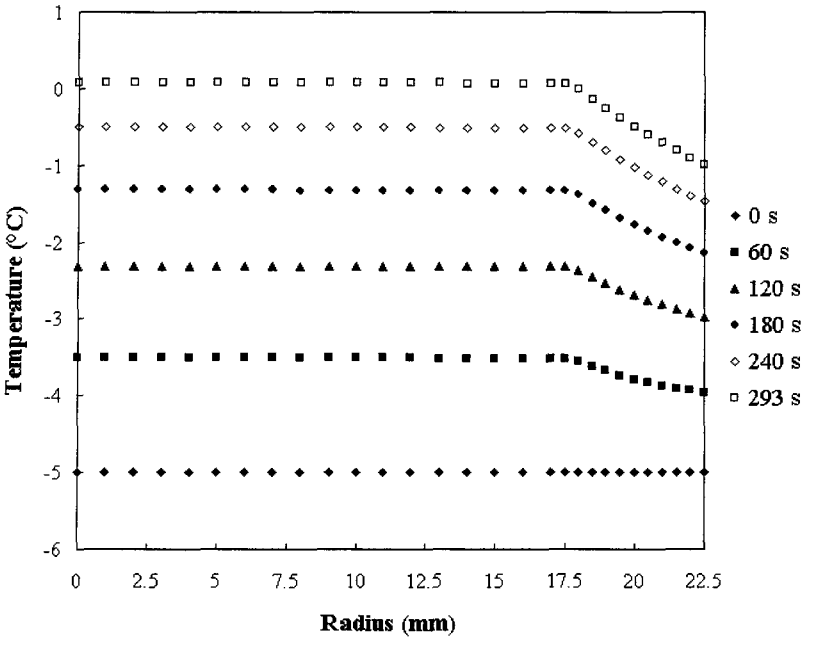

At wind speed of 10 m/s, -5 °C air temperature, 5 mm ice thickness, 1700 A electric current

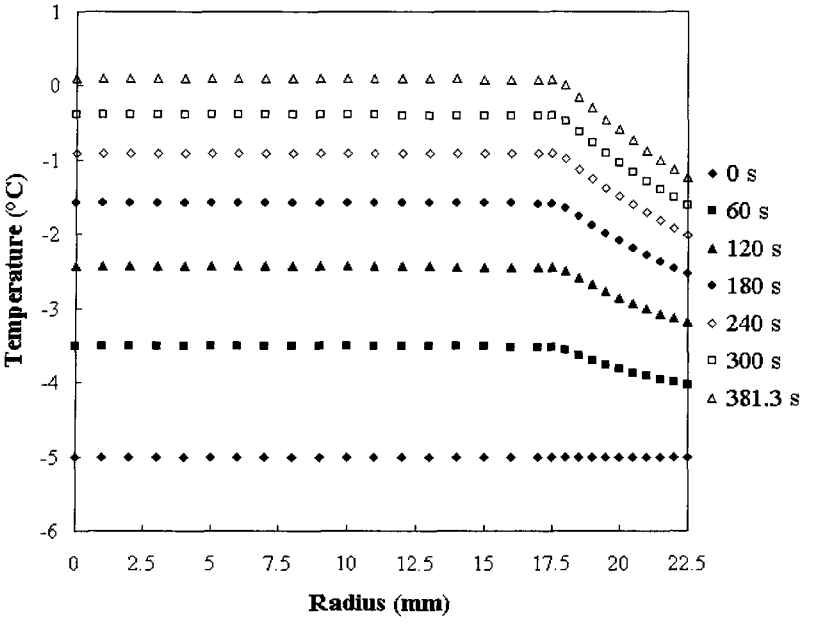

At wind speed of 20 m/s, -5 °C air temperature, 5 mm ice thickness, 1700 A electric current

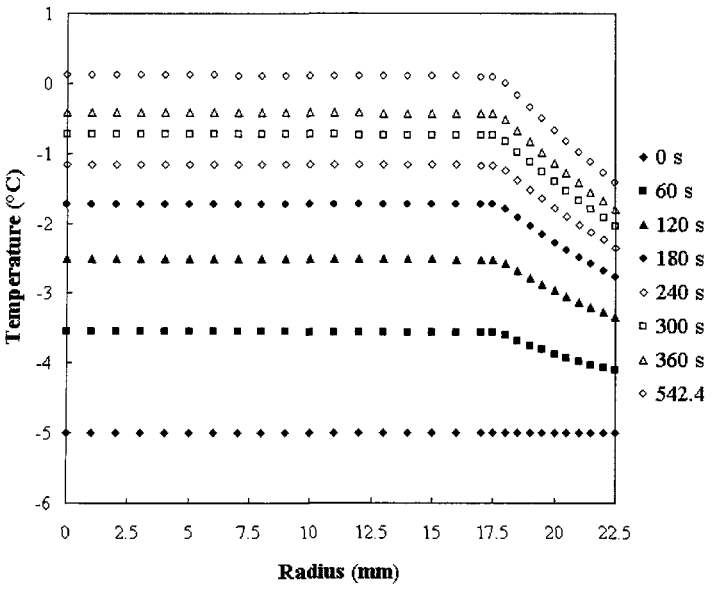

At wind speed of 30 m/s, -5 °C air temperature, 5 mm ice thickness, 1700A electric current

Comparing ice shedding using AC and DC currents from energy economisation aspect

Simulations described in 5.2.3.

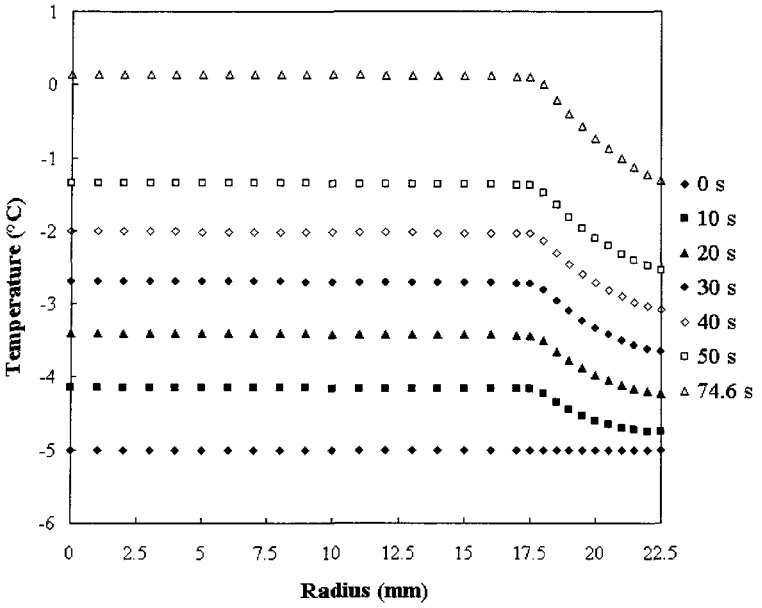

At wind velocity of 10 m/s, -5 °C air temperature, 5 mm ice thickness, DC current of 3000 A

Effect of equivalent thermal conductivity

Simulation parameters introduced in 5.2.4.

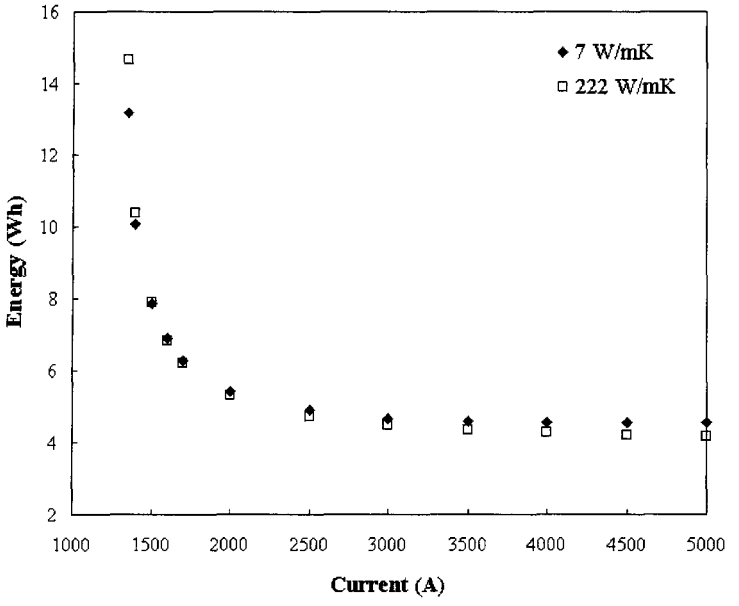

Required energy versus electric current for different equivalent thermal conductivities

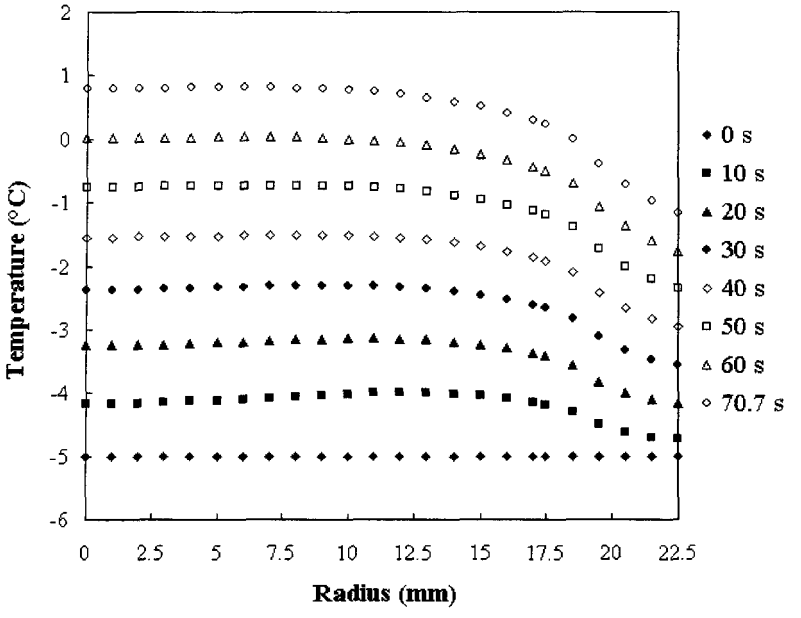

Temperature distribution obtained for wind speed of 10 m/s, -5 °C air temperature, 5 mm ice thickness, AC current of 3000 A and thermal conductivity of 7 W/mK

Effect of air temperature

Simulation parameters introduced in 5.2.5.

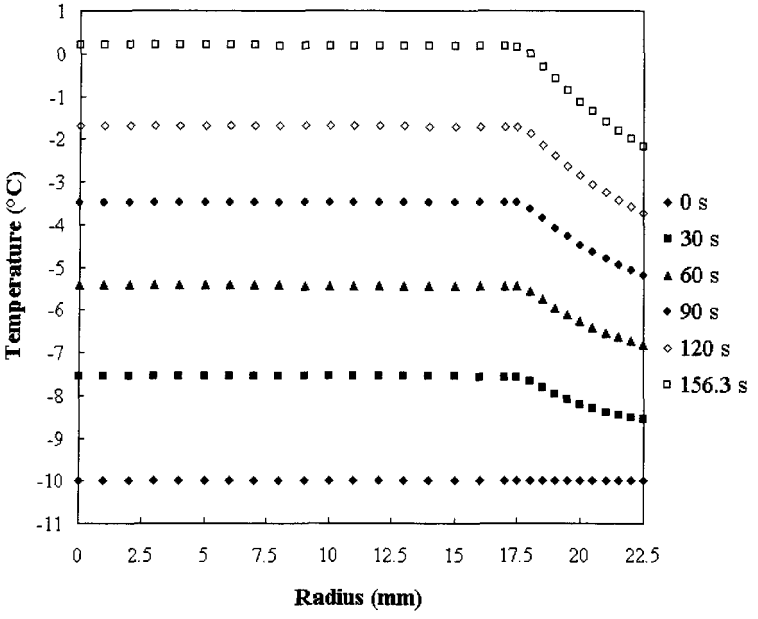

Temperature distribution obtained for wind speed of 10 m/s, -10 °C air temperature, 5 mm ice thickness, AC current of 3000 A

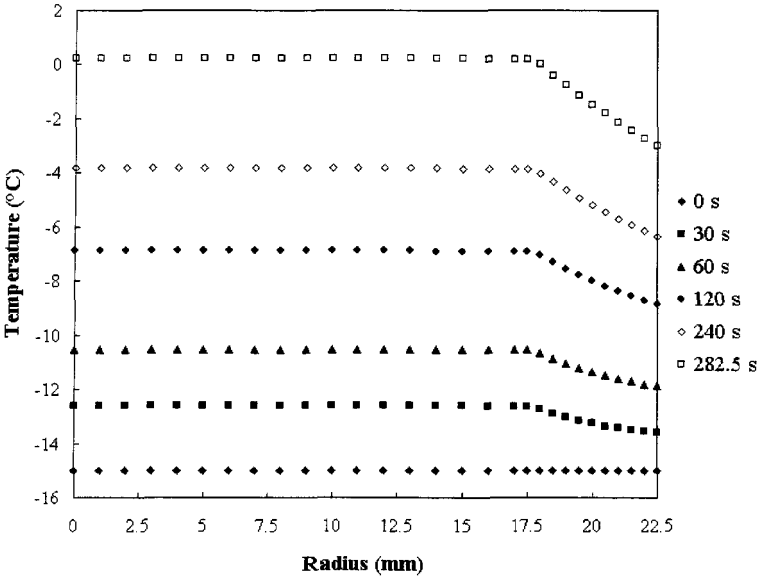

Temperature distribution obtained for wind speed of 10 m/s, -15 °C air temperature, 5 mm ice thickness, AC current of 3000 A

Effect of ice thickness

Simulation parameters introduced in 5.2.6.

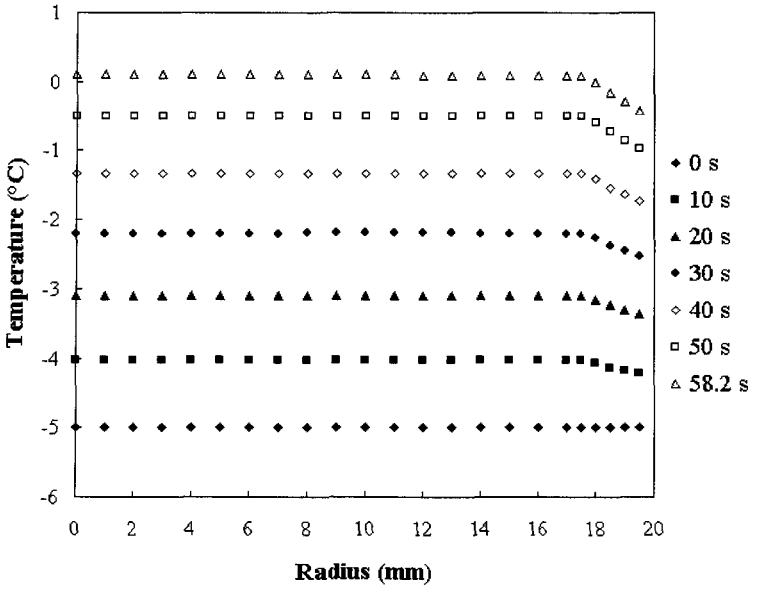

Temperature distribution obtained for wind speed of 10 m/s, -5 °C air temperature, 2 mm ice thickness, AC current of 3000 A

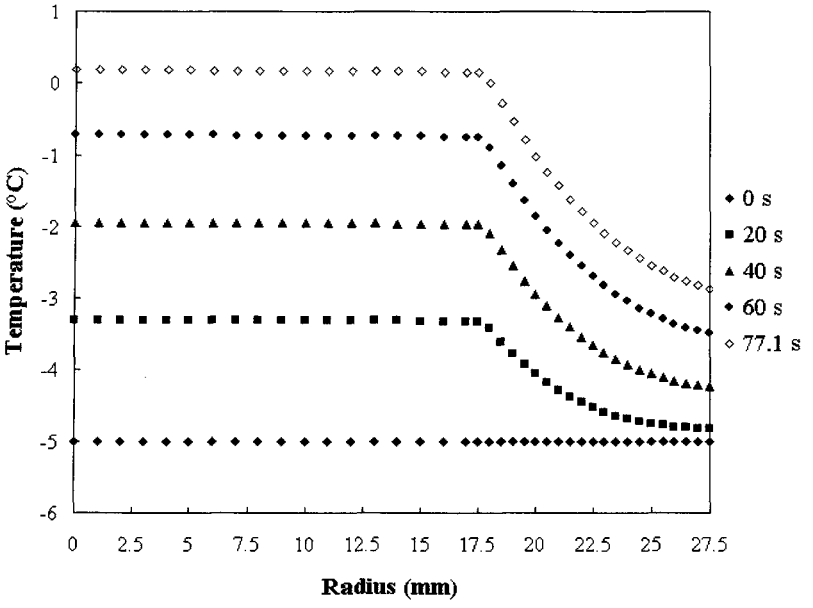

Temperature distribution obtained for wind speed of 10 m/s, -5 °C air temperature, 10 mm ice thickness, AC current of 3000 A

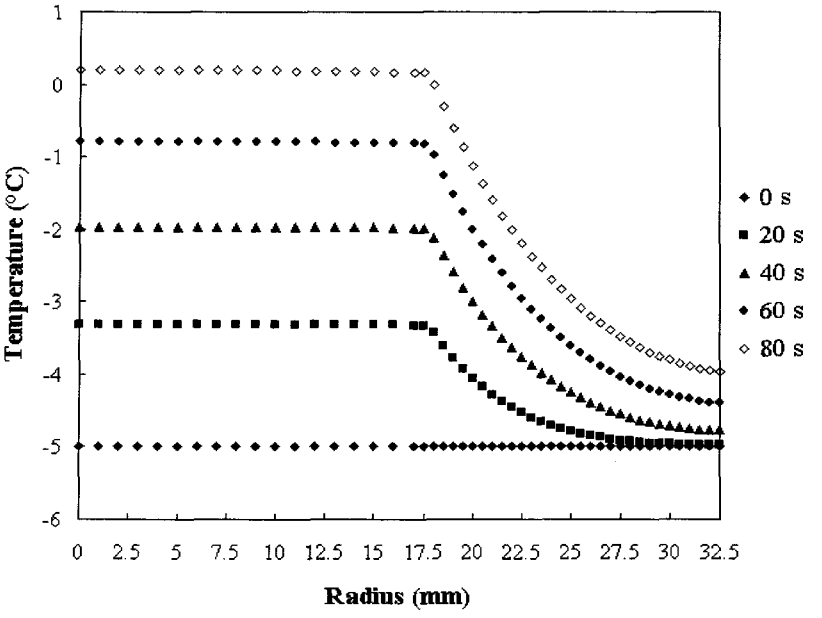

Temperature distribution obtained for wind speed of 10 m/s, -5 °C air temperature, 15 mm ice thickness, AC current of 3000 A

APPENDIX 4 EXPERIMENTAL STUDY OF DE-ICING BY JOULE HEATING

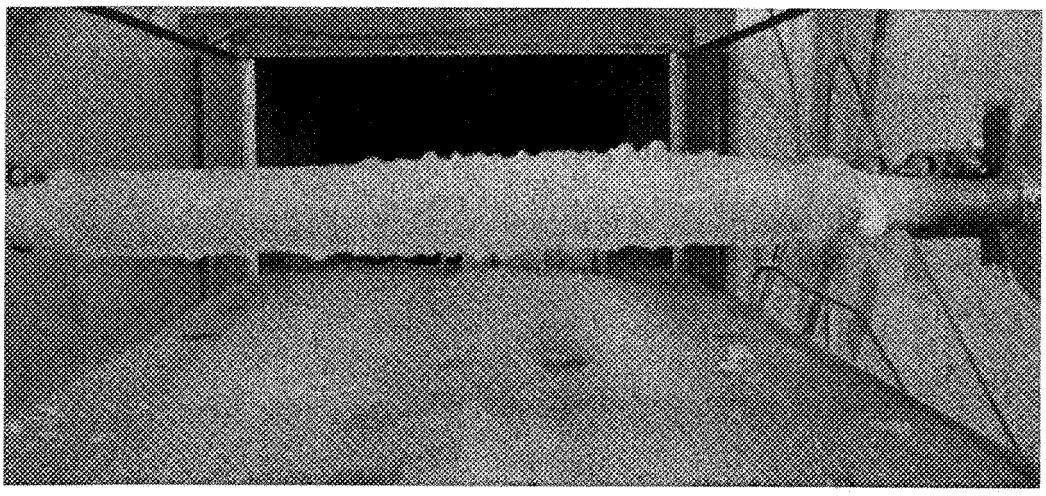

End of ice accumulation process

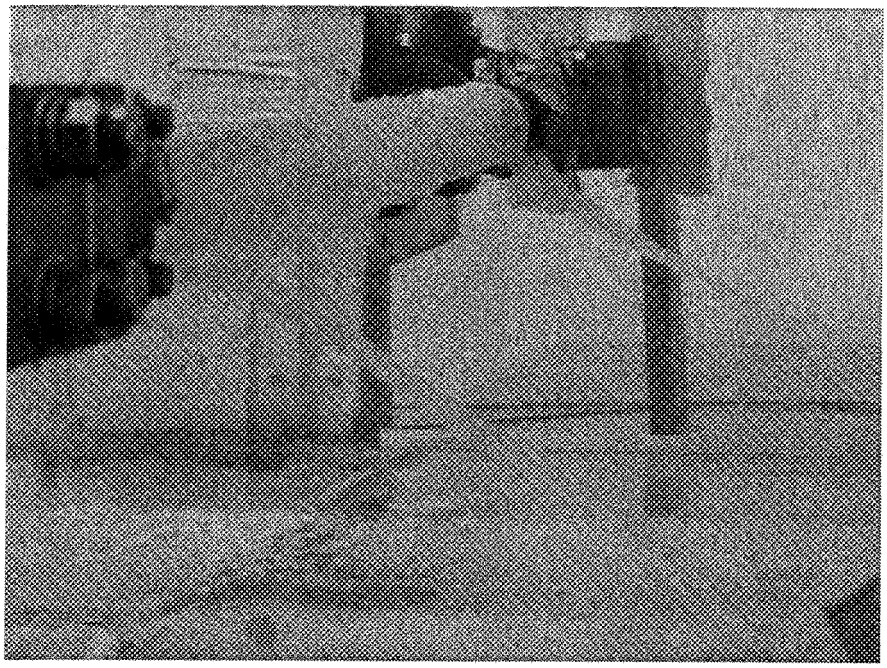

Rotated ice sleeve due to wind force on icicles

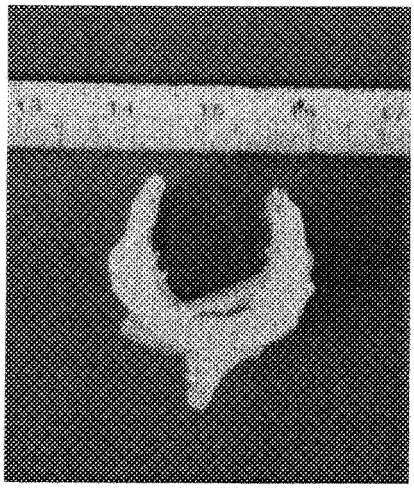

Cross-section of removed ice sleeve, relatively small electric current intensity, validation case with electric current of 1700 A, wind speed of 10 m/s and -10 °C air temperature

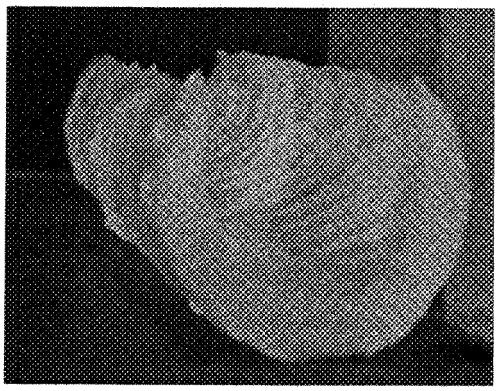

Patterns of the outer strands inside of the ice core, validation case N° 3

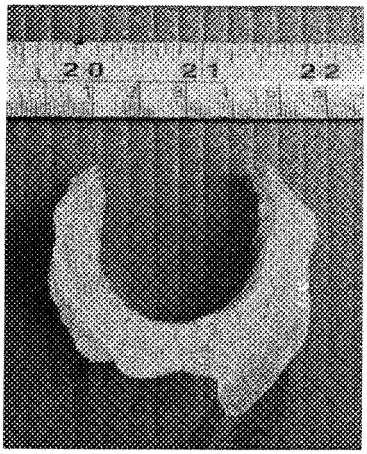

Cross-section of the removed ice sleeve, validation case N° 4

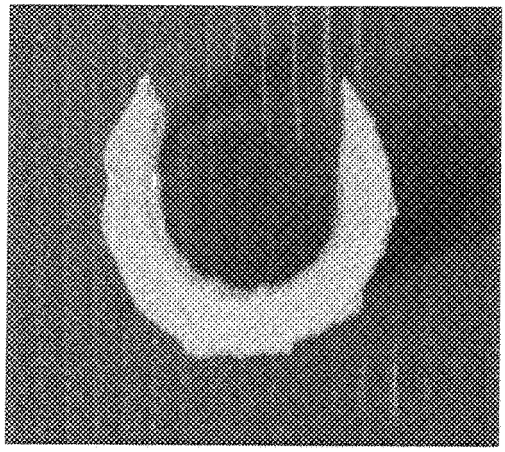

Cross-section of the removed ice sleeve, validation case N° 5

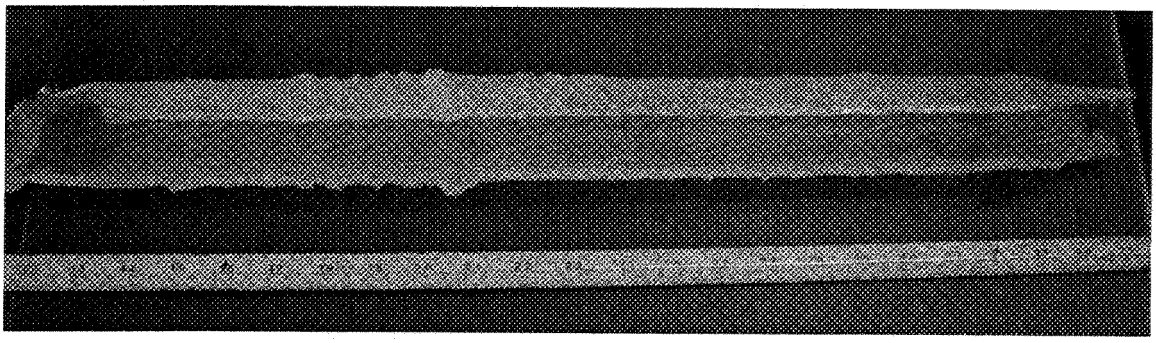

Removed ice sleeve, validation case N° 3

Atmospheric parameters measured during ice accumulation in wind tunnel

N°	Wind speed (m/s)	Air temperature (°C)	LWC* (g/m^3)	MVD* (μm)	RH (%)	Duration (min)	Ice diameter (mm)
6.	7.0	-4.4	3.901	51.18	98	60	46.3
7.	6.9	-4.4	3.825	51.18	97	60	45.2
8.	7.3	-4.4	4.125	51.18	97	60	46.9
9.	9.0	-9.8	5.329	51.18	94	60	64.0
10.	9.4	-9.7	5.563	51.18	94	60	62.0
11.	8.9	-9.7	5.262	51.18	94	60	63.0

APPENDIX 5 SIMULATING THE FLOW FIELD IN A WIND TUNNEL

The airflow in the tunnel is simulated by CFD code (CFX-5.6) based on the finite volume technique. The boundary conditions are applied at the spray bar section (inlet) and at the center of test section (outlet). The inlet and outlet velocities are prescribed in Cartesian coordinate system. The boundary condition at inlet corresponds to the measured velocity distribution in x direction (the above showed equations are the input).

The horizontal distribution of the velocity field is not uniform along the x axis. The non-uniformity is caused by the 90° curve in the wind tunnel that is approximately 1.7 meter before the spray bar section. This non-uniformity is decreasing with decreasing wind velocity. The horizontal velocity distribution is uniform in the test section especially at low (5 m/s in test section) wind speed conditions. The vertical air velocity distribution is moderately uniform at the spray bar and test section also. The non-uniformity of the velocity at the spray bar section influences the liquid water content and droplet size distribution in the test section.

Free stream velocity of 5 m/s

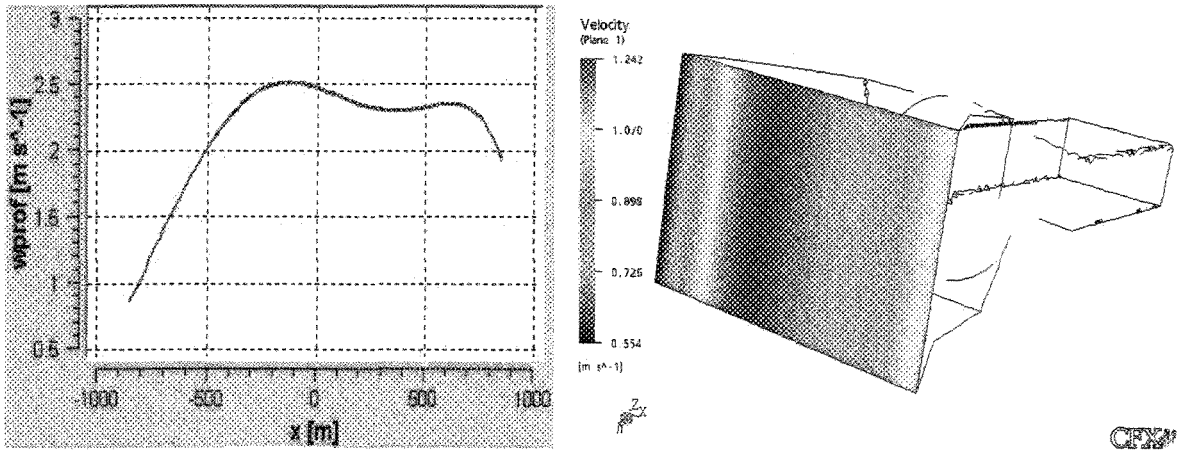

Inlet velocity distribution along x axis of inlet

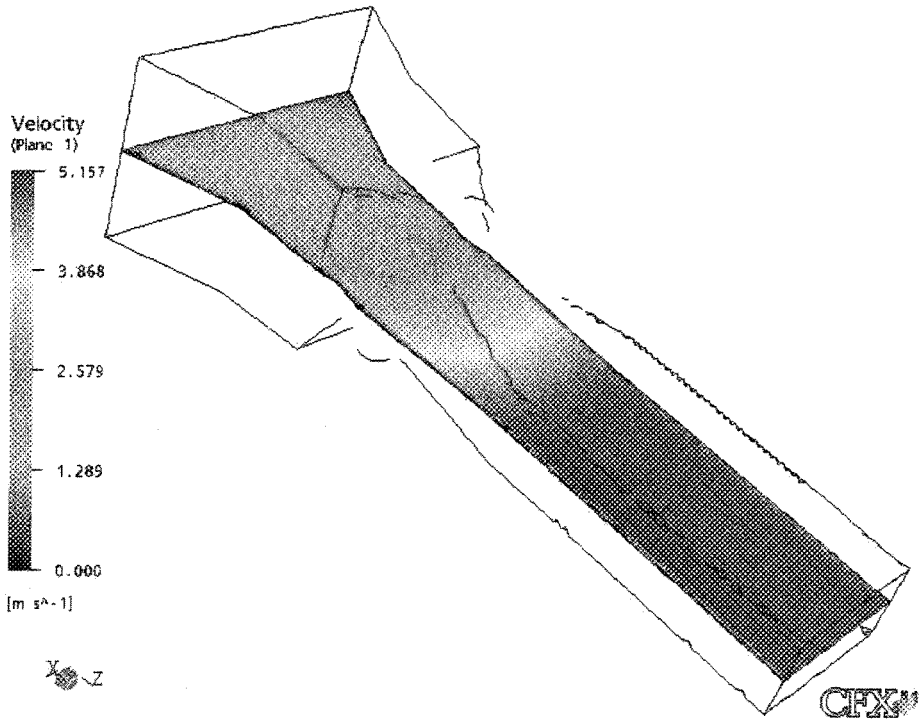

Horizontal velocity distribution

Free stream velocity of 10 m/s

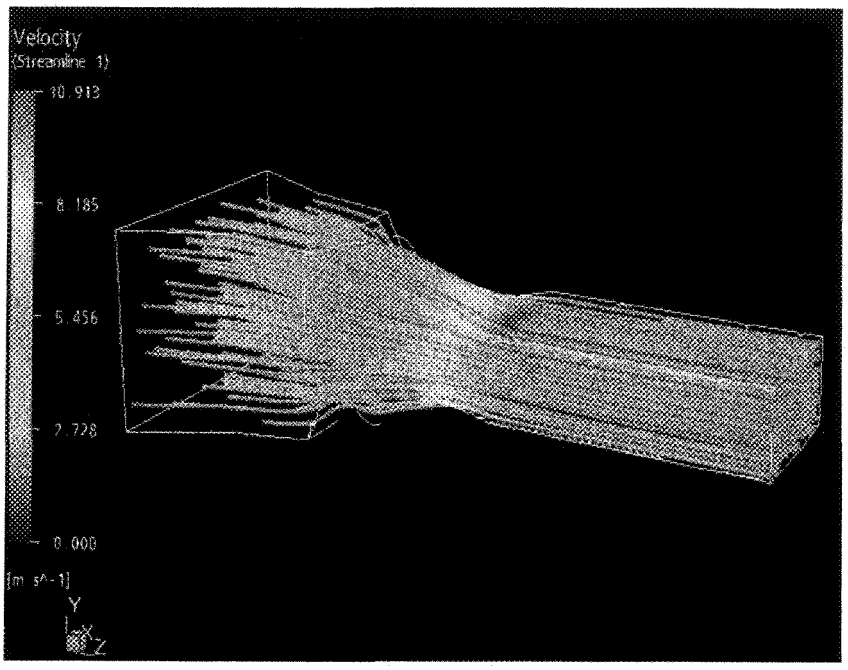

Streamlines in the tunnel

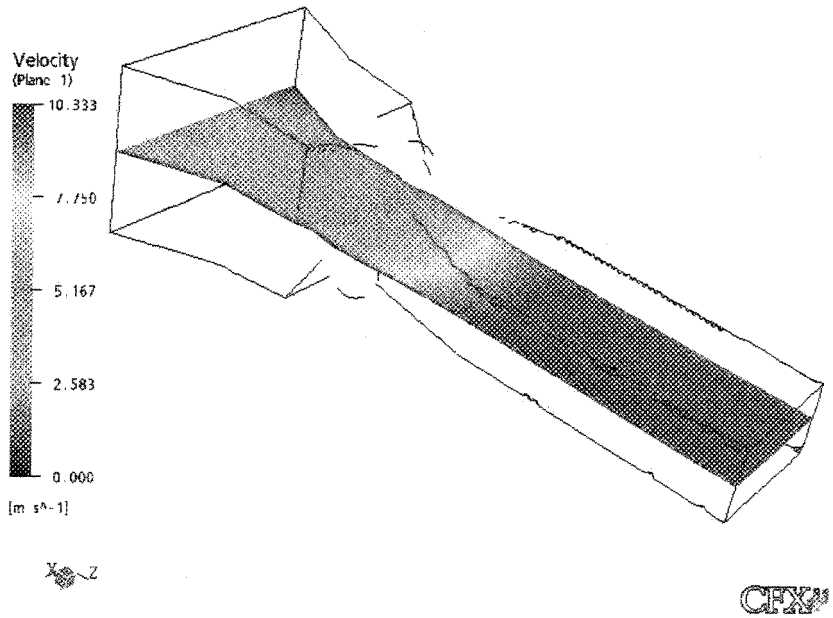

Horizontal velocity distribution

Free stream velocity of 20 m/s

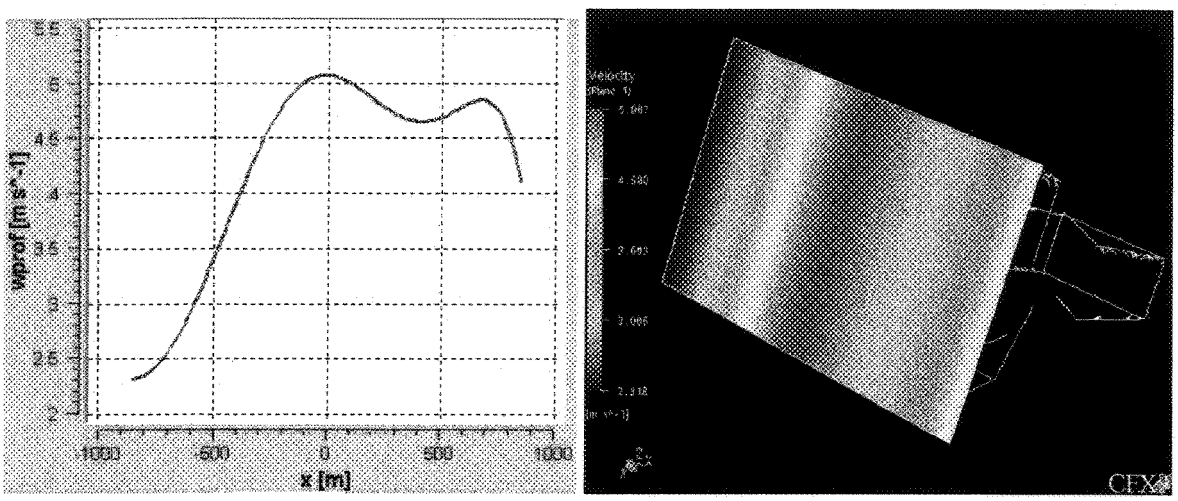

Velocity distribution along x-axis of inlet plane

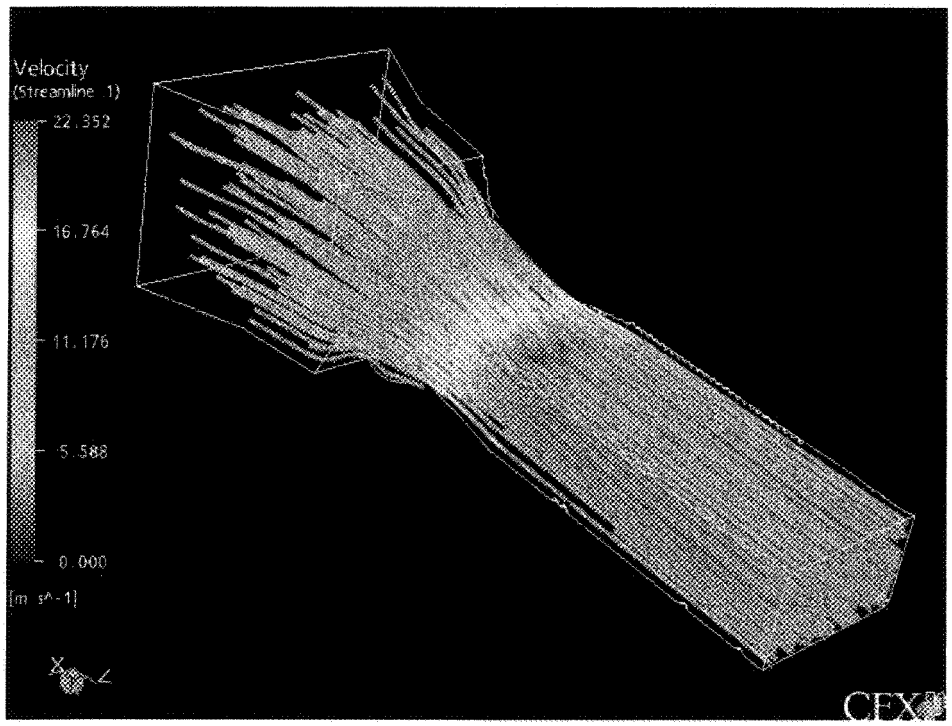

Streamlines in the tunnel

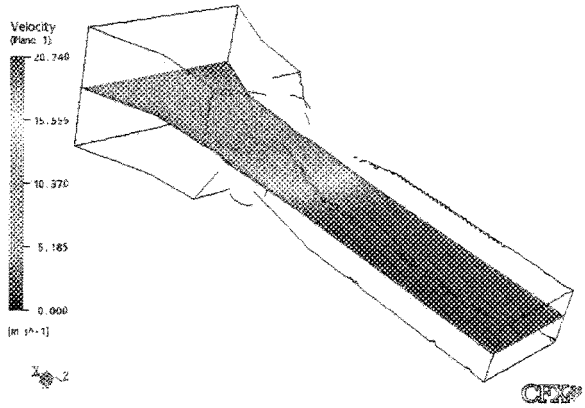

Horizontal velocity distribution

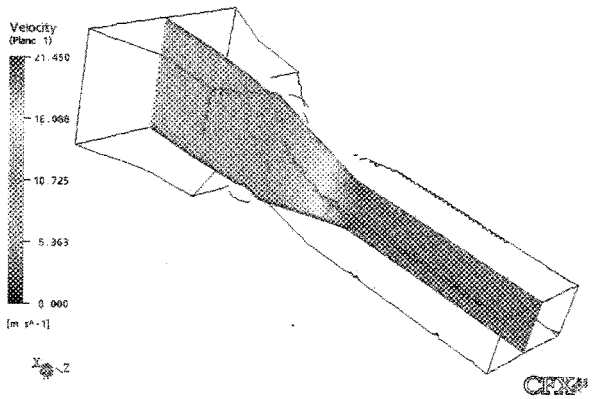

Vertical velocity distribution

Free stream velocity of 30 m/s

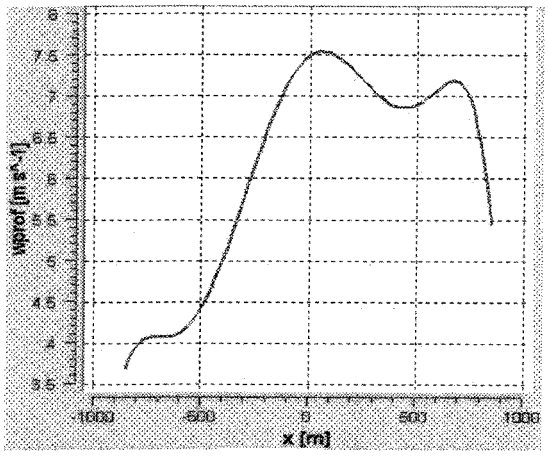

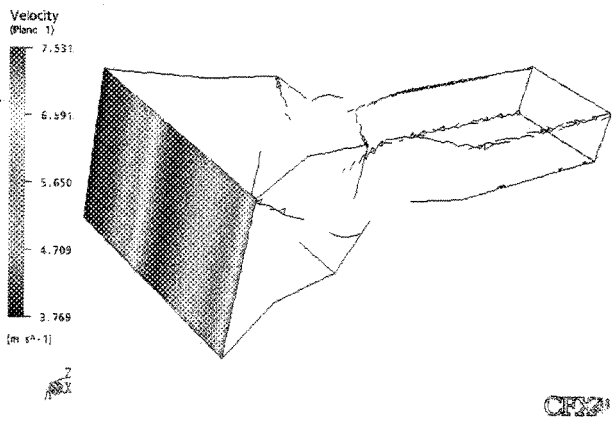

Inlet velocity distribution along x-axis

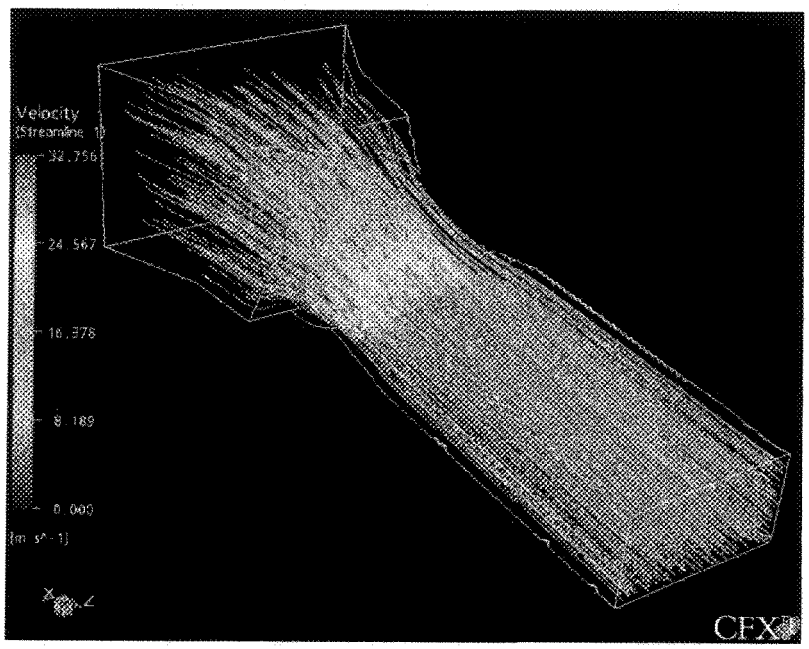

Streamlines in the tunnel

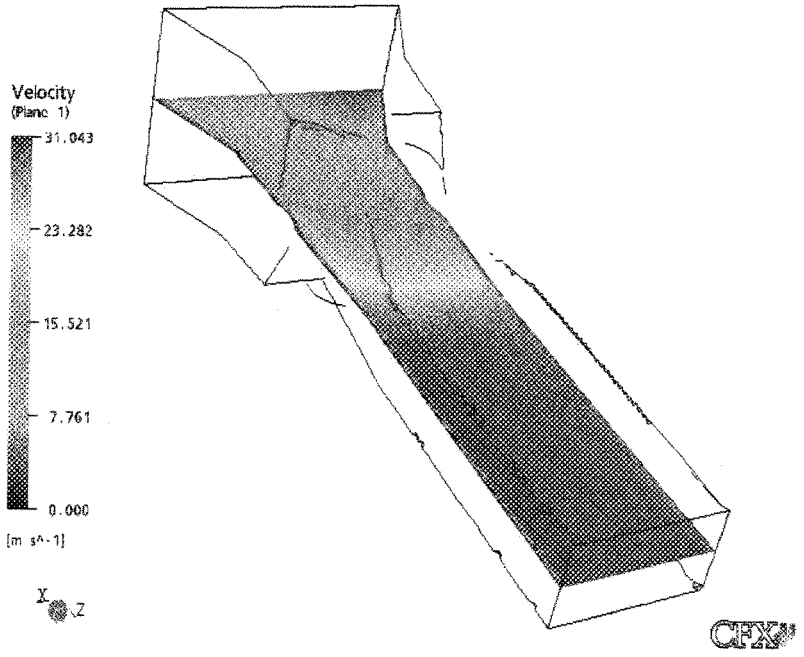

Horizontal velocity distribution

APPENDIX 6 VISUALIZING THE AIRFLOW AROUND STRANDED CONDUCTOR USING TUFTS ATTACHED TO LEEWARD SURFACE

Photos taken at 5 m/s

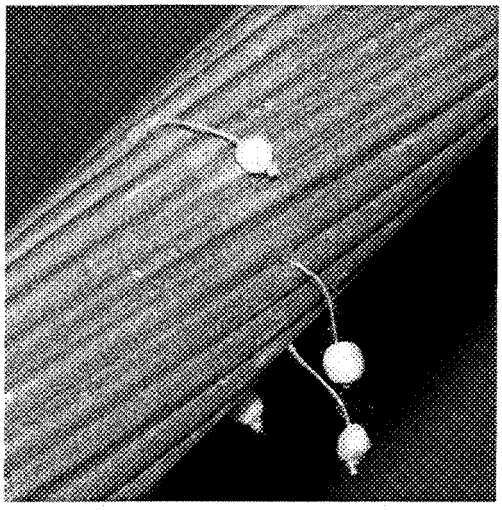

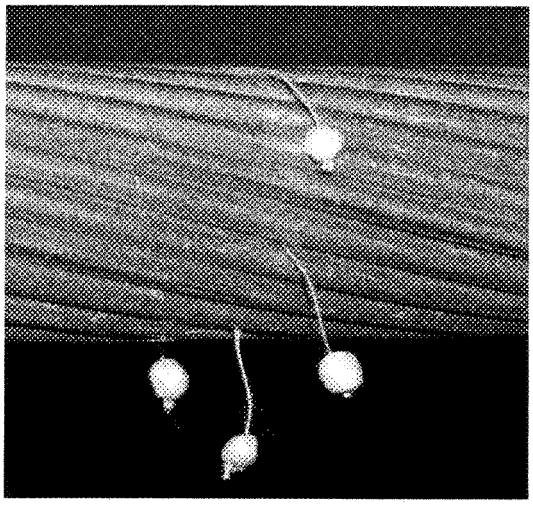

Photos taken at 10 m/s

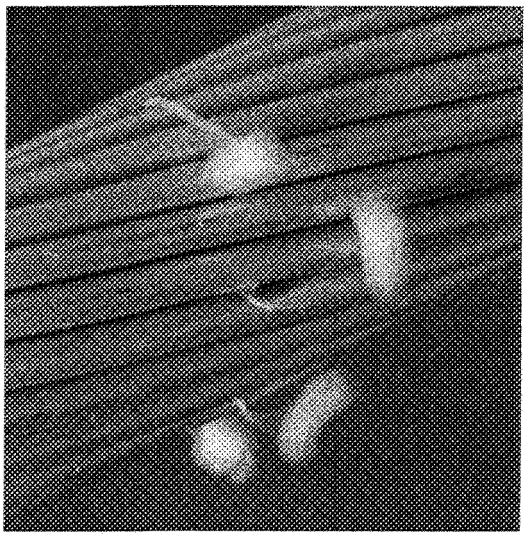

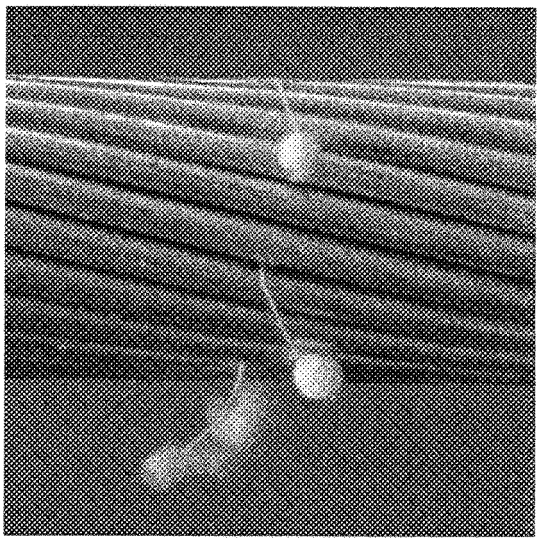

Photos taken at 20 m/s

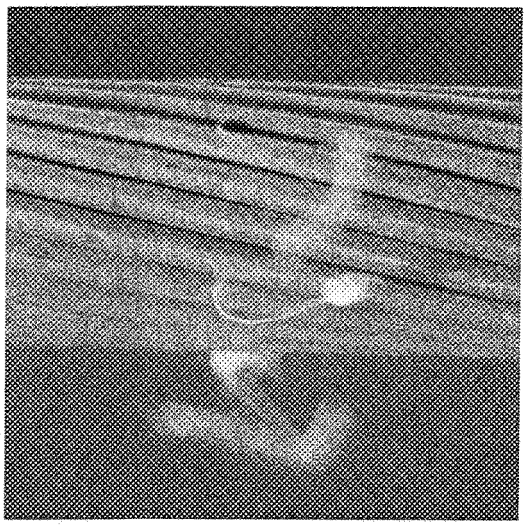

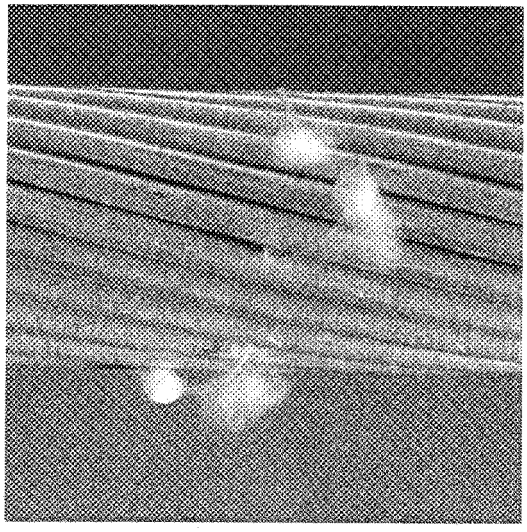

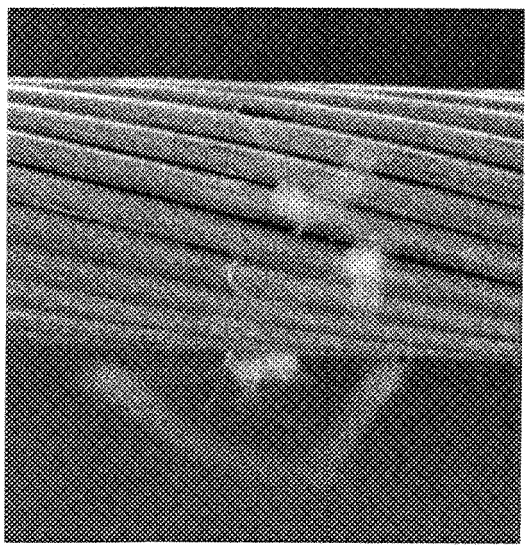

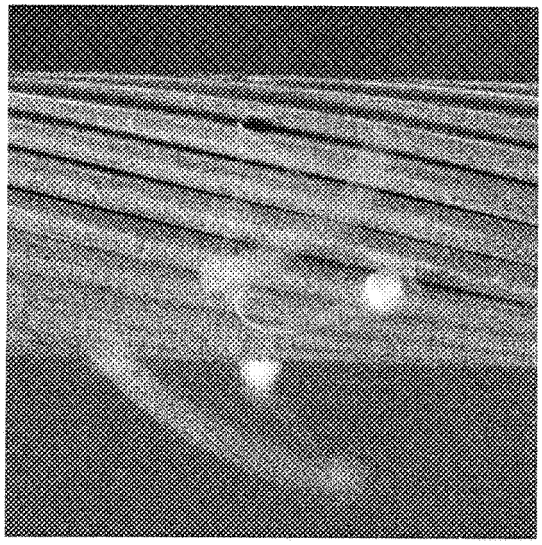

APPENDIX 7 NUMERICAL RESULTS OBTAINED BY CFX-10

The numerical results in this section refer to the "Test case" that was introduced in section 8.4.3. If there are deviations from this case, they are always mentioned below the figures.

The two- and three dimensional simulations of flow are obtained for stranded conductor with outer diameter of 31.7 mm. The outside layer of this twisted conductor consists of 20, 4.3 mm diameter strands.

The numerical results are obtained by using Ansys CFX code. This commercial CFD (Computational Fluid Dynamic) software is based on finite volume technique.

Appendix 7.1 Effect of domain size on flow around smooth circular cylinder

Velocity and pressure distributions

It is shown in the figures presented below that the average velocity increases with decreasing domain size. This is due to the tunnel blockage effect described in section 7.3.2. It is also clear that Domain 1 is a small computational domain for this physical problem, since the results interfere with boundary conditions at upper wall. Obviously, results obtained in Domain 3 show less interference with boundaries. However, comparing the velocity and pressure distribution close to the cylinder surface in Domain 2 and 3, no significant difference could be noticed. Actually, there is just a slight difference in the velocity field around the boundary layer separation. Note that the negative pressure area near the separation region is greater in Domain 1 than in Domains 2 or 3. This is also due to the tunnel blockage effect. The turbulent kinetic energy is also greater in the smaller simulation domain as result of tunnel blockage. No difference was observed in the temperature distributions around the cylinder obtained for the three domains analyzed.

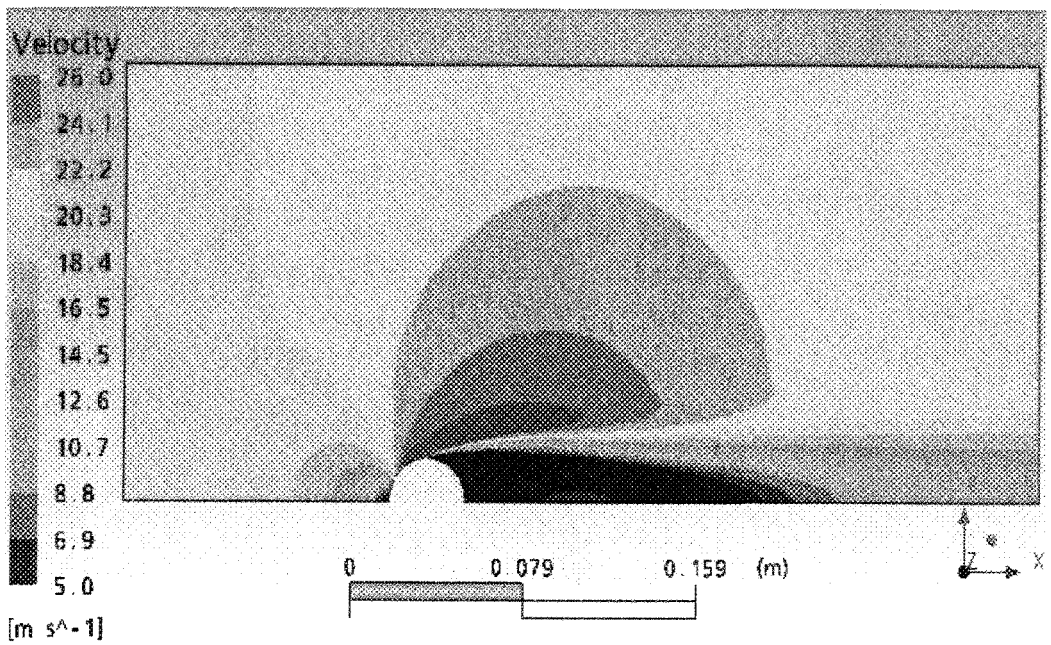

Velocity distribution in Domain 1 in a range of 5÷26 m/s

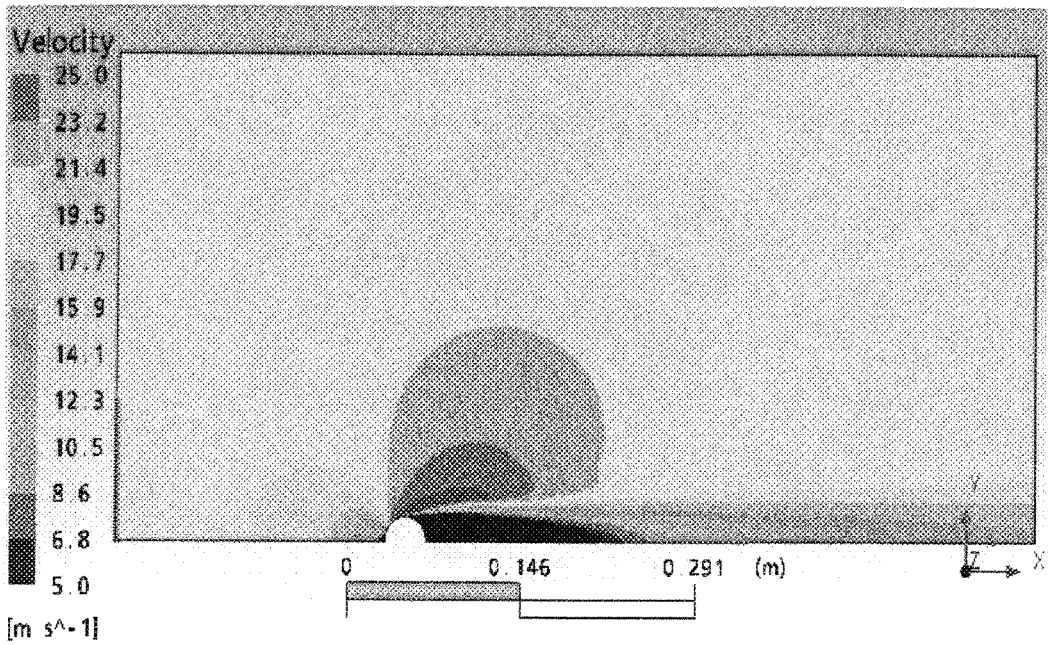

Velocity distribution in Domain 2 in a range of 5÷25 m/s

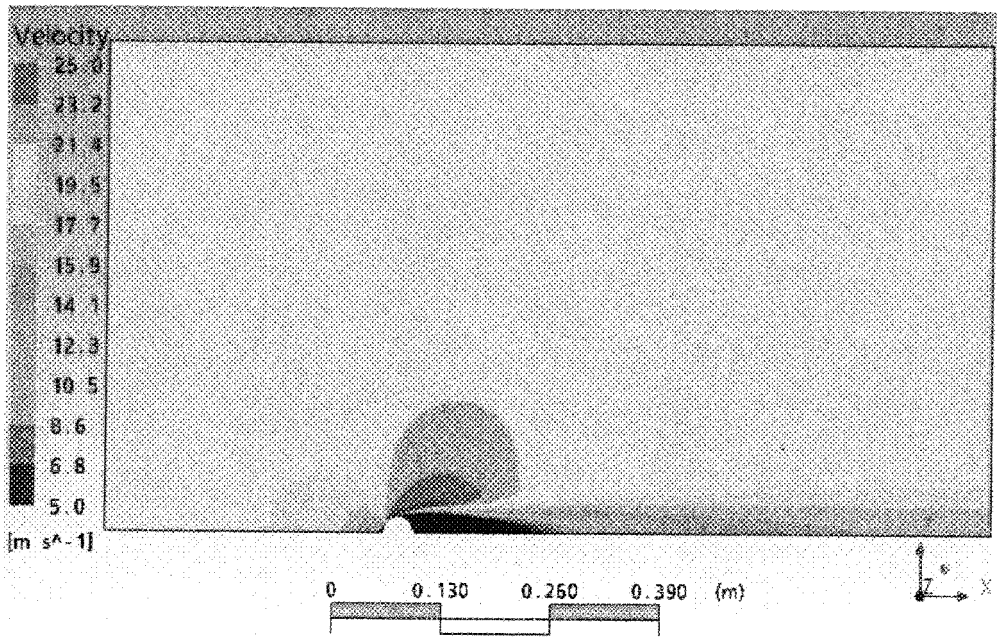

Velocity distribution in Domain 3 in a range of 5÷25 m/s

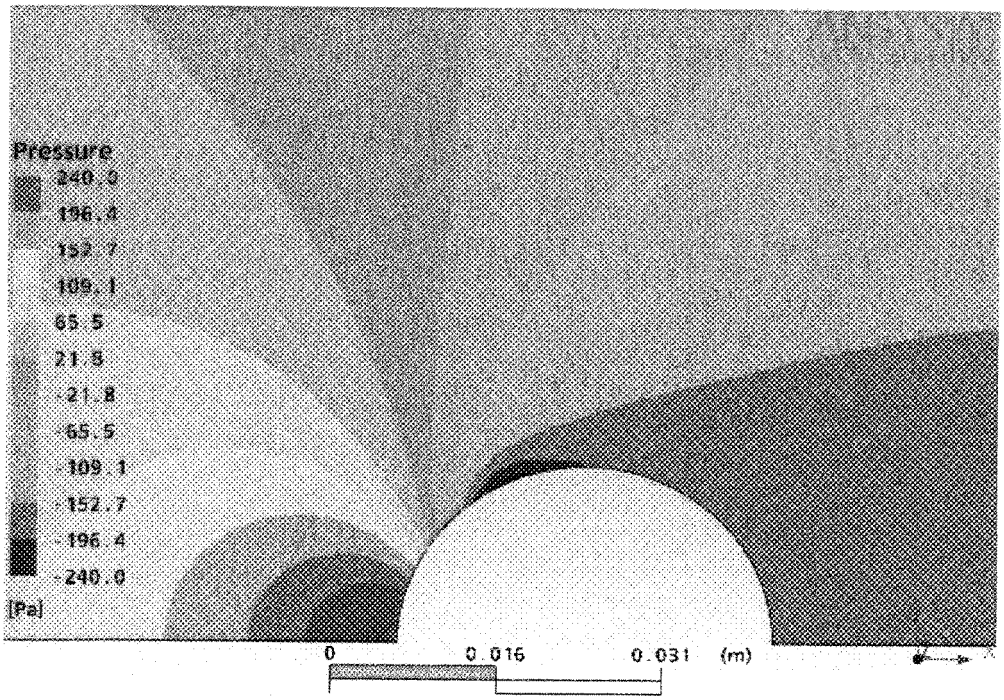

Pressure distribution of airflow around a half perimeter of smooth cylinder in Domain 1

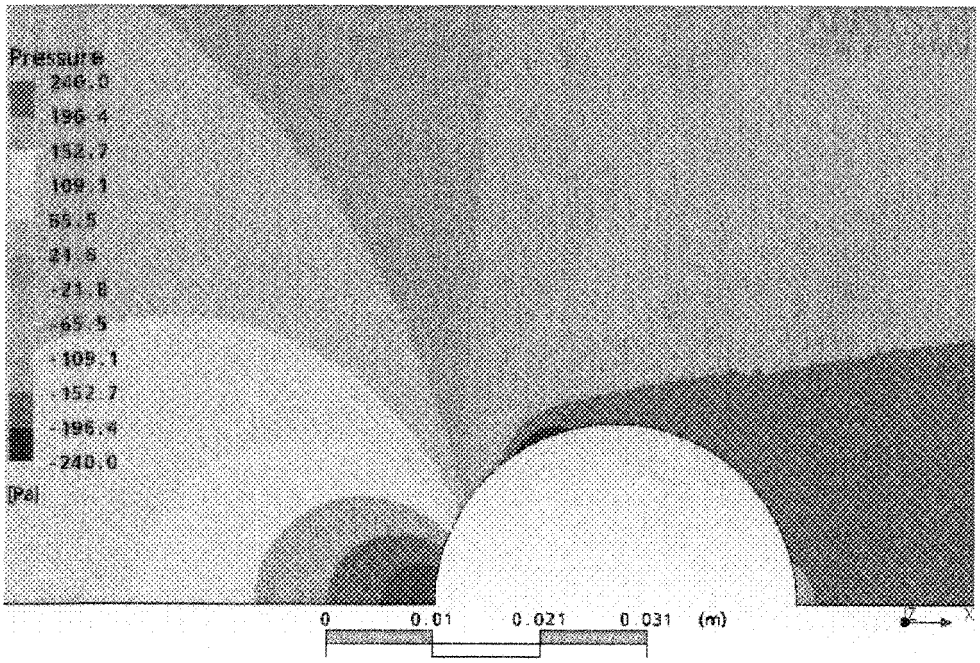

Pressure distribution of airflow around a half perimeter of smooth cylinder in Domain 3

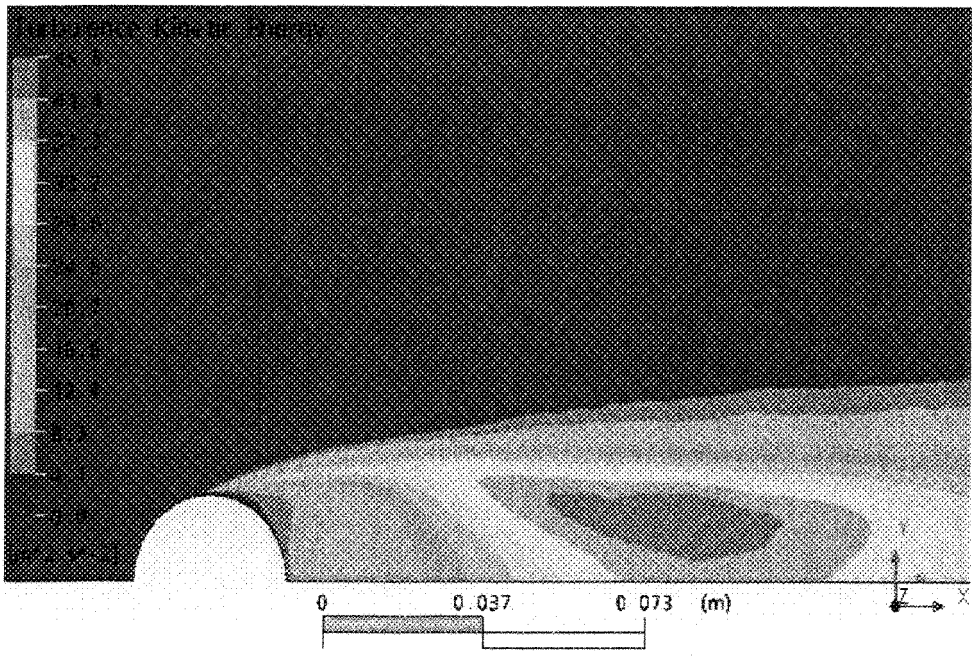

Turbulence kinetic energy of airflow in Domain 1

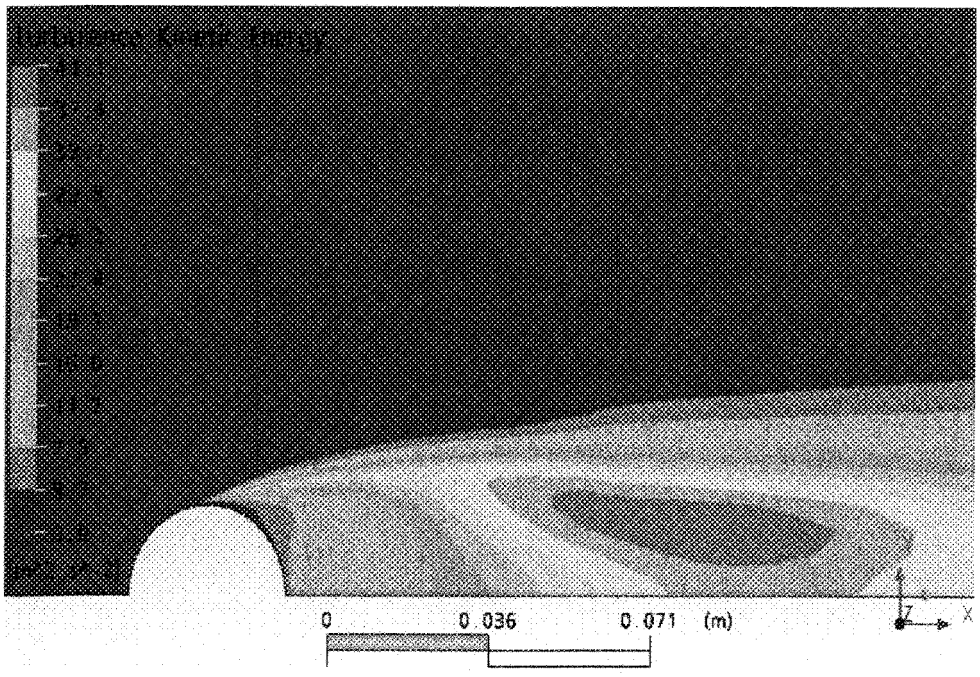

Turbulence kinetic energy of airflow in Domain 2

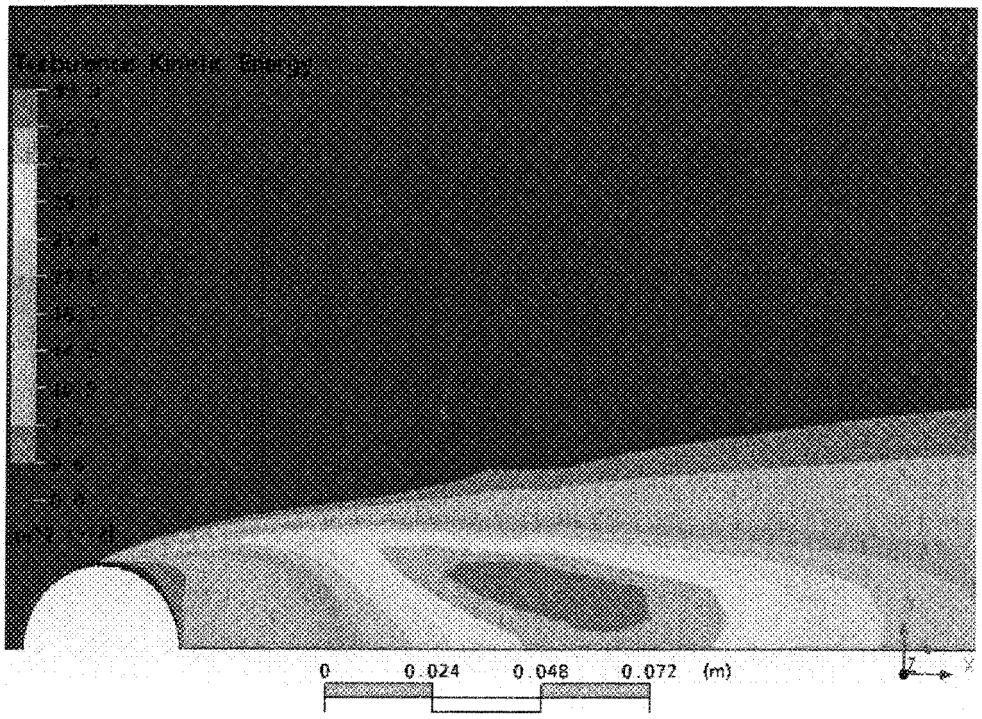

Turbulence kinetic energy of airflow in Domain 3

Appendix 7.2 Effect of turbulence intensity on airflow around smooth cylinder

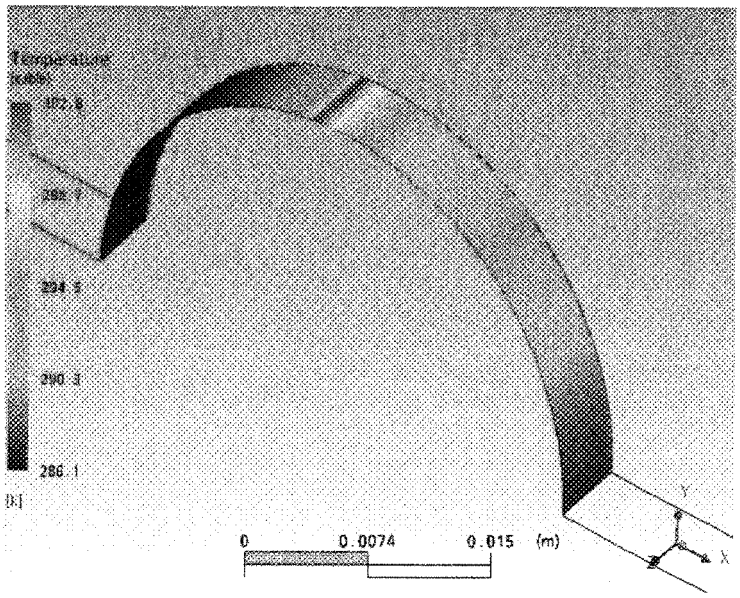

Surface temperature of half cylinder obtained for 1% inlet turbulence intensity and turbulent viscosity ratio of 1 (airflow along x-axis toward positive values)

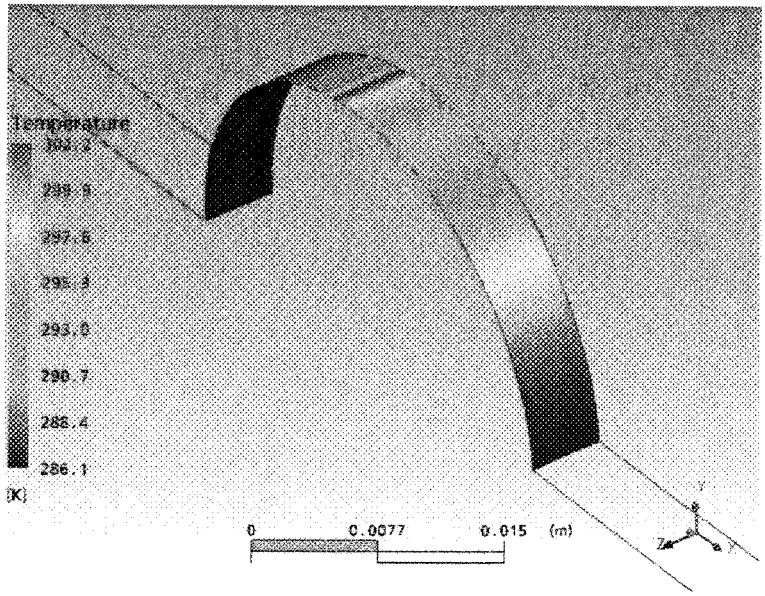

Surface temperature of half cylinder obtained for 10% inlet turbulence intensity and turbulent viscosity ratio of 1 (airflow along x-axis toward positive values)

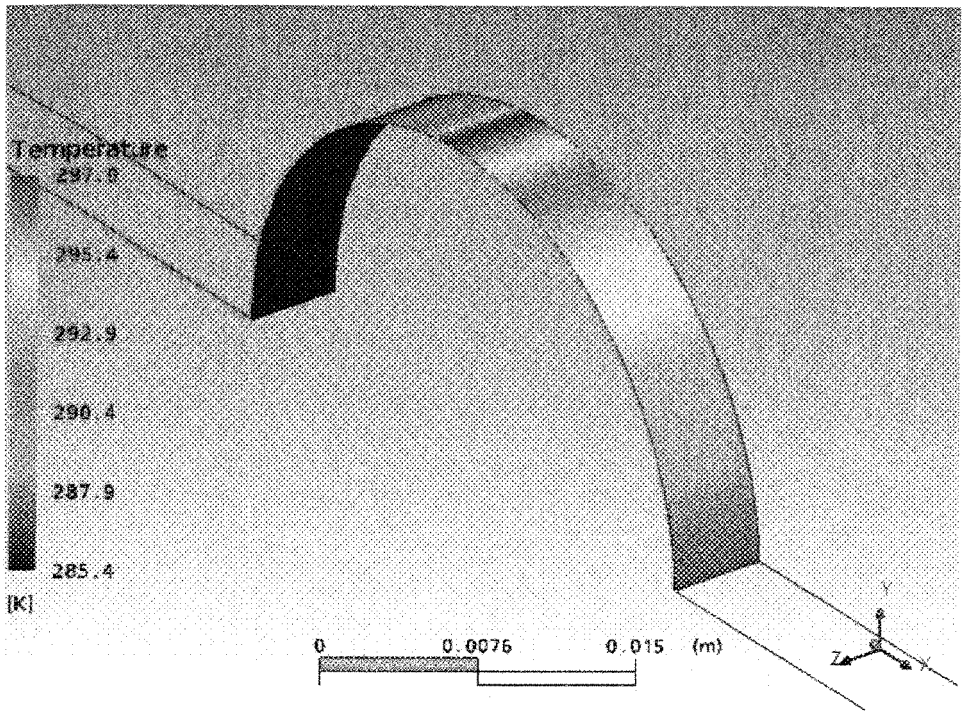

Surface temperature of half cylinder obtained for 10% inlet turbulence intensity and viscosity ratio of 10 (airflow along x-axis toward positive values)

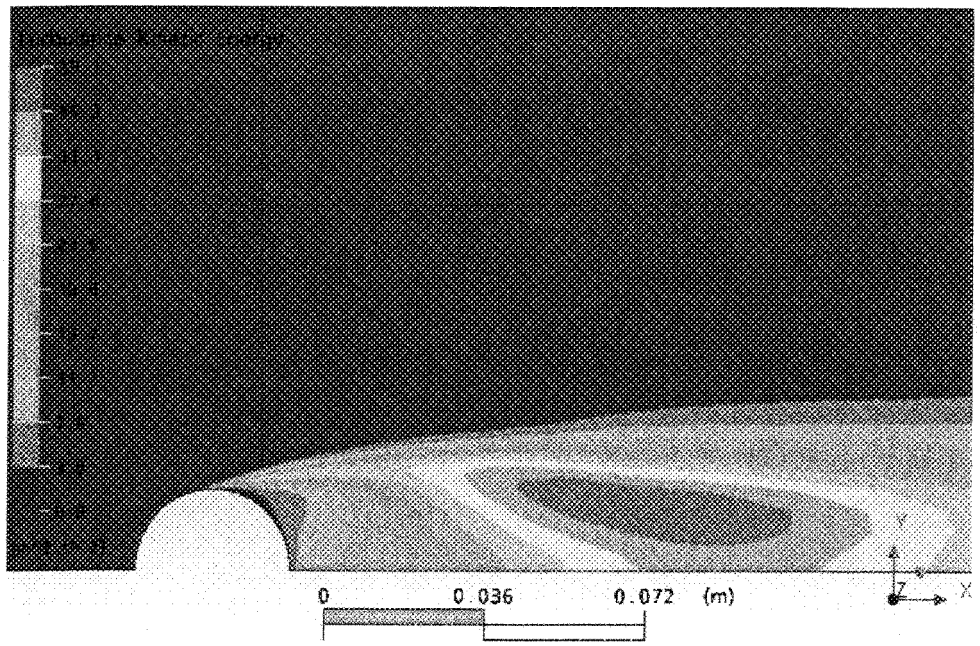

Turbulence kinetic energy distribution around circular cylinder, inlet turbulence is defined with Tu=1% and viscosity ratio of 1

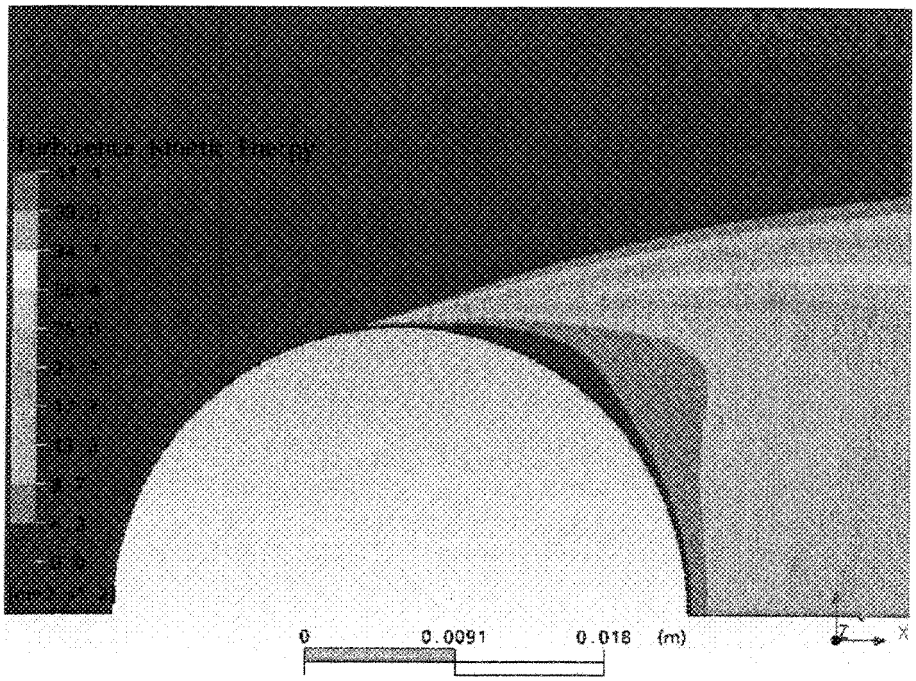

Turbulence kinetic energy distribution around circular cylinder, inlet turbulence is defined with Tu=10% and viscosity ratio of 1

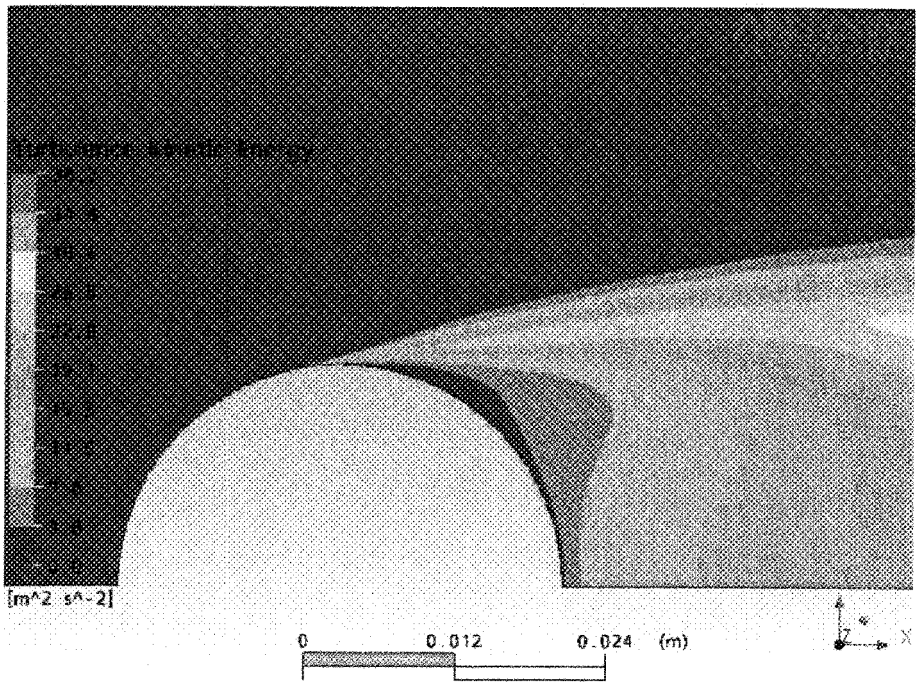

Turbulence kinetic energy distribution around circular cylinder, inlet turbulence is defined with Tu=10% and viscosity ratio of 10

Appendix 7.3 Characteristics of flow field around a smooth circular cylinder

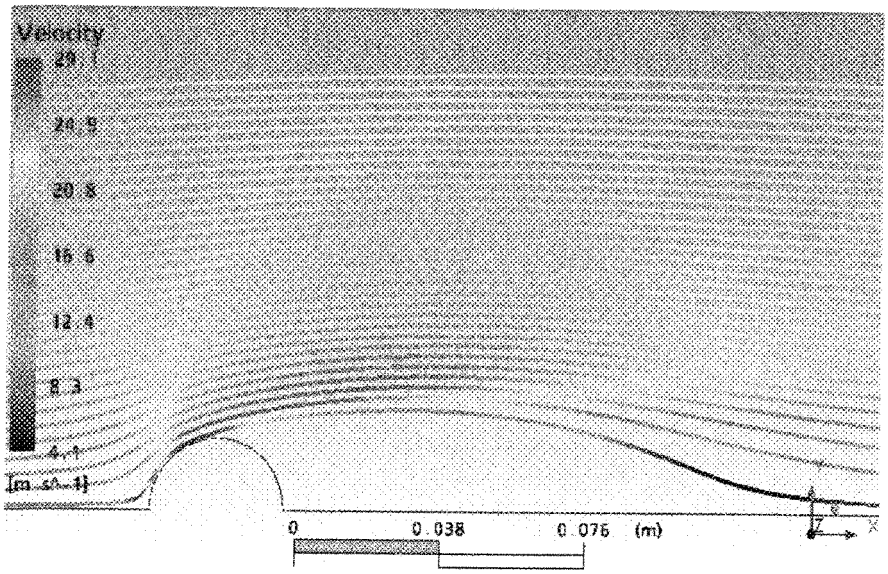

Streamlines around half perimeter of smooth circular cylinder

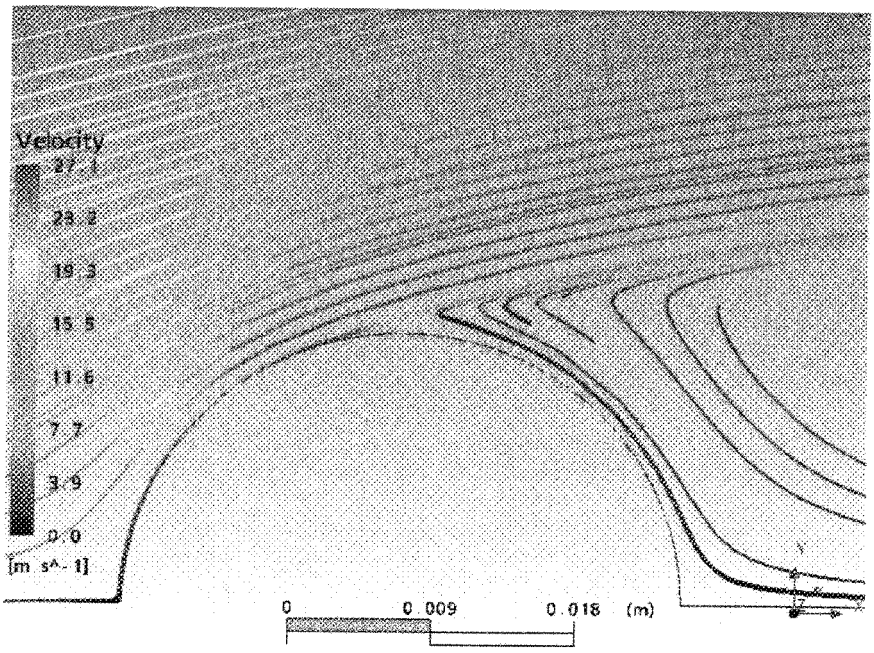

Streamlines near half surface of smooth circular cylinder

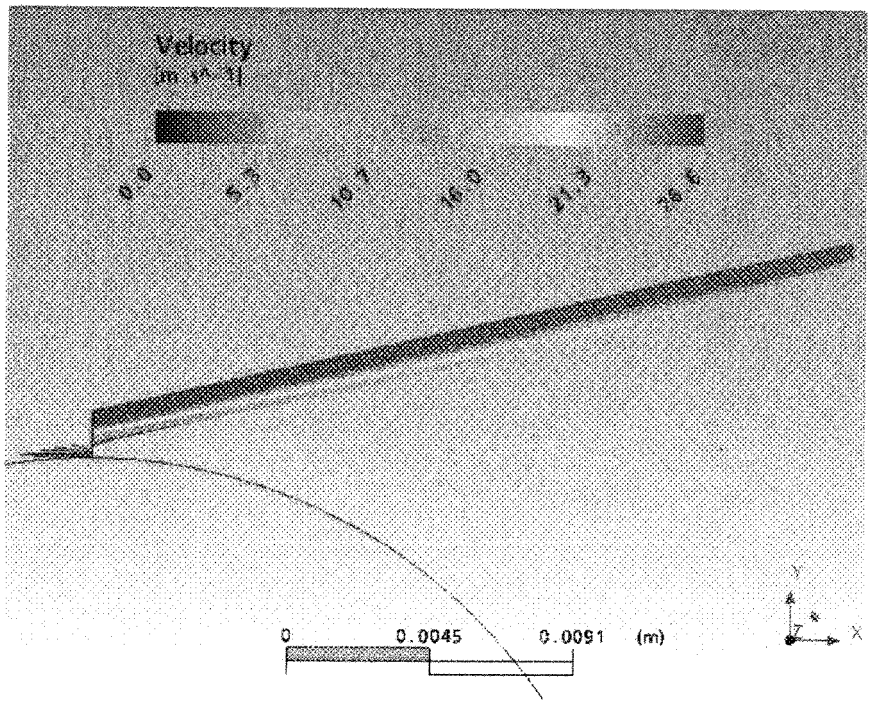

Velocity of boundary layer flow at 90° (stagnation point is at 0°)

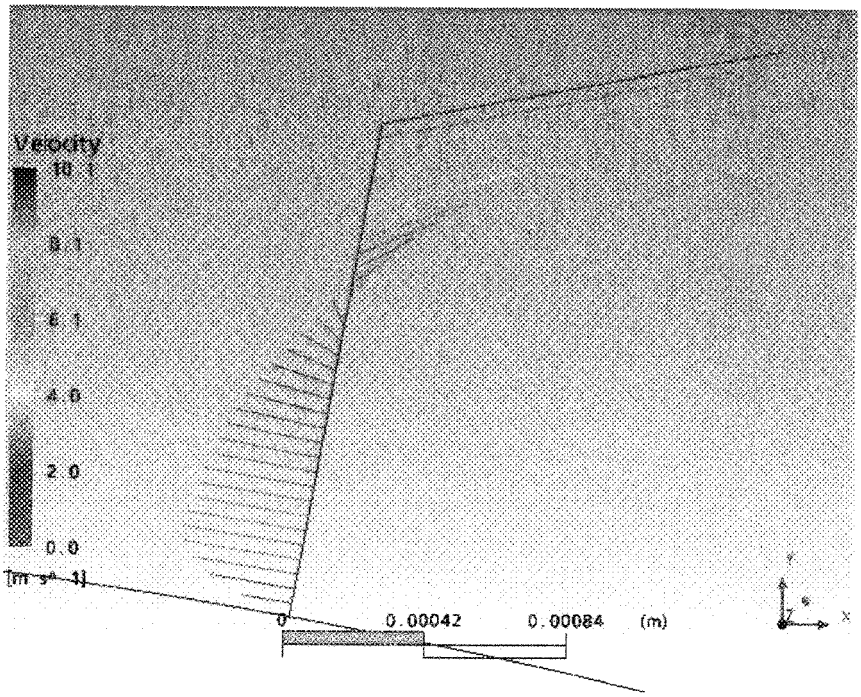

Velocity of boundary layer flow at 100° (stagnation point is at 0°)

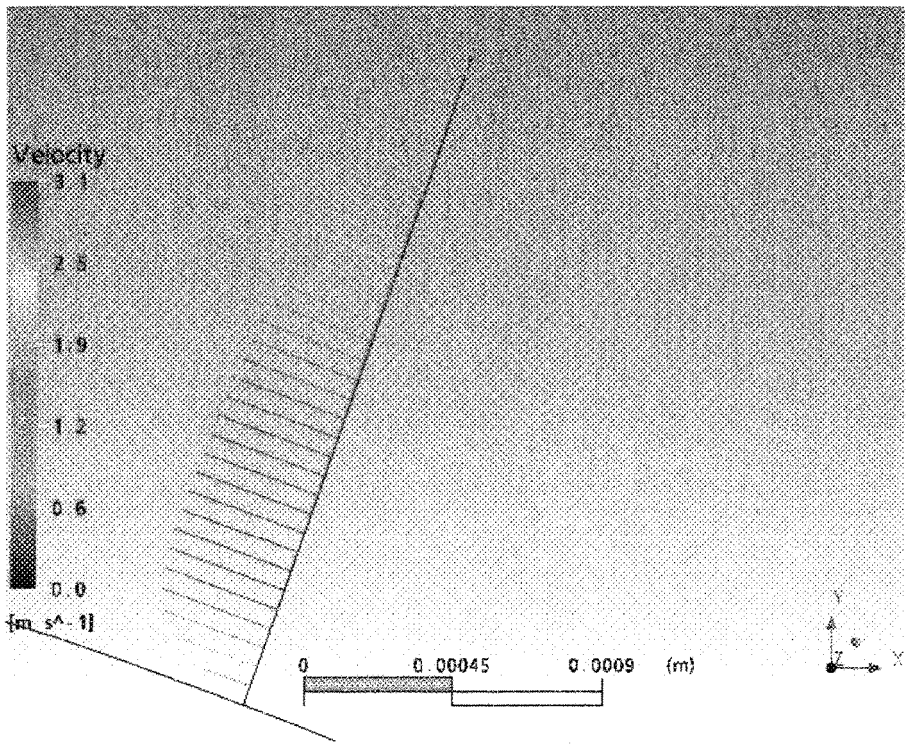

Velocity of boundary layer flow at 110° (stagnation point is at 0°)

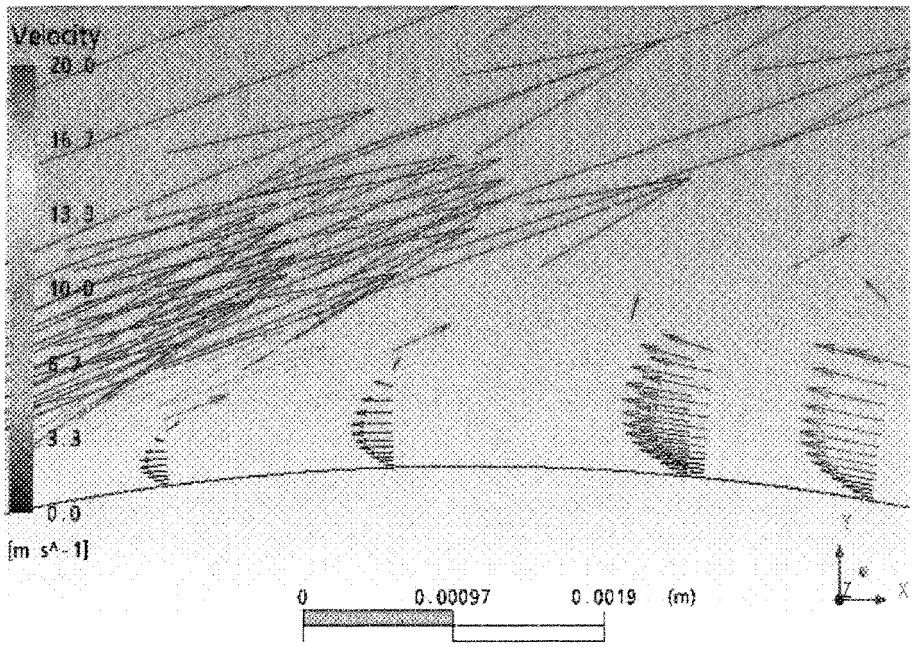

Adverse flow near wall causing boundary layer separation

Appendix 7.4 Numerical results for smooth cylinder obtained by using different turbulence models

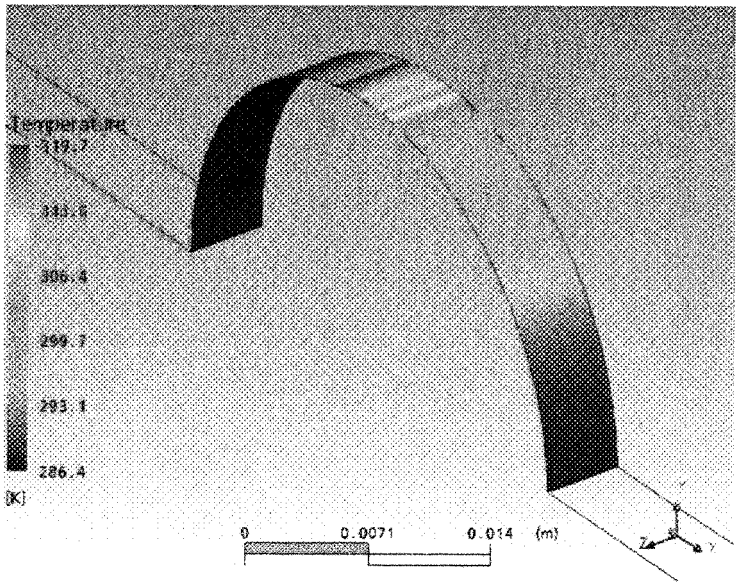

Surface temperature of half cylinder obtained by using SST with Transition model (airflow along x-axis toward positive values)

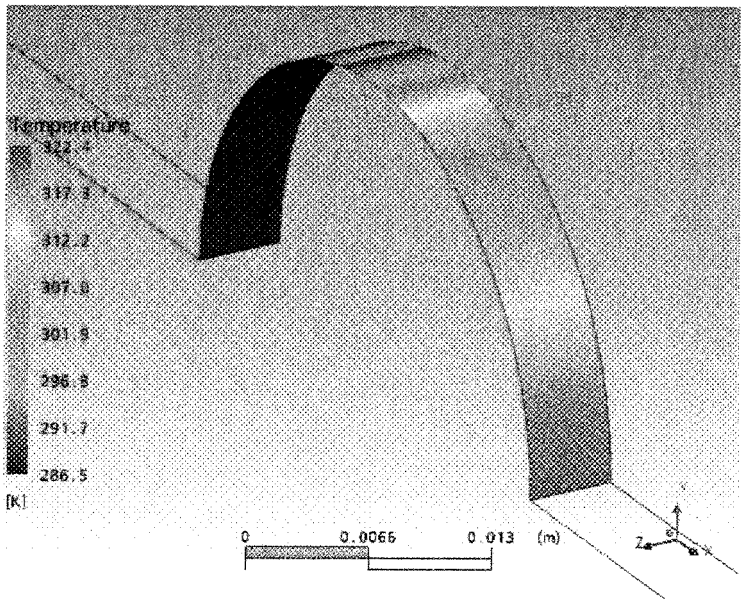

Surface temperature of half cylinder obtained by using k-omega model (airflow along x-axis toward positive values)

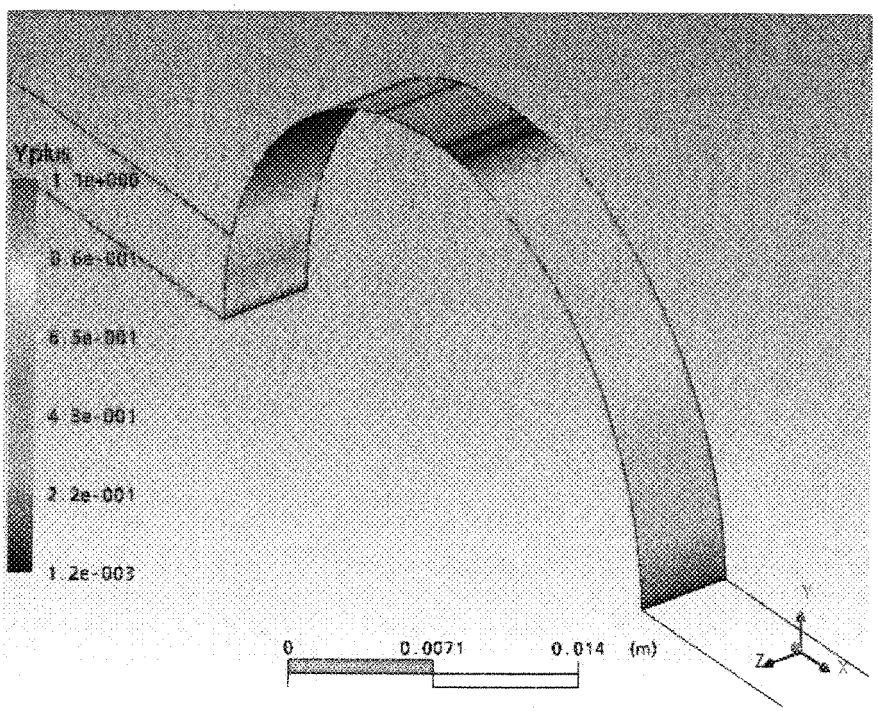

y^+ distribution along the cylinder surface (using SST turbulence model with Transition model)

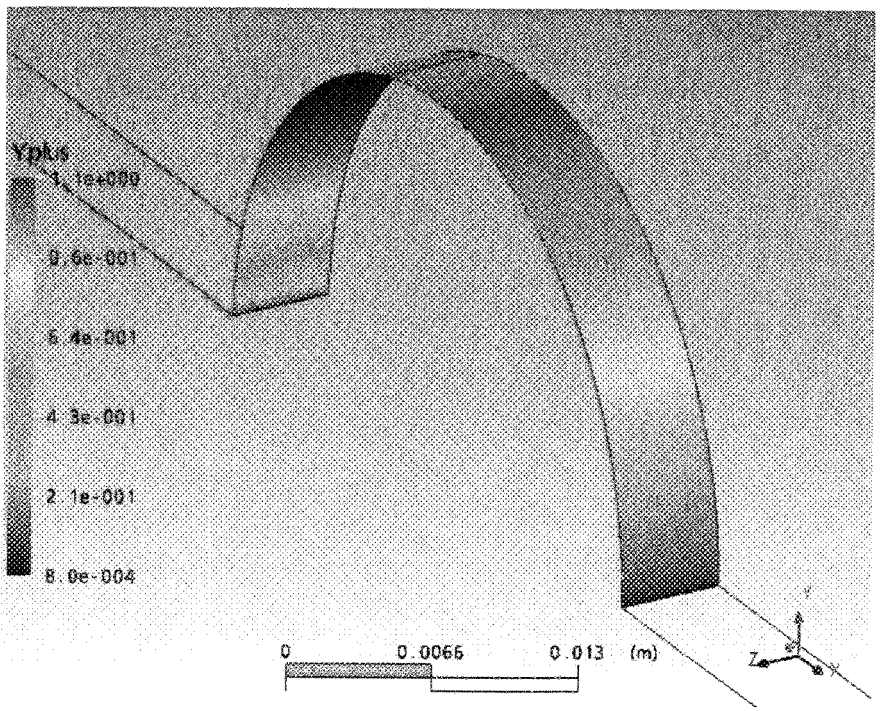

y^+ distribution along the cylinder surface (using k-omega turbulence model)

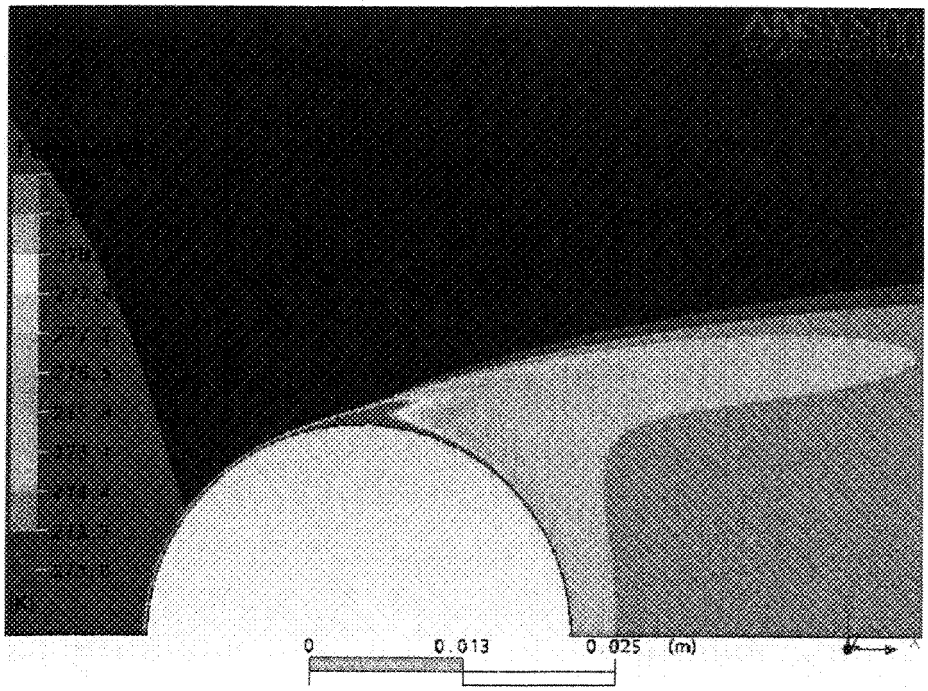

Air temperature in range of 273÷280 K obtained by using SST with Transition model

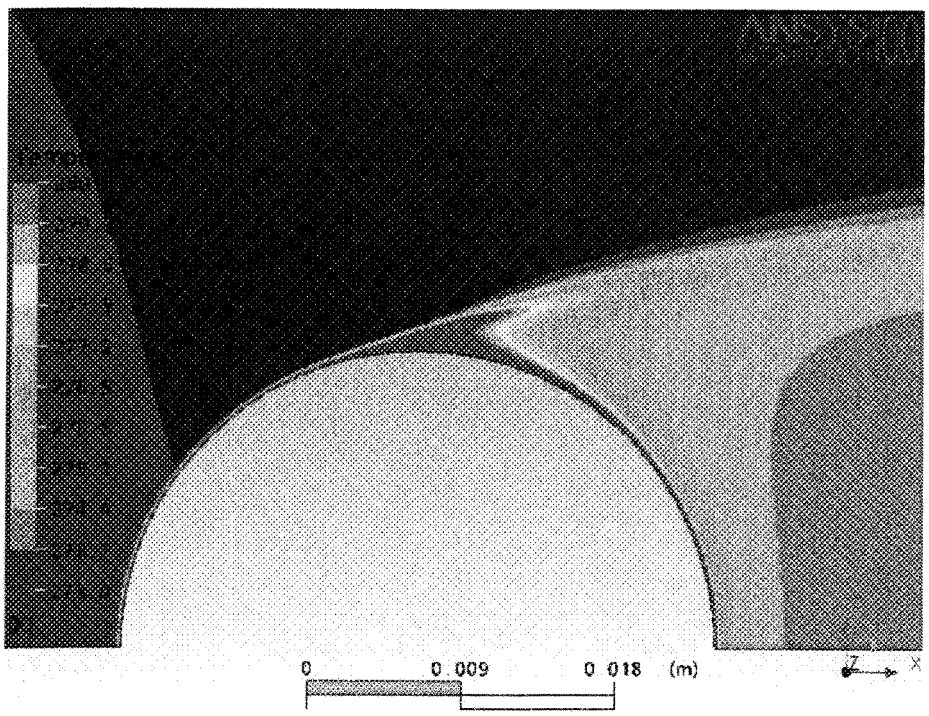

Air temperature in range of 273÷280 K obtained by using k-omega model

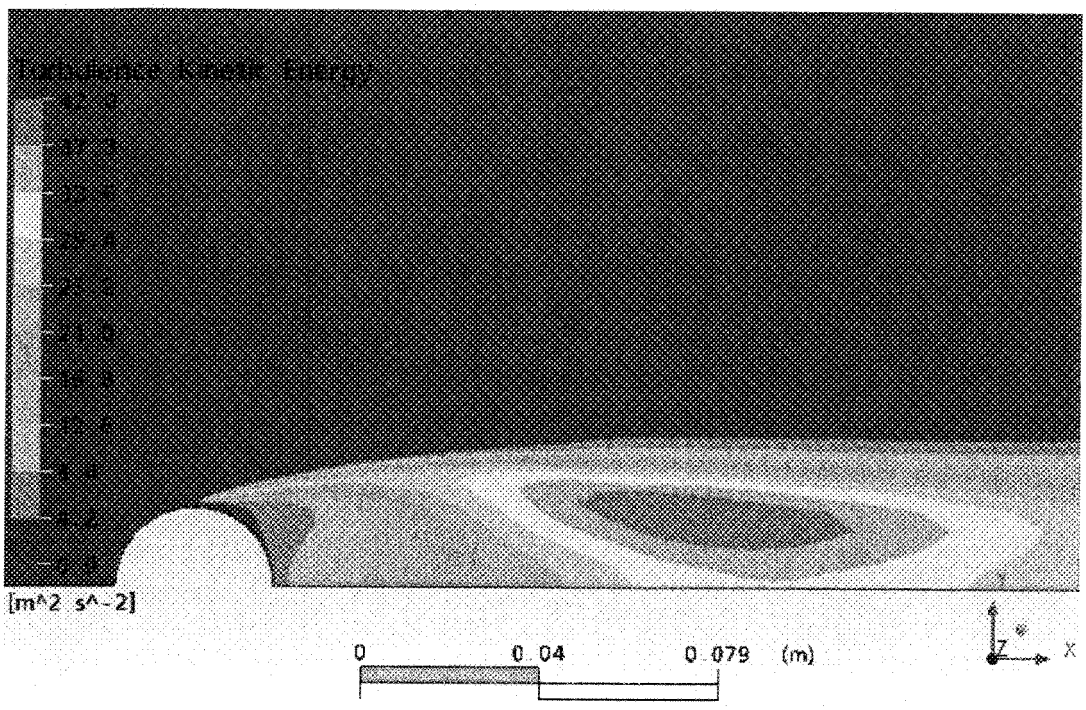

Turbulence kinetic energy of the flow obtained by using SST with Transition model

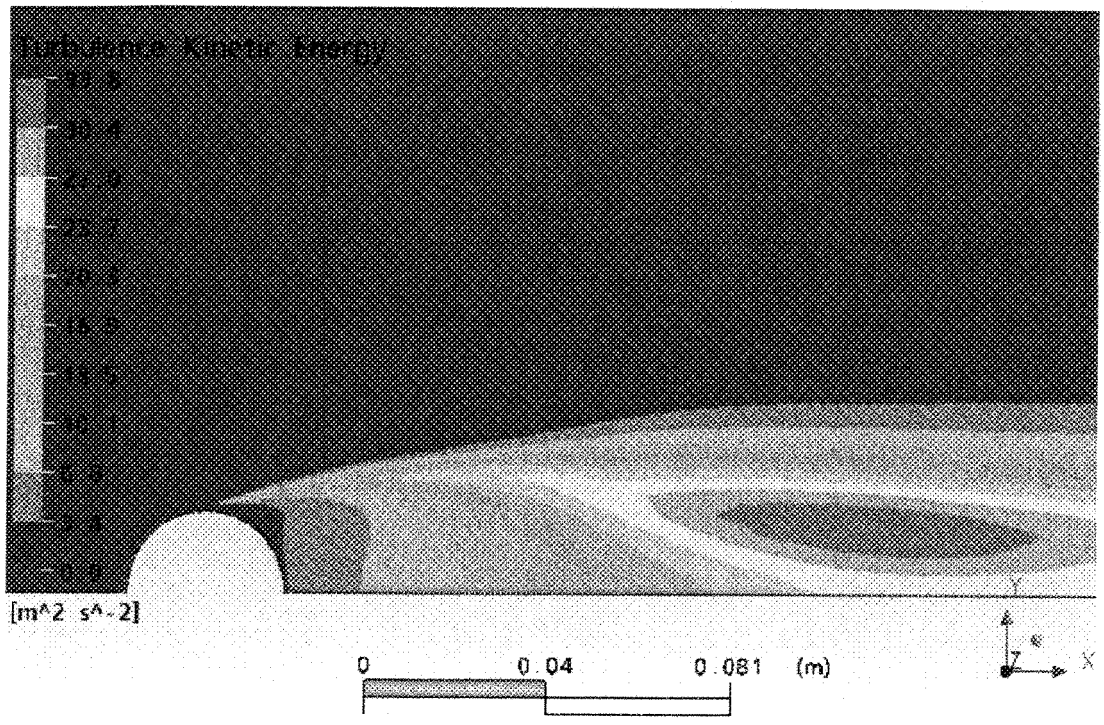

Turbulence kinetic energy of the flow obtained by using k-omega model

Appendix 7.5 Computational grid of flow around 2D stranded conductor

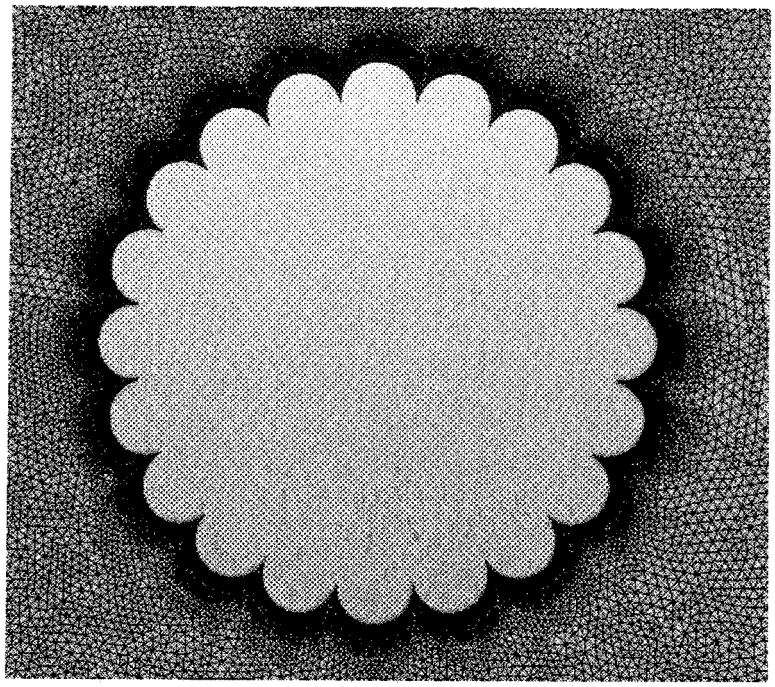

Mesh around stranded surface of the conductor

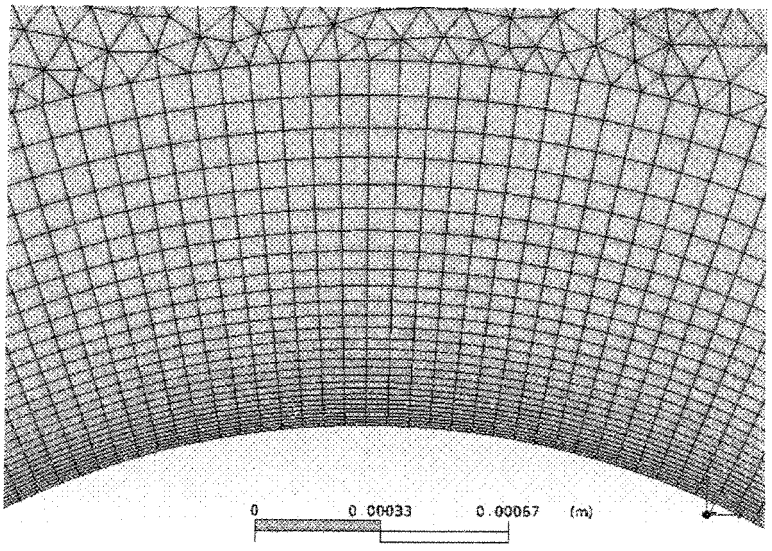

Inflation layers perpendicular to strand surface

Appendix 7.6 Flow field around stranded surface at Re number of 45520

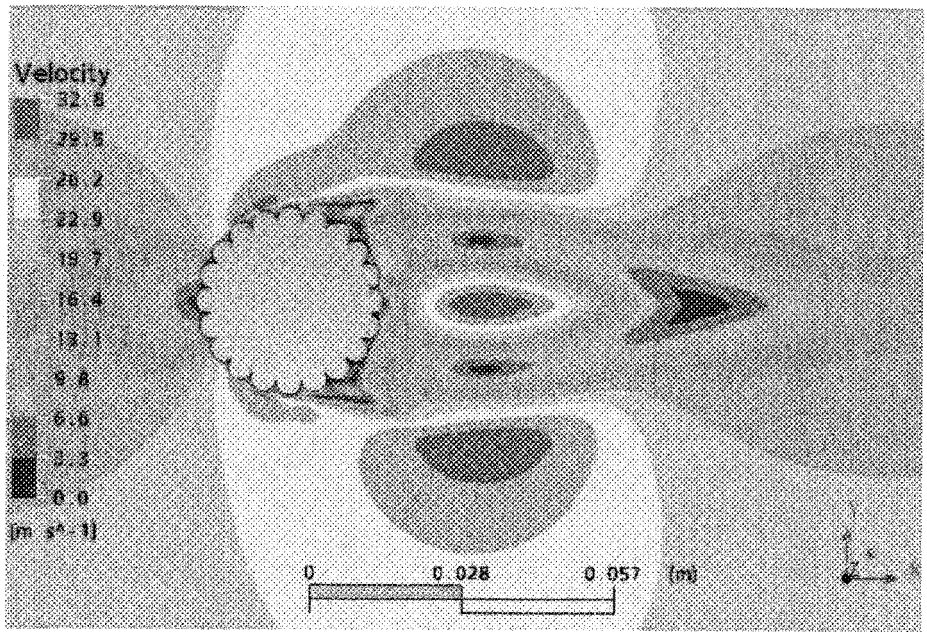

Velocity distribution of airflow around stranded conductor (initial guess from steady simulation)

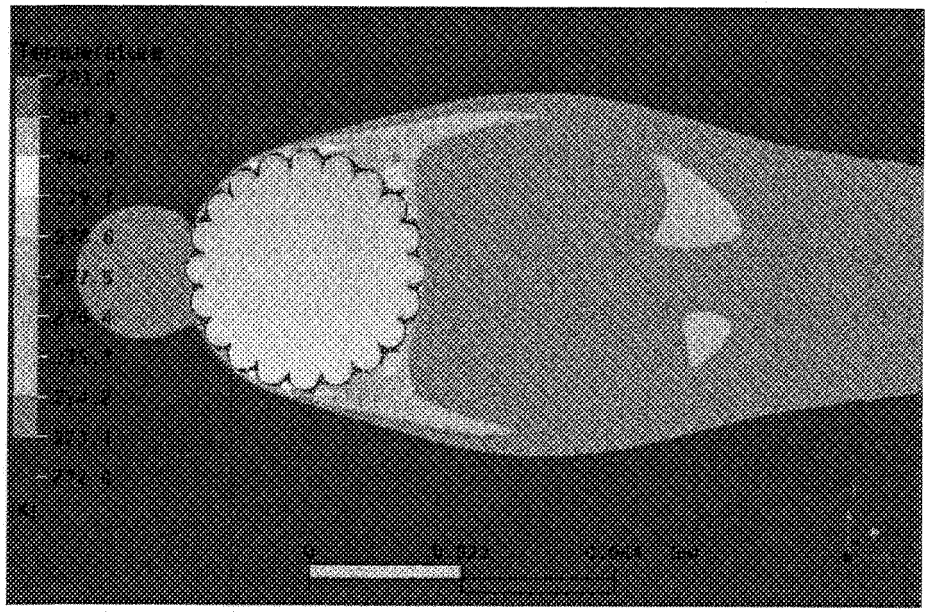

Air temperature distribution around stranded conductor (initial guess from steady simulation)

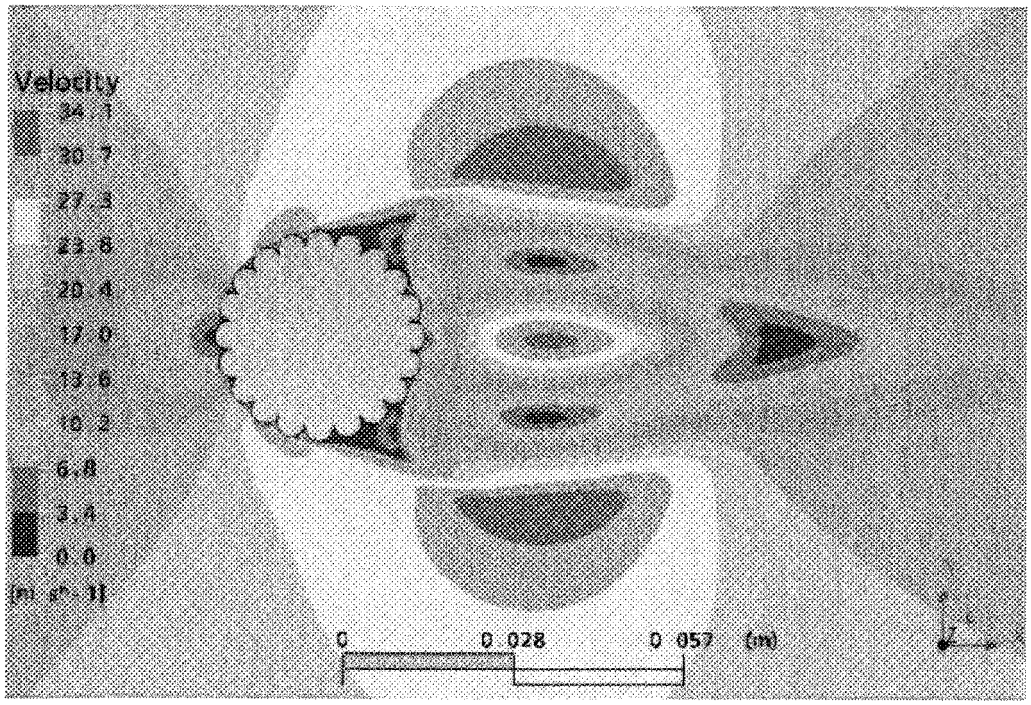

Velocity distribution of airflow around stranded conductor after 0.0018 s transient simulation time

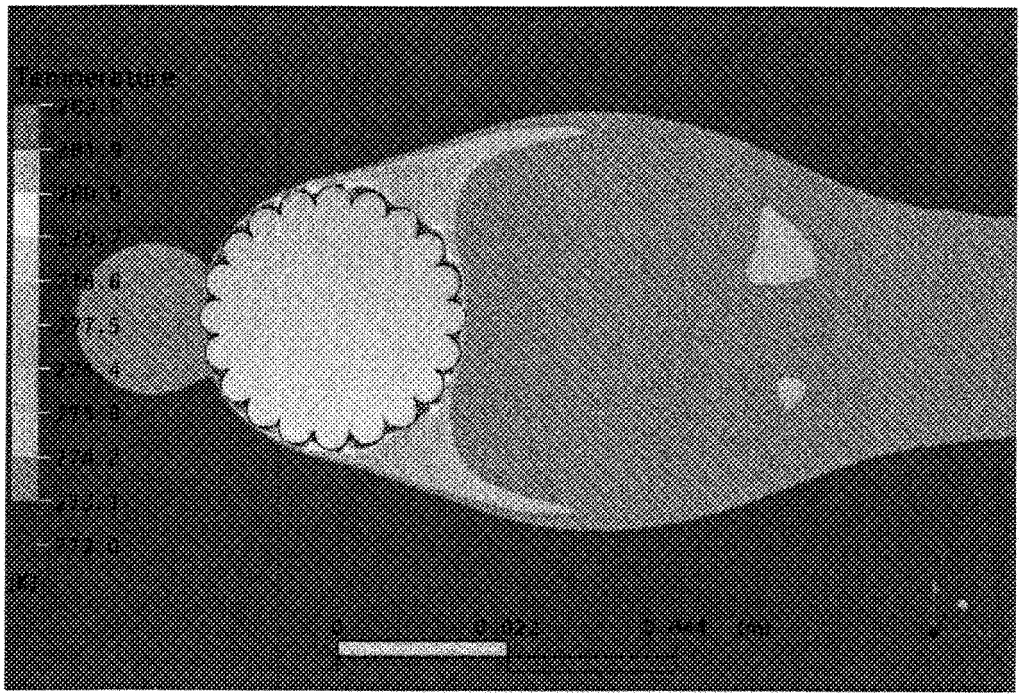

Air temperature distribution around stranded conductor after 0.0018 s transient simulation time

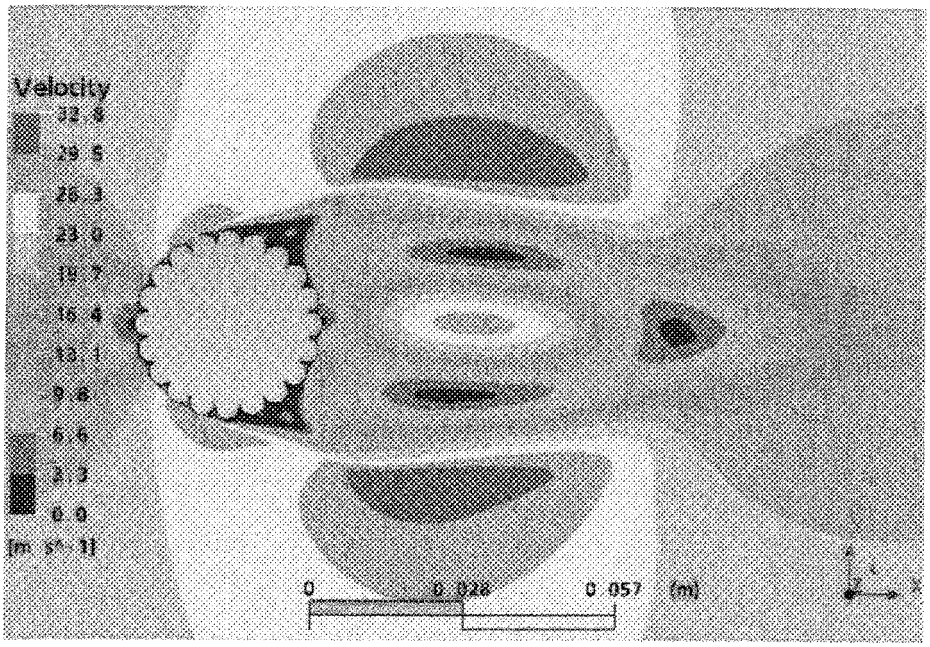

Velocity distribution of airflow around stranded conductor after 0.005 s transient simulation time

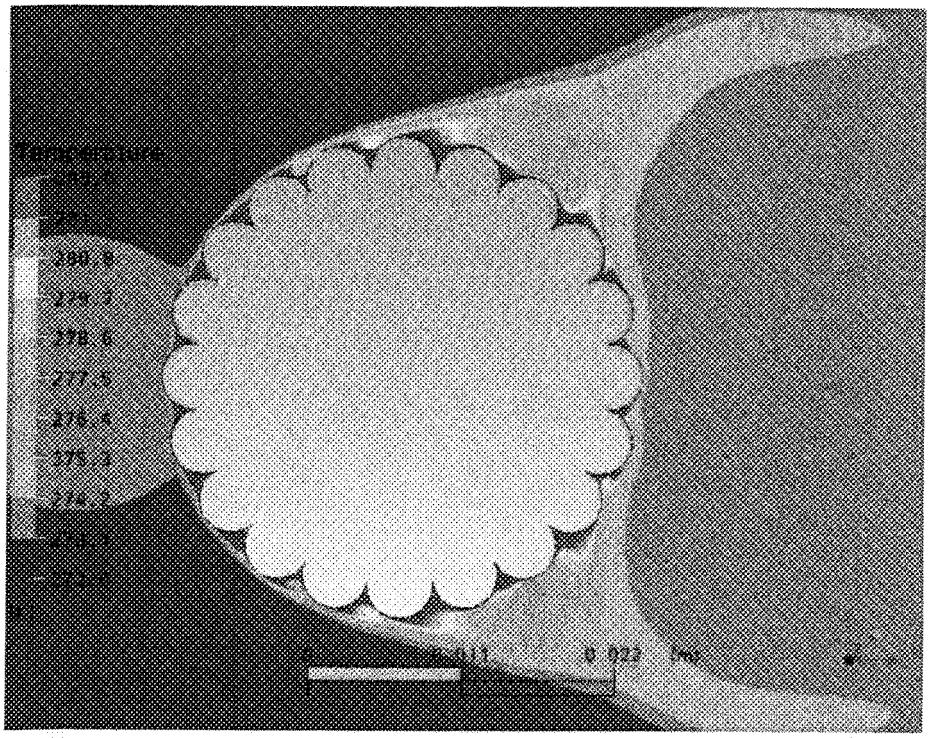

Air temperature distribution near stranded conductor surface after 0.005 s transient simulation time

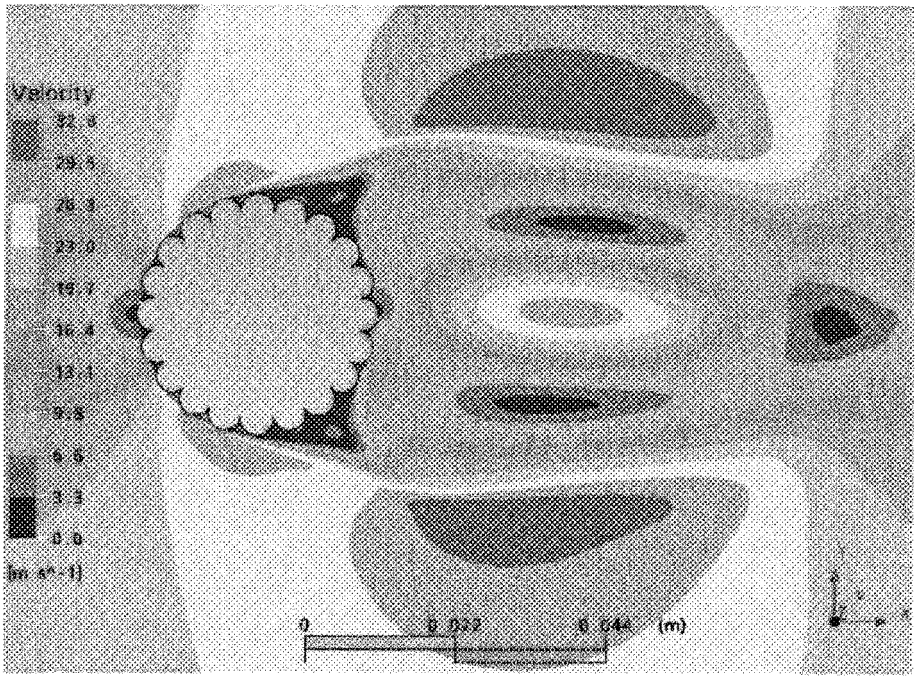

Velocity distribution of airflow around stranded conductor after 0.007 s transient simulation time

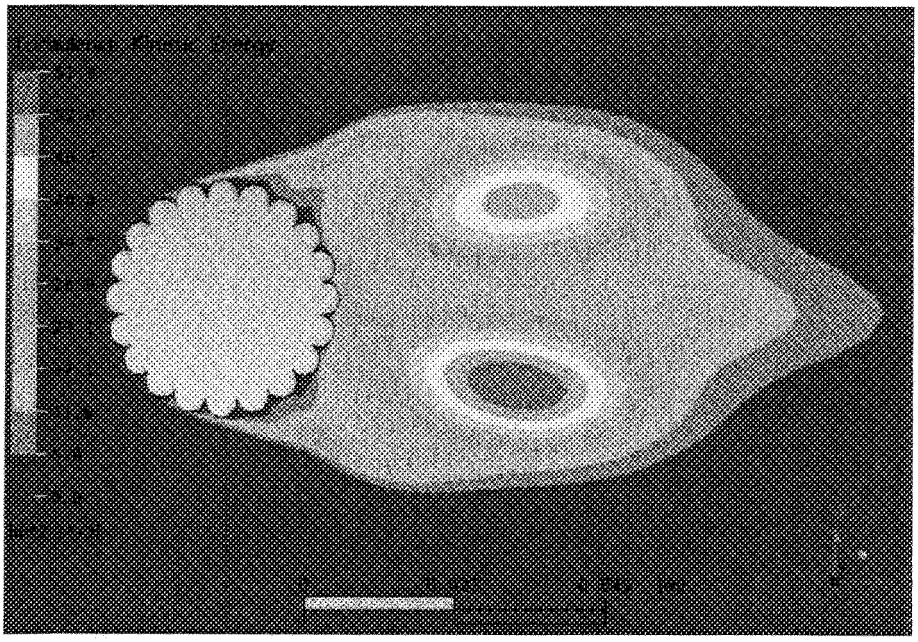

Turbulence kinetic energy of airflow after 0.007 s transient simulation time

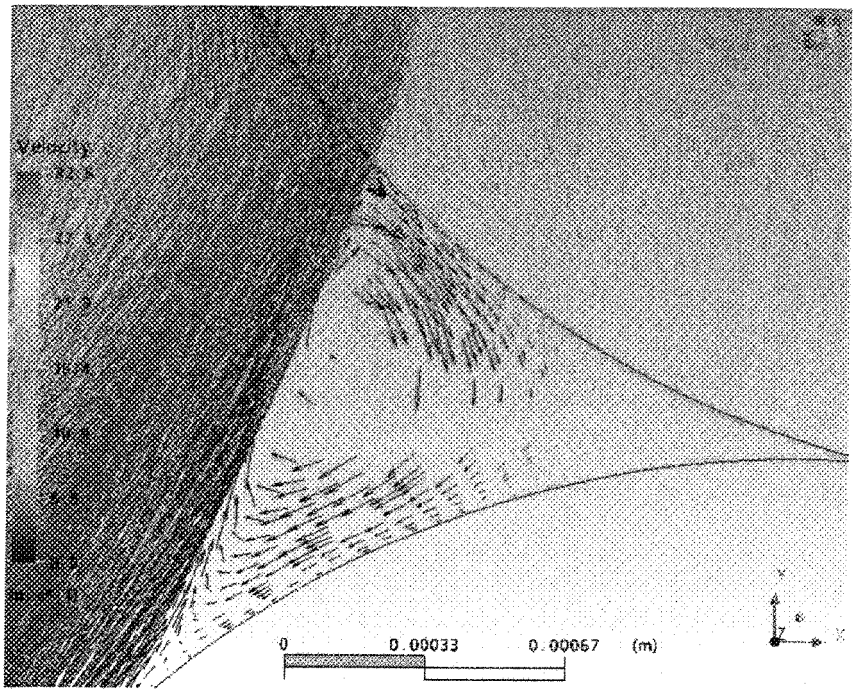

Airflow in channel between first and second strands (first strand in the stagnation point)

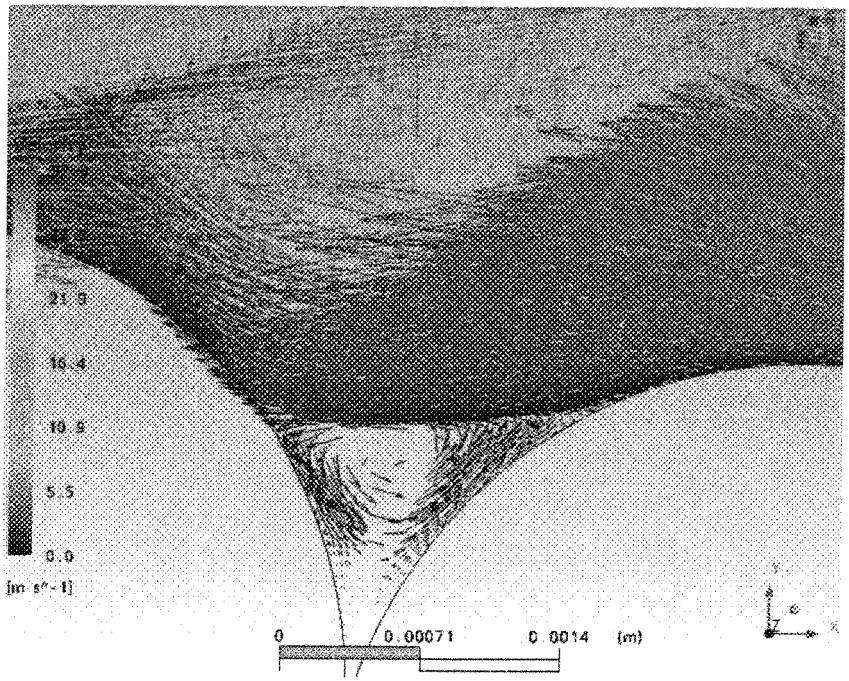

Airflow in channel between strand six and seven (first strand in the stagnation point)

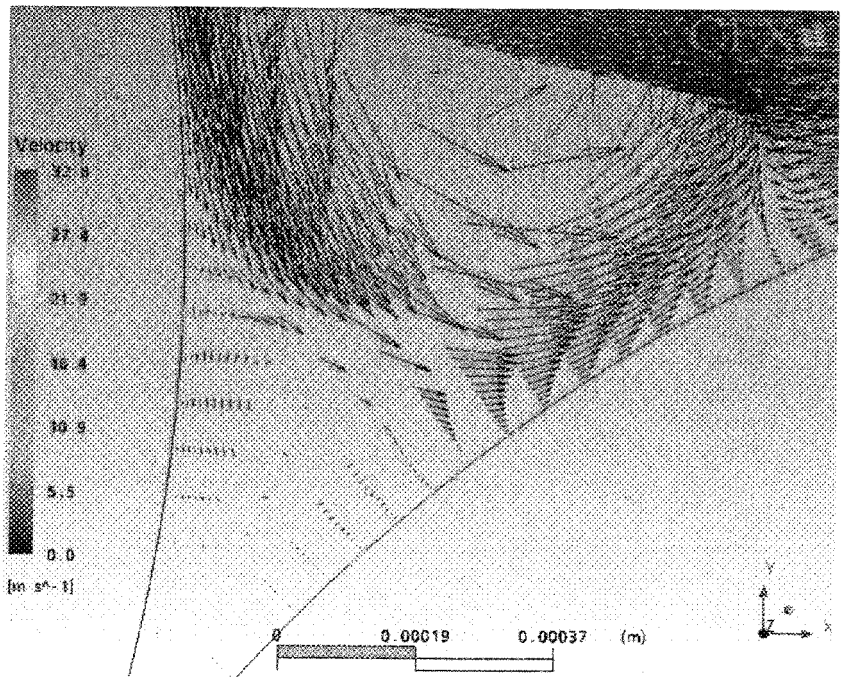

Airflow in channel between strands seven and eight, small scale (first strand in the stagnation point)

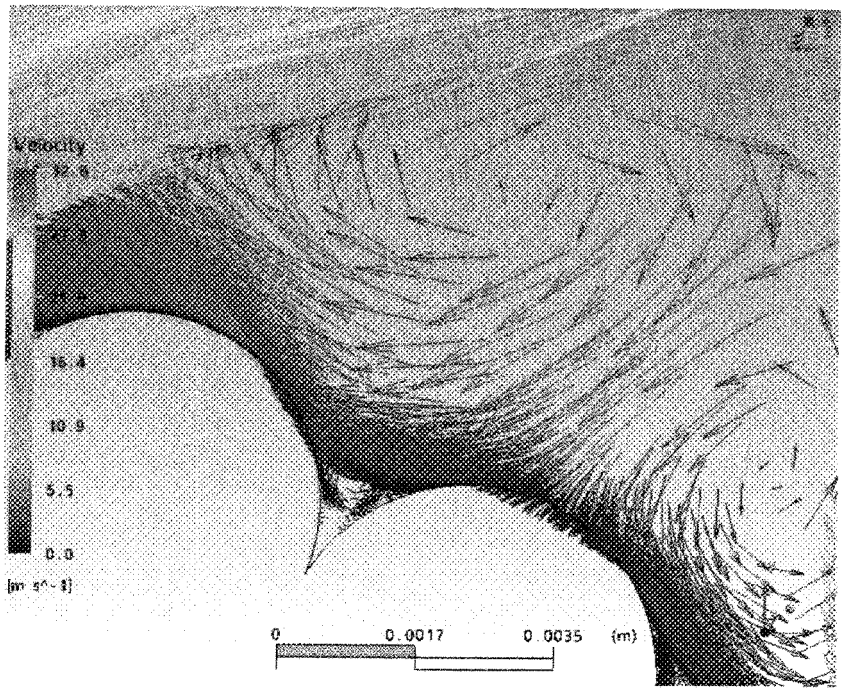

Airflow in channel between strand seven and eight, large scale (first strand in the stagnation point)

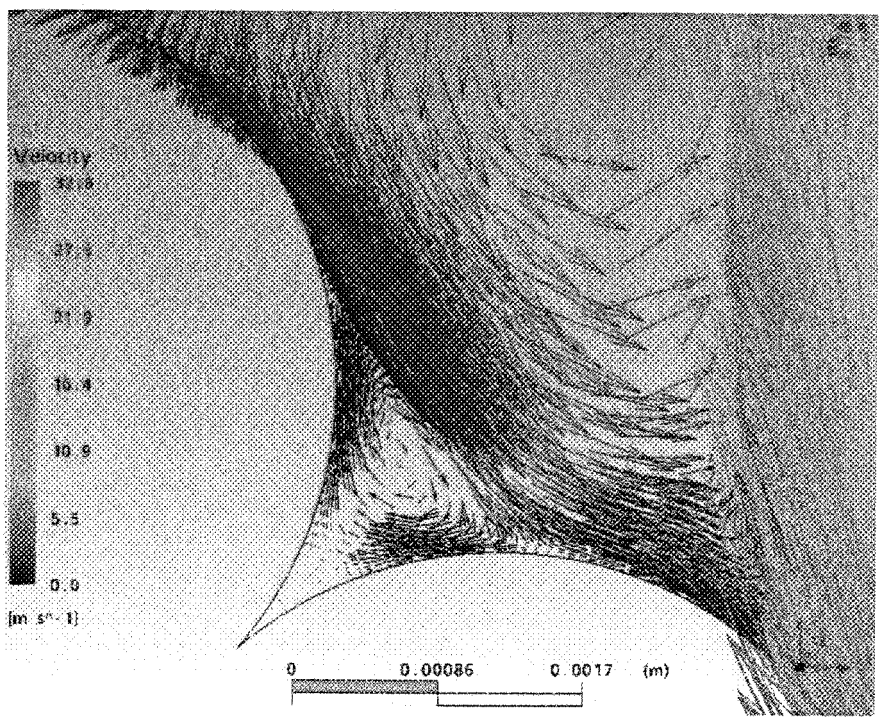

Airflow in channel between strand eight and ninth (first strand in the stagnation point)

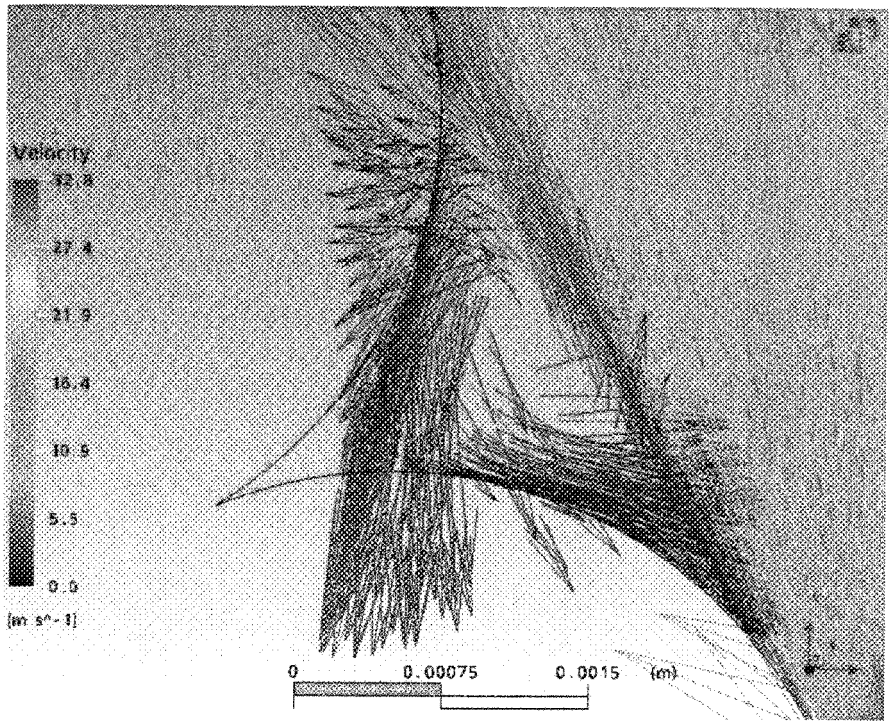

Airflow in channel between strand ninth and ten (first strand in the stagnation point)

Appendix 7.7 Results obtained for 2D stranded conductor at Re number of 41028

The following numerical results correspond to flow at Reynolds number of 41028 that is based on the stranded conductor outer diameter of 31.7 mm. First, the physical model was run in steady state (17 iteration steps) in order to start a convergence simulation. After, the transient simulation was started using the steady results as initial guess. The transient results were monitored continuously. The steady state solution was considered to be achieved, when two consecutive transient results correspond to each other in certain range.

The outer diameter of 2D stranded conductor is 31.7 mm, while it outside layer consists of 20 strands. The strand diameter is 4.3 mm. The velocity of the free stream is 20 m/s.

The applied mesh parameters accord to the case of smooth cylinder. The calculated y^+ values are in range of 0.0015÷1.815, except in two nodes, where extremely low values were reached. Later, the results obtained in these two nodes were not considered. The plot of y^+ distribution around stranded conductor surface is showed in the figure below.

The calculated overall Nu number from the numerical simulation results is *146.74* based on the conductor outer diameter (31.7 mm). This is calculated from the average value of HTC results in 1280 nodes along the half perimeter of stranded conductor upper part.

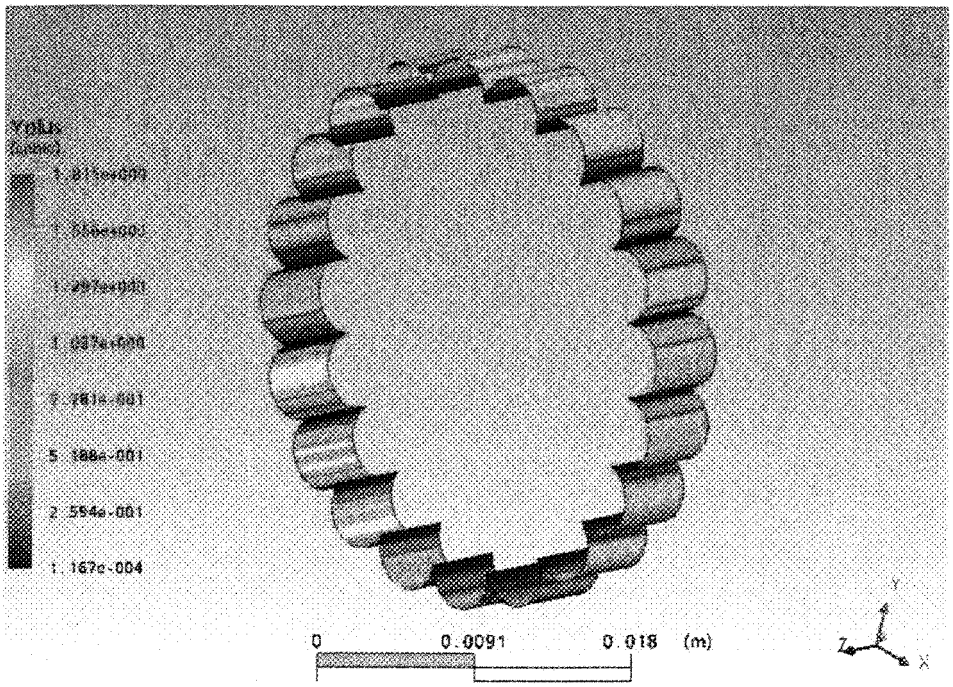

y^+ distribution around stranded surface of 2D conductor

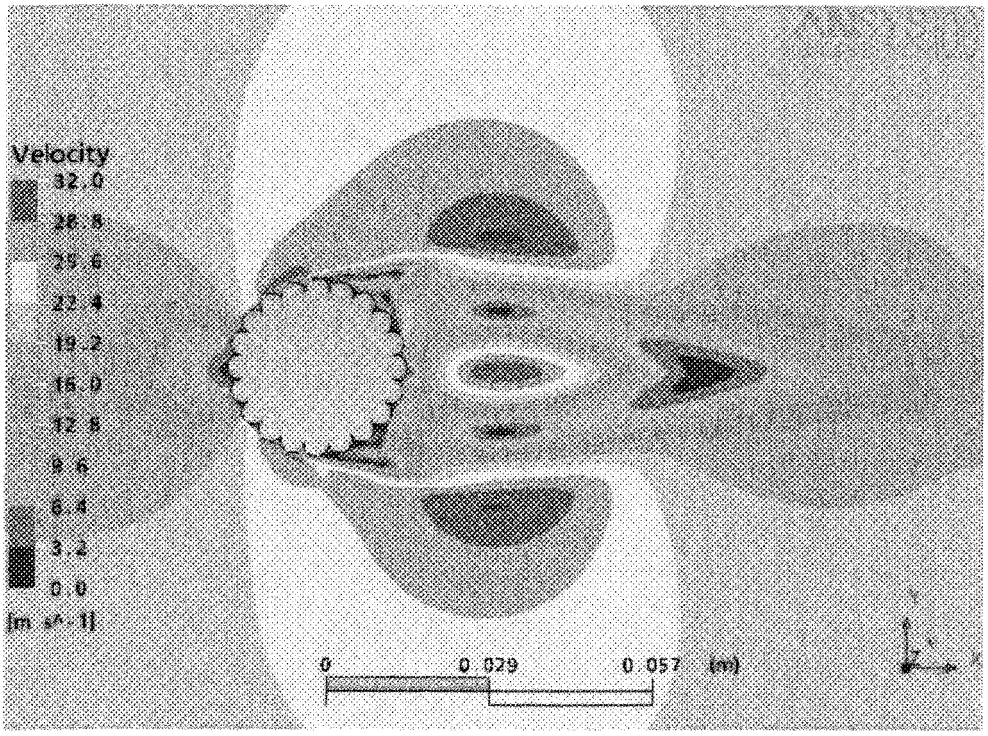

Velocity distribution around stranded conductor after 0.001 s transient time

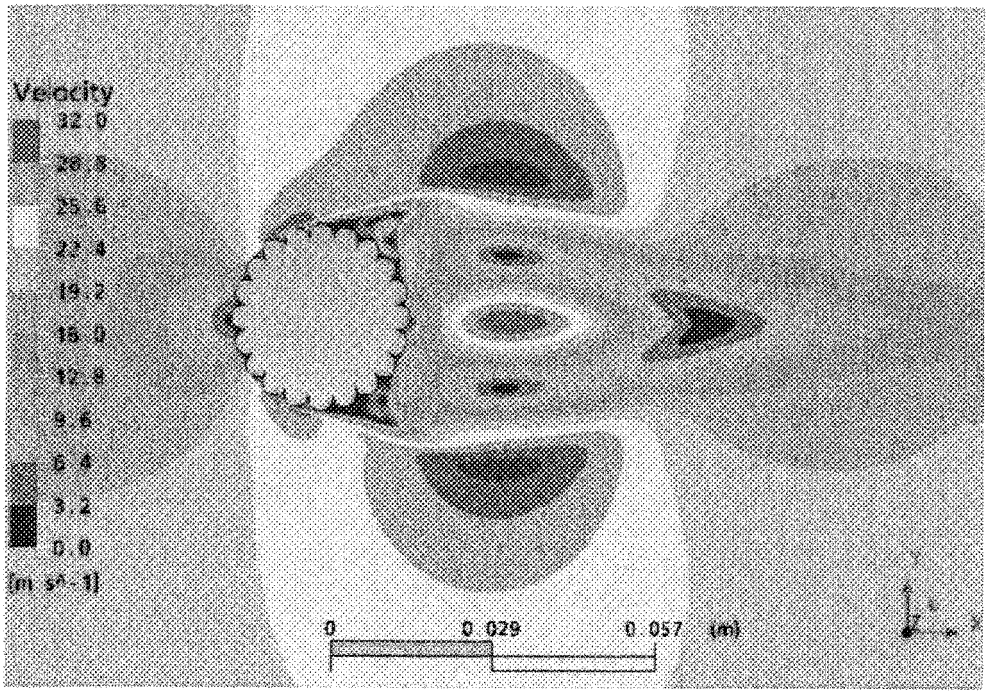

Velocity distribution around stranded conductor after 0.0018 s transient time

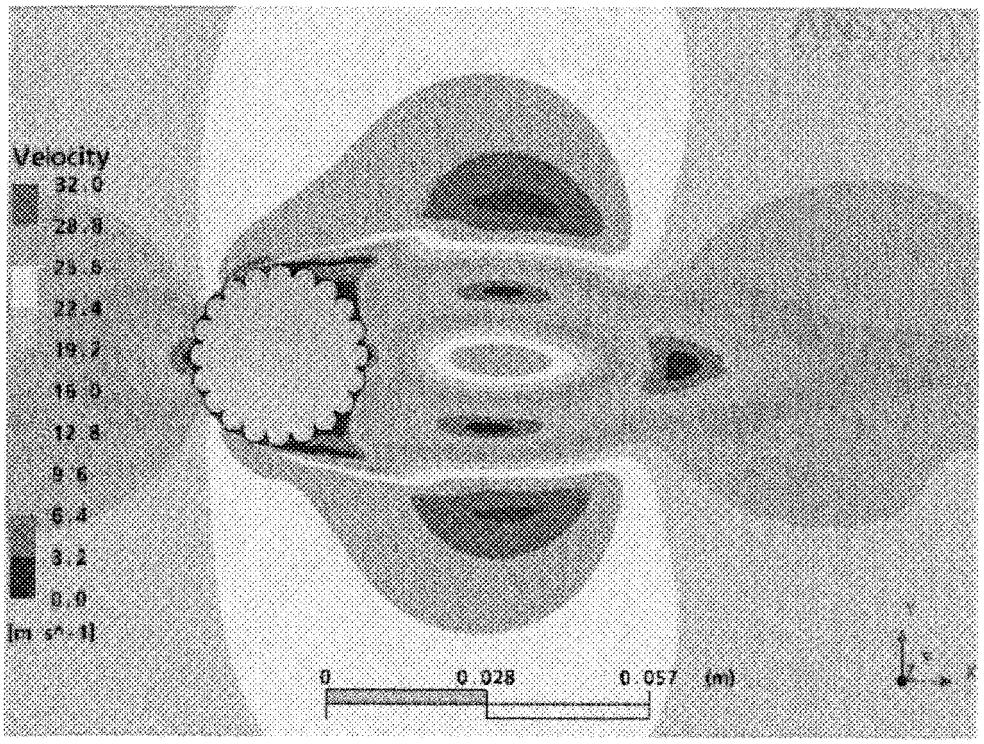

Velocity distribution around stranded conductor after 0.0039514 s transient time

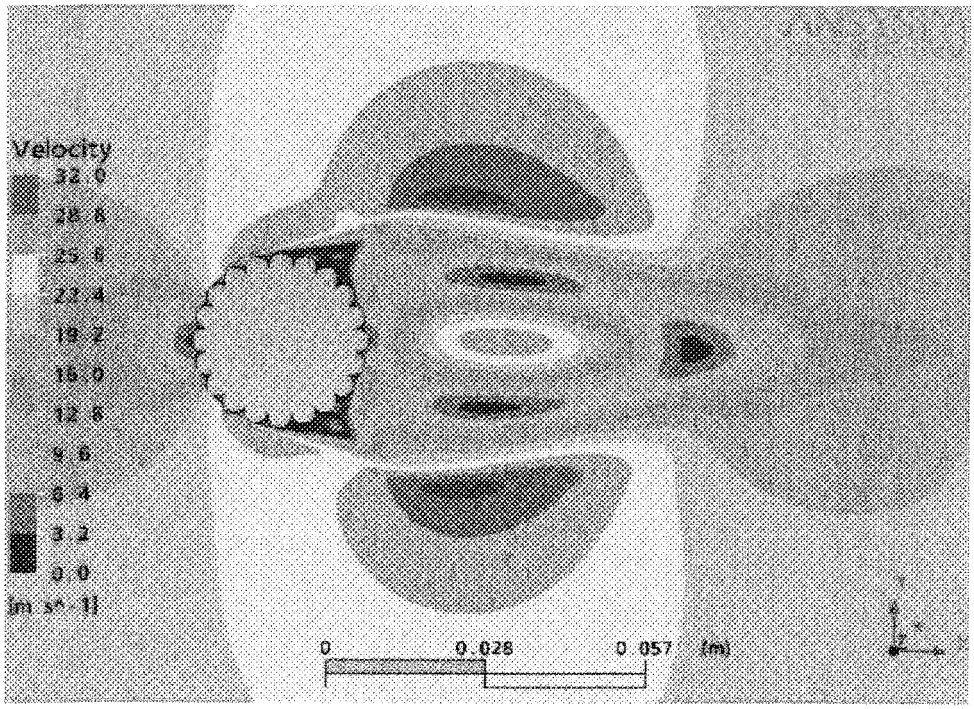

Velocity distribution around stranded conductor after 0.0050025 s transient time

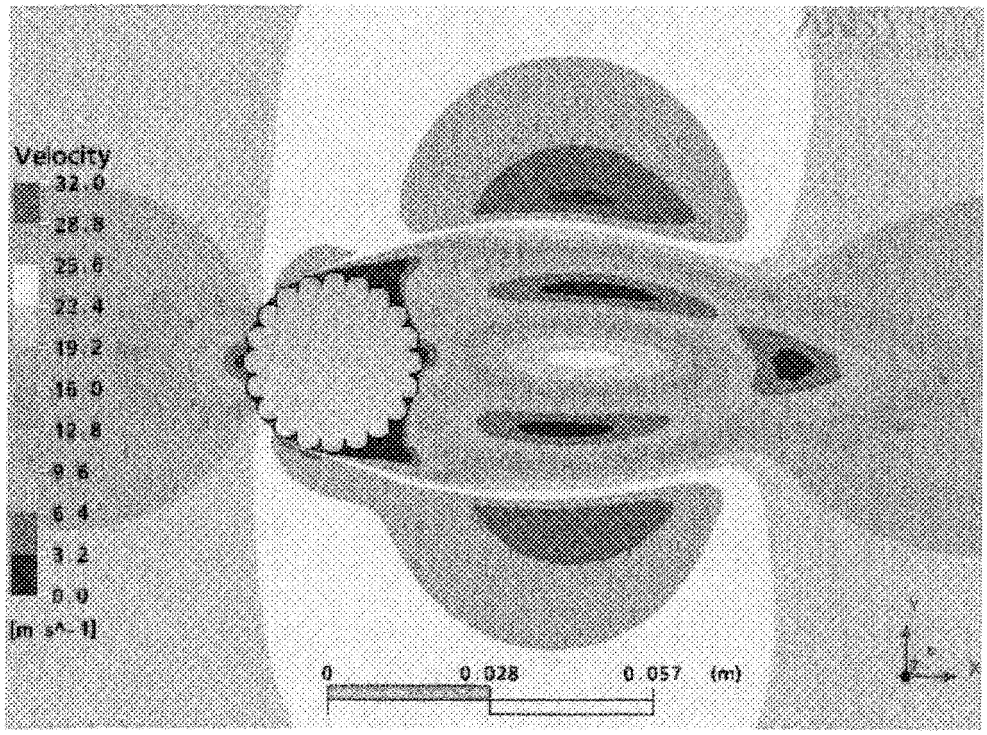

Velocity distribution around stranded conductor after 0.0071 s transient time

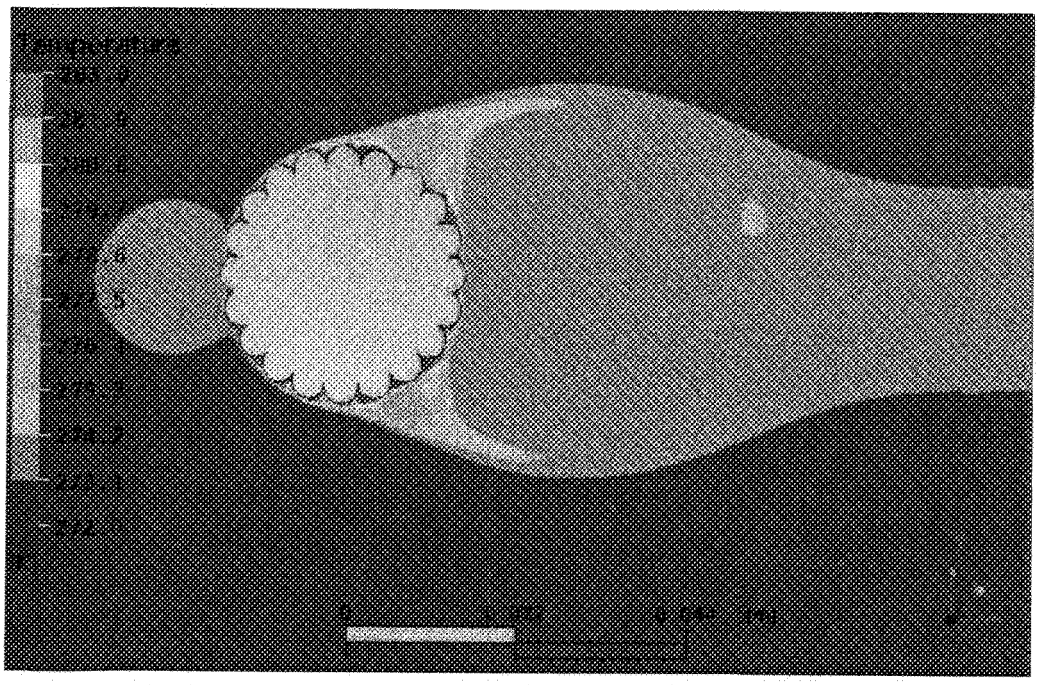

Temperature distribution around stranded conductor after 0.001 s transient time

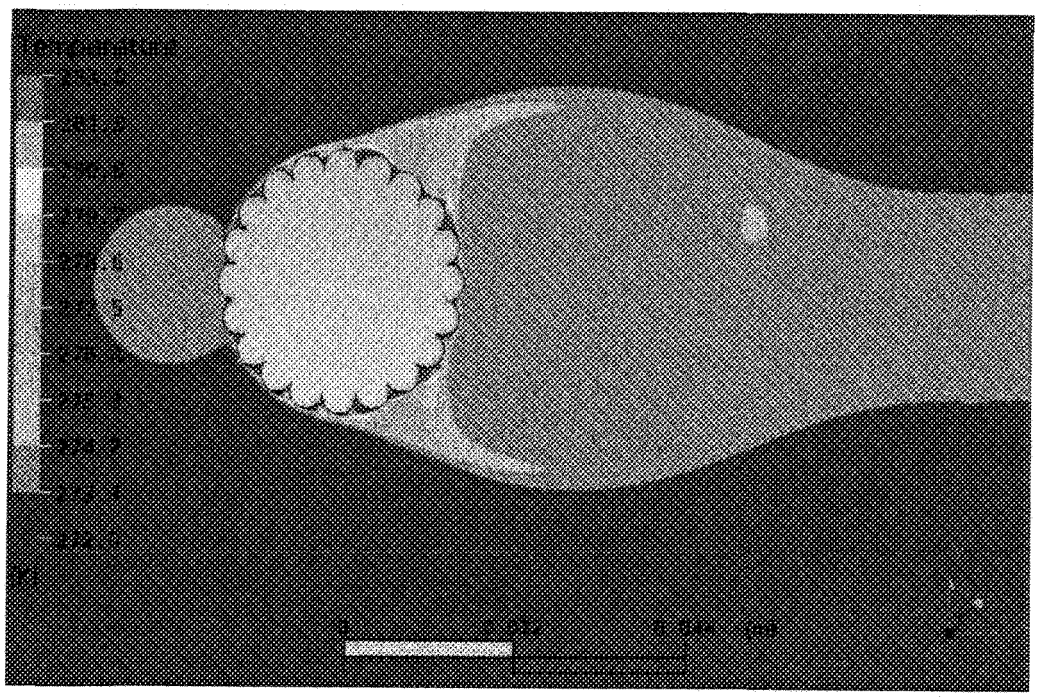

Temperature distribution around stranded conductor after 0.0018 s transient time

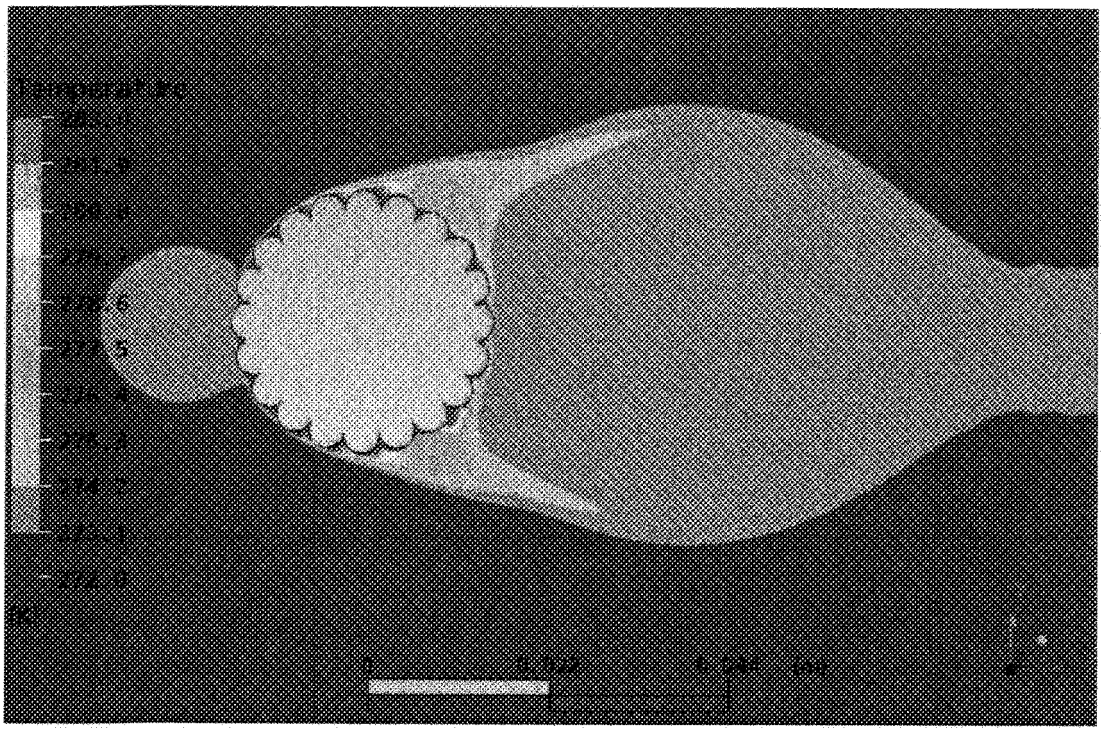

Temperature distribution around stranded conductor after 0.0039514 s transient time

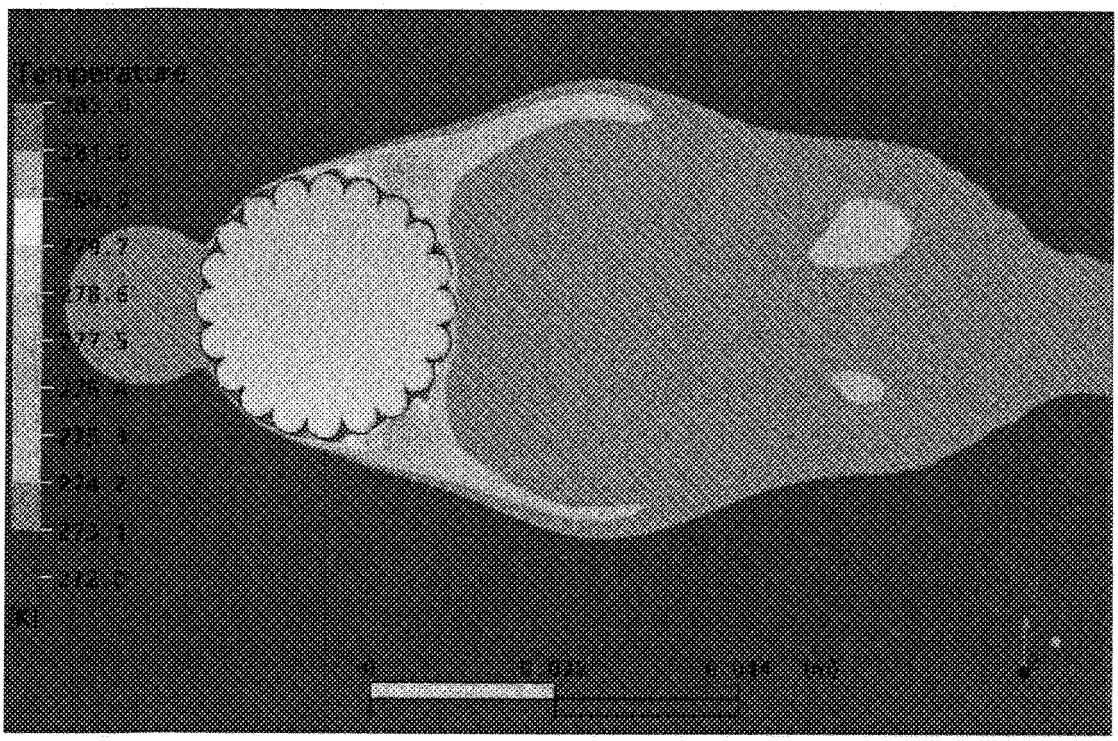

Temperature distribution around stranded conductor after 0.0054025 s transient time

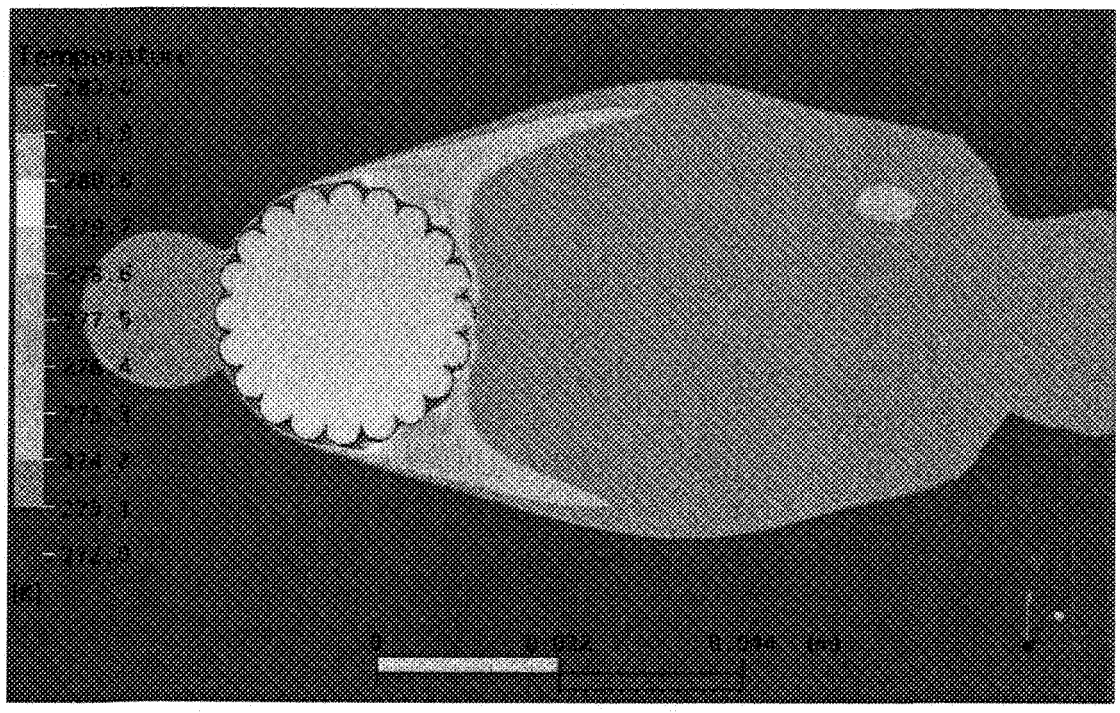

Temperature distribution around stranded conductor after 0.0071 s transient time

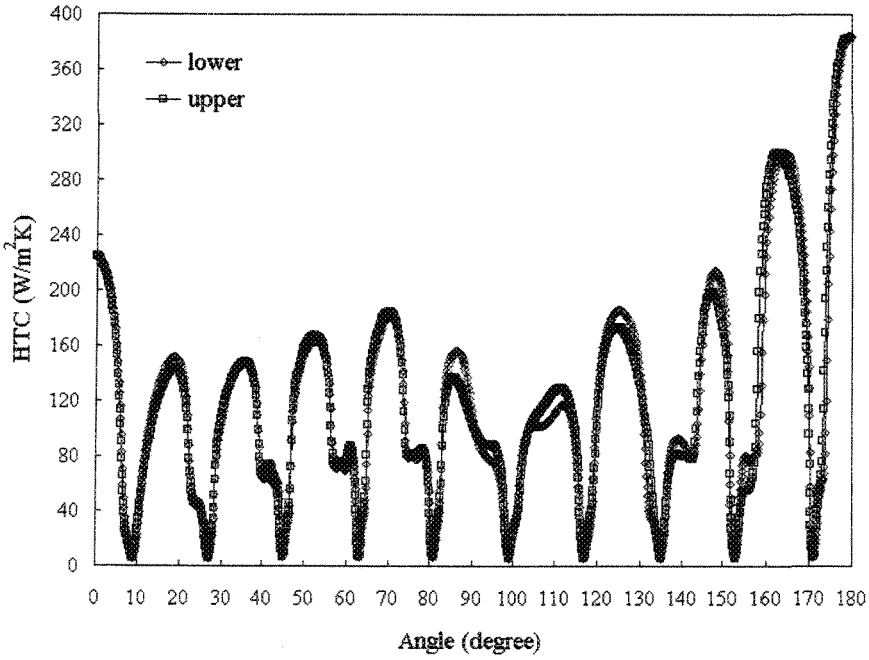

Heat transfer coefficient distribution around upper and lower part of stranded conductor (stagnation point is at zero degree)

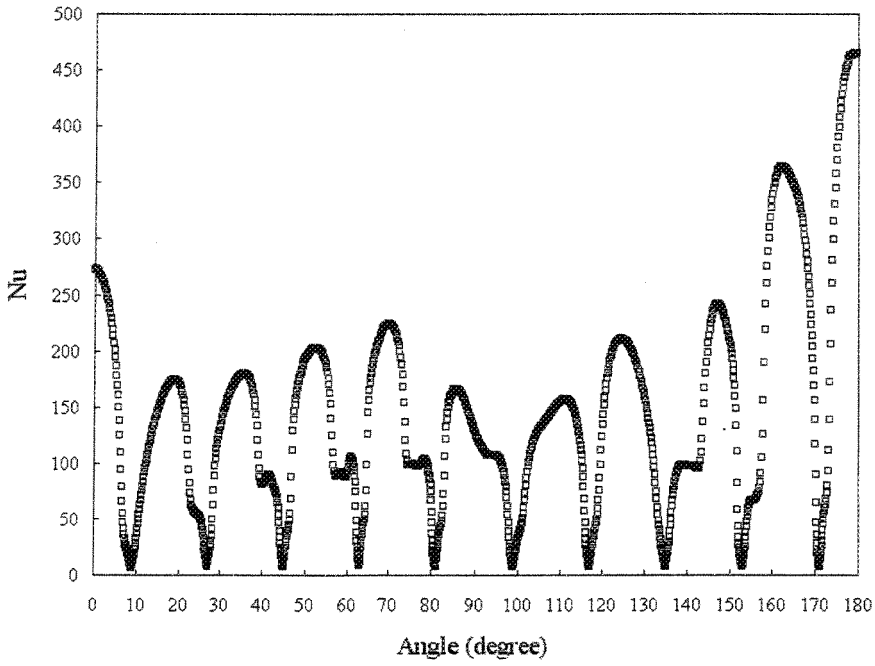

Nu number (based on outer diameter of 31.7 mm) distribution along upper half perimeter of stranded conductor

Appendix 7.8 Non-stable numerical results of flow around 2D stranded conductor at Re number of 41028

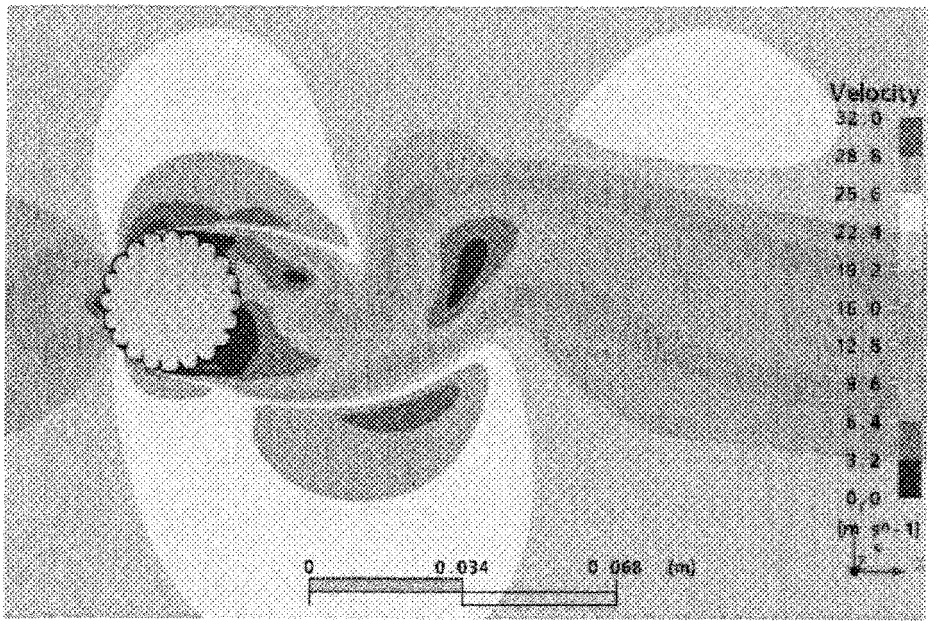

Non-stable velocity field around stranded surface in range of 0÷32 m/s

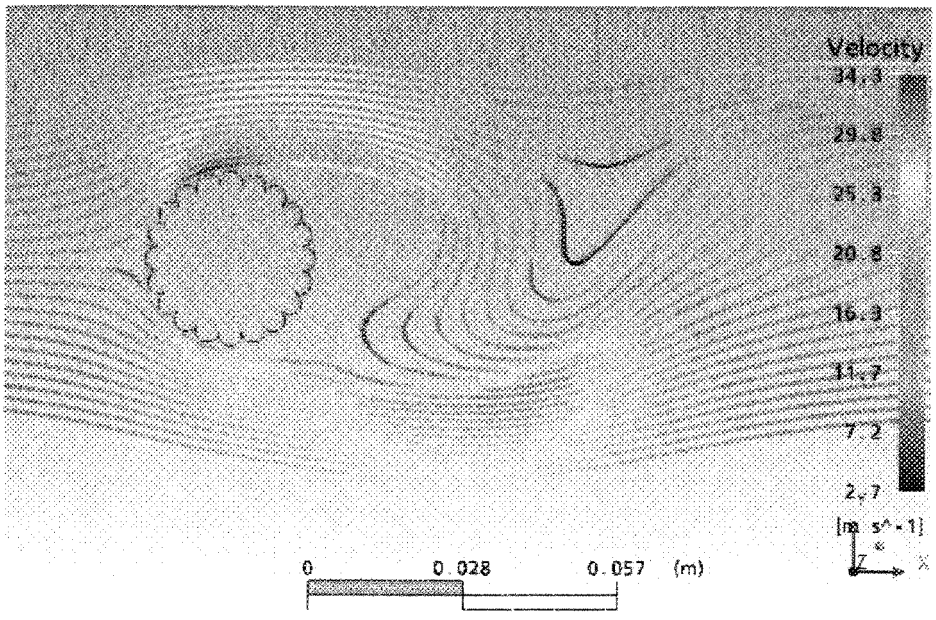

Streamlines around 2D stranded conductor

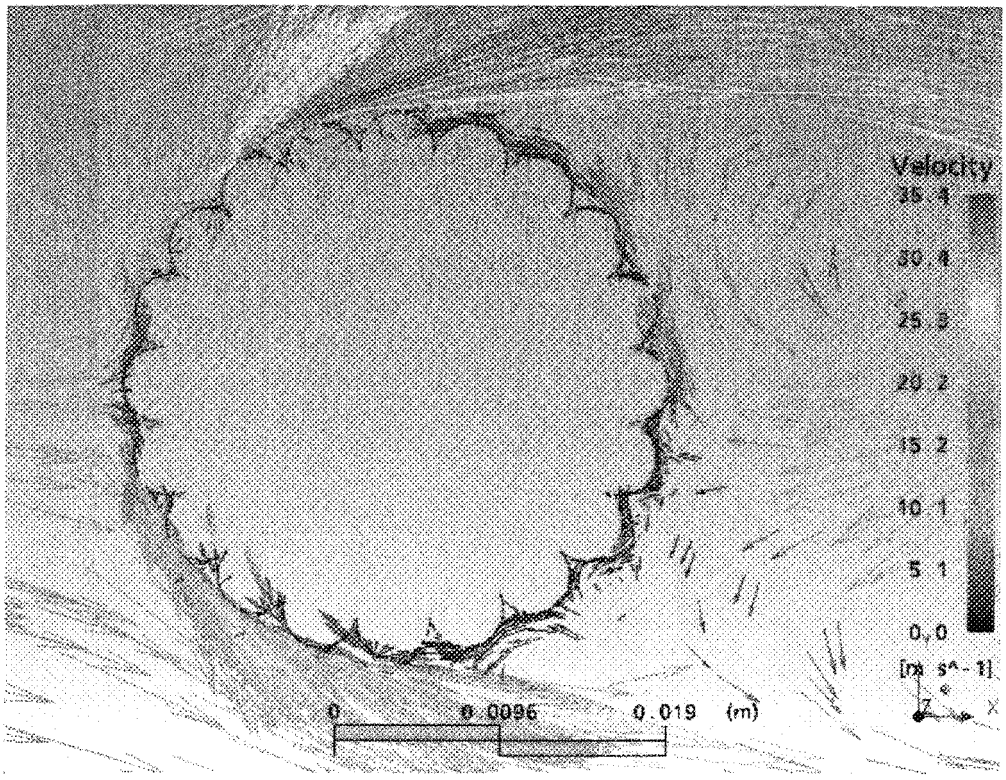

Flow around 2D stranded conductor (vector plot)

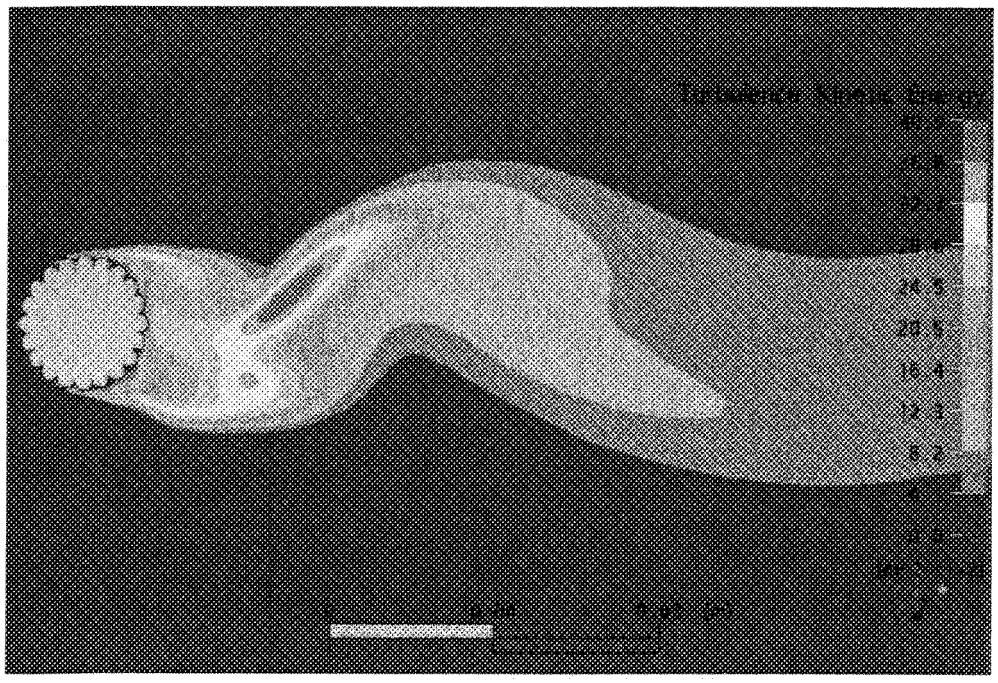

Turbulence kinetic energy in wake flow after stranded conductor

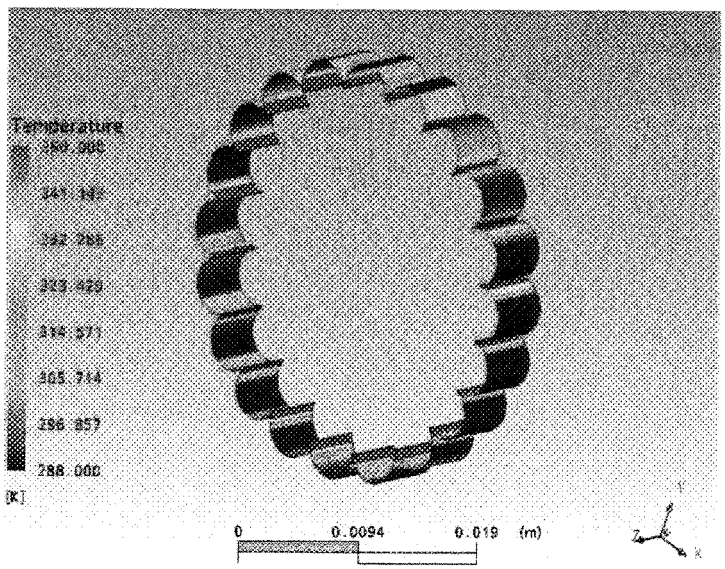

Temperature of 2D stranded conductor surface in range of 288÷350 K

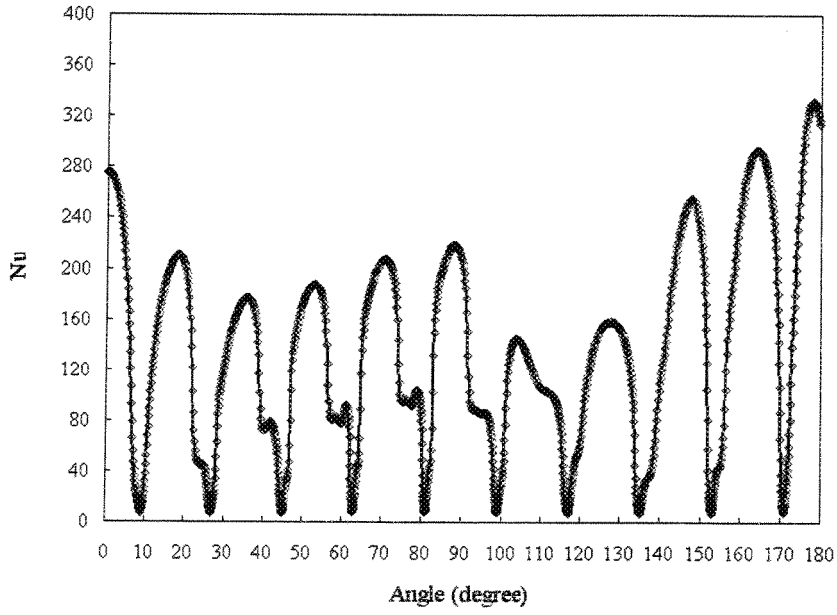

Nu number (based on outer diameter of 31.7 mm) distribution around upper half of stranded conductor (non-stable solution)

The calculated overall Nu number from the non-stable results along the perimeter is *138.19*, which is slightly smaller than it is obtained from stable solution.

Appendix 7.9 Numerical solutions of flow around 3D stranded conductor

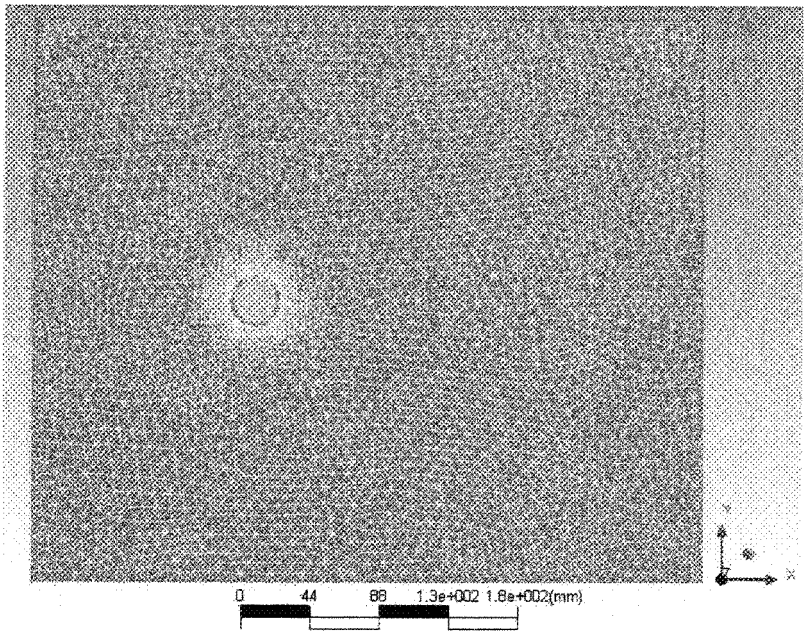

Surface mesh of computational domain

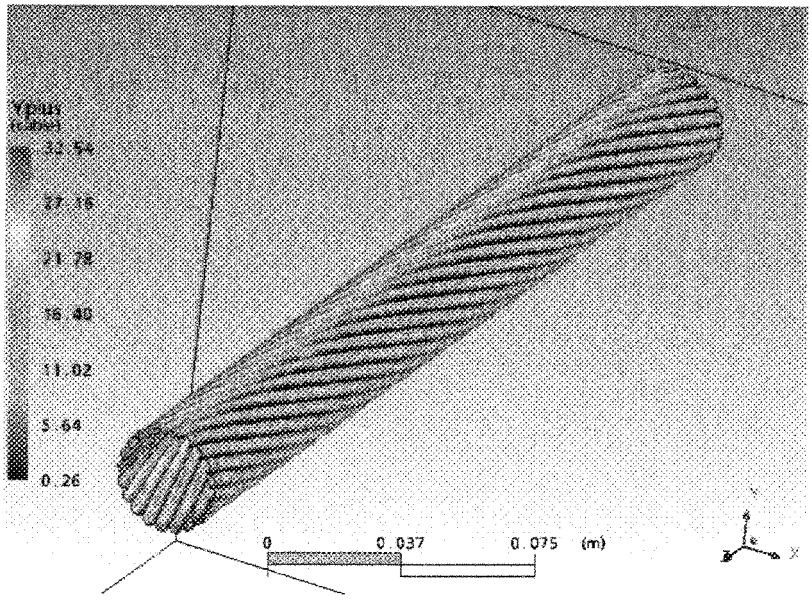

Distribution of y^+ values on twisted conductor surface

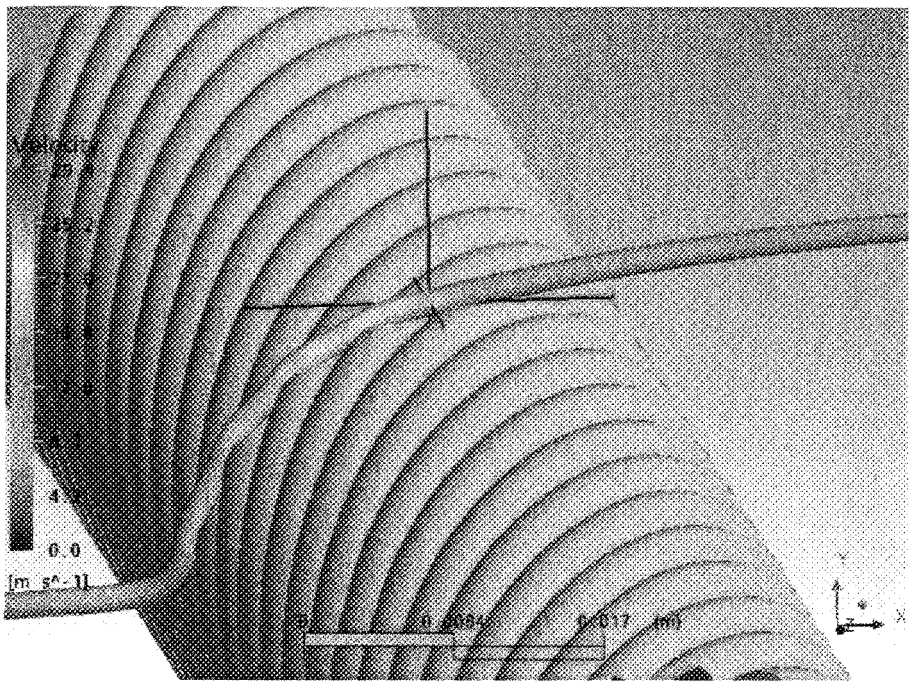

Streamlines at windward side of the conductor

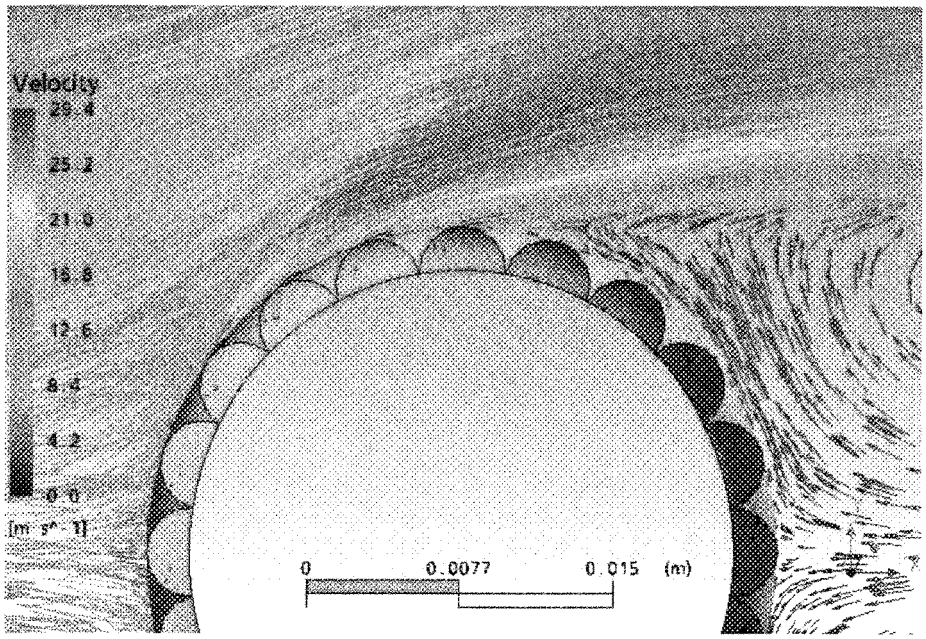

Flow field close to surface of stranded and twisted conductor (2D vector plot)

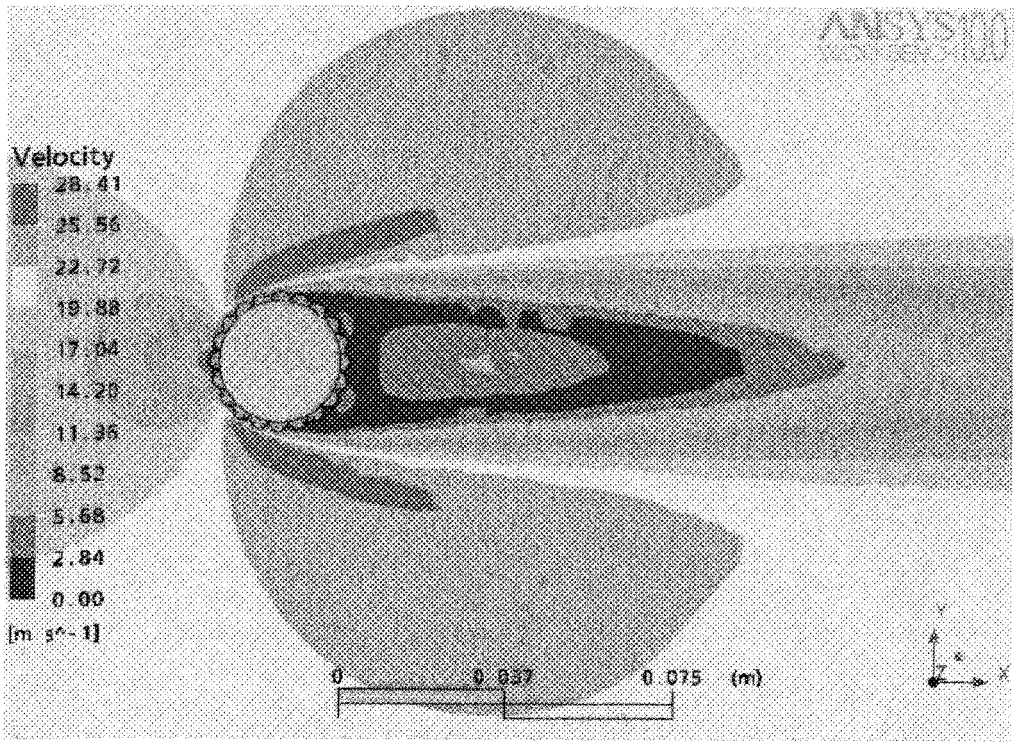

2D velocity field around twisted conductor at z=0.225 m

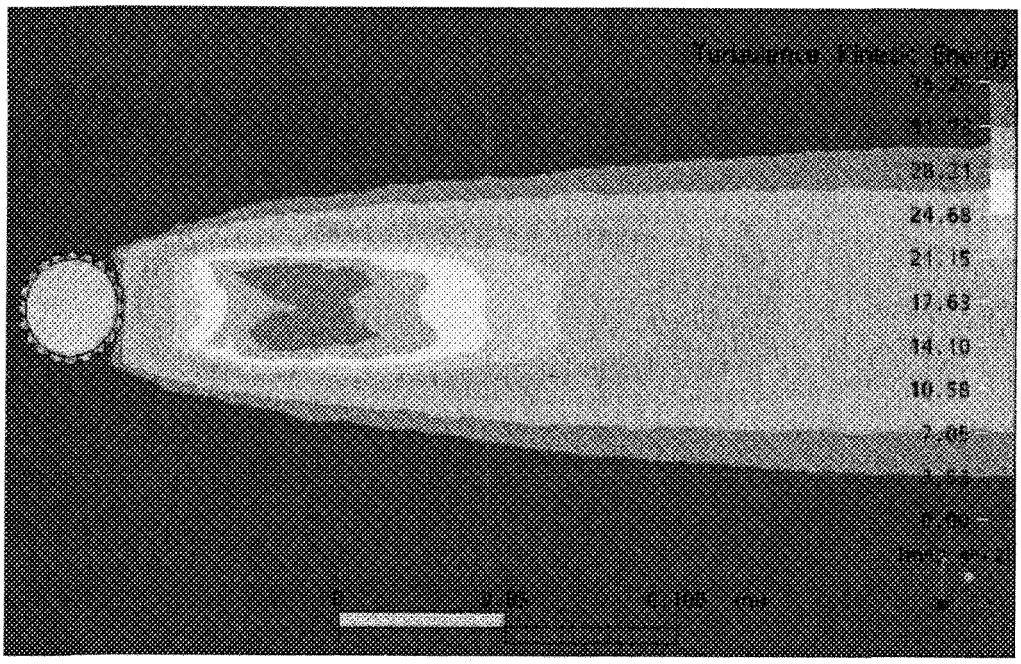

Turbulence kinetic energy distribution in wake flow after stranded and twisted conductor (2D plot at plane z=0.15 m, center plane of fluid domain)

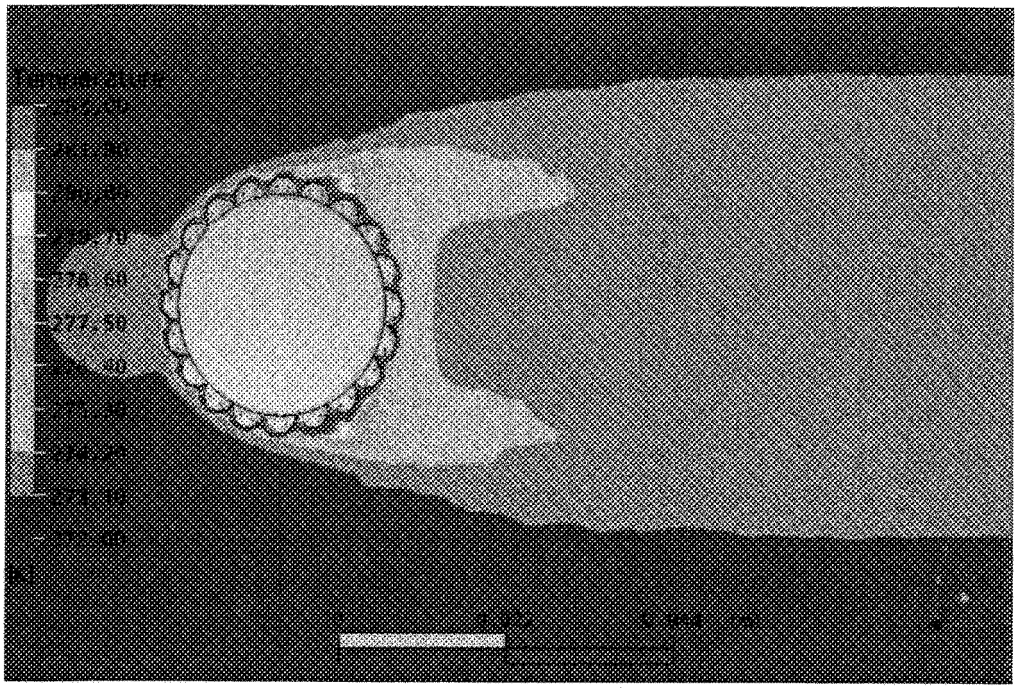

Temperature of airflow around twisted and stranded conductor in range of 272÷283 K (2D plot at plane z=0.15 m, center plane of fluid domain)

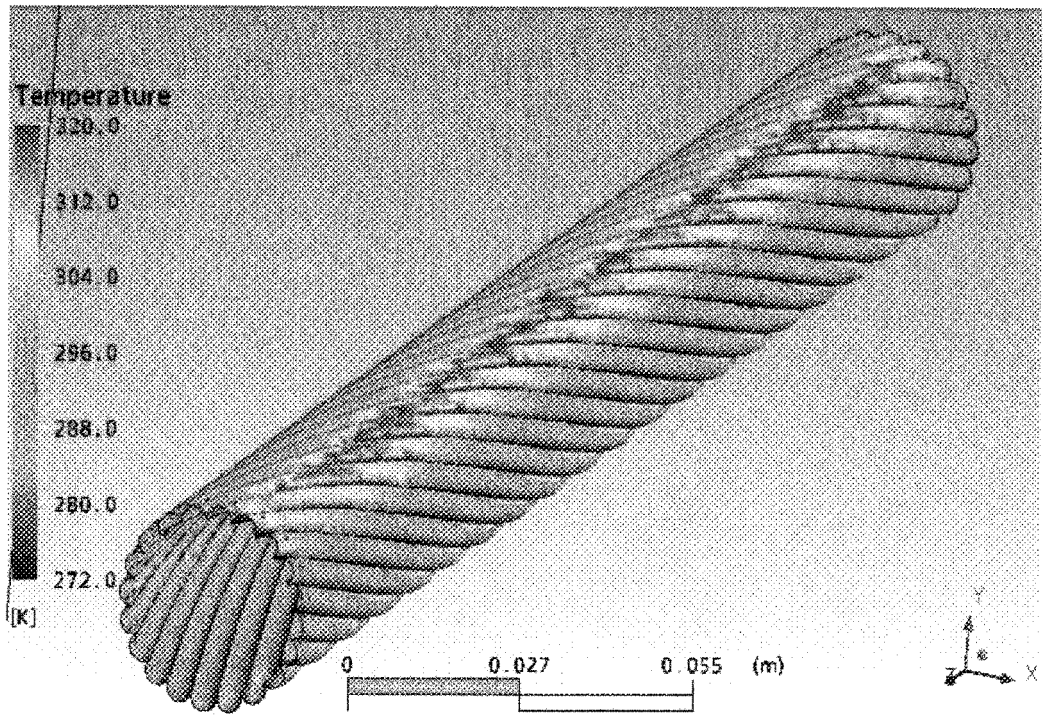

Temperature of conductor rear surface in range of 272÷320 K

APPENDIX 8 THE BESSEL FUNCTIONS REAL AND IMAGINARY

The Bessel functions real and imaginary can be calculated using Kelvin's series as follows [23]:

$$ber(u) = 1 - \frac{u^4}{2^2 \cdot 4^2} + \frac{u^8}{2^2 \cdot 4^2 \cdot 6^2 \cdot 8^2} - \ldots$$

$$bei(u) = \frac{u^2}{2^2} - \frac{u^6}{2^2 \cdot 4^2 \cdot 6^2} + \frac{u^{10}}{2^2 \cdot 4^2 \cdot 6^2 \cdot 8^2 \cdot 10^2} - \ldots$$

The graphical representation of these functions and the absolute value of their addition are showed by the Figure below:

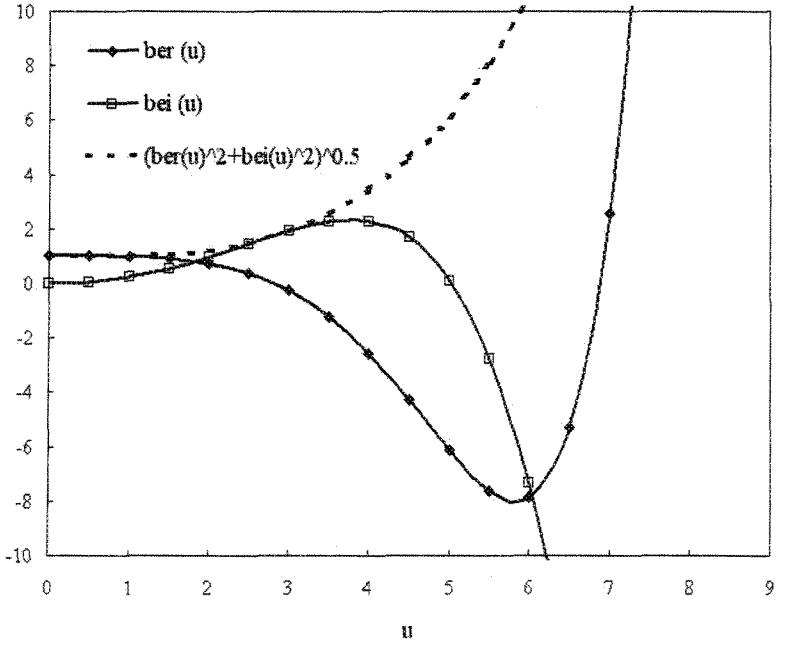

Special Bessel functions and their absolute value

APPENDIX 9 THERMOCOUPLE INSTALLATIONS

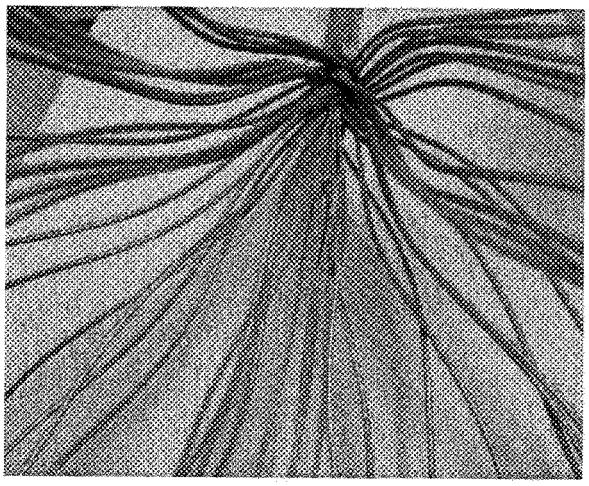

Thermocouple installed in the steel core

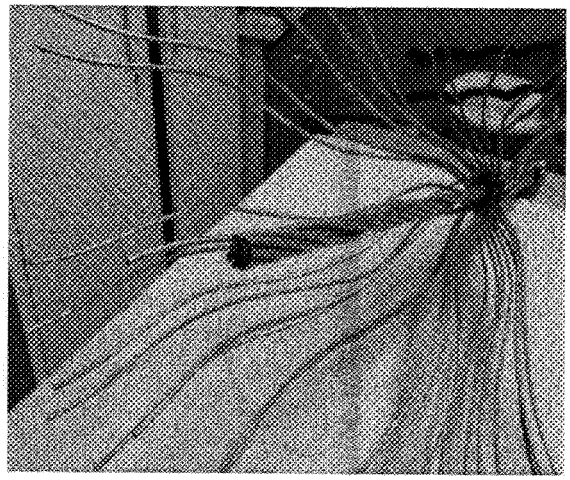

Closing the steel core

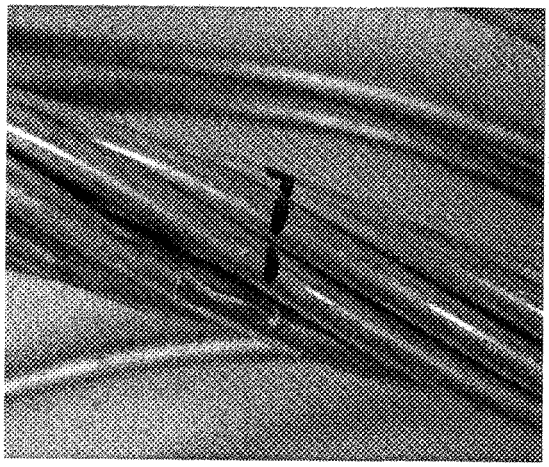

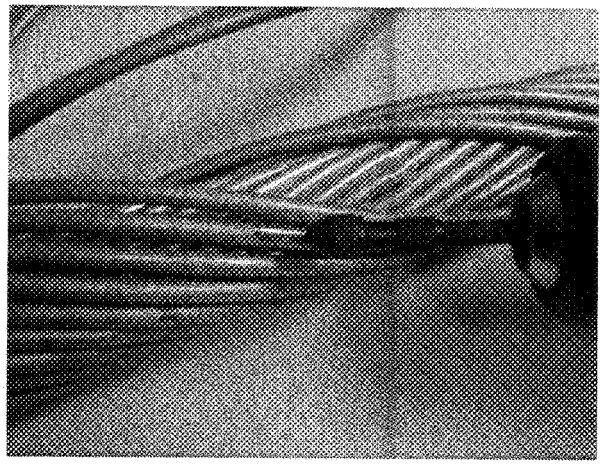

Installing thermocouples in the aluminium strands

APPENDIX 10 CALIBRATING TRANSFORMER CIGELE-S5000A

The transformer is recalibrated with current transformer Flexcore 126-502 in range of 0-4500 A. Totally 130 measurements have been made. The current transformers (CT) output is measured with two serially connected digital multimeters. The calibration of transformer is divided in certain ranges depending on Variac positions, and on measurement precision.

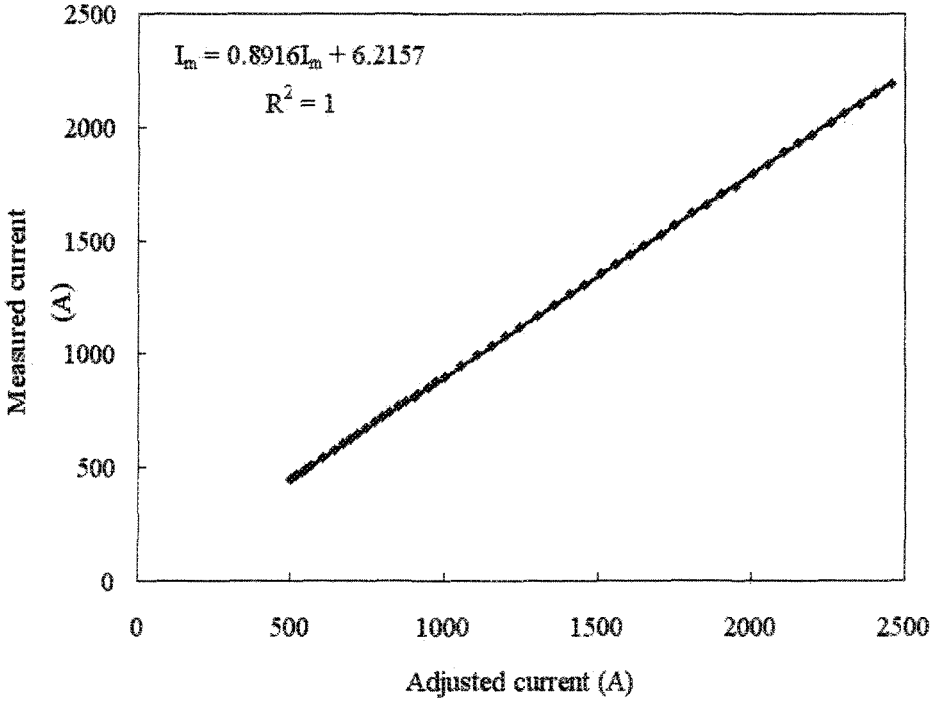

Calibration curve using in first position of Variac

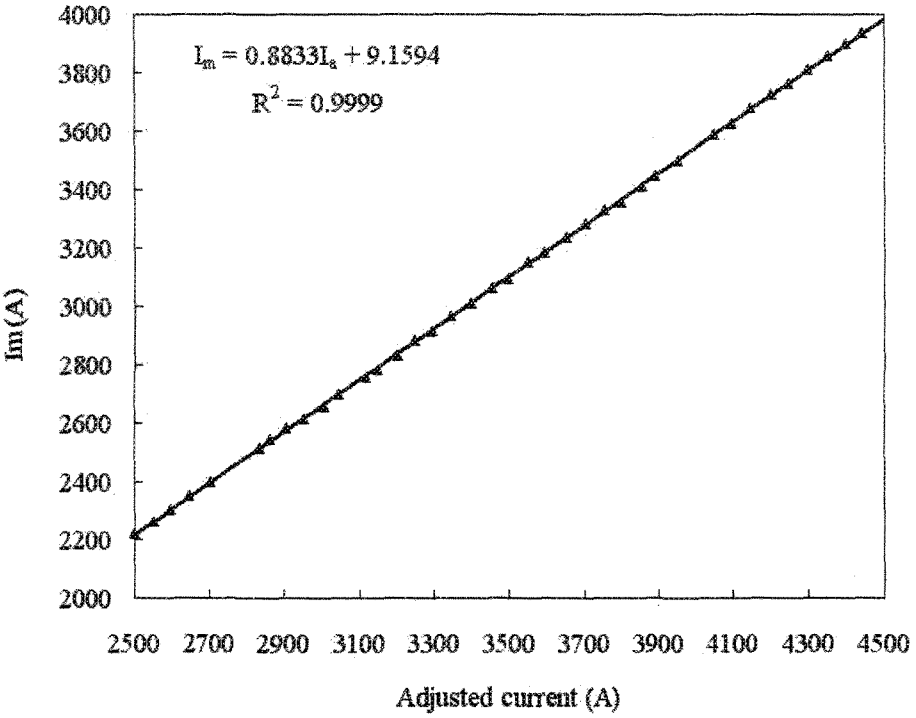

Calibration curve using in second position of Variac